

AD-A213 344

GL-TR-89-0124(IV)
Report PSI-9032/TR-901

CANOE II: DYNAMICS OF ATMOSPHERIC INFRARED
THERMOCHEMICAL EXCITATION

W.T. Rawlins
L.G. Piper
M.E. Fraser
H.C. Murphy
T.R. Tucker
A. Gelb

Physical Sciences Inc.
Research Park
P.O. Box 3100
Andover, MA 01810

March 1989

Final Report
24 March 1985 - 24 May 1989

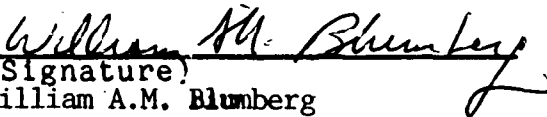
APPROVED FOR PUBLIC RELEASE; DISTRIBUTION UNLIMITED

GEOPHYSICS LABORATORY
AIR FORCE SYSTEMS COMMAND
UNITED STATES AIR FORCE
HANSCOM AIR FORCE BASE, MA 01731-5000

89 10 10152

"This technical report has been reviewed and is approved for publication"


(Signature)
STEVEN M. MILLER
Contract Manager


(Signature)
William A.M. Blumberg
Branch Chief, Acting

FOR THE COMMANDER


(Signature)
R. EARL GOOD
Director

This report has been reviewed by the ESD Public Affairs Office (PA) and is releasable to the National Technical Information Service (NTIS).

Qualified requestors may obtain additional copies from the Defense Technical Information Center. All others should apply to the National Technical Information Service.

If your address has changed, or if you wish to be removed from the mailing list, or if the addressee is no longer employed by your organization, please notify AFGL/DAA, Hanscom AFB, MA 01731. This will assist us in maintaining a current mailing list.

Do not return copies of this report unless contractual obligations or notices on a specific document requires that it be returned.

UNCLASSIFIED

SECURITY CLASSIFICATION OF THIS PAGE

REPORT DOCUMENTATION PAGE

1a. REPORT SECURITY CLASSIFICATION UNCLASSIFIED			1b. RESTRICTIVE MARKINGS N/A since unclassified		
2a. SECURITY CLASSIFICATION AUTHORITY N/A since unclassified			3. DISTRIBUTION / AVAILABILITY OF REPORT Approved for public release; distribution unlimited		
2b. DECLASSIFICATION / DOWNGRADING SCHEDULE N/A since unclassified					
4. PERFORMING ORGANIZATION REPORT NUMBER(S) PSI-9032/TR-901 (Volume IV)			5. MONITORING ORGANIZATION REPORT NUMBER(S) GL-TR-89-0124 (IV)		
6a. NAME OF PERFORMING ORGANIZATION Physical Sciences Inc.		6b. OFFICE SYMBOL (if applicable)		7a. NAME OF MONITORING ORGANIZATION Geophysics Laboratory	
6c. ADDRESS (City, State, and ZIP Code) Research Park, P.O. Box 3100 Andover, MA 01810			7b. ADDRESS (City, State, and ZIP Code) Hanscom Air Force Base, MA 01731-5000		
8a. NAME OF FUNDING / SPONSORING ORGANIZATION GL		8b. OFFICE SYMBOL (if applicable)		9. PROCUREMENT INSTRUMENT IDENTIFICATION NUMBER F19628-85-C-0032	
8c. ADDRESS (City, State, and ZIP Code) Hanscom Air Force Base, MA 01731-5000			10. SOURCE OF FUNDING NUMBERS		
			PROGRAM ELEMENT NO. 61102F	PROJECT NO. 2310	TASK NO. G4
			WORK UNIT ACCESSION NO BJ		
11. TITLE (Include Security Classification) CANOES II: Dynamics of Atmospheric Infrared Thermochemical Excitation					
12. PERSONAL AUTHOR(S) Rawlins, Wilson T.; Piper, Lawrence G.; Fraser, Mark E.; Murphy, Henry C.; Tucker, Thomas P.; and Gelb, A.					
13a. TYPE OF REPORT Final		13b. TIME COVERED FROM 850324 TO 890524		14. DATE OF REPORT (Year, Month, Day) 1989 March	
15. PAGE COUNT 242					
16. SUPPLEMENTARY NOTATION Volume I: pages 1-92; Volume II: pages 93-372; Volume III: pages 373-624; Volume IV: pages 625-862					
17. COSATI CODES			18. SUBJECT TERMS (Continue on reverse if necessary and identify by block number)		
FIELD	GROUP	SUB-GROUP	Infrared emission, Oxygen, Nitrogen, Nitric oxide, Ozone, Molecular dynamics, Vibrational excitation, Atmospheric background		
19. ABSTRACT (Continue on reverse if necessary and identify by block number)					
<p>In the electron disturbed upper atmosphere, electronically excited metastable forms of oxygen and nitrogen are formed by electron impact processes. These species dissipate their energy into the atmosphere largely by collisional quenching and chemical reaction. Specific species and reactions of interest include: (1) electronically and/or vibrationally excited nitrogen, N_2^*, its spectroscopy, energy pooling and interactions with O, O_2 and trace, infrared-active atmospheric species such as CO, CO_2, and N_2O; (2) metastable atomic nitrogen, $N(^2D, ^2P)$, reaction kinetics and product branching ratios in interactions with the above atmospheric species; (3) various metastable states of O_2, O_2^*, and their potential as auroral precursors of infrared radiation.</p>					
20. DISTRIBUTION / AVAILABILITY OF ABSTRACT <input checked="" type="checkbox"/> UNCLASSIFIED/UNLIMITED <input type="checkbox"/> SAME AS RPT <input type="checkbox"/> OTIC USERS			21. ABSTRACT SECURITY CLASSIFICATION UNCLASSIFIED/UNLIMITED		
22a. NAME OF RESPONSIBLE INDIVIDUAL Steven Miller			22b. TELEPHONE (Include Area Code)		22c. OFFICE SYMBOL GL/OPI

DD FORM 1473, 84 MAR

83 APR edition may be used until exhausted.

All other editions are obsolete.

UNCLASSIFIED

UNCLASSIFIED

SECURITY CLASSIFICATION OF THIS PAGE

19. ABSTRACT (Continued)

from other atmospheric species; and (4) the role of metastable-metastable O_2/N_2 interactions as potential sources for non-linear infrared effects which might occur in strong aurorae. This document reports on the results from a four-year coupled experimental program using the COCHISE and FAKIR facilities to investigate these issues in fundamental detail.

UNCLASSIFIED

SECURITY CLASSIFICATION OF THIS PAGE

CONTENTS

<u>Section</u>	<u>Page</u>
APPENDICES	
P. ROVIBRATIONAL EXCITATION OF NITRIC OXIDE IN THE REACTION OF O ₂ WITH METASTABLE ATOMIC NITROGEN	627
Q. ROVIBRATIONAL EXCITATION OF CARBON MONOXIDE BY ENERGY TRANSFER FROM METASTABLE NITROGEN	683
R. CLASSICAL TRAJECTORY STUDY OF OZONE RECOMBINATION DYNAMICS: THE CHAPERON MECHANISM	729
S. FORMATION AND STABILIZATION DYNAMICS OF OZONE COMPLEXES	755
T. MULTICOLLISIONAL TRAJECTORY STUDIES OF VIBRATIONALLY/ROTATIONALLY EXCITED OZONE MOLECULES BY ARGON ATOMS	795
U. RELAXATION OF VIBRATIONALLY EXCITED OXYGEN MOLECULES BY COLLISION WITH OXYGEN ATOMS.	815

Accession For	
NTIS GRA&I	<input checked="" type="checkbox"/>
DTIC TAB	<input type="checkbox"/>
Unannounced	<input type="checkbox"/>
Justification	
By	
Distribution/	
Avail. and/or Codes	
Avail. and/or	
Dist	Special
A-1	



APPENDIX P

(SR-340 reproduced in its entirety)

J. Phys. Chem. 93, 1097 (1989)

ABSTRACT

The dynamics of the reactions of $N(^2D, ^2P)$ with O_2 have been investigated by observing the initial vibrational state population distributions of $NO(X^2\Pi)$ formed in the interaction of oxygen and discharge-excited nitrogen in a cryogenically pumped, low pressure reaction volume. Infrared chemiluminescence from vibrationally and rotationally excited $NO(v=1-14)$ was observed in the 5 to 7 μm spectral region, and spectral data were analyzed to obtain $NO(v,J)$ number densities. The results show multimodal vibrational and rotational distributions, indicative of several concurrent processes. In particular, extensive rotational excitation is evident in several vibrational levels of NO , resulting in sharply peaked R-branch band heads characteristic of $J \geq 80$. Surprisal analysis was applied to the data to infer the contributions of the various reaction pathways. This analysis indicates that all the possible reaction pathways for producing $NO(X^2\Pi)$, some of which lead to formation of metastable atomic oxygen, occur with significant probability. The results are discussed in terms of their implications for the detailed collisional dynamics of the reactions, and their relevance to the study of upper atmospheric auroral chemistry.

INTRODUCTION

The importance of the reactions



as the principal source of NO in the Earth's mesosphere and thermosphere was suggested by Frederick Kaufman and others in 1967.¹ Following the direct rate coefficient measurements and product yield determinations of Lin and Kaufman,²

first reported in preliminary form in 1970,³ atmospheric modeling studies⁴ showed that the $N(^2D)$ reaction accounted for the large upper atmospheric production of NO observed in rocket experiments.⁵ A number of subsequent laboratory investigations⁶⁻⁸ have provided refinements of the original^{2,9} kinetic measurements, and atmospheric modeling studies^{10,11} have continued to examine the roles of these reactions in odd nitrogen chemistry of the quiescent and auroral upper atmosphere.

From both an aeronomic and reaction dynamic point of view, the potential of the above class of reactions to form excited state products, such as $NO(v)$, $O(^1D, ^1S)$, and $NO(a^4\Pi, v)$, is of great interest. In a detailed experimental study, Kennealy et al.¹² showed that Reaction (1) is an efficient source of highly vibrationally excited $NO(v)$ (up to 12 quanta with a strongly non-statistical vibrational state distribution), with implications that $O(^1D)$ might be formed as well. Rocketborne infrared spectra of a strong aurora showed extensive auroral excitation of $NO(v)$;¹³ these results were successfully modeled¹¹ in terms of direct formation by the reaction of aurorally produced $N(^2D)$ with O_2 as studied in the laboratory.

The possible reaction pathways for Reaction (1) are shown in Table 1. Also shown are the reaction exothermicities, the maximum energetically accessible (rotationless) vibrational levels in the product NO molecules, and the C_s symmetry species for adiabatic conversion of reactants to products. The symmetry species were determined^{6,14} using the adiabatic correlation rules for atom-diatom reactions having non-linear intermediate complexes, as described by Shuler.¹⁵ Note that, despite the correlation of both reactants and products to doublet and quartet A' and A'' surfaces, the reaction of $N(^2P)$ to form ground state atomic oxygen (Reaction 3a) has no adiabatic route; this results from application of the so-called "non-crossing rule" derived by

analogy to avoided crossings in atom-atom collisions.¹⁴ As we will discuss later, this is not sufficient reason to rule out the occurrence of this reaction pathway. Clearly, if significant reaction exothermicity goes into product vibrational excitation, it should be possible to identify the relative contributions of the various $\text{NO}(X^2\Pi)$ product channels by examining the infrared fluorescence "signatures" in the fundamental vibration-rotation transitions in the 5 to 8 μm spectral region.

The objective of the present study is to examine the detailed vibrational and rotational energy partitioning in $\text{NO}(X^2\Pi)$ formed from Reactions (2) and (3). We have used the technique of nascent-product infrared chemiluminescence spectroscopy under near-single collision conditions in the COCHISE (Cold Chemiluminescence Infrared Stimulation Experiment) cryogenic reactor/spectrometer facility at the Air Force Geophysics Laboratory. Previous investigation¹² of these reactions on the COCHISE apparatus showed extensive NO vibrational excitation, principally from $\text{N}(^2\text{D})$, and inferred the possibility of $\text{O}(^1\text{D})$ formation via Reaction (2b) from surprisal analysis of the NO vibrational distributions. In addition, evidence of significant rotational excitation was observed at the lowest pressures employed. However, the results were affected by the presence of unidentifiable underlying spectral features at the short and long wavelength ends of the spectra, and the contributions due to $\text{N}(^2\text{P})$ could not be unambiguously assessed. In the present work, we have taken advantage of increased sensitivity and dynamic range to remove contributions from background radiation and to extend the results to higher vibrational levels. We have identified previously unknown spectral features as R-branch band heads resulting from extensive rotational excitation ($J=100$) in each of at least eight vibrational levels, which we attribute to formation by $\text{N}(^2\text{P})$. We have inferred detailed product channels via surprisal

analysis of the NO internal energy distributions; the results indicate that the $N(^2D)$ and $N(^2P)$ reactions with O_2 proceed by very different molecular dynamic mechanisms.

EXPERIMENTAL MEASUREMENTS

The design and operation of the COCHISE facility have been described in detail elsewhere.¹⁶ In brief, the entire radiative environment of the experiment is maintained at a base temperature of approximately 20 K, which effectively eliminates background radiation within the 2 to 20 μm operating range of the apparatus. The detection system consists of a scanning grating monochromator and a liquid-helium-cooled Si:As detector. Reagent gases are introduced into the reaction cell through temperature-controlled feed lines as shown in Figure 1. $N(^2D, ^2P)$ are produced (together with $N(^4S)$ and excited metastable states of N_2) by passing a flowing N_2/Ar mixture at approximately 1 torr through four parallel microwave discharges (2450 MHz, 50 W) prior to expanding into a low-pressure (approximately 3 mtorr), cryogenically pumped interaction volume. A counterflow gas (O_2 or Ar) enters the volume from the opposite side to combine with the discharge-excited gas in a stagnation region along the axis of the cell, which coincides with the axis of the cylindrical field of view of the detection system. In the case of an unreactive counterflow, this interaction provides an arrested relaxation condition for studies of infrared fluorescence arising from discharge excitation processes.¹⁷⁻¹⁹ However, in the present experiments, an O_2 counterflow reacts promptly in the field of view with the effluents of the N_2/Ar discharges to give readily identifiable chemiluminescence from vibrationally excited NO under conditions where diffusive loss dominates over radiative or collisional cascade.¹²

For most experiments, reagent gases were introduced at controlled temperatures of 80 to 90 K; no temperature dependence in the fluorescence intensity or general spectral distribution was observed at temperatures up to 120 K. In each discharge tube, the Ar flow rate was held at 640 $\mu\text{mole/s}$, and the N_2 flow rate was systematically varied from 5 to 86 $\mu\text{mole/s}$ (0.8 to 12 percent N_2). Mass-balanced counterflows of either O_2 or Ar were used to produce chemiluminescence or determine background fluorescence levels, respectively. Under these conditions, the gas residence time in the active discharge is approximately 2 to 5 ms, the transit time from the discharge exit to the field of view is ~ 0.5 ms, and the residence time in the field of view is ~ 0.3 ms.

Infrared fluorescence spectra were obtained in the 4 to 8 μm region with spectral resolutions of 0.007 to 0.040 μm (2.8 to 16 cm^{-1} at 5 μm). Some 50 spectral scans were required to survey the parameter space of N_2 mole fraction, O_2 mole fraction, temperature, discharge power, and spectral resolution (including foreground and background scans). The uncertainty in the observed wavelengths (due to a slight periodic fluctuation in the cryogenic monochromator scan rate) is ± 0.003 μm ; absolute wavelengths were calibrated using the well-resolved band center of the $\text{CO}(1\rightarrow 0)$ vibrational transition excited by energy transfer from discharge-excited nitrogen.^{16,20} The spectral data were acquired via phase sensitive detection, using a computer-interfaced lock-in amplifier and chopping the discharges with a 23 Hz square wave. The observed intensities were corrected to radiometric units using blackbody calibrations of the absolute spectral responsivity of the detection system.

RESULTS AND ANALYSIS

Spectral Data

An example fluorescence spectrum observed in the interaction of discharged N_2/Ar with O_2 is shown in Figure 2 for the highest usable spectral resolution. Spectral scans in which the O_2 in the counterflow was replaced by Ar revealed the presence of weak underlying radiation from various sources throughout the bandpass of interest (4 to 8 μm). These consist of: 1) Ar(I) Rydberg lines between 4 and 5 μm ; 2) $N_2(W^3\Delta_u-B^3\Pi_g)$ bands near 6.5 and 7.5 μm (the (1,0) and (2,1) bands, respectively); and 3) broad but structured emission extending from 5.2 μm to approximately 7.5 μm . We have previously investigated the first two emission systems in some detail: the Ar(I) radiation²¹ is scattered light from the discharges, and the $N_2(W-B)$ emission¹⁹ arises from discharge-excited species which survive long enough to radiate in the field of view. The third background contribution occurs with signal-to-noise ratios which are too low to permit conclusive identification; however it appears that this feature arises from $NO(v)$ formed in the discharges due to ppm-level oxygen impurity in the discharged gas. The fluorescence spectral distribution is "collapsed" toward shorter wavelengths (lower vibrational levels), indicative of substantial collisional deactivation as expected for the ~ 1 torr discharges. The maximum intensity of this feature is about one order of magnitude less than that of the chemiluminescence signal, but the contribution to the observed spectrum from the background emission is significant for wavelengths below 5.4 μm and above 6.4 μm ($v \leq 2$ and $v \geq 12$, respectively). Accordingly, the chemiluminescence spectra were corrected for background contributions by subtracting companion background spectra obtained immediately before or after each scan, with all conditions identical except for the substitution of an Ar counterflow instead of O_2 . An unfortunate

result of this subtraction procedure was to limit the dynamic range at long wavelengths and hence the maximum observable vibrational level. The bulk of the remaining chemiluminescence, between 5.2 and 6.5 μm , can be readily identified through its vibrational and rotational spacings as $\text{NO}(X^2\Pi, v'=1-14)$. The maximum spectral intensity occurs for $v'=5-7$, and the rotational distributions in this portion of the spectrum signify near-thermal equilibrium with the gas temperature. Also present in the background-corrected spectra is a series of eight sharp, red-degraded features between 4.95 and 5.55 μm (cf. Figure 2). These features, which have a constant spacing of $31 \pm 2 \text{ cm}^{-1}$, are reproducible in wavelength and relative intensity for all NO chemiluminescence experiments. The features between 4.9 and 5.2 μm were noted in earlier investigations;¹² however, poorer signal-to-noise ratios precluded systematic examination, and the usable spectral resolution in those experiments was too low to reveal the presence of the additional features extending into the main NO band. It is clear that the presence of these features could significantly affect the vibrational analysis of the NO spectrum. Furthermore, the three features between 4.95 and 5.15 μm are coincident with similar spectral features recently observed by a rocket-borne interferometer in an overhead aurora,²² suggesting that this emission represents a previously unknown aeronomic phenomenon.

The observed spectral features do not correspond to any of the possible transitions that might be excited in the experiments, e.g., vibrationally excited NO^+ or N_2O , or electronic transitions of NO, N_2 , and O_2 . However, it is straightforward to show that the observed band positions correspond well to those predicted for R-branch band heads of the vibrational transitions of $\text{NO}(X^2\Pi)$ itself. The presence of such band heads in a vibrational transition requires an extraordinary degree of rotational excitation. For the $(v', v'') =$

(1,0) transition, for example, the vertex of the Fortrat parabola occurs for $J' \sim 80$, a rotational energy in excess of 1.3 eV. Thus it appears that the vibrational transitions for at least $v'=1-8$ have strongly bimodal rotational distributions, with Boltzmann "temperatures" ranging from ~ 100 to ~ 10000 K. The rotational states contributing to the R-branch band heads ($J' \sim 60-100$) should also exhibit P-branch structure extending to 8 or 9 μm ; unfortunately, due to the low signal-to-noise ratios at the longer wavelengths, we cannot examine the P-branch distributions to determine the detailed rotational population distributions at large J' . Furthermore, due to extensive overlap by the relatively intense, rotationally "thermal" component beyond 5.6 μm , we cannot determine whether there are weak rotationally excited components for vibrational levels $v' > 8$. By comparison, in experiments where CO/Ar counterflows are used, we observe similar band head formation in several vibrational levels of the CO($\Delta v=1$) system from rotational/vibrational excitation by energy transfer from active nitrogen;²⁰ these measurements have sufficient intensity to permit resolution of the P-branch structure at large J' , and show that a two-temperature bimodal description provides a reasonable approximation to the rotational state populations. In order to examine trends in the relative intensities of the "hot" and "cold" rotational components of NO, as well as in the vibrational distributions, several experimental parameters were independently varied. Spectra were obtained over the ranges: discharge power, 10 to 50 W; gas temperature, 80 to 120 K; counterflow O₂ mole fraction, 0.0 to 1.0 (Ar diluent); and discharge N₂ mole fraction, 0.008 to 0.12 (Ar diluent). Increasing the discharge power gave increased signal intensity with no discernible effect on the spectral distributions. Increasing the gas temperature did not affect the observed spectral intensities or distributions except for slight increases in the "thermal" rotational temperatures.

Reduction of the counterflow O_2 mole fraction gave a corresponding decrease in spectral intensity, with no significant effect on the spectral distributions. Reduction in the discharge N_2 mole fraction by a factor of 15 gave a factor of ~ 2 decrease in overall signal intensity, with ~ 30 percent apparent reduction in the relative high- J' contributions. This latter effect is significant for the present observations, and will be discussed further in terms of the derived vibrational state populations below.

Spectroscopic Analysis

The spectral data were analyzed to determine detailed vibrational state populations using a linear least squares spectral fitting method which we have employed for a number of vibrational excitation studies.^{12,13,16-18} The method consists of computing instrument-convolved basis functions for each $\Delta v=1$ vibration-rotation transition using an accurate spectroscopic formalism, and fitting those functions to an observed spectrum to determine the individual integrated intensity of each vibrational transition. These values can then be transformed into upper vibrational state number densities through application of the appropriate band transition probabilities.

The vibration-rotation energies and transition frequencies of $NO(X^2\Pi)$ were computed explicitly,²³ including the effects of spin-orbit coupling, vibrational anharmonicity, vibration-rotation interaction, and centrifugal distortion; effects of electronic rotational interaction (λ -type doubling) are negligible for these experiments ($< 0.1 \text{ cm}^{-1}$). The spectroscopic constants used for the computations are shown in Table 2. For the most part, these are the same values given by Goldman and Schmidt²⁴ and used by Rawlins et al.¹³ to fit high resolution auroral spectra. The single exception is the value of β_e , the correction term to the centrifugal constant D_v , which we adjusted in order to better reproduce the positions of the R-branch band heads. The value of β_e

given in Table 2 is about twice that used by Rawlins et al,¹³ who reversed an apparent error of sign in the value given by Goldman and Schmidt.²⁴

Comparison of the D_v values of Goldman and Schmidt to subsequent work by Amiot and Vergés²⁵ indicates a 2 percent uncertainty in D_v at room temperature, which encompasses the change we require for β_e .

For the limited spectral resolution of these experiments, a complete description of the line-by-line rotational intensities is not feasible, nor does adequate information exist for extending these intensities to the high rotational levels observed here. As an approximate treatment, we have used band-averaged Einstein coefficients together with Hönl-London scaling of the relative rotational strengths. The relative intensity of the i^{th} optically thin rotational line emanating from the state (v', J', Q') is then given by

$$I_i = hc \frac{\nu_i^4}{\nu_B^3} S_i(P, Q, R) A_{v', v''} N_{v'} \frac{\exp(-E(J', Q')/kT)}{Q(v')}$$

where ν_i and ν_B are the transition frequencies of the line and the band center, respectively, $S_i(P, Q, R)$ are the appropriate Hönl-London factors as given by Herzberg,²³ $A_{v', v''}$ is the thermally averaged Einstein coefficient for the band, $N_{v'}$ is the population of the emitting vibrational level, and $Q(v')$ is the spin-orbit/rotational partition function for the emitting vibrational level. Note that here we have assumed that the $^2\Pi_{1/2}$ and $^2\Pi_{3/2}$ spin-orbit states are in thermal equilibrium, which in fact seems to be the case, at least for the rotationally thermal component of the spectrum where spin non-equilibrium would be the most apparent.

The individual line-by-line vibrational basis sets are convolved with the instrumental scan function (in this case, an isosceles triangle with full width at half maximum as the spectral resolution) and are fit to each

experimental spectrum by linear least squares to determine the products $N_v/A_v/v''$. The individual upper state number densities are then determined by application of band-averaged Einstein coefficients for each transition (see below).

In the fitting procedure, the bimodal rotational distributions in each of the lowest eight vibrational levels were approximated by two separate vibrational populations with Boltzmann rotational distributions corresponding to thermal (~ 100 K) and "hot" (~ 10000 K) temperatures. These temperatures were independently varied to optimize the fits to the appropriate rotational contours, and were found to be typically 120 ± 10 and 10000 ± 4000 K. The quoted uncertainties are based on the variations required to produce recognizable deviations from the observed bandshapes near 5.6 to $6.0 \mu\text{m}$ and 4.9 to $5.2 \mu\text{m}$ for the "cold" and "hot" components, respectively. Within these ranges of temperature parameters, the vibrational distributions determined from the spectral fits were not significantly affected. We attempted to determine whether the rotational temperature for the "hot" component was dependent on vibrational level. While there was some indication that the R-branch band head structures required somewhat lower rotational temperatures for the higher vibrational levels, the limitations of signal-to-noise ratio, spectral resolution, and band overlap precluded a quantitative determination of this trend.

The band-averaged Einstein coefficients for each vibrational transition were chosen by logic analogous to that recommended by Rothman et al.²⁶ The value for the $(v', v'') = (1, 0)$ band was taken from the absorptivity measurement of Holland et al.,²⁷ and the scaling to higher v' followed relative values predicted by Billingsley²⁸ from ab initio calculations of the dipole moment function. This relative scaling is supported by experimental measurements of the $(\Delta v=2)/(\Delta v=1)$ branching ratios for $v' \leq 7$,²⁹ and the resulting values of

$A_{v',v''}$ appear to be reasonably accurate (approximately ± 30 percent or better). Recent COCHISE measurements of $(\Delta v=2)/(\Delta v=1)$ ratios extending to higher v' indicate more substantial uncertainty in the theoretical dipole moment function for $v' \geq 9$,³⁰ but the relative values of $A_{v',v''}$ for the fundamental band are probably not severely affected by this uncertainty. The values of $A_{v',v''}$, determined by the above procedure and used in the analysis of all data discussed in this paper, are listed in Table 3. It should be noted that, although the band-averaged Einstein coefficients are nearly independent of rotational temperature up to at least 600 K,²⁸ there may be effects at high J' due to rotation-vibration coupling and uncoupling of spin and orbital angular momentum (transition to Hund's case (b)), as noted by Billingsley²⁸ for $J' \sim 30$. To test for this possibility, we performed more detailed computations accounting for spin uncoupling which indicate that the Case (a) Hönl-London factors provide a good approximation up to $J \sim 100$. More significantly, however, the high- J' states forming the band heads are sufficiently high in the NO manifold to probe the range of internuclear distance where the calculations of Billingsley indicate the onset of downward curvature in the dipole moment function, and where our recent $(\Delta v=2)/(\Delta v=1)$ data³⁰ indicate uncertainty in this calculated behavior. Thus the computed relative rotational intensity scaling may not be applicable to the R-branch band heads; the rotationally "hot" vibrational populations determined in this way are then somewhat uncertain. A more detailed determination of the absolute values of $A_{v',v''}(J')$, as well as experimental determination of the transition moment at large internuclear separation, are currently in progress.

Vibrational Population Distributions

A typical comparison of observed and computed least-squares fit spectra is illustrated in Figure 3, together with the contributions of the

rotationally "hot" and "cold" components. The values of $N_v/A_{v'v''}$ determined from the fit are plotted in Figure 4. The error bars indicate the statistical standard deviations ($\pm 1\sigma$) in the solutions. Application of the Einstein coefficients of Table 3 gives the upper state vibrational number densities with the same relative standard deviations. Uncertainties in the Einstein coefficients, which cannot be evaluated statistically and are the same for all the data analyzed, are not shown in our plots of the vibrational populations.

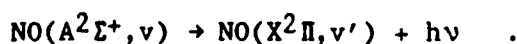
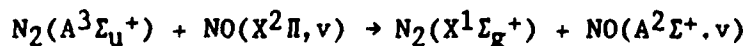
In general, relative vibrational population distributions obtained by omitting the background correction procedure and the "hot" rotational contributions gave excellent agreement with values determined earlier in COCHISE for $v'=1-12$ ¹² and with values inferred for Reaction (2), $v'=1-7$ from electron beam excitation of air.³¹ Application of background correction reduces the apparent relative population in $v'=1$ by about 10 percent and that for $v'=12$ by more than a factor of two from the previous determination; in addition the present experiments provide information for levels up to $v'=14$. Inclusion of the rotationally "hot" states gives a further reduction of the "cold" $v'=1$ population by a factor of ~ 2 , with only minor effects on the higher levels. As described above, the relative distributions were not affected significantly by variations in experimental parameters. Accordingly, the solutions for a series of five spectra, obtained sequentially with spectral resolution of $0.013 \mu\text{m}$ and carefully optimized signal-to-noise ratio, were averaged together to give a set of absolute vibrational state populations corresponding to the condition $T = 80 \text{ K}$, discharge power = 50 W , and discharge N_2 mole fraction = 0.12 , to be used for subsequent kinetic analysis. This composite averaged distribution is shown in Figure 5, and is well representative of relative distributions determined for all experimental conditions. The remainder of

this paper deals with kinetic interpretations of the results in Figure 5 to determine product branching fractions for the reactions in Table 1.

KINETIC INTERPRETATIONS

Based on the results of previous studies,^{12,31} it is reasonable to expect that the rotationally "thermal" vibrational distribution in Figure 5 arises largely from the reaction of $N(^2D)$ with O_2 . However, the rotationally "hot" vibrational distribution may arise from another process involving reaction or energy transfer of other excited species formed in the discharge. The principal energetic species emanating from the Ar/ N_2 microwave discharges for our fast flow conditions and surviving into the field of view are $N(^4S, ^2D, ^2P)$ and $N_2((X^1\Sigma_g^+, v), A^3\Sigma_u^+, W^3\Delta_u, a'^1\Sigma_u^-, w^1\Delta_u)$.¹⁹ The flux of charged species escaping the discharge region is negligibly small; this is verified by the observation of no excitation in CO and N_2 counterflows upon interaction with the effluents of 100% Ar discharge. Based on a combination of discharge modeling calculations (using methods¹⁸ and electron-impact cross sections³² described elsewhere), direct observations of discharge effluents in a flow reactor at room temperature,³³ and observations of infrared-radiating states of N_2 in COCHISE,¹⁹ we can assemble a set of anticipated discharge effluent number densities for the present experiments at a discharge N_2 mole fraction of ~ 0.1 , as shown in Table 4. The molecular metastables arise principally from direct excitation of N_2 by electrons (characteristic electron energies are 6 to 8 eV in dilute N_2 /Ar mixtures) and metastable argon, and the atomic metastables are produced primarily by electron-impact excitation of $N(^4S)$ formed from N_2 dissociation. Clearly, $N(^4S)$ is the dominant species, but is too unreactive with O_2 at these temperatures to produce significant $NO(v)$.^{12,34} Similarly, we do not expect any of the molecular metastables to

react with O_2 to form $NO(v)$, as a four-center collision complex would be required. An interesting possible route for $NO(v)$ excitation is via energy transfer from $N_2(A)$ to NO^{35} that is formed by N^* reactions in the field of view:



The $NO(v')$ distribution that is formed by the rapid radiative cascade step is governed by the Franck-Condon factors for the transition and is similar to that observed for the rotationally "hot" component in Figure 5. However, due to the low number densities of both $N_2(A)$ and NO in the interaction volume, the $NO(v')$ number densities obtained from this process are about four orders of magnitude smaller than those observed in the measurements. Furthermore, although rotational excitation of $NO(A)$ has been observed in this process,³⁵ there is insufficient exoergicity to account for the much greater rotational excitation observed here. By similar kinetic arguments, it is straightforward to eliminate other electronic energy transfer processes, as well as the possibility of rotational excitation by energy transfer to NO from translationally excited atoms emanating from the discharge. While translational excitation of atoms is known to occur by energy transfer from Ar metastables,^{36,37} this energy is moderated within microseconds in the 1 torr discharge tubes, and the number density of "hot" atoms reaching the field of view will be miniscule. Finally, the possibility for collisional quenching from a high vibrational level of NO into a high rotational level of a low vibrational level (V, R transfer), analogous to processes observed for HF ,³⁸

can also be dismissed. To excite the high J' levels we observe would require quenching of vibrational levels 5 to 12 or higher. Since we observe very low relative populations for $v \geq 10$ under conditions of 20 to 30 collisions per observed NO(v) molecule, this would require essentially gas-kinetic quenching of NO(v) by Ar. This is highly unlikely, since direct measurements of the v -dependent quenching of NO(v) by O_2 ³⁹ and of CO(v) by CO_2 ⁴⁰ indicate quenching rate coefficients (by whatever mechanism) which are less than 1 percent gas-kinetic even for seven or more vibrational quanta of excitation. Thus any amount of rotational excitation produced by V,R transfer will be insignificant in our experiments. Similarly, the observed vibrational distributions are not perturbed by collisional deactivation by O, O_2 , N_2 , N, or Ar, as demonstrated in the earlier work of Kennealy et al.¹² We conclude that the observed vibrational distributions represent composites of the initial product distributions from the reactions of N(2D , 2P) listed in Table 1. Based on the results of Ref. 31, the rotationally "cold" distribution appears to arise largely from the N(2D) reactions; by process of elimination, the rotationally "hot" distribution appears to result from N(2P) reactions with O_2 .

Due to the composite nature of these product state distributions, it is difficult to assign the individual reaction channels unambiguously. However, it is instructive to examine the observed composite distributions with the aid of surprisal theory. This approach postulates the existence of an exponential gap law for an individual metathetic reaction:⁴¹

$$P(v) = P^0(v) \exp(-\lambda f_v) / \exp(\lambda_0)$$

where f_v is the fraction of the reaction exoergicity appearing as vibrational energy in the product, $P(v)$ is the observed relative vibrational population,

and $P^0(v)$ is the statistical "prior" distribution obtained when all final translational, rotational, and vibrational states are equally probable. Thus the ratios of the observed and statistical vibrational populations should be exponential in the vibrational energy E_v , with the exponential fall-off constant λ quantifying the departure of the observed distribution from a completely statistical product distribution. While this theory does not necessarily hold for all chemical reactions, it does provide useful guidelines for the interpretation of product state distributions in terms of the molecular reaction dynamics. The prior distributions were determined from the usual relationship for a vibrating rotator:⁴¹

$$P^0(v) = \frac{(1 - f_v)^{3/2}}{\sum_{v=0}^{\infty} (1 - f_v)^{3/2}}$$

Computed prior distributions are shown in Figure 6 for the reactions in Table 1.

Application of surprisal analysis to the vibrational distributions of Figure 5 is by no means straightforward as it is impossible to obtain linear plots of $\ln(P(v))$ versus f_v for any single assumed elementary reaction from Table 1. Thus it appears that each distribution, thermal and rotationally excited, is a composite of distributions for more than one reaction channel. Previous work, employing differential quenching of $N(^2D)$ and $N(^2P)$ by N_2 in electron-irradiated N_2/O_2 mixtures, provides strong evidence that the inverted, rotationally thermal distribution of Figure 5a is due to the $N(^2D)$ reaction channels.³¹ We therefore believe that the rotationally excited distribution of Figure 5b results from reactions of $N(^2P)$ with O_2 . The rotational excitation required for band head formation, $J \sim 80-120$, is about

2-3 eV. This plus the number of vibrational levels observed (at least 8) gives a reaction exoergicity of 4-5 eV that is only satisfied by Reaction (3a). A combination of Reactions (3b) and (3c), with roughly equal contributions from each in approximately statistical distributions, can also account for the relatively large populations observed in the $v=1,2$ states. Furthermore, a statistical combination of all three reaction paths (3a, 3b, and 3c) in equal contributions gives an excellent fit to the data, as shown in Figure 7. It is also interesting to note from Figure 7 that the observed populations of $v'=12-14$ from the rotationally "thermal" distribution also fall on the statistical curve for Reaction (3). This does not signify a discrepancy in rotational excitation effects, because the spectral contributions from these states are so weak that it is not possible to identify their rotational distributions with any accuracy, and we cannot determine whether their production is associated with the rotationally thermal reaction channel (i.e., $N(^2D)$) or with the rotationally "hot" reaction ($N(^2P)$). As will be shown below, the data for $v=13-14$ seem less consistent with the trends identified for production by $N(^2D)$, so it is possible that the observed populations for these states arise primarily from Reaction (3). The intermediate states $v=9-11$ should also be produced in this reaction, but at levels which are obscured by production of $NO(v)$ from Reaction (2). Similarly, population of levels $v>14$ by Reaction (3a) may occur but cannot be observed in these experiments because of signal-to-noise limitations. It should be noted that, while the contributions of Reactions (3b, c) are implied by the fit in Figure 7, they can by no means be demonstrated conclusively from these data, as we do not have any positive identification of the energetic O^* products of these reactions. Nevertheless, the inclusion of these reactions is consistent with the data and with the picture of a completely statistical product

distribution for the $N(^2P)$ reaction, as will be discussed below.

Alternatively, the entire rotationally hot distribution may be due to Reaction (3a) alone, with non-linear surprisal behavior.

We examine the "thermal" component of the observed $NO(v)$ distribution by first noting that correction must be made for partially thermalized contributions from the reaction branch which produces rotationally "hot" $NO(v)$. These contributions are especially evident for levels $v=1-3$, where the rotationally thermal populations closely parallel those for the rotationally excited products. To illustrate this effect, we show in Figure 8 the surprisal plots for Reactions (2a, 2b) where no correction is made for thermalized high- J contributions. This plot shows two interesting effects: 1) the populations for $v'=1,2$ deviate significantly from the trend for $v'=3-7$; and 2) Reaction (2a) appears to make no contribution for $v' < 8$, as evidenced by the break in slope at $v'=7$. This general behavior was noted in the surprisal treatment of similar $NO(v)$ distributions in the previous work of Kennealy et al.¹²

Since each initial $NO(v,J)$ molecule is subjected to 20 to 30 collisions (mostly with Ar and O_2) during its residence time in the field of view, it is reasonable to expect substantial rotational thermalization, with deactivation of low to middle rotational levels occurring at nearly every collision and deactivation of the high rotational levels proceeding more slowly. Our data for $v'=1-3$ indicate that, at most, half of the rotationally excited $NO(v,J)$ initially formed is thermalized within 30 collisions. This corresponds to an effective rate coefficient on the order of $\sim 10^{-11} \text{ cm}^3 \text{ s}^{-1}$, in agreement with a similar value obtained by Taherian et al.⁴² for thermalization of highly rotationally excited $NO(v,J)$ formed from NO_2 photofragmentation in He. To correct the "cold" distributions for this contribution from the "hot" reaction

channel, we assume as an upper bound that essentially all the $v'=1$ population is due to thermalized $\text{NO}(v,J)$, scale the "hot" populations accordingly to approximate the contributions from the "hot" channel, and subtract. The maximum correction thus obtained is large for low v' but is minor near the peak of the distribution.

The remaining population distribution, plotted in Figure 9, shows an inversion peaking at $v'=7$. Noting that $v'=8$ is the thermodynamic limit for Reaction (2b), we show in Figure 10 the combined surprisal plots for Reaction (2b) ($v'=2-7$) and Reaction (2a) ($v'=8-11$). The composite population distribution determined from the surprisal fits of Figure 10 is given by the dashed curve in Figure 9. Excellent linearity in the surprisal analysis is now evident, as is the implication that Reaction (2b) accounts for all the $\text{NO}(v)$ production for $v' \leq 7$. In contrast to Reaction (3), the reaction of $\text{N}(^2\text{D})$ with O_2 appears to be strongly channeled into a specific product configuration; this will be discussed further below. The corrected product state distribution for Reaction (2), inferred from Figure 10 and plotted in Figure 9, represents a lower bound for $v' \leq 8$; the upper bound is that of Figure 5a (no "hot" channel correction). The fact that the lower bound gives linear surprisal for $v'=1-7$ and is consistent with a reasonable "hot" channel correction gives strong support for the choice of this distribution (Figure 9) as the actual nascent vibrational state distribution for Reaction (2).

The observed ratio of rotationally thermal to rotationally excited $\text{NO}(v' > 0)$ is approximately 3. Correcting for rotational thermalization effects and using surprisal extrapolations to higher vibrational levels (see below), the apparent ratio of $\text{N}(^2\text{D})$ to $\text{N}(^2\text{P})$ contributions could be as small as ~ 0.5 . However, as noted above, our determination of the number densities of the high- J states may be uncertain owing to effects of curvature in the dipole

moment function on the scaling of the rotational line strengths to high J . Thus the ratio of production rates for Reactions (2) and (3) cannot be precisely determined from the present data, but may be of order unity or less for temperatures of 80 to 100 K. This is in significant contrast to our expectations based upon room temperature kinetic data. As shown in Table 4, for room temperature discharges similar to those used in COCHISE, we typically observe number density ratios of $[N(^2D)]/[N(^2P)] \sim 3$ at the discharge exit using atomic resonance absorption and fluorescence techniques.³³ Taken together with the rate coefficient ratio of $k_2/k_3 \sim 2$ at room temperature,^{8,33,43} this would indicate a ratio of $NO(v)$ production rates of about 6. There are several possible implications from this discrepancy: 1) our underestimate of the high- J line strengths may be far more severe than expected; 2) there may be a significant unreactive component (i.e., direct energy transfer to O_2 without NO formation) for Reaction 2 at low temperature;⁴⁴ and 3) the rate coefficients for Reactions (2) and (3) may follow opposite temperature dependencies, i.e., k_3 may follow a negative temperature dependence, such that k_2/k_3 becomes considerably smaller at low temperatures. All of these possibilities have significant implications for auroral chemistry, and we are continuing to pursue them in the laboratory.

The final vibrational distribution shown in Figure 9 for Reaction (2) is in significant disaccord with the results of Green et al.³¹ inferred from electron beam experiments at higher pressures. Specifically, the corrected relative populations from Figure 9 for $v'=1-3$ are much lower than the initial relative populations for these levels inferred from a time-resolved kinetic analysis of $NO(v)$ distributions created and partially relaxed in a pulsed electron beam experiment irradiating N_2/O_2 mixtures. Green et al.³¹ convincingly eliminated $N(^2P)$ as a precursor in their experiment by noting that

the $\text{NO}(v)$ precursor was quenched by N_2 (with a rate coefficient appropriate for $\text{N}(^2\text{D})$), whereas $\text{N}(^2\text{P})$ is not.⁶ Under electron beam conditions, much of the N^* production is due to dissociative recombination of N_2^+ and NO^+ , which would tend to favor $\text{N}(^2\text{D})$ formation, so that the relatively small $\text{N}(^2\text{P})$ contribution would be difficult to identify. This is in contrast to microwave discharge conditions, where there is much less ionization and $\text{N}(^2\text{D}, ^2\text{P})$ are excited by direct electron impact. Thus, Green et al.'s large populations at low v' are probably not due to Reaction (3), unless there is some unforeseen excitation or deexcitation mechanism which would cause $\text{N}(^2\text{P})$ to follow an unexpected kinetic behavior under their experimental conditions. However, their kinetic analysis relied heavily on the assumption of single quantum collisional deactivation of $\text{NO}(v)$. While this appears to be a reasonable approximation for describing the loss rate of a given vibrational level,³⁹ it may lead to a significant underestimate of the production rate for the lowest levels by multiquantum deactivation of higher levels by atomic oxygen. In classical trajectory studies of $\text{O} + \text{O}_2(v)$ collisions, we have observed a similar effect, with efficient multiquantum ($\Delta v = 2-4$) deactivation of $\text{O}_2(v)$ resulting in rapid population of lower vibrational levels from initially excited higher states.⁴⁵ Thus the discrepancy between the present results for Reaction (2) and those of Green et al.³¹ for the lower vibrational levels of $\text{NO}(v)$ may be due to the effects of multiquantum $\text{O} + \text{NO}(v)$ deactivation in their experiments. In addition, the rapid quenching of $\text{N}(^2\text{P})$ by O^{46} may compete very effectively with Reaction (3) for their electron bombardment conditions. Alternatively, our upper-bound correction for rotational thermalization may be too large (i.e., rotational thermalization is slower than one might expect from the data of Ref. 42), and the product distribution of Reaction (2b) simply does not follow linear surprisal behavior.

In an attempt to discriminate between $N(^2D)$ and $N(^2P)$ effects on the observed $NO(v)$ distributions, we obtained data from five spectral scans over a range of a factor of ~ 15 in initial N_2 mole fraction in the discharge gas mixture, as described above. For this range of conditions, the relative production rates for $N(^2D)$ and $N(^2P)$ in the discharges remain constant to within 10%, but the N_2 quenching contribution to the loss rate of $N(^2D)$ in the sidearm will provide some variation in the $N(^2D)/N(^2P)$ ratio entering the reaction zone. Unfortunately, due to the short residence time in the discharge sidearms, this amount of variation in $[N_2]$ will provide only about a 30 percent variation in this ratio, with the ratio decreasing with increasing N_2 flow rate. In the experiments, we observe the ratio of rotationally thermal to rotationally "hot" $[NO(v)]$ (summed over all observed v levels) to decrease systematically by a factor of 1.3 with increasing N_2 flow rate, as expected for the production of thermal $NO(v)$ by Reaction (2) and of rotationally "hot" $NO(v)$ by Reaction (3). This result is then consistent with the conclusions from the analysis of the population distributions. However, there is sufficient scatter in the data that an average ratio for all the scans gives a $\pm 2\sigma$ uncertainty of 26 percent, so the observed trend lies only slightly outside the scatter of the data.

DISCUSSION

The surprisal parameters determined from the above data analysis provide a basis for extrapolation of the results to other vibrational levels for which direct observations cannot be obtained. For the $N(^2D)$ reaction, we find that the branch for $O(^1D)$ production (Reaction (2b)) can account for all the production of $NO(v'=1-7)$, with a surprisal parameter $\lambda = -6.25 \pm 0.14$ (99% confidence level), while the remaining production of $NO(v' \geq 8)$ is due to the $O(^3P)$

branch (Reaction (2a)), with $\lambda = 9.16 \pm 1.19$. The relative initial populations of NO(v) determined from these surprisal fits are shown in Table 5. Summing the initial populations for each branch over all v gives the branching ratio $k_{2b}/k_2 = 0.76$ at ~ 100 K. Similarly, for the N(2P) reaction we infer (at most) equal branching ratios for formation of O(1S), O(1D), and O(3P), with essentially statistical product state distributions (see Table 5).

The aeronomic implications of the present conclusions for the auroral upper atmosphere are quite significant. The production of O(1D , 1S) from these reactions has an impact on interpretations and modeling of ultraviolet and visible airglow and auroral emissions from these states and from other species, such as N $_2$ (A $^3\Sigma_u^+$) and metastable states of O $_2$, which are believed to be linked to their production.⁴⁷ Our interpretation that v=1-2 are inefficiently populated in Reaction (2) is a significant revision of previous conclusions,^{12,31} and will have an important bearing on the interpretation of observed auroral NO(v) distributions, which often show hitherto unexplained "inversions" in the population of v=2 (v=1 is known to be strongly populated by non-chemiluminescent processes).^{11,13} These results also impact the current views on the roles of O-atom deactivation of higher vibrational levels and of Reaction (3) as sources of the observed populations in lower vibrational levels under certain conditions, suggesting that these processes are more important than previously thought. Furthermore, the high degree of rotational excitation provided by the N(2P) reaction will have a dramatic effect on the high-altitude infrared spectrum of auroral NO(v) emission, as evidenced by the R-branch band heads for v=1-3 observed in a recent rocketborne interferometer flight.²² The presence of these R-branch band heads to the blue of the main band means that the corresponding P-branch distributions must appear to the red. Our calculations indicate that the

unrelaxed P-branch contributions from the observed eight rotationally excited vibrational states can provide more intensity in the 6 to 8 μm range than the emission from high vibrational levels (for any rotational distribution) produced from Reactions (2a) or (3a). Our observations further indicate that the very high J levels responsible for these contributions are deactivated relatively slowly in Ar/O₂/N₂ mixtures. The extent of collisional coupling in the COCHISE experiments is similar to that expected for NO(v) at altitudes of 110 to 120 km (assuming the primary loss for NO(v) is by radiative cascade). Thus sensitive, high-resolution measurements of the NO(v,J) spectrum above ~ 100 km in a strong aurora could ultimately provide a means of estimating the N(²D)/N(²P) ratio and hence the energetics of the auroral event.

Our approach to describing the rotationally "hot" distributions deserves some comment. Due to limitations of spectral resolution and sensitivity, we are unable to directly observe any part of the rotational distributions other than the distinctive R-branch band heads. Thus there is no clear indication that the low to intermediate J-levels are populated, either in the initial reaction or on the time scale of the measurements. It is conceivable that the initial rotational populations are statistical, or that the initial population of high-J is rapidly randomized by collisions to give an apparently statistical distribution. Such a distribution would have the behavior:

$$P_v^0(J) \propto (2J + 1)\{(E - E_v) - E_r\}^{1/2}$$

where E_r , E_v , and E are the rotational, vibrational, and total reaction energies, respectively. Thus the rotational "temperature" would depend on the vibrational energy of the emitting state, with higher vibrational levels exhibiting "colder" rotational distributions. We cannot clearly discern this

effect in the NO(v,J) spectra, except for the disappearance of obvious band heads above $v'=8$. However, in similar studies of CO(v,J) excitation by energy transfer from active nitrogen,²⁰ we are able to fit the observed rotational distributions better with the statistical formula than with a Boltzmann (v-independent) description. Planned improvements in the measurement sensitivity for NO(v,J) may permit us to address this issue more accurately in the future.

The observed product state distributions imply strongly contrasting behavior in the reaction dynamics of the N(²D) and N(²P) reactions with O₂. For Reaction (2b), the high degree of selectivity for the highest accessible vibrational levels is characteristic of a direct, abstraction reaction with a repulsive approach configuration and a very short-lived collision complex. It would appear that successful reactive encounters require maximum vibrational motion along the product N--O coordinate, perhaps as a result of a barrier in the N--O₂ entrance channel. The behavior for Reaction (2a) is somewhat surprising, since the reaction appears to occur only when Reaction (2b) is thermochemically forbidden. This behavior suggests that all reactive N--O₂ encounters proceed initially along the ²A' surface leading to O(¹D) formation, but some, with too much N--O₂ motion in the product channel (insufficient motion along the NO--O coordinate) to form O(¹D) undergo enough motion in the collision complex to dissociate to highly vibrationally excited NO + O(³P) via transition to one of the other ²A' or ²A" surfaces that are available (cf. Table 1). Thus there may be no direct path, or perhaps a large energy barrier, to O(³P) formation in Reaction (2). If the occurrence of this reaction branch indeed depends upon the lifetime of the collision complex, then its contribution may diminish substantially at elevated collision energies (or higher temperatures). The direct reaction, Reaction (2b), ought

to follow at least a $T^{1/2}$ temperature dependence, or possibly one somewhat stronger due to the presence of an energy barrier in the entrance channel. For comparison, Slinger et al.⁴⁸ observed essentially no activation energy for quenching of $N(^2D)$ by O_2 between 240 and 370 K; however, the temperature dependence for NO formation has never been determined. Clearly, the effects of temperature dependence on this reaction need to be studied in more detail, as the present data base lends somewhat ambiguous support to the possibility of an unreactive energy transfer channel at lower temperatures. This possibility has been suggested in interpretations of aeronomic data on emission from excited states of O_2 ,⁴⁹ albeit on controversial grounds.⁵⁰

In contrast to $N(^2D)$, $N(^2P)$ appears to react with O_2 through a long-lived collision complex, resulting in complete randomization of the reaction energy. The appearance of high rotational excitation is characteristic of a highly attractive approach configuration. The collisions must satisfy the principles of conservation of angular momentum and energy:

$$(2\mu E_i)^{1/2} b_i = (2\mu E_f)^{1/2} b_f + Jh/2\pi$$

$$E_i + \Delta E = E_f + E_v + BJ^2$$

where μ is the reduced mass of $N-O_2$, E_i and E_f are the initial and final center-of-mass collision energies, b_i and b_f are the initial and final impact parameters, ΔE is the exoergicity of the reaction, E_v is the product vibrational energy, and BJ^2 approximates the product rotational energy after the collision. It is straightforward to show⁵¹ that large values of J can be achieved through highly attractive collisions in which large initial impact parameters are converted to small final impact parameters, with the concurrent

result that the final center-of-mass kinetic energy is small. By analogy to the well-studied reaction dynamics for $O(^1D)$ with H_2 ⁵² and HCl ,⁵³ this type of collision can occur through a C_{2v} insertion approach, leading to a highly attractive ONO collision complex. Such a complex would probably undergo enough vibrational periods to completely randomize the internal energy, giving rise to statistical product state distributions. With so much Lissajous motion in the complex, the adiabatic correlation rules given by Shuler¹⁵ would have little relevance,^{14,15} so there is no basis for the previously suggested^{6,14} prohibition of Reaction (3a). The reaction rate coefficient may increase substantially with decreasing temperature, owing to both the dynamics of the initial insertion approach (favored for less O_2 rotational motion) and the increased lifetime of the collision complex at lower temperatures. This trend, together with those suggested above for Reaction (2), is consistent with our observation of an unexpectedly large k_3/k_2 ratio at ~ 100 K.

It is interesting to compare our results for Reaction (3) with those of Taherian et al.⁴² for $NO(v,J)$ observed in the photolysis of NO_2 . Their experiments, conducted at 157.6 nm, are nearly isoenergetic with the $N(^2P) + O_2$ reaction, and may probe portions of the same ONO surface. They observed excitation of high rotational states comparable to those reported here, together with a partial vibrational distribution which is not inconsistent with our statistical picture. Most interestingly, they have identified the excitation of $v=21$, confirming that $O(^3P)$ is a primary product of the photodissociation process. However, the authors report upper bounds for $O(^1D, ^1S)$ formation which indicate these to be minor product channels at best. Such a result for Reaction (3) would not give a good surprisal fit to our data, but certainly cannot be ruled out on that basis alone. Alternatively, this disparity between our results and theirs may arise from the much

larger phase space sampled in reactive collisions. It is clear that more definitive product state identifications are required to confirm our preliminary assignment of the product branching ratios of Reaction (3).

CONCLUSIONS

We have used the technique of low-pressure infrared chemiluminescence to investigate the vibrational and rotational excitation of $\text{NO}(X^2\Pi)$ formed in the reactions of $\text{N}(^2\text{D}, ^2\text{P})$ with O_2 near 100 K. The initial vibrational distributions obtained from the experiments are composites from several reaction channels. The results of surprisal analysis indicate that $\text{N}(^2\text{D})$ reacts with O_2 via a direct abstraction mechanism, probably on a repulsive potential surface, to give a product vibrational distribution which is sharply peaked to high vibrational levels. This interpretation also implies that reaction to form $\text{O}(^1\text{D})$ comprises 76 percent of the total $\text{NO}(v)$ production at these temperatures. In contrast, the results indicate that $\text{N}(^2\text{P})$ reacts with O_2 through a long-lived complex, perhaps via an insertion mechanism on an attractive potential surface, to give essentially statistical product state distributions with extensive rotational excitation of the molecular products. The observed $\text{NO}(v)$ distributions are consistent with approximately equal contributions from the reaction channels forming $\text{O}(^1\text{S})$, $\text{O}(^1\text{D})$, and $\text{O}(^3\text{P})$ as products.

The results of this work amplify and extend the information obtained from previous studies of these reactions, and provide additional insights into the kinetics and spectroscopy of vibrationally excited NO in the auroral upper atmosphere. However, the results of the present investigations raise a number of issues requiring further study, including the temperature dependencies of the various reaction pathways, the possibility for quenching collisions which do not produce $\text{NO}(X^2\Pi)$, confirmation of $\text{O}(^1\text{D}, ^1\text{S})$ production, and quantitative

determination of the rotational line intensities at high J. We are continuing to address these issues through experiments on the COCHISE facility as well as with discharge-flow reactors using resonance fluorescence and laser-based diagnostics. In addition, these reaction systems lend themselves well to theoretical investigations of quantum mechanical potential energy surfaces and semiclassical collision dynamics.

ACKNOWLEDGEMENTS

The authors benefitted from numerous discussions and suggestions by many scientific colleagues, especially B.D. Green (PSI), G.E. Caledonia (PSI), K.W. Holtzclaw (PSI) and W.A.M. Blumberg (AFGL). The contributions of L.G. Piper (PSI) were essential for interpreting the formation and kinetics of discharge-excited species. The identity of the R-branch band heads was first suggested to WTR by Michael Mumma (NASA/Goddard) in the context of the rocketborne observations. We are also grateful for the assistance of Henry Murphy (PSI) with the experimental work, and of Lauren Cowles, Margrethe DeFaccio, and Melanie Clawson (all of PSI) in the analysis of the data. This work was performed under Contract F19628-85-C-0032 with the Air Force Geophysics Laboratory, and was sponsored by the U.S. Air Force Office of Scientific Research under Task 2310G4 and by the Defense Nuclear Agency under Project SA, Task SA, Work Unit 115.

REFERENCES

1. (a) Kaufman, F., Ref. 19 in a paper by T. M. Donahue, Invited Papers from the Fifth International Conference on The Physics of Electronic and Atomic Collisions, p.32, Leningrad, 1967; (b) R. B. Norton, ESSA Tech. Memo. IERTM-ITSA 60, 1967.
2. Lin, C. L. and Kaufman, F., J. Chem. Phys. 55, 3760 (1971).
3. Lin, C. L. and Kaufman, F., papers presented at DASA Symposia on the Physics and Chemistry of the Upper Atmosphere, Stanford Research Institute, June 1969 and Philadelphia, June 1970.
4. (a) Norton, R. B. and Barth, C. A., J. Geophys. Res. 75, 3903 (1970); (b) Strobel, D. F., Hunten, D. M., and McElroy, M. B., J. Geophys. Res. 75, 4307 (1970).
5. (a) Barth, C. A., Ann. Geophys. 22, 198 (1966); Planetary Space Sci. 14, 623 (1966); (b) Meira, L. G., J. Geophys. Res. 76, 202 (1971).
6. Schofield, K., J. Phys. Chem. Ref. Data 8, 723 (1979).
7. Iannuzzi, M. P. and Kaufman, F., J. Chem. Phys. 73, 4701 (1980).
8. Piper, L. G., Donahue, M. E., and Rawlins, W. T., J. Chem. Phys. 91, 3883 (1987).
9. Black, G., Slanger, T. G., St. John, G. A., and Young, R. A., J. Chem. Phys. 51, 116 (1969).
10. Kondo, Y. and Ogawa, T., J. Geomag. Geoelectr. 28, 253 (1976); 29, 65 (1977).
11. Caledonia, G. E. and Kennealy, J. P., Planet. Space Sci. 30, 1043 (1982).
12. Kennealy, J. P., Del Greco, F. P., Caledonia, G. E., and Green, B. D., J. Chem. Phys. 69, 1574 (1978).

13. Rawlins, W. T., Caledonia, G. E., Gibson, J. J., and Stair, A. T., Jr., J. Geophys. Res. 86, 1313 (1981).
14. Donovan, R. J. and Husain, D., Chem. Reviews 70, 489 (1970).
15. Shuler, K. E., J. Chem. Phys. 21, 624 (1953).
16. Rawlins, W. T., Murphy, H. C., Caledonia, G. E., Kennealy, J. P., Robert, F. X., Corman, A., and Armstrong, R. A., Appl. Opt. 23, 3316 (1984).
17. Rawlins, W. T. and Armstrong, R. A., J. Chem. Phys. 87, 5202 (1987).
18. Rawlins, W. T., Caledonia, G. E., and Armstrong, R. A., J. Chem. Phys. 87, 5209 (1987).
19. Fraser, M. E., Rawlins, W. T., and Miller, S. M., J. Chem. Phys. 88, 538 (1988).
20. Fraser, M. E., Rawlins, W. T., and Miller, S. M., J. Chem. Phys., to be submitted.
21. Rawlins, W. T., Gelb, A., and Armstrong, R. A., J. Chem. Phys. 82, 681 (1985).
22. Picard, R. H., Winick, J. R., Sharma, R. D., Zachor, A. S., Espy, P. J., and Harris, C. R., Advances Space Research, in press, 1987.
23. Herzberg, G., Molecular Spectra and Molecular Structure: I. Spectra of Diatomic Molecules, Van Nostrand, Toronto, 1950.
24. Goldman, A., and Schmidt, S. C., J. Quant. Spectrosc. Radiat. Transfer 15, 127 (1975).
25. Amiot, C., and Vergés, J., J. Mol. Spectrosc. 81, 424 (1980).
26. Rothman, L. S., Goldman, A., Gillis, J. R., Gamache, R. R., Pickett, H. M., Poynter, R. L., Husson, N., and Chedin, A., Appl. Opt. 22, 1616 (1983).
27. Holland, R. F., Vasquez, M. C., Beattie, W. H., and McDowell, R. S., J. Quant. Spectrosc. Radiat. Transfer 29, 435 (1983).

28. Billingsley, F. P. II, J. Mol. Spectrosc. 61, 53 (1976); J. Chem. Phys. 62, 864 (1975), 63, 2267 (1975); AFCRL-TR-75-0586, Air Force Geophysics Laboratory, Hanscom AFB, Massachusetts 01731, 13 November 1975. ADA019790
29. Green, B. D., Caledonia, G. E., and Murphy, R. E., J. Quant. Spectrosc. Radiat. Transfer 26, 215 (1981).
30. Rawlins, W. T., Fraser, M. E., and Miller, S. M., manuscript in preparation.
31. Green, B. D., Caledonia, G. E., Blumberg, W. A. M., and Cook, F. H., J. Chem. Phys. 80, 773 (1984).
32. Caledonia, G. E., Davis, S. J., Green, B. D., Piper, L. G., Rawlins, W. T., Simons, G. A., and Weyl, G., AFWAL-TR-86-2078, Air Force Wright Aeronautical Laboratories, Wright Patterson AFB, OH 45433-6563, 1986.
33. Piper, L.G. and Rawlins, W.T., unpublished work.
34. Winkler, I. C., Stachnik, R. A., Steinfeld, J. I., and Miller, S. M., J. Chem. Phys. 85, 890 (1986).
35. Piper, L. G., Cowles, L. M., and Rawlins, W. T., J. Chem. Phys. 85, 3369 (1986).
36. Piper, L. G., Clyne, M. A. A., and Monkhouse, P. B., J. Chem. Soc. Faraday 2 78, 1373 (1982).
37. Rawlins, W. T., and Piper, L. G., Proc. Soc. Photo-Opt. Instrum. Eng. 279, 58 (1981).
38. Haugen, H.K., Pence, W.H., and Leone, S.R., J. Chem. Phys. 80, 1839 (1984); Yang, X.F. and Pimentel, G.C., J. Chem. Phys. 81, 1346 (1984).
39. Green, B. D., Caledonia, G. E., Murphy, R. E., and Robert, F. X., J. Chem. Phys. 76, 2441 (1982).
40. Caledonia, G. E., Green, B. D., and Murphy, R. E., J. Chem. Phys. 71, 4369 (1979).

41. Bernstein, R. B., and Levine, R. D., "Role of Energy in Reactive Molecular Scattering: An Information-Theoretic Approach," in Advances in Atomic and Molecular Physics II, edited by D. R. Bates and B. Bederson (Academic, New York, 1975), pp. 216-297; Bernstein, R. B., Chemical Dynamics via Molecular Beam and Laser Techniques, Oxford University Press, New York, 1982.
42. Taherian, M. R., Cosby, P. C., and Slinger, T. G., J. Phys. Chem. 91, 2304 (1987).
43. Phillips, C.M., Steinfeld, J.I., and Miller, S.M., J. Phys. Chem. 91, 5001 (1987).
44. Note that Lin and Kaufman (Ref. 2) reported unit probability for reactive quenching at room temperature, based on observations of atomic oxygen formation. However, our own measurements using discharge-flow/resonance fluorescence (L. G. Piper and W. T. Rawlins, unpublished work) indicate that copious atomic oxygen is formed in other processes in the afterglow, so this result may be questionable. See also M. E. Fraser and L. G. Piper, this issue.
45. Gelb, A., and Rawlins, W. T., Physical Sciences Inc. TR-582 under Air Force Contract No. F19628-85-C-0032, December 1986.
46. Young, R.A. and Dunn, O.J., J. Chem. Phys. 63, 1150 (1975).
47. Vallance Jones, A., Meier, R.R., and Shefov, N.N., J. Atm. Terr. Phys. 47, 623 (1985) and references therein.
48. Slinger, T. G., Wood, B. J., and Black, G., J. Geophys. Res. 76, 8430 (1971).
49. Torr, M. R., Welsh, B. Y., and Torr, D. G., J. Geophys. Res. 91, 4561 (1986).

50. Slanger, T. G., Llewellyn, E. J., McDade, I. C., and Witt, G., J. Geophys. Res. 92, 7753 (1987); Torr, M. R., Owens, J. K., and Torr, D. G., J. Geophys. Res. 92, 7756 (1987).
51. Poppe, D., Chem. Phys. 111, 17 (1987); 111, 21 (1987).
52. e.g., Whitlock, P. A., Muckerman, J. T., and Fisher, E. R., J. Chem. Phys. 76, 4468 (1982); Aker, P. M., and Sloan, J. J., J. Chem. Phys. 85, 1412 (1986), and references therein.
53. Luntz, A. C., J. Chem. Phys. 73, 5393 (1980); Schinke, R., J. Chem. Phys. 80, 5510 (1984), and references therein.

Table 1. Pathways for NO Formation from $N(^2D, ^2P) + O_2$

Reaction	Adiabatic Surfaces	$\Delta H^{\circ}_{298\text{ K}}$ kcal/mole	Maximum v for NO
2 $N(^2D_u) + O_2(^3\Sigma_g^-)$			
a $\rightarrow NO(X^2\Pi) + O(^3P_g)$	$2^2A' + 2^2A'' + ^4A' + ^4A''$	- 86.80	18
b $\rightarrow NO(X^2\Pi) + O(^1D_g)$	$2A'$	- 41.43	8
3 $N(^2P_u) + O_2(^3\Sigma_g^-)$			
a $\rightarrow NO(X^2\Pi) + O(^3P_g)$	None	-114.28	26
b $\rightarrow NO(X^2\Pi) + O(^1D_g)$	$2A''$	- 68.91	14
c $\rightarrow NO(X^2\Pi) + O(^1S_g)$	$2A''$	- 17.67	3
d $\rightarrow NO(a^4\Pi) + O(^3P_g)$	$2A' + ^4A' + 2^4A''$	- 3.3	1

Table 2. Spectroscopic Constants for $\text{NO}(X^2\Pi)^{a,b}$

ω_e	1903.937
$\omega_e x_e$	13.970
$\omega_e y_e$	$- 3.7 \times 10^{-3}$
$\omega_e z_e$	5.0×10^{-5}
B_e	1.70488
α_e	0.017554
D_e	5.36×10^{-6}
β_e	5.0×10^{-8}
A_e	123.28
X_e	0.256

^aValues are from Ref. 24 except for β_e (see text).
^bUnits are appropriate for calculation of transition frequencies in cm^{-1} .

Table 3. Band-Integrated Einstein Coefficients for NO ($\Delta v=1$) Emission^a

v'	$A_{v',v''}, s^{-1}$
1	13.4
2	25.3
3	36.2
4	45.8
5	54.2
6	60.1
7	66.3
8	71.2
9	75.0
10	77.7
11	79.4
12	80.0
13	79.5
14	78.2
15	76.4
16	74.1
17	71.3
18	68.1
19	64.3
20	60.0

^aDetermined from data of Ref. 27 and scaled according to predictions of Ref. 28 (see text).

Table 4. Estimated Number Densities of Energetic Discharge Effluents^a

Species	Number Density, molecules cm ⁻³	
	Discharge Exit	Reaction Zone
N(⁴ S)	2 x 10 ¹⁴	7 x 10 ¹¹
N(² D)	(1-4) x 10 ¹²	0.3-1 x 10 ¹⁰
N(² P)	(0.5-1) x 10 ¹²	1-3 x 10 ⁹
N ₂ (X ¹ Σ _g ⁺ , v=1-7)	3 x 10 ¹⁵	1 x 10 ¹³
N ₂ (A ³ Σ _u ⁺)	1 x 10 ¹²	3 x 10 ⁹
N ₂ (W ³ Δ _u , v=1-2)	3 x 10 ¹⁰	3 x 10 ⁸ b
N ₂ (a, ¹ Σ _u ⁻)	1 x 10 ¹²	3 x 10 ⁹
N ₂ (w ¹ Δ _u , v=0-2)	6 x 10 ¹⁰	1 x 10 ⁸ b

^aMicrowave discharge conditions given in the text, approximately 10% N₂ in Ar.

^bBased on direct observations reported in Ref. 19. Higher vibrational levels are affected by radiative losses during transit from discharge exit to reaction zone.

Table 5. Surprisal Predictions of Relative Initial Populations of NO(v) in the Reactions of N(²D, ²P) with O₂

v	N _v /ΣN _v	
	N(² D) + O ₂ ^a	N(² P) + O ₂ ^b
0	1.36(-02) ^c	2.67(-01)
1	2.49(-02)	1.85(-01)
2	4.37(-02)	1.18(-01)
3	7.22(-02)	7.10(-02)
4	1.12(-01)	5.72(-02)
5	1.58(-01)	5.03(-02)
6	1.87(-01)	4.37(-02)
7	1.53(-01)	3.77(-02)
8	1.24(-01)	3.21(-02)
9	5.51(-02)	2.69(-02)
10	2.84(-02)	2.23(-02)
11	1.44(-02)	1.81(-02)
12	7.17(-03)	1.44(-02)
13	3.47(-03)	1.13(-02)
14	1.62(-03)	8.82(-03)
15	7.11(-04)	7.50(-03)
16	2.83(-04)	6.43(-03)
17	9.01(-05)	5.43(-03)
18	1.51(-05)	4.50(-03)
19		3.67(-03)
20		2.88(-03)
21		2.23(-03)
22		1.67(-03)
23		1.13(-03)
24		9.00(-04)
25		3.20(-04)
26		6.00(-05)

$$^a k_{2a}/k_{2b} = 0.285 \quad ^b k_{3a}/k_{3b} = k_{3c}/k_{3b} = 1$$

^c1.36(-02) signifies 1.36 × 10⁻²

- Figure 1 Diagram of the COCHISE reaction chamber. The physical dimensions of the cell are 0.6 m in length and 0.4 m in diameter.
- Figure 2 Spectrum of fluorescence observed in the interaction of O_2 with discharged N_2/Ar (12% N_2). Spectral resolution is 0.007 μm FWHM. Gas temperature is 80 K.
- Figure 3 Comparison of computed and observed $NO(v)$ spectra. Discharge: 12% N_2 in Ar; Counterflow: O_2 ; Gas temperature: 80 K; spectral resolution: 0.013 μm FWHM; corrected for background emission from the discharges. (a) comparison of calculated (heavy line) and observed (light line) spectra. (b) Contribution to computed spectrum from rotationally "cold" component, $T_{ROT} = 120$ K, $v=1-14$. (c) Contribution to computed spectrum from rotationally "hot" component, $T_{ROT} = 10,000$ K, $v=1-8$. The sharp features between 4.9 and 5.6 μm are the R-branch band heads for $v=1-8$.
- Figure 4. Vibrational band intensities determined from spectral fit in Figure 3
- Figure 5. Average vibrational population distributions for (a) rotationally thermal and (b) rotationally "hot" portions of the NO chemiluminescence

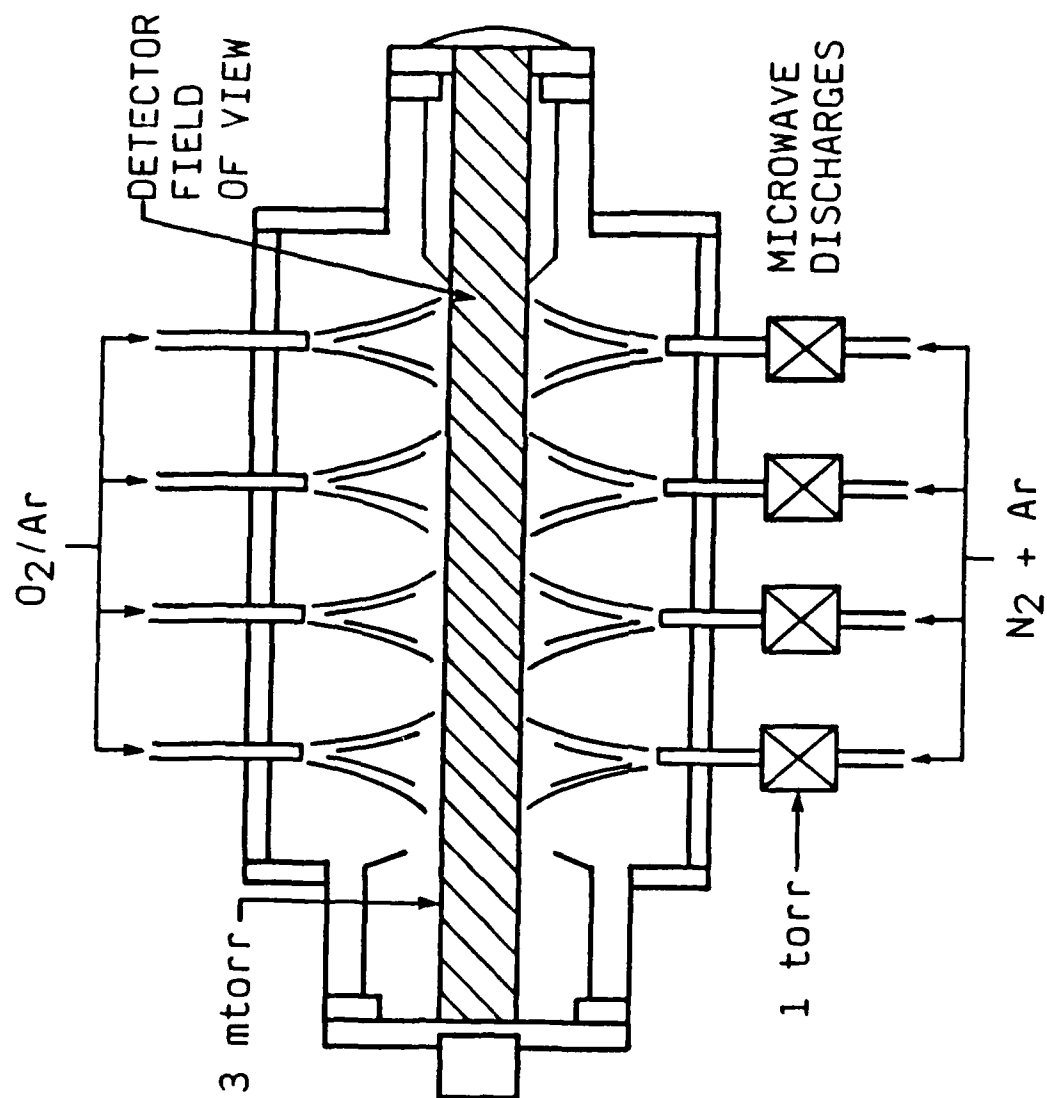
Figure 6. Computed prior distributions for $\text{NO}(v)$ formed in $\text{N}^* + \text{O}_2$ reactions. (a) $\text{N}(^2\text{D}) + \text{O}_2$: ●, $\text{O}(^3\text{P})$ product; ■, $\text{O}(^1\text{D})$ product; (b) $\text{N}(^2\text{P}) + \text{O}_2$: ○, $\text{O}(^3\text{P})$ product; □, $\text{O}(^1\text{D})$ product; ∇, $\text{O}(^1\text{S})$ product

Figure 7. Comparison of rotationally "hot" populations for $v=1-8$ and rotationally "thermal" populations for $v=12-14$ to composite prior distribution for the $\text{N}(^2\text{P}) + \text{O}_2$ reaction (curve)

Figure 8. Surprisal plots for $\text{NO}(v)$ formed from two branches of the $\text{N}(^2\text{D}) + \text{O}_2$ reaction, using the population data from Figure 5a. The lines correspond to surprisal parameters λ of -6.1 and 7.4 for the $\text{O}(^1\text{D})$ and $\text{O}(^3\text{P})$ branches, respectively.

Figure 9. Rotationally thermal populations, corrected for maximum thermalized high- J component. The dashed curve represents populations determined from the surprisal analysis of Figure 10.

Figure 10. Surprisal plots and weighted least squares fits for $\text{NO}(v)$ formed from two branches of the $\text{N}(^2\text{D}) + \text{O}_2$ reaction: data corrected for maximum thermalized high- J component. Error bars have been omitted from some of the data points for clarity. The least squares lines correspond to surprisal parameters λ of -6.25 and 9.16 for the $\text{O}(^1\text{D})$ and $\text{O}(^3\text{P})$ branches, respectively.



A-6942

FIGURE 1

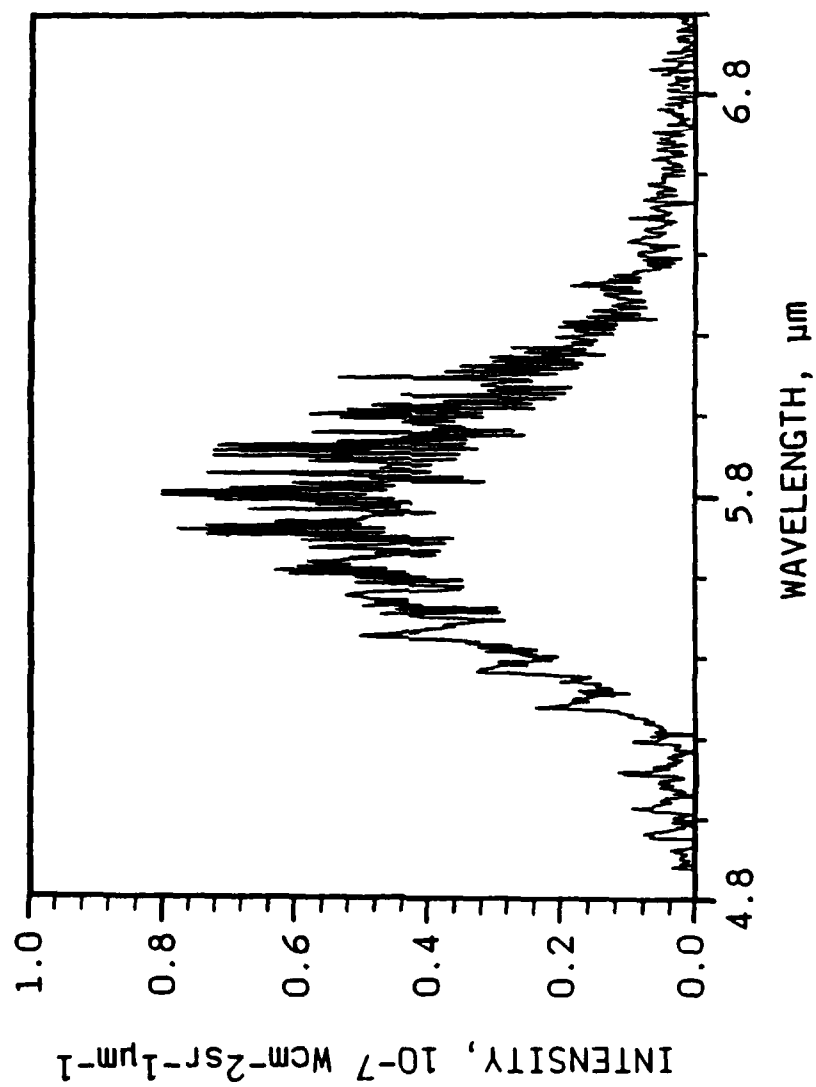
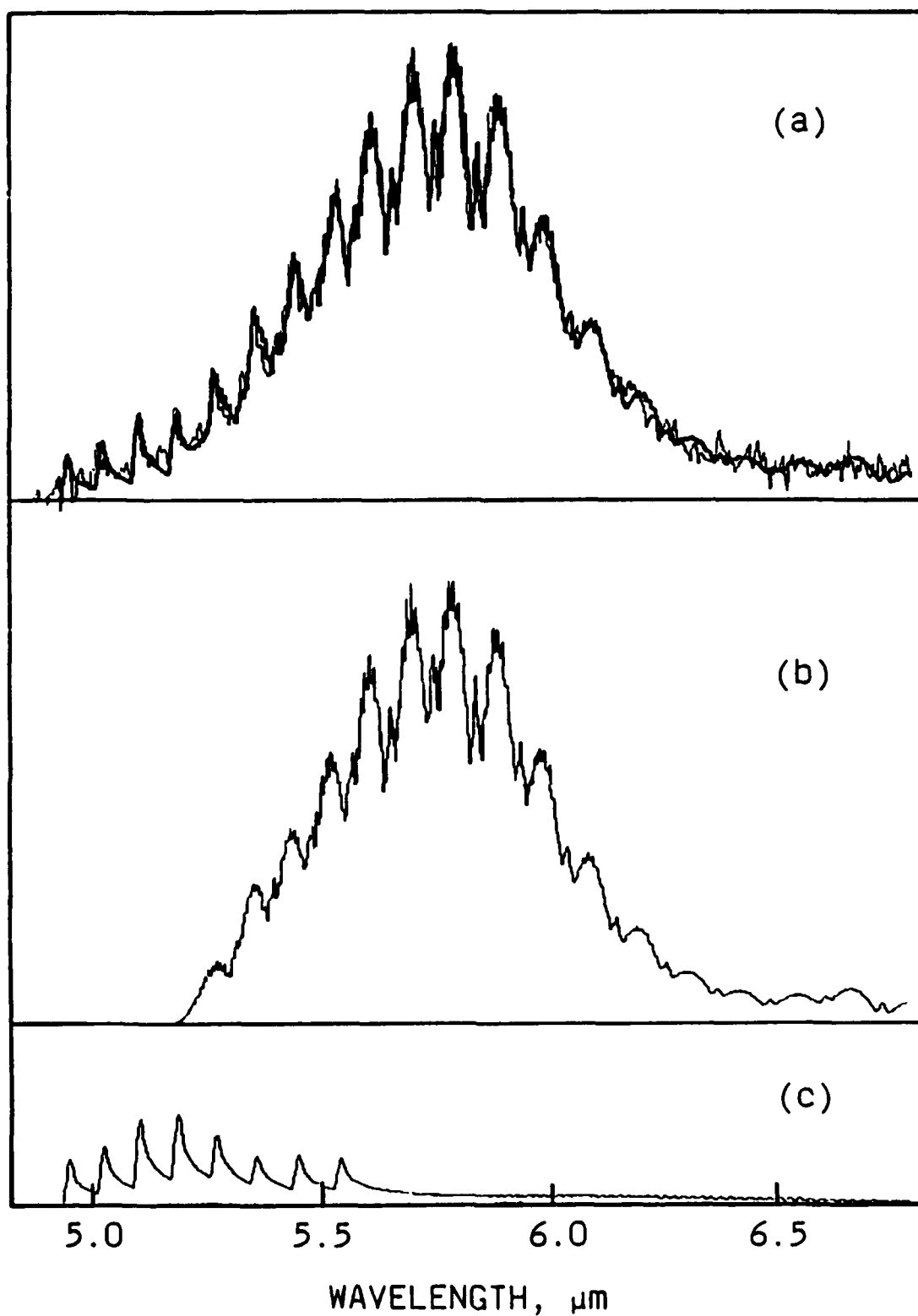
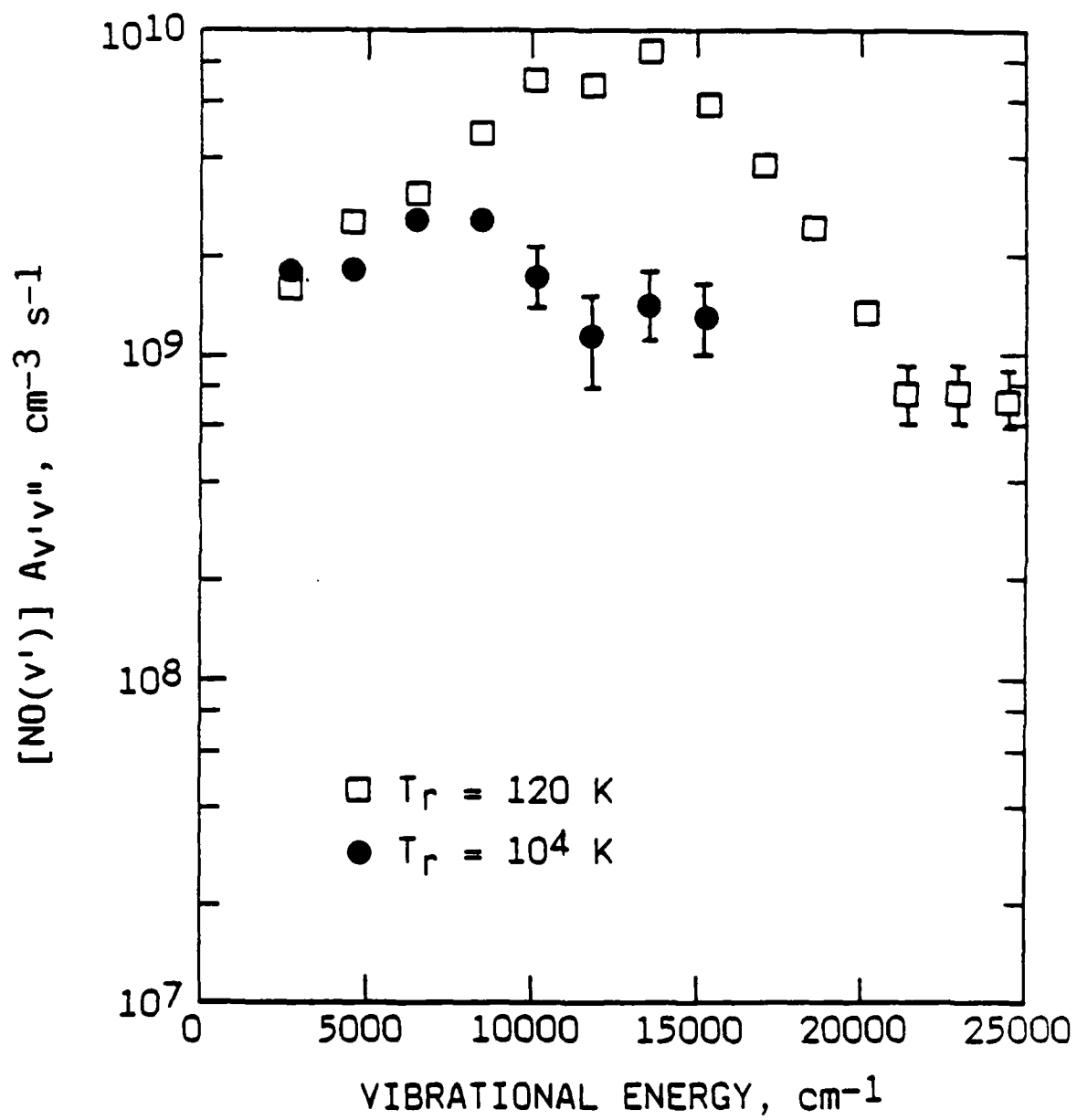


FIGURE 2



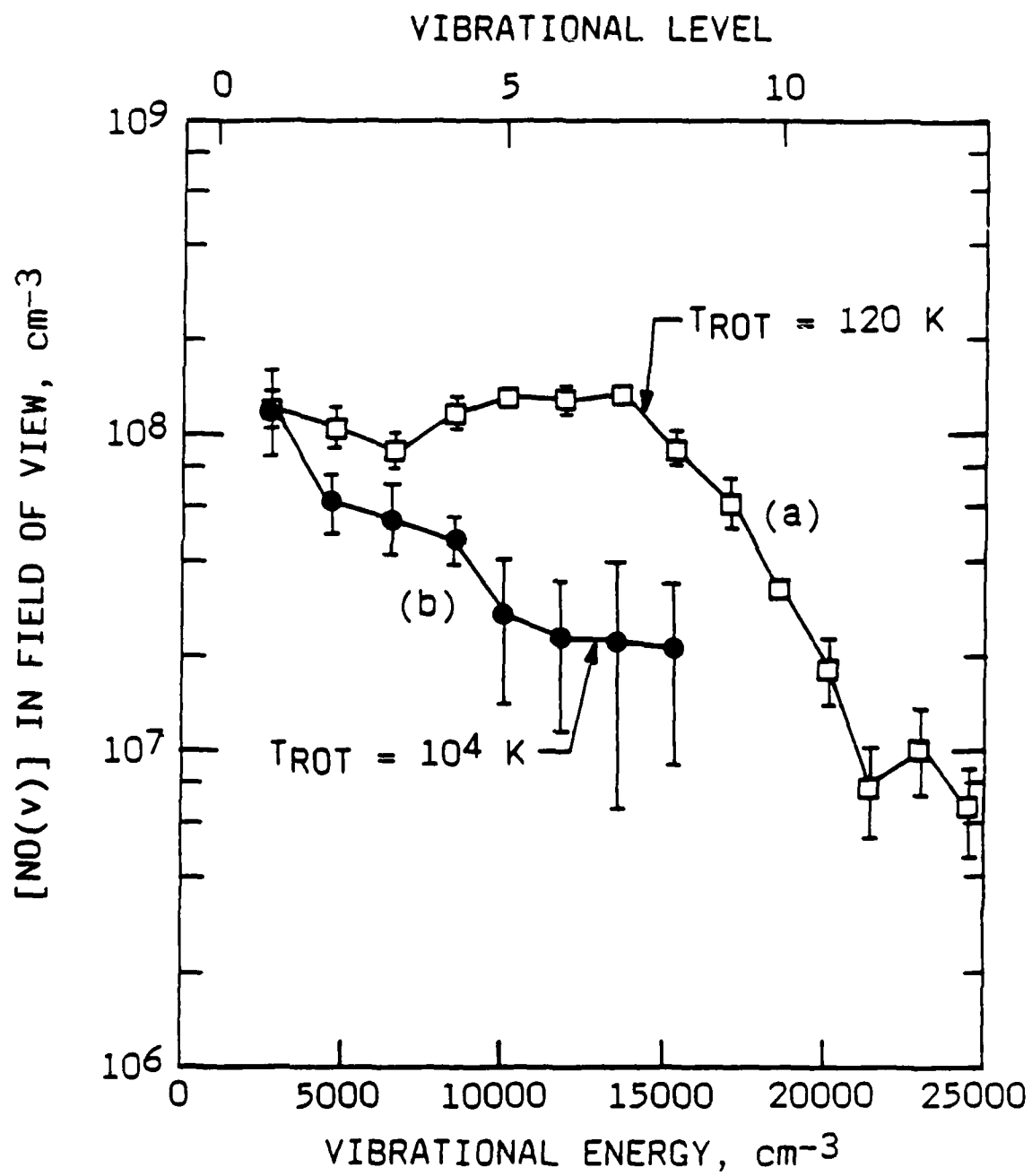
A-6944

FIGURE 3



A-6945

FIGURE 4



A-6946

FIGURE 5

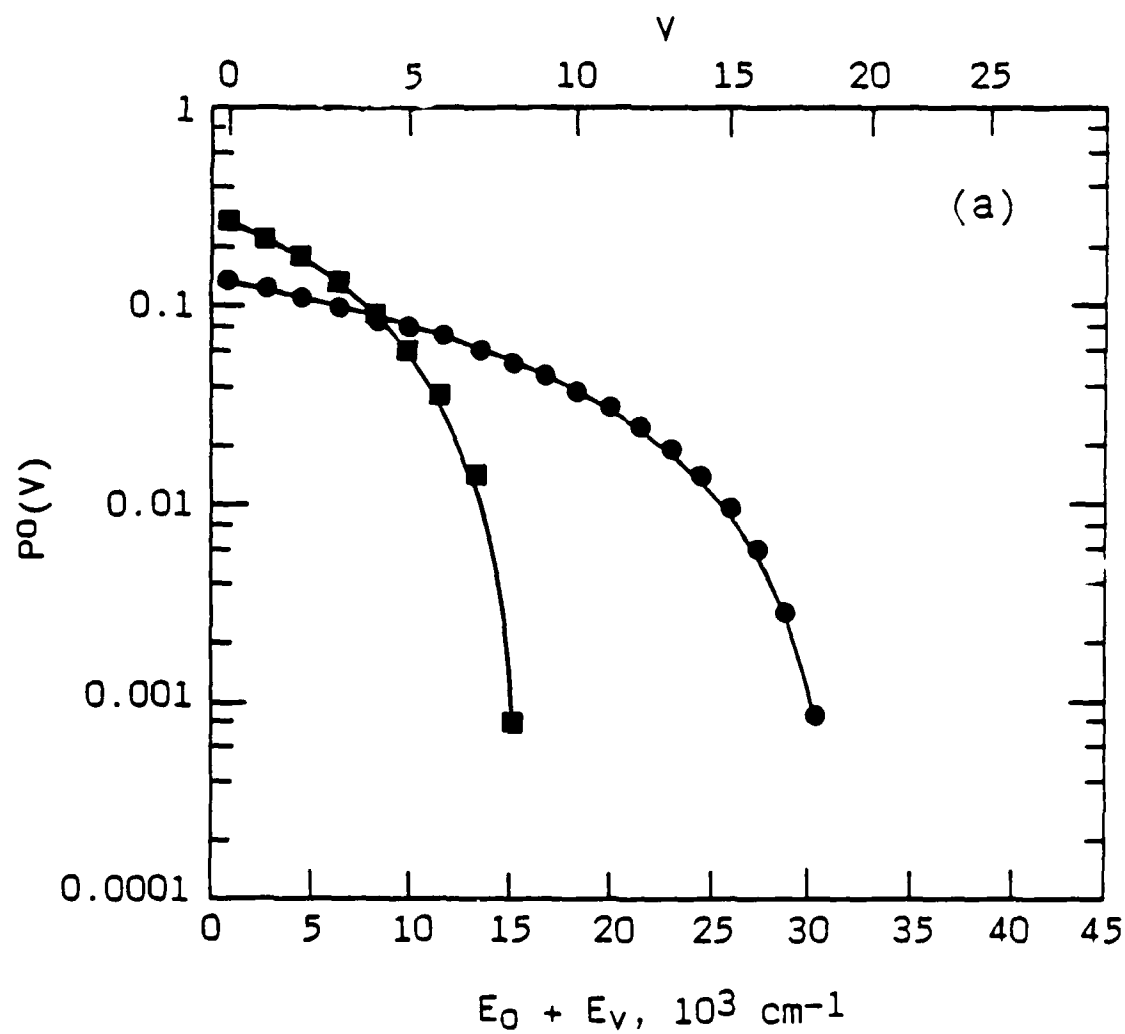


FIGURE 6a

A-6947

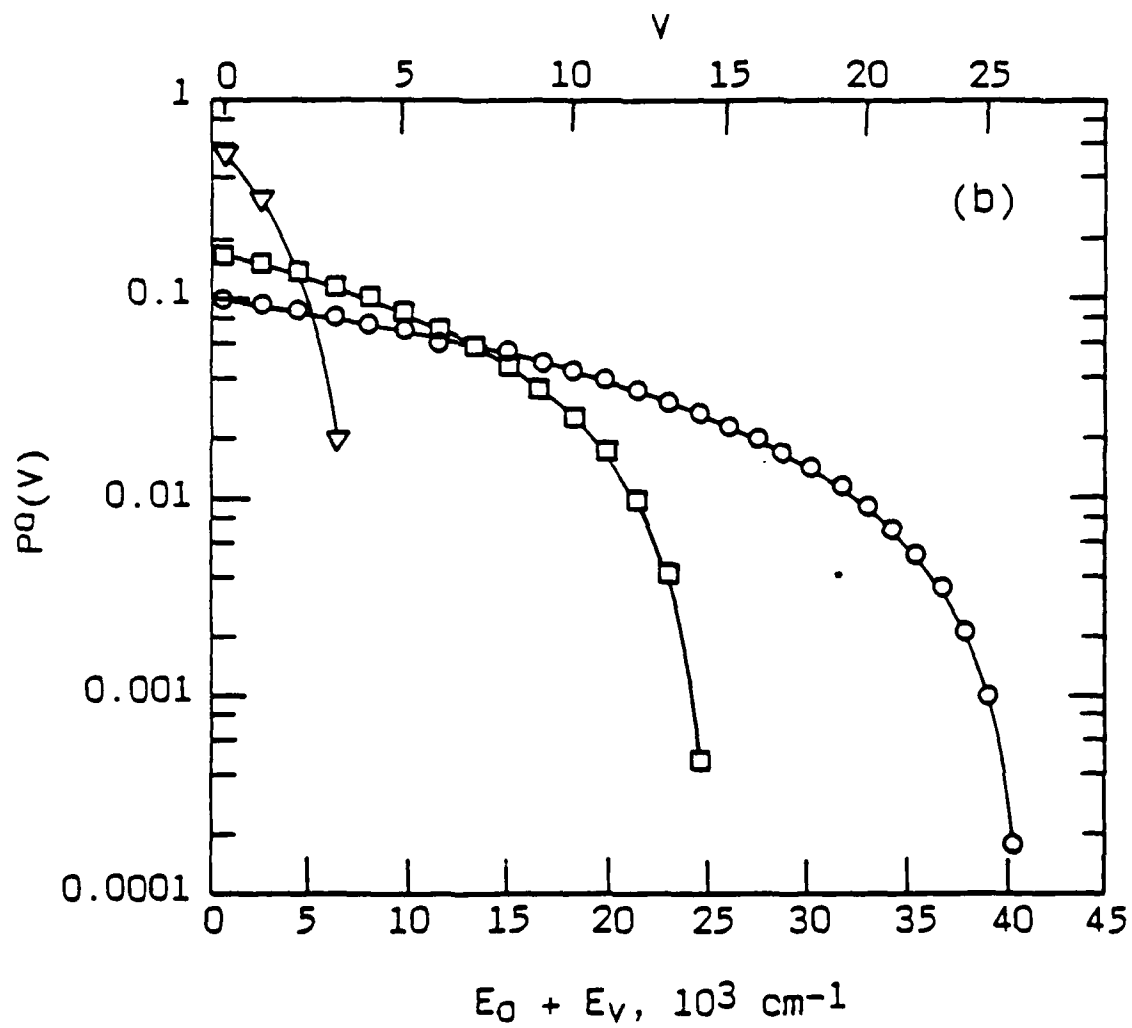


FIGURE 6b

A-6948

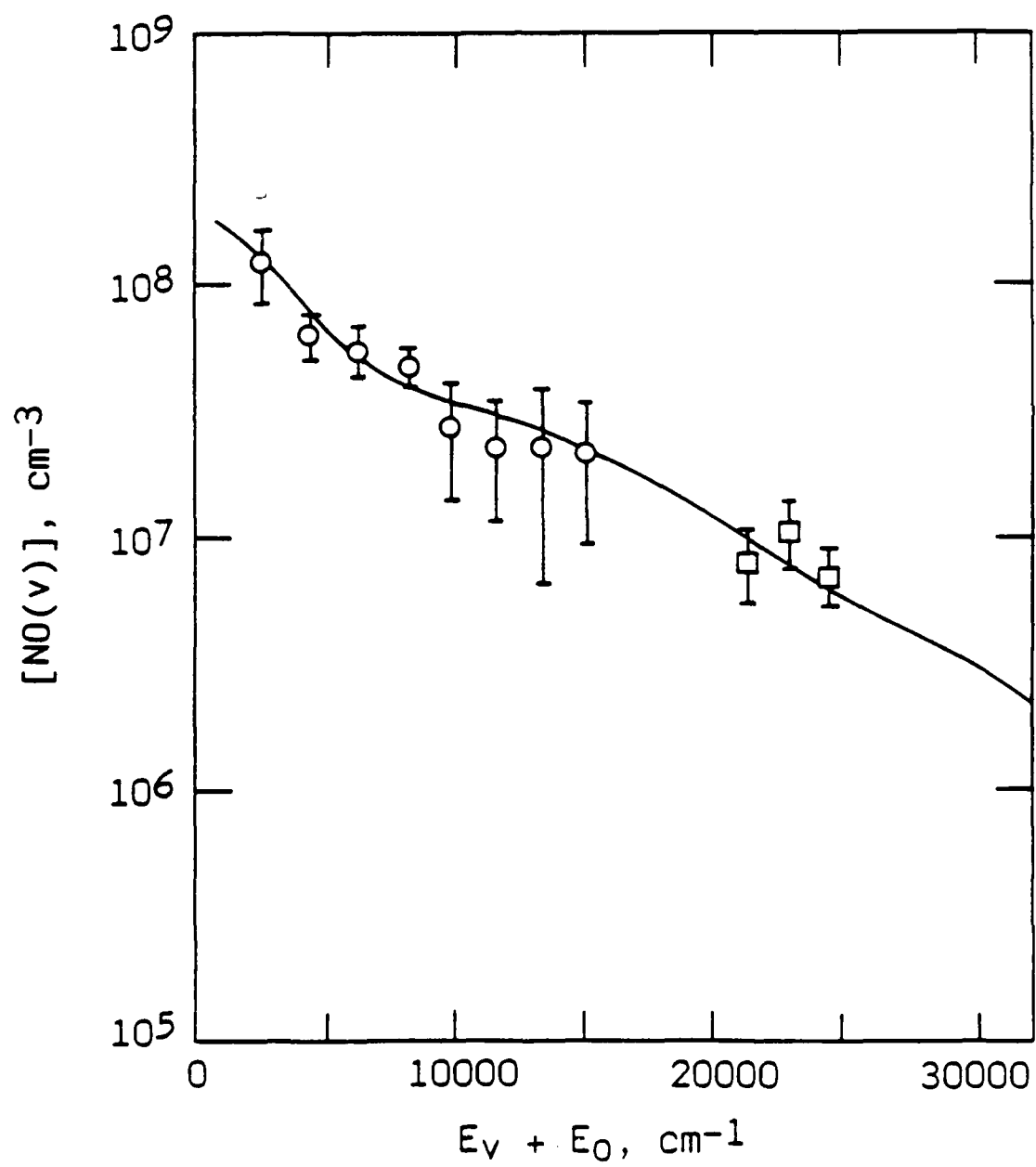


FIGURE 7

A-6949

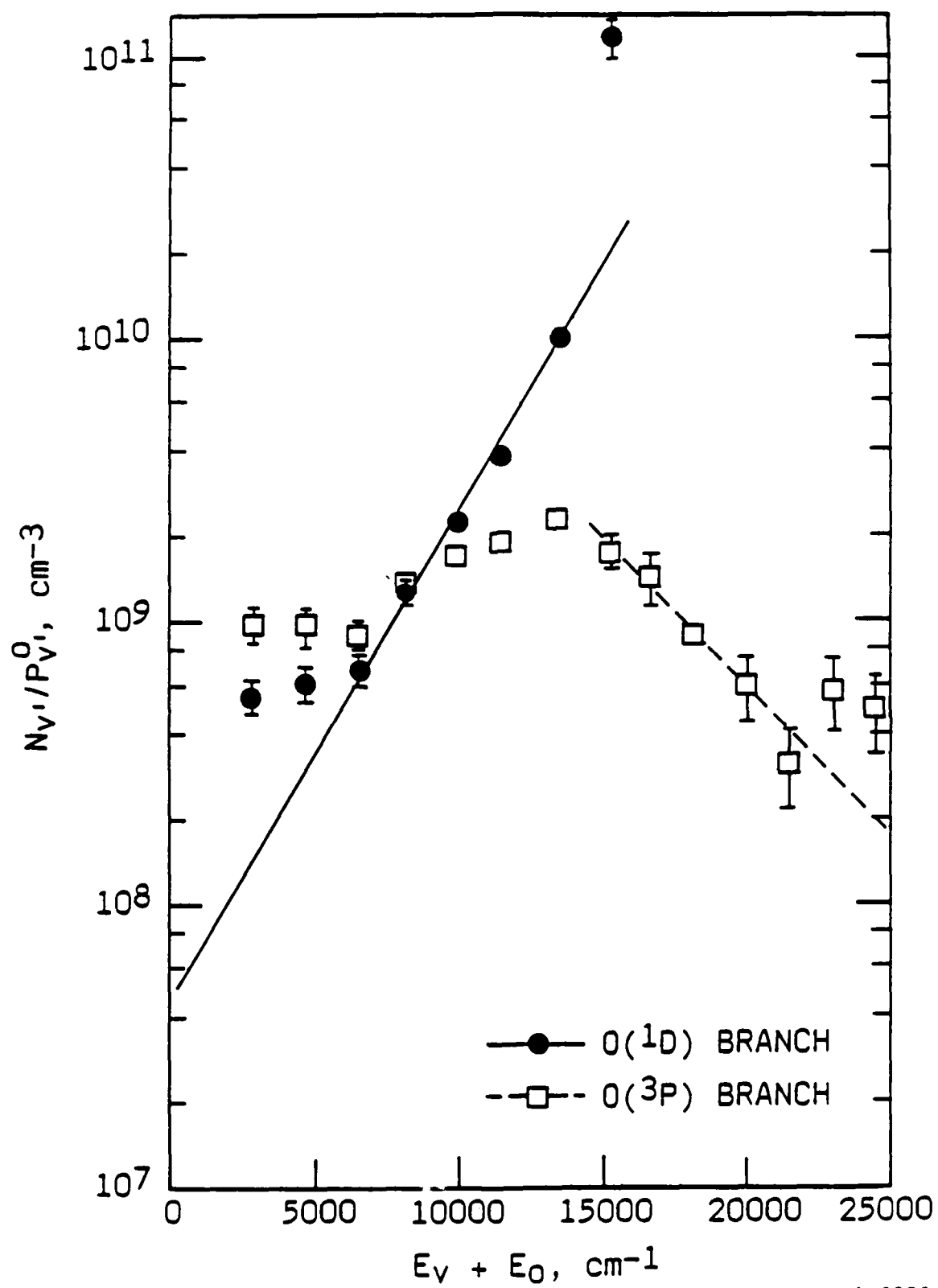


FIGURE 8

A-6950

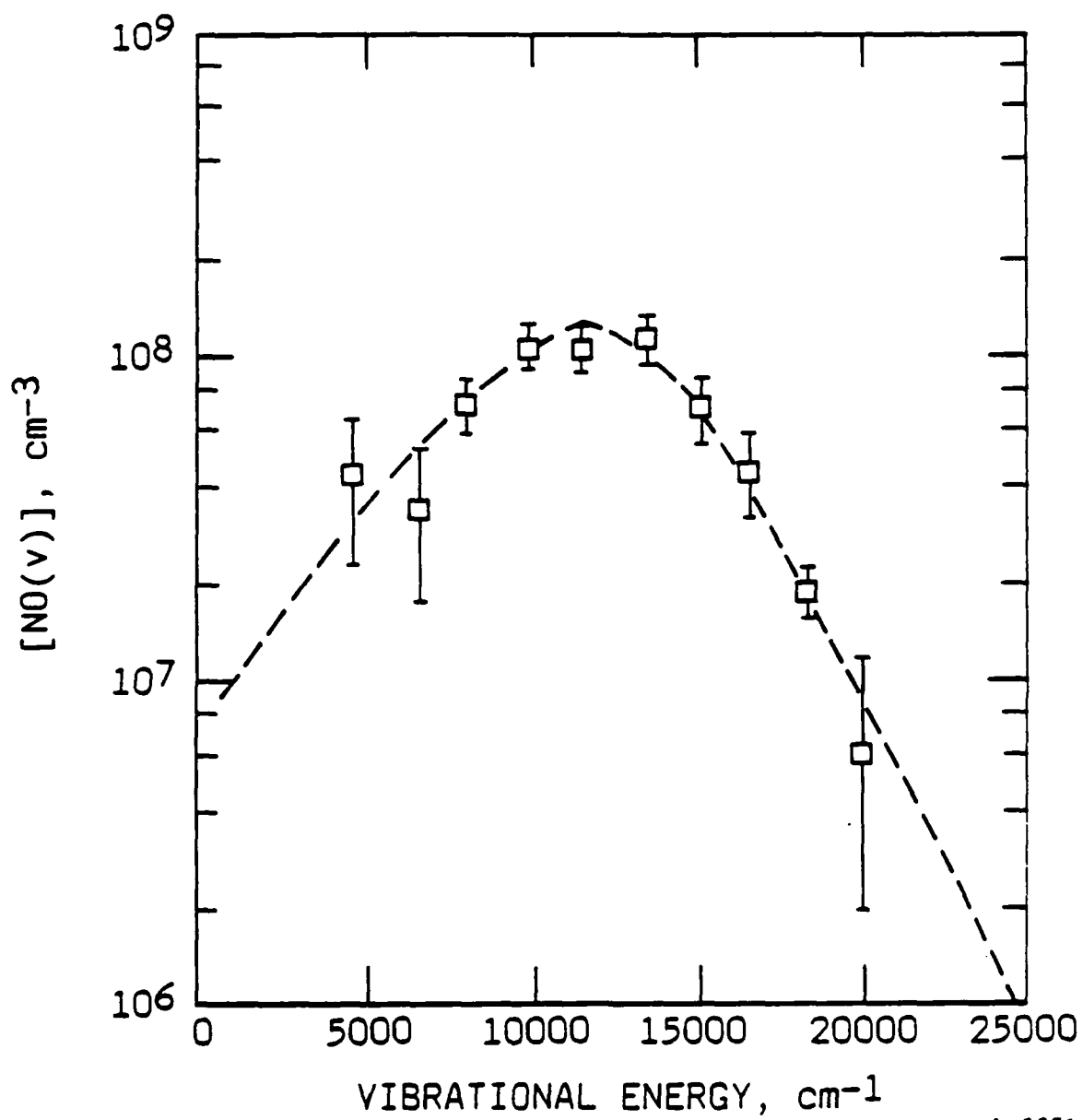


FIGURE 9

A-6951

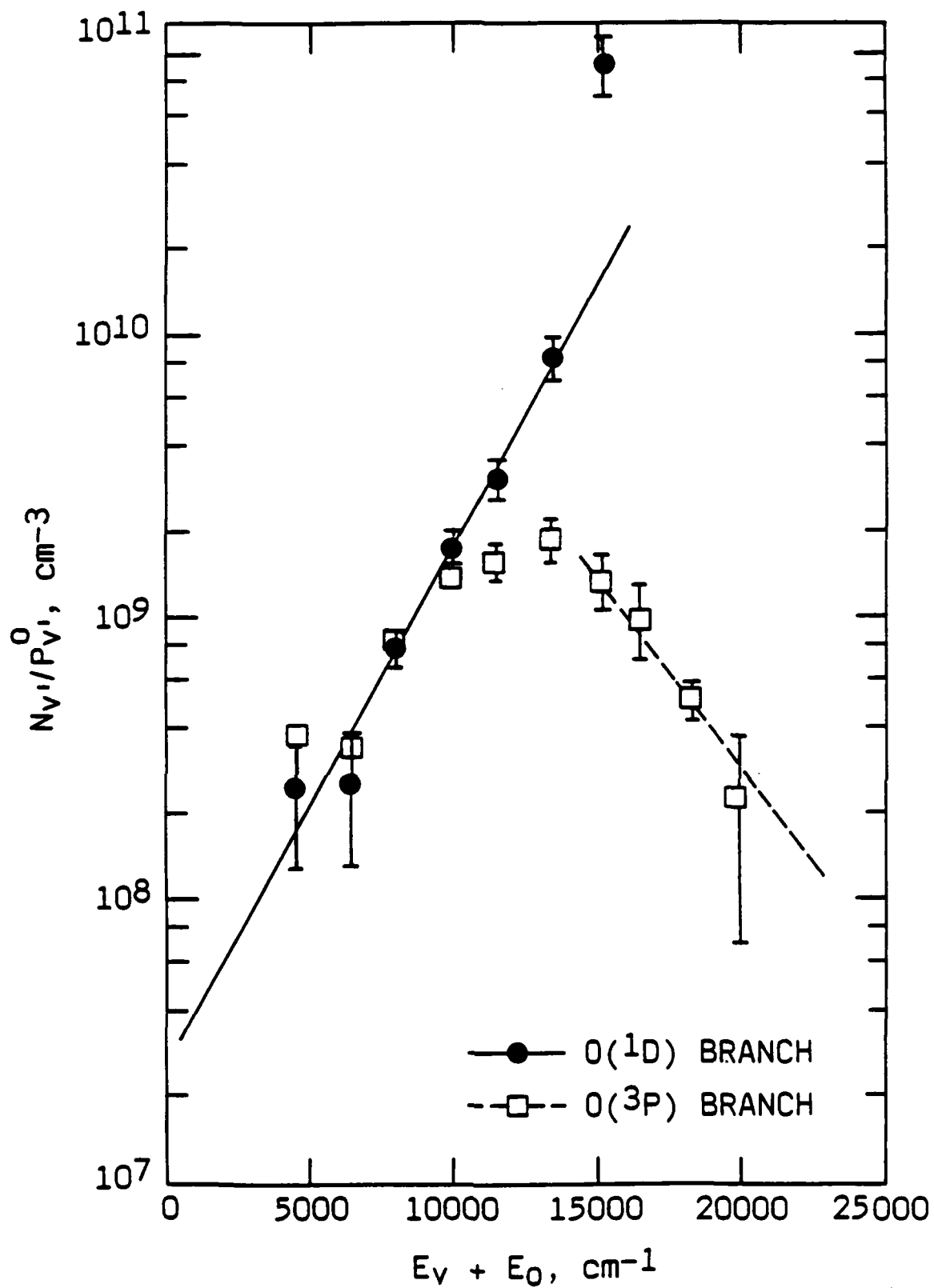


FIGURE 10

A-6952

APPENDIX Q

(SR-408 reproduced in its entirety)

J. Phys. Chem., submitted (1989)

ROVIBRATIONAL EXCITATION OF CARBON MONOXIDE BY
ENERGY TRANSFER FROM METASTABLE NITROGEN

Mark E. Fraser and Wilson T. Rawlins

Physical Sciences Inc.
Research Park, P.O. Box 3100
Andover, MA 01810

and

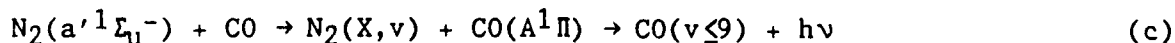
Steven M. Miller

Air Force Geophysics Laboratory/OPI
Hanscom AFB, MA 01731

J. Chem. Phys., submitted

ABSTRACT

CO fundamental vibration-rotation band emission resulting from the interaction of discharged nitrogen with carbon monoxide has been studied at low pressure (~3 mt) in a cryogenic apparatus. The spectra exhibit bimodal rotational distributions; we have identified fourteen vibrational levels of a thermalized component and eight vibrational levels from a rotationally excited component. The rotationally excited emission is adequately reproduced by a statistical distribution, $E = 3.7$ eV, which provides sufficient population in the region of the Fortrat reversal ($J \sim 90$) to account for the observed R-branch band head formation. The excitation reactions are:



Single and two-quantum transfer from $N_2(v)$, reactions (a) and (b), contributes to the thermalized $CO(v=1,2)$ populations. Radiative cascade from $CO(A)$ produced by quenching of $N_2(a')$, reaction (c), also contributes to the thermalized populations. Based on kinetic and energetic arguments we have determined another branch of $N_2(a')$ quenching to be responsible for the rotationally excited component.

Surprisal analysis of the rotational excited component vibrational distribution indicates two dynamic mechanisms. We have modeled this distribution with equal contributions from a direct ($v \leq 4$) and a statistical (all v) process. The vibrational distributions of the rotationally thermal component are reproduced by $CO(A^1\Pi)$ radiative cascade and a contribution from reaction (d).

INTRODUCTION

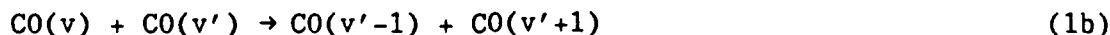
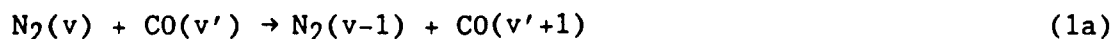
The dynamics of energy disposal in quenching/reaction of excited state species may be determined from the nascent electronic-vibrational-rotational-translational distributions of the product molecules. The observed product state distributions reflect the details of the interaction mechanisms and provide insight into the nature of the potential energy surfaces. We have previously reported observations of infrared chemiluminescence from vibrationally and rotationally excited NO generated from the reaction of metastable atomic nitrogen with molecular oxygen.¹ Surprisal analysis of the data supports two mechanisms: a direct abstraction reaction (N^2D) + O_2 producing rotationally thermal but vibrationally excited NO and an insertion reaction $N(^2P) + O_2$ giving essentially statistical vibrational and rotational product state distributions.

This paper reports observations of highly rovibrationally excited CO formed by energy transfer between carbon monoxide and nitrogen metastables. The observed CO fundamental spectra contain rotationally thermalized emission for $v \leq 14$ and rotationally excited bands for $v \leq 8$. The rotationally excited component appears as R-branch band heads that require significant populations in high rotational levels near the vertex of the Fortrat parabola ($J_{\text{vertex}} \sim 90$). The energetics of both the thermal and rotationally excited components are attributable to an energy transfer process which deposits up to ~ 3.7 eV into CO rovibrational states.

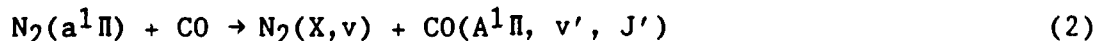
Modest energy depositions (typically < 1 eV) in CO internal states have been observed in photochemical and abstraction reactions. In general, large fractions of the energy above threshold are manifested in product internal states. For example, photolysis of OCS at 157 nm² of acetone³ at 193 nm, and H_2CO ^{4,5} produces vibrationally excited CO with rotational excitations up to 0.9 eV. Studies of energy partitioning in CO from the reaction of hot H atoms with CO_2 indicates nearly 1.0 eV in CO internal states⁶ with the rotational distribution in the $v=0$ level following a statistical model.

Greater energy depositions are observed for energy transfer reactions since these interactions have little or no threshold energy. Quenching by $O(2^1D)$,⁷ $Na(3^2P)$,^{8,9} $I(5^2P_{1/2})$,¹⁰ and $Br(4^2P_{1/2})$,¹⁰ and $Hg(6^3P_1$ and $6^3P_0)$ ¹¹ have been observed to produce vibrationally excited CO. Rotational excitations of ≤ 0.8 eV have been reported for the $Na(3^2P) + CO$ quenching reaction⁹ which accounts for a large fraction of the total 2.1 eV exoergicity.

The excitation process observed here is energy transfer from a metastable state of nitrogen. Energy transfer to CO from discharged nitrogen has been examined closely, particularly with respect to the N_2 -CO laser.^{12,13} High CO vibrational excitation is produced from near-resonant $N_2(v)$ energy transfer and subsequent $CO(v)$ collisional up-pumping,^{14,15} reactions (1a and b).



Although high CO vibrational levels are produced in this manner, no rotational excitation is observed, which is consistent with the small energy defect for the near-resonant process. The energy defect from $N_2(a^1\Pi)$ quenching,¹⁶ reaction (2) has been determined



to be largely manifested in rotation but the total energy defect is small ($< 1000 \text{ cm}^{-1}$), much less than the rotational excitations observed here. The quenching of $N_2(A^3\Sigma_u^+)$ by CO ¹⁷ produces $CO(a^3\Pi)$ with no reported observations of a $CO(v,J)$ product channel.

The energy transfer process reported here represents a previously unobserved quenching reaction of CO with metastable nitrogen. We will show that consideration of kinetic and energetic constraints positively identifies $N_2(a'^1\Sigma_u^-)$ as the responsible agent. We will also present and discuss the

results of surprisal analysis of the observed vibrational distributions which indicates the rotationally excited component to be formed by two distinct mechanisms.

EXPERIMENTS

These experiments were performed in the COCHISE (COLD CHemiexcitation Infrared Stimulation Experiment) cryogenic discharge afterglow apparatus which is described in detail elsewhere.¹⁸ Excitation of nitrogen is achieved with four parallel microwave discharges (2450 MHz, 50 W) of flowing N₂/Ar mixtures at ~1 torr total pressure. A diagram of the reaction chamber is shown in Figure 1. After exiting the discharge tubes the gas expands into a low pressure (~3 mt), cryogenically pumped chamber (~20 K) where the molecules enter the collimated field of view of a scanning monochromator/infrared detector assembly. Residence times in the discharge tubes are on the order of 3 to 5 ms; an average time of flight of 0.5 ± 0.1 ms is required for the gases to exit the discharge tubes and enter the field of view. Opposing flows of argon/carbon monoxide are used to create a quasi-static interaction region along the centerline of the field of view, resulting in partial rethermalization of the expansion cooled rotational distributions. The gas residence time in the field of view is ~0.3 ms. Gaseous helium refrigerant maintains all internal temperatures at 20 K, excepting the gas lines and optics which are held at 80 and 40 K, respectively.

The infrared emissions are observed by a cryogenic 0.5 m Czerny-Turner monochromator equipped with a liquid-helium-cooled arsenic-doped silicon detector and a grating blazed at 3 μ m. A chopper located in front of the monochromator entrance slit modulates the signal at 23 Hz. Data collection is performed with a computer-interfaced lock-in amplifier. The absolute uncertainty in the wavelengths (due to monochromator drive error) of the data is ± 0.003 μ m. The data were corrected for instrument responsivity using blackbody calibration spectra taken in the 300 to 370 K range. The uncertainty in the

accuracy of the blackbody temperature is ± 3 K, which results in a relative error of ± 14 percent for $4.0/6.0$ μm intensity ratios. Spectra were taken for N_2/Ar mixtures with N_2 mole fractions of 0.005 to 0.12, with a mass-balanced counterflow of CO/Ar with CO mole fractions of 0.018 to 0.35. The data were taken typically at a spectral resolution of 0.013 μm (FWHM).

RESULTS

In all, 24 emission spectra of the CO fundamental region were obtained at various N_2 and CO mole fraction conditions. The conditions are similar to those in which nitric oxide fundamental emission was examined.¹ The general features of the emissions are relatively invariant with CO mole fraction but the intensity of the $\text{CO}(1-0)$ emission exhibits a strong mole fraction dependence as shown in Figure 2.

The envelope degrading to the red of the $\text{CO}(1-0)$ band center at 4.666 μm is due to the $\Delta v=1$ progression from $v \leq 14$. The five sharp red-degraded features to the blue of the $\text{CO}(1-0)$ band center, which have a spacing of 29.2 ± 1.4 cm^{-1} , cannot be attributed to CO thermalized vibrational emission. These bands have not been previously observed in published spectra of CO fundamental emission taken at higher pressures (>1 torr).¹⁹⁻²¹ At low pressure with the COCHISE apparatus, these features are observed under all conditions that produce the CO fundamental emission. They have been observed to remain unstructured even at the highest resolution employed (0.0067 μm). Under low nitrogen mole fraction conditions, in which the $\text{CO}(1-0)$ emission intensity is greatly reduced, eight bands are observed with three progressing into the thermalized $\text{CO}(\Delta v=1)$ envelope. Considering the overlap of the CO thermalized emission, identification of eight such features represents a lower limit.

These emissions are not observed in the absence of nitrogen in the discharge mixture. Thus, Argon metastables and residual ions do not contribute.

We have determined these features are not due to $\text{CN}(v)$, electronic N_2 transitions, or NCO . The spectral shape of these features, sharply peaked and degraded to the red, is similar to the nitric oxide R-branch band heads identified in spectra of chemiluminescence produced from the reaction of discharged nitrogen with oxygen.¹ CO forms band heads similarly; at sufficiently high rotational excitation band heads will form in the R-branches and the P-branches will extend to the red and do not form band heads. We have used a spectral generation technique to predict the band shapes and positions of the CO R-branch band heads. The methodology and result will be presented in detail in the following section. Using this technique the sharp red-degraded features have been positively identified as CO R-branch band heads. These features are sufficiently intense that we have been able to determine an optimum rotational distribution. Additionally, the P-branches of the rotationally excited component associated with the R-branch band heads are identifiable which verifies both the spectral assignment and confirms the appropriate choice of rotational distribution.

SPECTRAL ANALYSIS

The data have been analyzed using a spectral generation linear least squares fitting technique.²² A computed infinite resolution spectrum is convolved with the instrument scan function (in this case, a symmetric triangle with full width at half maximum as the spectral resolution) to create a basis set for each vibrational transition. The basis sets are then fit to each experimental spectrum using a linear least squares method yielding a determination of the product of the upper state density and the spontaneous emission coefficient of the transition, $N_{v'} A_{v',v''}$.

The spectroscopic data used in this study are from Huber and Herzberg.²³ The data were sufficient to adequately reproduce the line positions of both the rotationally thermalized emission features and the R-branch band heads.

The rotational temperature used to reproduce the CO vibrational progression to the red of 4.6 μm was determined empirically by reproduction of the observed branch structure. The optimum temperature was determined to be 80 K indicating this emission system is rotationally thermalized. The rotational distribution was treated by a simple Boltzmann expression, so that band-integrated vibrational number densities and transition probabilities were used. The transition probabilities were calculated using the dipole moment function of Chackerian et al.²⁴ Fourteen vibrational levels of thermalized CO emission have been positively identified from the data. This corresponds to vibrational excitation of 3.425 eV.

The band-averaged transition probabilities used for the rotationally excited component are the same as those for the thermalized CO emission. We believe these values to be accurate since the CO ground state is $^1\Sigma$ and therefore not subject to spin-uncoupling at high J' as discussed for NO. In addition, the dipole moment function of Chackerian et al.²⁴ extends to $v'=40$, well above the internuclear separation of the highest V' and J' levels encountered in this study. Thus, Hönl-London scaling of the band-averaged transition probabilities is sufficient to accurately determine the populations of the rotationally excited component.

The 5 cm^{-1} resolution (at 5.0 μm) of the spectral data is insufficient for rotational resolution of the R-branch band heads so the chosen rotational distributions are those which best reproduce the band shapes and peak positions. To adequately fit the R-branch band head features by a Boltzmann distribution requires temperature of approximately 20,000 K. Although the fits to the lower vibrational levels are adequate, higher vibrational levels are poorly fit and are better described by lower Boltzmann rotational temperatures. This is evidence for an anti-correlation between rotational and vibrational excitation; i.e., the lowest vibrational levels contain the most rotational excitation. Such anticorrelations have been observed in photolysis experiments, abstraction reactions and energy transfer processes.^{2-7,9} In these instances, the observed rotational distributions are sometimes best described by a statistical model.⁶

Such a model distributes the population statistically over the accessible states. The model which incorporates the observed anticorrelation between vibrational and rotational excitation is given by,

$$P_v^0(J) \propto (2J + 1) \{ (E_T - E_v) - E_J \}^{1/2} \quad (3)$$

where E_T is the total energy available for product states, E_v is the vibrational energy, and E_J is the energy of the particular rotational level. Figure 3 contrasts the relative population distributions predicted by Boltzmann and statistical models. The statistical model contains greater relative population in the higher rotational levels at the expense of the lower. Thus, rotational band head formation, which requires significant population of rotational levels in the region of the Fortrat parabola vertex ($J_{\text{vertex}} = 92$ for $v=1$), is readily facilitated by a statistical distribution.

We have examined several values of E_T to determine which produces the best fit to the data, i.e., reproduction of the positions and spectral shapes of the observed eight band heads. Values of E_T below 3.0 eV reproduce the lower vibrational levels well but the predicted band heads at higher vibrational levels are broadened and red-shifted. The responsible mechanism may be seen from Figure 3. At higher E_v , and lower E_r , the relative population of the rotational levels near the region of the reversal decreases which causes the observed effects. Values of E_T greater than 4.0 eV predict band head formation for vibrational levels ten or greater. We prefer a value of E_T between these two bounds. Comparing fits using several values within this range, we have determined $E_T = 3.7$ eV to be optimum. Values within ± 0.2 eV of the optimum value produce adequate fits with only small differences.

Table 1 shows the energetics of CO band head formation for E_T of 3.7 eV. Shown are the values for E_r , the rotational level corresponding to the vertex of the Fortrat parabola, the rotational energy corresponding to this value of J , and the maximum rotational level allowable from E_r .

Figure 4 shows a typical fit to the data using 14 vibrational levels of rotationally thermalized emission and eight vibrational levels with a statistical rotational distribution corresponding to $E_T = 3.7$ eV. All of the principal spectral features are accurately reproduced. The only features not entirely reproduced fall within the 5.7 to 6.5 μm region. Figure 5 shows an enlarged view of this region from Figure 4. The fit is shown by the heavy line. The spacing of the bands shown in Figure 4 is ~ 6 cm^{-1} . These features have been observed in all spectra containing sufficient intensity in this wavelength region. The fit shows excellent reproduction of the spectral shapes but does not match the absolute intensity. Figure 4 shows that the thermalized emission does not contribute to this spectral region; the discrete features are reproduced by the P-branches of the rotationally excited component. Inclusion of $v \geq 8$ of the rotationally excited component improves the fits in this wavelength region. Due to overlap with the thermalized CO envelope, however, unique determination of the populations is not possible, so we have generally excluded these bands from the fits. We describe in the Discussion Section that unique fits may be obtained by fitting the rotational excited component as a single variable with the relative vibrational levels fixed in ratios from a modeled distribution. By comparing fits with different vibrational contributions to the rotationally excited component, we have determined that the majority of the intensity in the 5.7 to 6.5 μm region arises from the higher vibrational levels ($v' = 6-8$). The relative line spacings may be calculated (omitting D_v correction) from

$$\Delta\nu = P(J) - P(J=1) = (B_{v'} + B_{v''}) - (B_{v'} - B_{v''})(2J+1) . \quad (4)$$

For $v' = 6-8$ this wavelength region contains P-branch line spacings of ~ 6 cm^{-1} for rotational levels 50-80. The $\text{N}_2(\text{W}^3\Delta_u, v'=1 \rightarrow \text{B}^3\Pi_g, v''=0)$ emission in the 6.3 to 6.6 μm region, which we have previously examined and reported,²² and signal to noise considerations impede determination of the full extent of the P-branch structure. The reproduction of these features, however, by fits to the rotationally excited component confirms the identification of the CO R-branch band heads.

All 24 spectra have been fit using 14 thermalized CO emission bands and eight vibrational levels of the rotationally excited component, as shown in Figure 4. All the fits show similar reproduction of the principal features although many do not accurately reproduce the absolute emission intensity of the P-branch envelope. The discrepancy shown in Figure 4 is typical. Fits to this spectral region are improved by inclusion of higher vibrational levels of the rotationally excited component. Accurate determination of any contribution from the higher levels cannot be determined due to the overlap of these band systems with the thermalized envelope. Bounds for their relative populations will be discussed in the next section.

The statistical rotational distributions employed in these fits provide a better reproduction of the data, both in the R-branch spectral band shapes and the absolute intensity of the P-branches, than do Boltzmann rotational distributions. We consider the statistical model employed here to be a more accurate representation of the true rotational distributions but it cannot be considered to be a unique determination. Signal to noise considerations and band overlap do not permit unambiguous identification of the vibrational-level dependent rotational distributions. The true distributions may deviate from a purely statistical model, containing gaussian character as has been observed in other systems. However, the model employed here has successfully demonstrated an anticorrelation between vibrational and rotational excitation and permitted a bound of ~ 3.7 eV to be determined for the rotational excited component. Determination of this bound and its similarity to the vibrational excitation of the thermalized component, 3.425 eV, suggests that these two components arise from the same excitation process.

KINETIC INTERPRETATIONS

The kinetics of processes occurring in the COCHISE reaction chamber have been previously described.¹ Owing to the low number densities in the reaction zone, the short residence time in the field of view (0.3 ms), and the long

radiative lifetimes for the infrared chemiluminescent processes that we observe, reactions and quenching (excluding rotational) of the excited species created in the reaction zone can be neglected. Thus, vibrational quenching and CO(v) up-pumping, reaction (1b), can be ignored. The kinetics of [CO(v,J)] are therefore in steady-state according to the production rate and the lifetime of the excited species in the field of view,

$$d[\text{CO}(v,J)]/dt = k[M^*][\text{CO}] - \tau^{-1}[\text{CO}(v,J)] = 0 \quad (5)$$

where M* denotes the responsible excited species created in the microwave discharges, k is the excitation rate constant, and τ is the residence time in the field of view, 0.3 ms.

Figure 6 shows the absolute populations for the fit in Figure 4. The bimodal nature of the rotational distributions is apparent. The populations for the rotationally excited component exceed those of the thermal component of all vibrational levels except $v=1,2$. As noted in Figure 2, the lowest thermalized CO vibrational levels exhibit an N₂ mole fraction dependence. We have determined previously that only N₂(v) exhibits a strong variation in its discharge production rate with N₂ mole fraction over the range used here. Thus, relative increases in low CO vibrational population at higher nitrogen mole fraction must be due to the near-resonant energy transfer from N₂(v), reaction (1a).

As illustrated by Figure 2 the lowest CO vibrational populations exhibit a marked dependence with N₂ mole fraction. Examination of the determined populations for all the spectra indicates that only CO(v=1,2) are affected by nitrogen mole fraction. Since CO(v) up-pumping cannot occur under our experimental conditions, the excitation process must be single and two quantum transfer,





To determine the relative contribution of the $\text{N}_2(v)$ energy transfer process to the $\text{CO}(v=1,2)$ populations we have plotted the ratios of these populations to $[\text{CO}(v=3)]$ as a function of nitrogen mole fraction. Figure 7 shows one of these plots. Extrapolation of these curves to zero determines the relative $\text{CO}(v=1,2)$ populations which arise from sources other than $\text{N}_2(v=1,2)$ populations which arise from sources other than $\text{N}_2(v)$; i.e., from quenching of nitrogen metastables. For the data in Figure 7, the multiplicative factors are 3.0 and 1.5 for $\text{CO}(v=1,2)$, respectively. The multiplicative factors for all examined CO mole fractions have been determined to be approximately the same.

Using these factors the contributions to the thermalized $\text{CO}(v=1,2)$ populations from $\text{N}_2(v)$ transfer and E-V transfer may be separated. Figure 5 shows the $\text{CO}(v=1,2)$ number densities corrected for $\text{N}_2(v)$ transfer. The relative distributions in both the thermalized and rotationally excited components are now remarkably similar. The vibrational populations of the rotationally excited component exceed those of the thermalized component by typically ~30 percent. This is approximately the ratio determined for all the analyzed spectra. Ratios of the vibrational populations for each component exhibit no dependence on nitrogen or carbon monoxide mole fraction.

As shown in Figure 6 the fraction of the $\text{CO}(v=2)$ population attributable to two quantum transfer, reaction (6b), is small. An average ratio $[\text{CO}(v=2)]/[\text{CO}(v=1)]$ of 0.06 ± 0.01 from $\text{N}_2(v)$ transfer has been determined for all the observed spectra. This ratio is related to the rate coefficients for reactions (6a, b) in the following manner,

$$\frac{[\text{CO}(v=2)]}{[\text{CO}(v=1)]} = \frac{\sum_v k_v(\Delta v=2)[\text{N}_2(v)]}{\sum_v k_v(\Delta v=1)[\text{N}_2(v)]} \quad (7)$$

Equation (7) may be resolved for the ratio $\sum_v k_v(\Delta v=2)/\sum_v k_v(\Delta v=1)$ if the $N_2(v)$ distribution can be determined. Discharge-flow measurements using Penning ionization spectroscopy indicate the effluent of our microwave discharges may be represented by a ~6000 K "modified Treanor" distribution in $N_2(v)$.²⁵ A Treanor distribution contains enhanced populations at higher vibrational levels, relative to a Boltzmann distribution, that are created by collisional up-pumping.¹⁵ Using the modified Treanor distribution, we have determined $\sum_v k_v(\Delta v=2)/\sum_v k_v(\Delta v=1) = 0.1 \pm 0.04$. Owing to the known increase in k_v as a function of v ,^{12,13} the ratio determined here is likely representative of higher v (probably 7 to 8).

Figure 8 shows the average population distributions for the thermalized and rotationally excited components, normalized separately and shown with one standard deviation error bars. The population distributions from only eleven spectra were chosen for this average. The spectra containing large contributions to thermalized $CO(v=1,2)$ have been excluded since this emission envelope overlaps the $v=5-8$ levels of the rotationally excited component interfering with reliable population determinations of these levels.

The distributions shown in Figure 8 are similar but the distribution of the rotationally excited component appears to be relatively flat above $v=4$. We have examined the data carefully and determined this trend to be accurate. Fits to the data using a fixed relative vibrational distribution of the rotationally excited component following the distribution of the thermal component seriously underfits the data in the region of $v'=5-8$ of the R-branch band heads and in the region of the P-branches.

EXCITATION MECHANISM

Several processes which may account for all or a portion of the observed emissions require consideration. One possible mechanism for rotational

excitation of CO is energy transfer from translationally excited atoms emanating from the discharge. Translationally excited atoms may be produced in the discharges by energy transfer from Ar metastables. Translationally hot H atoms have been reported to excite V,R states of CO.²⁶ We may discount such processes in our apparatus due to rapid energy accommodation of any "hot" atoms in the 1 torr discharge tubes. The number density of such species reaching the field of view will be miniscule. Collisional quenching of high CO vibrational levels into high rotational levels of lower vibrational levels (V,R transfer), analogous to processes observed for HF,^{27,28} may also be dismissed. To excite the high J' levels we observed would require nearly gas kinetic multiquantum ($\Delta v \leq 8$) quenching of CO(v). This is unlikely since direct measurements of the v-dependent quenching of CO(v) by CO₂²⁹ indicate the total quenching rate coefficients to be less than 1 percent gas kinetic. Under quasi-resonance conditions, collisional quenching diatomics in low v, high J levels into high v, low J levels (R,V transfer) may have rate coefficients of 10⁻¹¹ cm³ s⁻¹.³⁰ The resonance conditions are given by

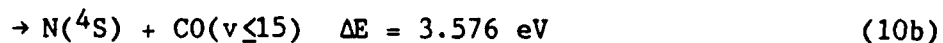
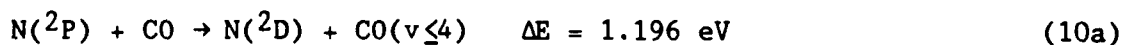
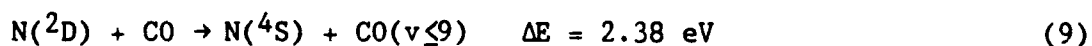
$$\frac{\omega_v}{\omega_J} = \frac{\omega_e}{4B_e J} \quad (8)$$

For CO, resonance is satisfied at J' ~120 which is populated only at the lowest vibrational level for the statistical model. Therefore, R,V transfer should not contribute significantly to the higher vibrational levels of the observed thermalized emissions.

With other possibilities excluded, the mechanism for CO(v,J) excitation must be energy transfer from one or more of the metastable nitrogen species created in the discharge. We have previously determined that to account for the CO(v,J) excitation observed here the energy transfer reaction must be at least ~3.7 eV exoergic. This constraint, combined with kinetic considerations from Eq. (8), may be used to determine the identity of the responsible species.

Summing the populations of the thermalized and rotationally excited components, a product $k[M^*] \sim 0.5 \text{ s}^{-1}$ is required to account for the observed emissions. The measured quenching kinetics for many of the metastable nitrogen species is shown in Table 2. This table contrasts the number densities of the metastable species required in the interaction zone to account for the observed emissions with the number densities determined from modeling studies. The number density calculations have employed the room temperature rate coefficients in the absence of data at 80 K.

Quenching of the metastable nitrogen atoms are shown in reactions (9) and (10). $N(^2D)$ may deposit 2.38 eV into CO



rovibrational states which is well below the $\sim 3.7 \text{ eV}$ needed to account for the observed emissions. Additionally, the kinetics of this reaction indicate that contributions to the spectra from this source would be negligibly small. The energetics of $N(^2P)$ quenching to form $N(^4S)$ matches the required $\sim 3.7 \text{ eV}$ well. However, the recently determined rate coefficient³¹ for quenching of $N(^2P)$ by CO is several orders of magnitude too small for reactions (10a, b) to be the $CO(v,J)$ excitation mechanism.

Excitation of $CO(v \leq 14)$ by energy transfer from $N_2(X, \text{high } v)$ requires multi-quantum transfer from $v \leq 14$. The determined contributions to the thermalized $CO(v=1,2)$ populations from $N_2(v)$ energy transfer are consistent with a preferred channel for single-quantum exchange and a less favored channel for two-quantum exchange. We have found no evidence for multi-quantum exchange.

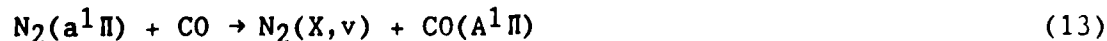
$N_2(A^3\Sigma_u^-)$ quenches with CO to form $CO(a^3\Pi)$.³³ Although the



rate coefficient for the quenching process is known³³ the absolute yield for reaction (11) has not been measured. Reaction of $CO(a)$ with another CO molecule produces vibrationally excited CO ^{36,37} with a rate coefficient for the process near gas-kinetic ($k_{12} \sim 1 \times 10^{-10} \text{ cm}^3 \text{ s}^{-1}$ at room temperature).^{38,39} Quenching of $N_2(A)$ may produce rovibrationally excited CO directly from a branch in reaction (11). Since $N_2(A)$ lies 6.17 eV above $N_2(X, v=0)$, such a process would be sufficiently energetic. The determined $N_2(A)$ quenching rate coefficient, however, is too small for this process or any derived reactions, such as reaction (12), to be responsible. Additionally, the activation barrier determined for this process by Slinger⁴⁰ indicates the rate constant to be $< 10^{-13} \text{ cm}^3 \text{ s}^{-1}$ at 80 K.

The $N_2(W^3\Delta_u, w^1\Delta_u)$ states are sufficiently energetic to produce the observed $CO(v, J)$ emissions; 7.36 eV and 7.35 eV above the ground state, respectively. The quenching reactions of these two species have not been reported in the literature. We have determined $N_2(W^3\Delta_u, v=1-5)$ and $N_2(w^1\Delta_u, v=0-2)$ number densities in COCHISE directly from their IR radiance over the 2 to 4 μm region. Their concentrations in the interaction region are $3 \times 10^8 \text{ cm}^{-3}$ and $1 \times 10^8 \text{ cm}^{-3}$, respectively. Even if these species quench CO with rate coefficients near gas kinetic, they cannot account for the observed $CO(v, J)$ emissions.

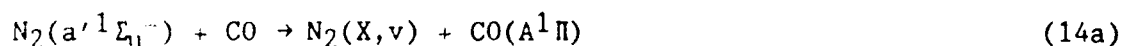
Quenching of $N_2(a^1\Pi)$ is rapid, forming $CO(A^1\Pi)$.³⁴ Since the



yield of $CO(A)$ formation from this reaction has not been determined, a channel forming $CO(v, J)$ is possible. $N_2(a)$ may deposit any fraction of the available

8.4 eV into CO rovibrational states from such a process. However, the radiative lifetime of $N_2(a)$ is short, $56 \pm 4 \mu s$,⁴¹ which makes the number density of this species in the interaction zone to be too small to account for the observed emissions. The upper limit for $N_2(a)$ number density shown in Table 2 has been determined for the noise level of discharged Ar/ N_2 spectra at the wavelength $N_2(a-a')$ features would occur.²²

The possible quenching reactions of the $N_2(a' {}^1 \Sigma_u^-)$ with CO are



$N_2(a')$ may deposit up to 8.5 eV into CO electronic, vibrational and rotational states. The branching ratio forming CO(A) has been measured as 20^{+10}_{-8} percent.³⁵ This value, however, was based on an $80^{+40}_{-20} \mu s$ lifetime for the $N_2(a)$ state which has recently been revised to be $56 \pm 4 \mu s$.⁴¹ The corrected CO(A) branching ratio is 30 ± 8 percent. The remaining fraction must be divided between the other energetically accessible spin-allowed channels. These channels are rovibrationally excited CO(X), reaction (14b), and the $I {}^1 \Sigma^-$ and $D {}^1 \Delta$ states, reaction (14c). At room temperature the total quenching rate constant for reaction (14) is $1.1 \times 10^{-10} \text{ cm}^3 \text{ s}^{-1}$. Table 2 shows that the kinetics of this reaction are sufficient to account for the observed emissions.

Since $N_2(a')$ is the only species present in the interaction zone that satisfies both the kinetic and energetic constraints, we postulate that reaction (14b) is responsible for the observed CO(v, J) excitation. For this hypothesis to be correct, the branching fraction for reaction (14b) must be relatively large, constraining that for reaction (14c) to be small and, owing to the short radiative lifetime of CO(A), the thermalized populations must reflect a contribution from CO(A) radiative cascade.

DISCUSSION

Further interpretation of the data may be assisted by surprisal theory.^{42,43} This approach postulates the existence of an exponential gap law for an individual metathetic reaction:

$$P_v = P^0(v) \exp(-\lambda f_v) / \exp(\lambda_0) \quad (15)$$

where f_v is the fraction of the reaction exoergicity appearing as vibrational energy in the product, $P(v)$ is the observed relative vibrational population, and $P^0(v)$ is the statistical "prior" distribution obtained when all final translational, rotational, and vibrational states are equally probable. Thus, the ratios of the observed and statistical vibrational populations should be exponential in the vibrational energy E_v , with the exponential fall-off constant λ quantifying the departure of the observed distribution from a completely statistical product distribution. While this theory does not necessarily hold for all chemical interactions, it has proved useful in the analysis of rovibrational product distributions from several photo chemical and reactive interactions.

Both the vibrational extent of the thermalized CO emission ($v \leq 14$, $E \sim 3.4$ eV) and the rovibrational excitation of the rotationally excited component ($E_T \sim 3.7$ eV) can be attributed to an energy transfer process of 3.5 to 3.7 eV. Using a prior distribution for 3.7 eV determined from the usual relationship for a vibrating rotator,

$$P^0(v) = (1-f_v)^{3/2} / \sum_{v=0}^{v^*} (1-f_v)^{3/2} \quad (16)$$

the vibrational surprisal plot for the vibrational populations of the rotationally excited component has been plotted in Figure 9. The change in slope indicate two dynamic mechanisms are responsible for the rotationally excited component: one accounting principally for $v=1-4$ and another for the higher

vibrational levels. The relative populations of the rotationally excited component may be reproduced by a model composed of two such mechanisms as shown in Figure 10. The model is comprised by roughly equal contributions from a low v excitation process and a "statistical" process which contributes to all vibrational levels. The distribution used for the statistical process is the prior calculated for 3.7 eV. This model predicts populations for $v > 8$ of the rotationally excited component. Absolute populations of these levels cannot be determined from the spectra due to the overlap of these bands with the thermalized CO emission features. However, we have performed fits to the data using $v = 1-14$ of the rotationally excited component following the modeled distribution shown in Figure 10. The resulting fits do not exhibit any marked differences from fits excluding $v > 8$ of the rotationally excited component and the match to the absolute intensity in the P-branch region is generally improved. Under these conditions the determined populations of the thermalized component for $v > 4$ are decreased by an average of ~40 percent. Thus, the populations for $v > 8$ of the thermalized component shown in Figure 8 are upper limits.

Due to the implications of the model and the improvement in the P-branch fits, we believe that $v > 8$ for the rotationally excited component are present in the data. However, higher resolution studies will be required to confirm their presence and determine the true population distribution.

Similar analysis of the rotationally thermalized component must include the contribution of reaction (14a) to these populations from CO(A) radiative cascade. Quenching of $N_2(a' \Sigma_u^-, v=0)$ via reaction (14a) yields $CO(A^1\Pi, v \leq 2)$.³⁵ Owing to the short radiative lifetime of the CO(A) state, ~10 ns, all of the CO(A) created by this process will radiatively cascade to form CO($v \leq 9$) with a vibrational distribution reflecting the known branching ratios. Since the maximum energy defect for this process is ~3000 cm^{-1} , $N_2(a', v=0) + CO \rightarrow N_2(X, v=0) + CO(A, v=0)$, we do not expect substantial rotational excitation in the initially formed CO(A) state or, therefore, in the CO(X) populations created by radiative cascade.

Thermalization of the rotationally excited component may also contribute to the observed thermalized component populations. The fraction which may be thermalized will depend on the particular rotational distributions and the quenching rates at 80 K. There are no published quenching studies of high rotational levels of CO at low temperatures. However, studies of CO($v=0, J$) created by formaldehyde photodecomposition at room temperature have determined the rotational relaxation rate constant for transfer of population out of $J=12$ to be nearly gas kinetic, $3 \times 10^{-10} \text{ cm}^3 \text{ s}^{-1}$, and that for $J=36$ to be $5 \times 10^{-11} \text{ cm}^3 \text{ s}^{-1}$.^{44,45} Rotational levels in the region $J=80$ have rotational spacings of $>300 \text{ cm}^{-1}$, greatly exceeding the room temperature value of kT . Thus, quenching of these levels is expected to be significantly slower. At 80 K, kT exceeds the CO rotational spacings for only $J \leq 15$. Assuming this to be the maximum number of rotational levels that may be thermalized within the 20 to 30 collisions in the field of view limits the fractional contributions from the rotationally excited component to be 30 percent for high v and 6 percent for low v .

We may determine the maximum fraction of the CO thermal populations arising from thermalization of the rotationally excited component by fitting the observed thermal component population distribution to a model composed of thermalized and CO(A) radiative cascade contributions. The results of this analysis are shown in Figure 11. Reproduction of the observed distribution requires roughly 30 percent of the initially formed CO(v , high J) to be thermalized and a branching fraction for CO(A) excitation of 14 percent.

The determined contribution from CO(A) radiative cascade is about a factor of two lower than the recalculated branching ratio of Piper.²³ Our result could be consistent if the branching ratio for reaction (17a) decreases somewhat at lower temperatures. Conversely, the requirement of 30 percent thermalization of the initially formed rotationally excited component is larger than the established bound. Inclusion of $v > 8$ of the rotationally excited component in the fits decreases the $v > 4$ thermal populations by ~40 percent which reduces the fractional thermalization proportionately. Even with this

reduction, we still require rotational relaxation processes to be faster than our estimates or the nascent distributions to be bimodal. Bimodal rotational distributions have been observed in HF under near-nascent conditions.⁴⁶ These studies clearly indicate that determination of rotational relaxation must take the nature of the excited complex into account. The important factors are the rate of rotation and the relative velocities of the fragments. If the velocities are low and rate of rotation high, rapid rotational thermalization will occur. The similarities between the thermal and rotationally excited vibrational distributions strongly suggest a direct correlation. Whether the observed bimodal distributions arise from excitation followed by multi-collisional thermalization or near-nascent relaxation of the excited complex cannot be distinguished at these experimental conditions.

In summary, the results of surprisal analysis indicates two dynamic mechanisms are responsible for the rotationally excited component, one producing the low vibrational levels and another, more statistical mechanism contributing to all vibrational levels. CO(A) radiative cascade and a fixed fraction of the rotationally excited component are sufficient to account for the thermalized populations.

The dynamics of the $N_2(a') + CO$ quenching process are worthy of some comment. The interaction must satisfy conservation of angular momentum and energy,

$$(2\mu E_i)^{1/2} b_i = (2\mu E_f)^{1/2} b_f + Jh/2\pi \quad (17)$$

$$E_i + \Delta E = E_f + E_v + BJ^2 \quad (18)$$

where μ is the reduced mass, E_i and E_f are the initial and final center-of-mass collision energies, b_i and b_f are the initial and final impact parameters. ΔE is the exoergicity of the process, and BJ^2 approximates the product rotational energy after the collision. High rovibrational excitation of CO from $N_2(a')$

quenching is certainly energetically permissible. The observed CO rovibrational excitation of ~ 3.7 eV represents only 45 percent of the total exoergicity, the remainder presumably will be manifested in the N_2 internal modes. The manifestation of fractional energies of this magnitude in internal modes is common to many processes containing a large energy defect.

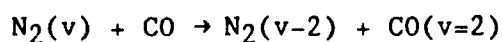
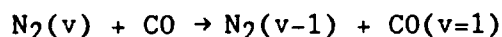
From Eq. (17), large values of J can be achieved through highly attractive collisions with large initial impact parameters and small final impact parameters with the concurrent requirement that the final center-of-mass kinetic energy is small.⁴⁷ Large initial impact parameters have been determined for the quenching of $Na(3^2P) + CO$ which is 2.1 eV exoergic. Two mechanisms were identified, a "direct" process involving colinear $Na-CO$ approach with an impact parameter of $16a_0$ and a "complex" formation mechanism from colinear $Na-OC$ approach with an impact parameter $13a_0$. Both mechanisms produce rovibrational excitation of CO with up to 0.8 eV in rotation. Extensive molecular orbital calculations of the $Na^* + CO$ interaction indicated the source of the rotational excitation to be a strong angular anisotropy of the potential energy surface. There are similarities between the $Na^* + CO$ process and the $N_2(a') + CO$ quenching process observed here. However, these similarities cannot be considered more than qualitative until extensive potential energy surface calculations can be performed.

CONCLUSIONS

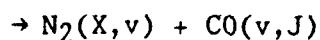
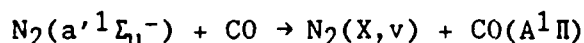
We have observed extensive rovibrational excitation in carbon monoxide from quenching of discharged nitrogen in a low pressure cryogenic apparatus. The CO fundamental emission spectra exhibit bimodal rotational distributions; 14 rotationally thermalized vibrational levels and eight rotationally excited vibrational levels have been identified. The spectral features due to the rotationally excited component are best fit by a statistical distribution, $E = 3.7$ eV. This distribution provides sufficient population in the region of the Fortrat reversal, $J \sim 90$, to account for the observed R-branch band head

formation. An energy transfer process of ~3.5 eV is sufficient to account for the vibrational extent of the thermal component. These two energetic limits are not different in our analysis.

Analysis of the data has identified a contribution to CO(v=1,2) of the thermalized component from



Based on kinetic and energetic arguments we have determined the energy transfer process



to be responsible for the observed rovibrational excitation. The branching ratio for CO(A¹Π) formation is 30±8 percent. In order to account for emissions observed here, CO(v,J) excitation must account for the remainder.

The energy transfer mechanism producing the rotationally excited component exhibits dynamic similarities to that determined for Na(2P) + CO; two mechanisms have been identified, one responsible for low vibrational levels and another that contributes to all accessible vibrational levels. Rigorous potential energy surface calculations will be required, however, to determine the true dynamics of the N₂(a') + CO interaction.

ACKNOWLEDGMENTS

The authors would like to acknowledge advice provided by B.D. Green, W.A.M. Blumberg, K.W. Holtzclaw, L.G. Piper, and W.J. Marinelli, and assistance provided by H.C. Murphy M. Gouveia, and M. DeFaccio. This work was performed under Contract F19628-85-C-0032 with the Air Force Geophysics Laboratory, and was sponsored by the U.S. Air Force Office of Scientific Research under Task 2310G4 and by the Defense Nuclear Agency under Project SA, Task SA, Work Unit 115.

REFERENCES

1. W.T. Rawlins, M.E. Fraser, and S.M. Miller, J. Phys. Chem. 93, XXXX (1989).
2. P.L. Houston, J. Phys. Chem. 91, 5388 (1987).
3. E.L. Woodbridge, J.R. Fletcher, and S.R. Leone, J. Phys. Chem. 92, 5387 (1988).
4. D.J. Bamford, S.V. Filsith, M.F. Foltz, J.W. Hepburn, and C.D. Moore, J. Chem. Phys. 82, 3032 (1985).
5. D. Debarre, M. Lefebure, M. Pialat, J.P.E. Tarar, D.J. Bamford, and C.B. Moore, J. Chem. Phys. 83, 4976 (1985).
6. D.R. Harding, R.E. Weston, and G.W. Flynn, J. Phys. Chem, in press.
7. R.G. Shortridge and M.C. Lin, J. Chem. Phys. 64, 4076 (1976).
8. D.S.Y. Hsa and M.C. Lin, Chem. Phys. Lett. 42, 78 (1976).
9. W. Reiland, H.U. Tittes, J.U. Hertel, V. Bonacil-Kontecky, and M. Persico, J. Chem. Phys. 77, 1908 (1982).
10. M.C. Lin and R.G. Shortridge, Chem. Phys. Lett. 29, 42 (1974).
11. H. Horigachi and S. Tsuchiya, J. Chem. Phys. 70, 762 (1979).
12. S. DeBenedictis and F. Cramarossa, Chem. Phys. 112, 363 (1987).

13. S. DeBenedictis, M. Capitelli, F. Cramarossa, R. D'Agostino, and C. Gorse, Chem. Phys. Lett. 112, 54 (1984).
14. C.E. Treanor, J.W. Rich, and R.G. Rehm, J. Chem. Phys. 48, 1978 (1967).
15. G.E. Caledonia and R.E. Center, J. Chem. Phys. 55, 552 (1971).
16. L.G. Piper, L.M. Cowles, and W.T. Rawlins, J. Chem. Phys. 85, 3369 (1986).
17. J.W. Dreyer, D. Perner, and C.R. Roy, J. Chem. Phys. 61, 3164 (1974).
18. W.T. Rawlins, H.C. Murphy, G.E. Caledonia, J.P. Kennealy, F.X. Robert, A. Corman, and R.A. Armstrong, Applied Optics 23, 3316 (1984).
19. N. Legay-Sommaire and F. Legay, Can. J. Phys. 48, 1966 (1970).
20. N. Washida, H. Bandow, and G. Inoue, Bull. Chem. Soc. Japan 56, 3748 (1983).
21. R. Farrenq, C. Rossetti, G. Gudachvili, and W. Urban, Chem. Phys. 92, 889, (1985).
22. M.E. Fraser, W.T. Rawlins, and S.M. Miller, J. Chem. Phys. 88, 538 (1988).
23. K.P. Huber and G. Herzberg, Molecular Spectra and Molecular Structure IV. Constants of Diatomic Molecules, Van Nostrand Reinhold, New York (1979).
24. C. Chackerian, R. Farrenq, G. Guelachvili, C. Rossetti, and W. Urban, Can. J. Phys. 62, 1579 (1984).
25. L.G. Piper and W.J. Marinelli, J. Chem. Phys. 89, 2918 (1988).
26. G.K. Chamba, G.C. McBane, P.L. Houston, and G.C. Schatz, J. Chem. Phys. 88, 5481 (1988).
27. H.K. Haugen, W.H. Pence, and S.R. Leone, J. Chem. Phys. 80, 1829 (1984).
28. X.F. Yang and G.C. Pimentel, J. Chem. Phys. 81, 1746 (1984).
29. G.E. Caledonia, B.D. Green, and R.E. Murphy, J. Chem. Phys. 71, 4369 (1979).
30. B. Stewart, P.D. Magill, J.P. Scott, J. Derouard, and D.E. Pritchard, Phys. Rev. Lett. 60, 282 (1988).
31. W.T. Rawlins, L.G. Piper, M.E. Fraser, and H.C. Murphy, PSI 9032/TR-901, Final Report, Contract F19628-85-C-0032, February 1989. GL-TR-89-0124
32. L.G. Piper, M.E. Donahue, and W.T. Rawlins, J. Chem. Phys. 91, 3883 (1987).

33. J.M. Thomas, F. Kaufman, and M.F. Golde, J. Chem. Phys. 86, 6885 (1987).
34. W.J. Marinelli, W.J. Kessler, B.D. Green, and W.A.M. Blumberg, J. Chem. Phys., in press.
35. L.G. Piper, J. Chem. Phys. 87, 1625 (1987).
36. T.G. Slanger, G. Black, and J. Fournier, J. Photochem. 4, 329 (1975).
37. Y.Z. Ionilch, A.L. Loenov, and L.S. Starenkova, Opt. Spectrosc. (USSR) 60, 444 (1986).
38. G.W. Taylor and D.W. Setser, J. Chem. Phys. 58, 4840 (1973).
39. W.G. Clark and D.W. Setser, Chem. Phys. Lett. 33, 71 (1975).
40. T.G. Slanger, B.J. Wood, and G. Black, J. Photochem. 2, 63 (1973).
41. W.J. Marinelli, W.J. Kessler, B.D. Green and W.A.M. Blumberg, submitted to J. Chem. Phys.
42. R.B. Bernstein and R.D. Levine, "Role of Energy in Reactive molecular Scattering: An Information-Theoretic Approach," in Advances in Atomic and Molecular Physics II, edited by D.R. Bates and B. Bederson, Academic, New York, 216 (1975).
43. R.D. Levine and R.B. Bernstein, "Thermodynamic Approach to Collision Processes," in Modern Theoretical Chemistry, Vol. II: Dynamics of Molecular Collisions Part B, edited by W.H. Miller, Plenar, New York, Chapter 7 (1975).
44. P. Ho and A. Smith, Chem. Phys. Lett. 90, 407 (1982).
45. P.L. Brechignac, Opt. Commun. 25, 53 (1978).
46. D. Poppe, Chem. Phys. 111, 17 (1987); 111, 21 (1987)

Table 1. Energetics of CO Band Heat Formation $E_T = 3.70$ eV

Vibrational Level	E_v (eV) ^a	$E_T - E_v$	J_{vertex}	$E_{J_{\text{vertex}}}$ (eV)	J_{max} ^b
1	0.266	3.434	92	1.966	123
2	0.528	3.172	91	1.907	118
3	0.788	2.912	90	1.848	114
4	1.044	2.656	90	1.831	109
5	1.296	2.404	89	1.774	104
6	1.546	2.154	88	1.719	98
7	1.792	1.908	87	1.665	93
8	2.035	1.665	87	1.648	87
9	2.274	1.426	86	1.600	81
10	2.511	1.189	85	1.544	74
11	.744	0.956	84	1.444	66
12	2.974	0.726	84	1.478	58
13	3.201	0.499	83	1.430	48
14	3.425	0.275	82	1.382	35

a. $E_{CO(v=0)} = 0$

b. Calculated from the value for $E_T - E_v$

Table 2. Measured CO Quenching Kinetics of N_2^* , N^*

Species	K_Q (300 K) $\text{cm}^{-3} \text{ s}^{-1}$	Number Density in COCHISE, cm^{-3}	
		Required for CO(v,J) Excitation	Estimated for Interaction Zone
$N(^2P)$	$\leq 1.5 (-14)^{31}$	$> 3 (13)$	1 to 3 (9)
$N(^2D)$	$1.7 (-12)^{32}$	$> 3 (11)$	3 to 10 (9)
$N_2(A^3\Sigma_u^+)$,			
v=0	$1.5 (-12)^{b33}$	$> 3 (11)$	1 to 3 (9)
v=4	$1.9 (-11)^{b33}$	3 (10)	1 to 3 (9)
$N_2(a^1\Pi_g)$	$2.8 (-10)^{a34}$	2 (9)	2 (6)
$N_2(a'^1\Sigma_u^-)$	$1.1 (-10)^{a35}$	4 (9)	3 (9)

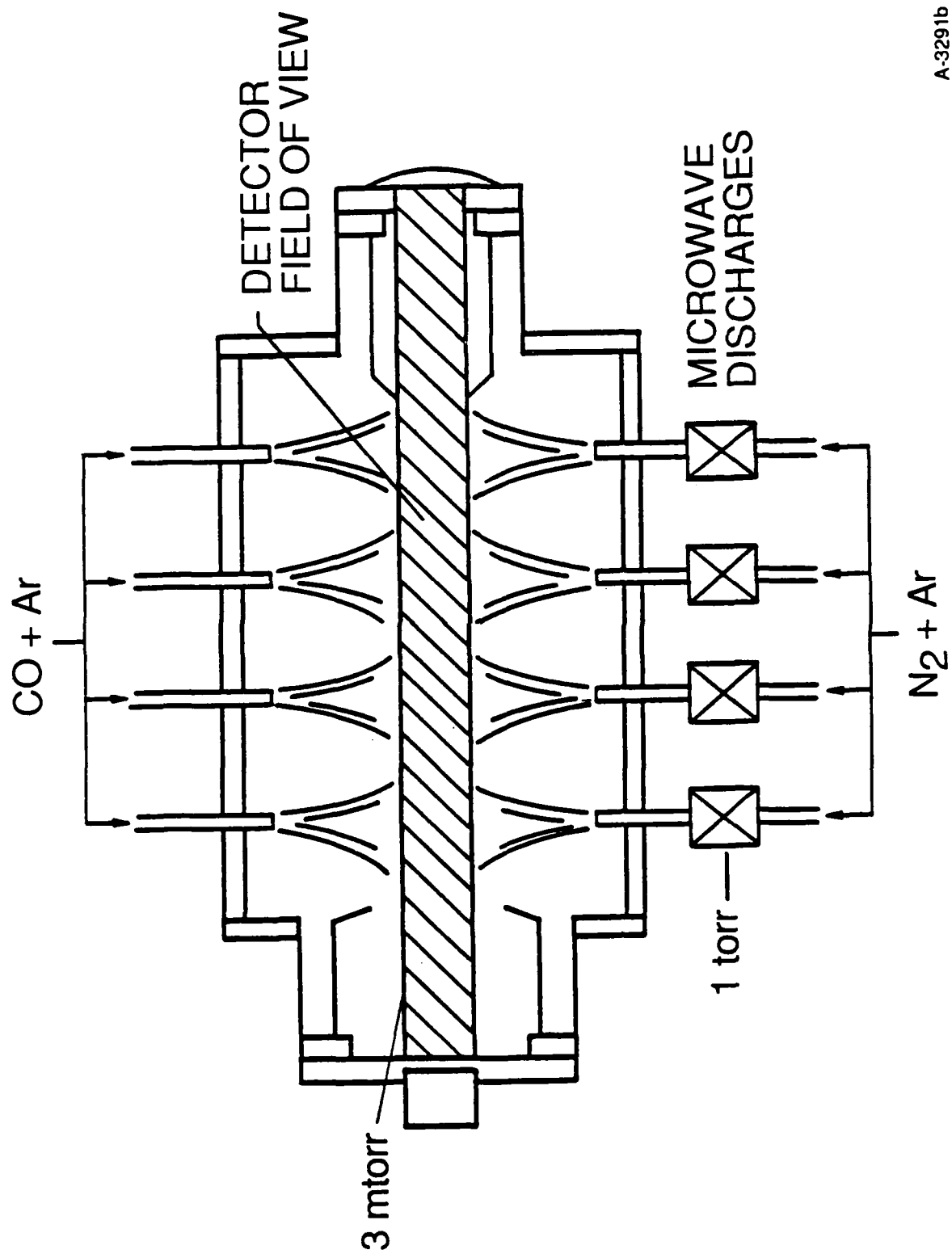
a. Includes excitation of $CO(A^1\Pi)$

b. Includes excitation of $CO(a^3\Pi)$

FIGURE CAPTIONS

- Figure 1. Diagram of the COCHISE reaction chamber. The physical dimensions of the cell are 0.6m in length and 0.4m in diameter.
- Figure 2. Data comparison. The dark line shows a typical spectrum obtained under conditions of 12 percent discharged N_2/Ar reacting with a counterflow of 33 percent CO/Ar . The light line shows data taken at 3.17 percent N_2/Ar with identical counterflow conditions.
- Figure 3. Comparison of rotational distributions. Shown are the relative rotational distributions for a 10^4 K Boltzmann and several statistical distributions.
- Figure 4. Data (light line) and best fit (dark line) (a) to thermalized (80 K) CO fundamental emission ($v'=1-14$) and CO rotationally excited bands using a statistical distribution with $E_T = 3.7$ eV. The data is the same used for the light line in Figure 2. The spectral resolution is $0.013 \mu m$. The thermalized CO and rotationally excited basis sets which comprise the best fit in (a) are shown in (b) and (c), respectively.
- Figure 5. Enlarged view of the 5.7 to $6.5 \mu m$ region of Figure 4. The data is shown by light line, the fit by a dark line.
- Figure 6. Determined population distribution versus E_v , for the fit shown in Figure 4. The thermalized component is shown as (), with contribution to thermalized $CO(v=1,2)$ as (), and the rotationally excited component is represented as ().
- Figure 7. Plot of the ratio of the $[CO(v=1,2)]$ to $[CO(v=3)]$ populations as a function of nitrogen mole fraction. The CO mole fraction for these data was 0.33.
- Figure 8. Averaged relative population distributions for 11 spectra. Both thermalized () CO and the rotationally excited component () are shown but have been normalized independently. The error bars represent one standard deviation.
- Figure 9. Vibrational surprisal plot for the rotationally excited vibrational populations. The populations are those from Figure 8.
- Figure 10. Model fit to the rotationally excited vibrational populations. The model, shown by solid line, has been produced by equal contributions from the direct ($v \geq 4$), (---), mechanism and the statistical mechanism (all v), (···).

Figure 11. Model fit to the rotationally "thermal" vibrational populations. The model (—) has been produced by a contribution of 14 percent branching fraction from reaction (14a), (— —), and 30 percent of the rotationally excited model, shown separately as direct (— —) and statistical contributors (· — ·). The relative populations have been normalized to the sum of the rotationally excited vibrational populations. The rotationally excited component is also shown (···).



A-3291b

FIGURE 1

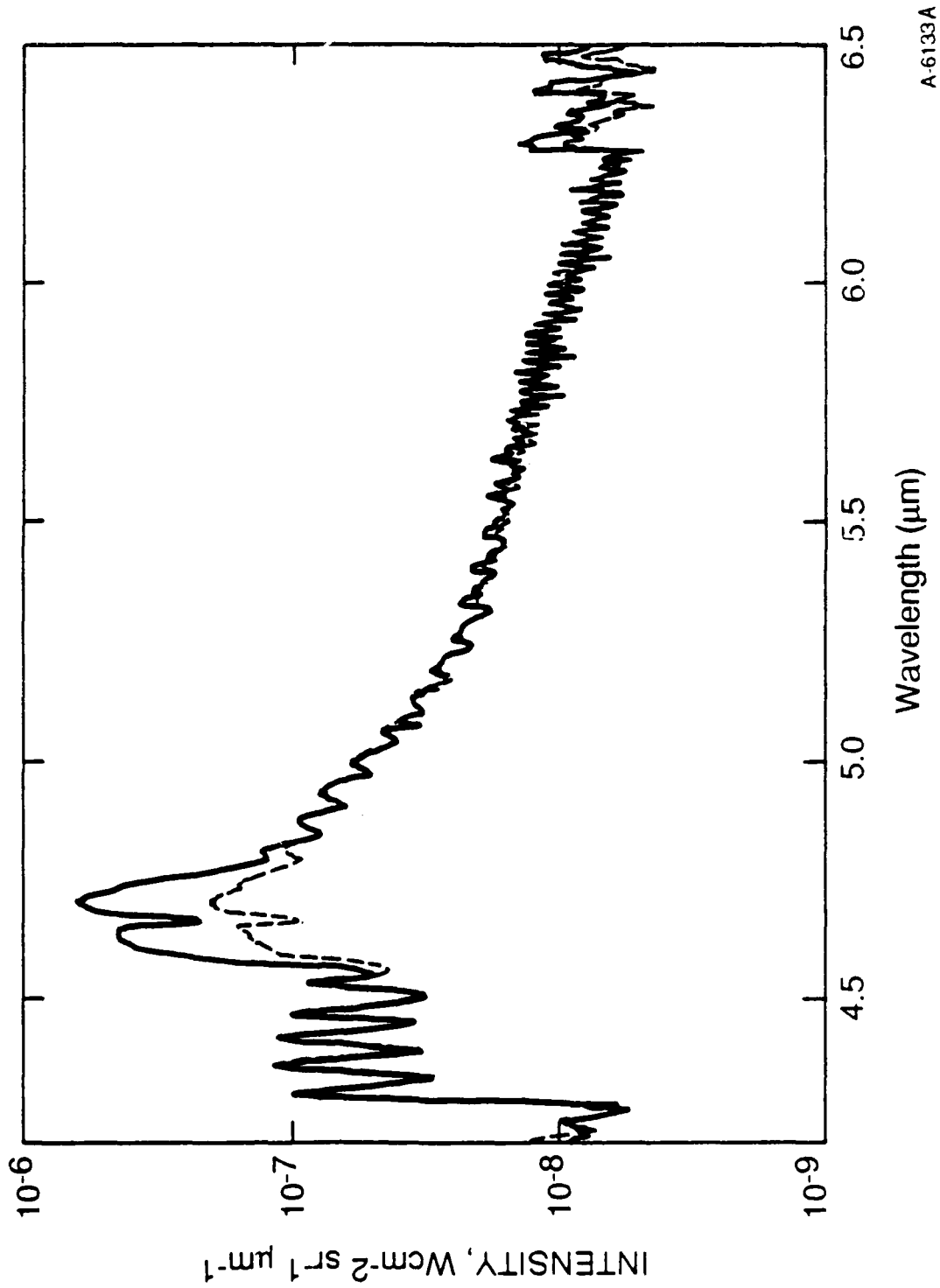


FIGURE 2

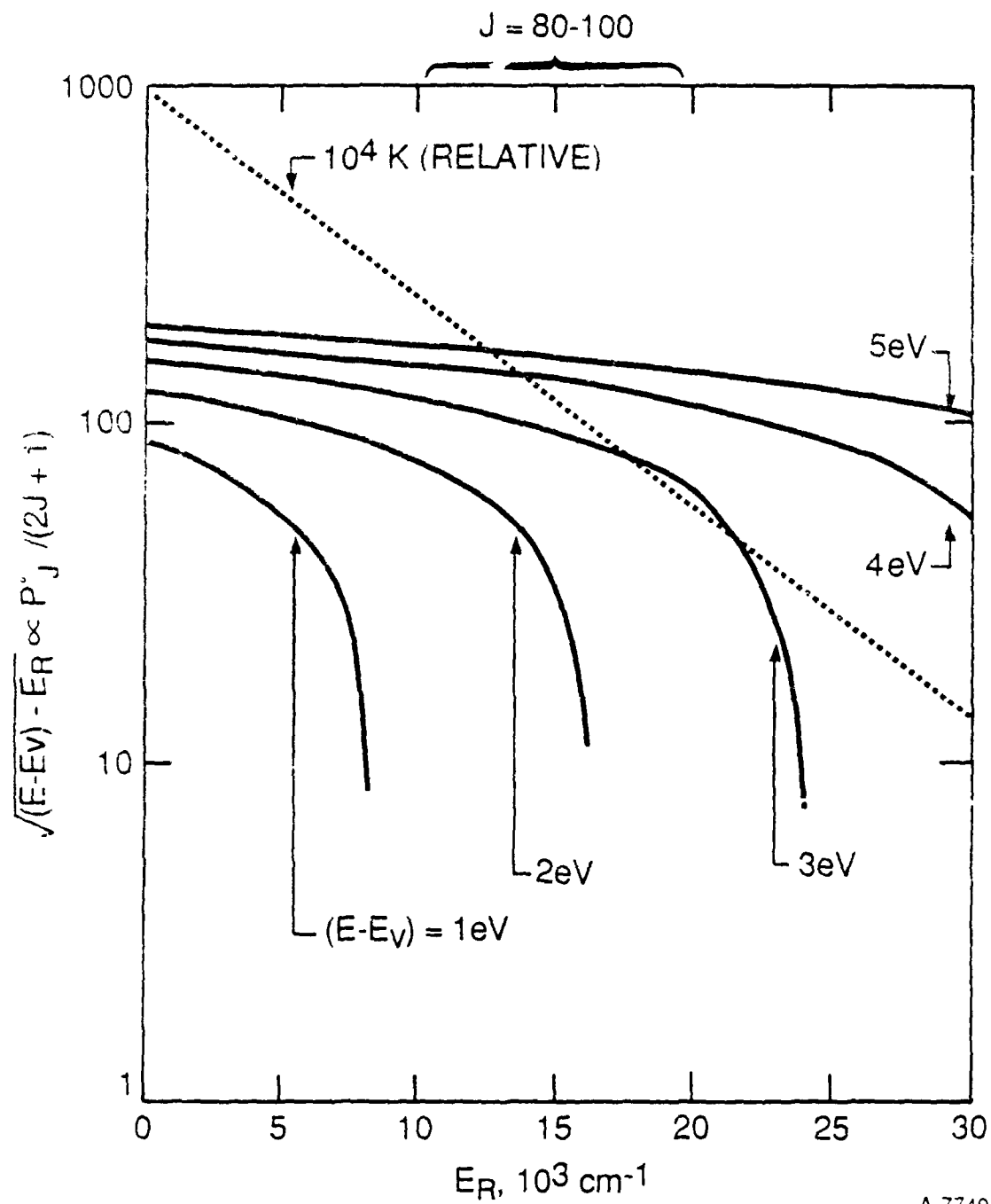


FIGURE 3

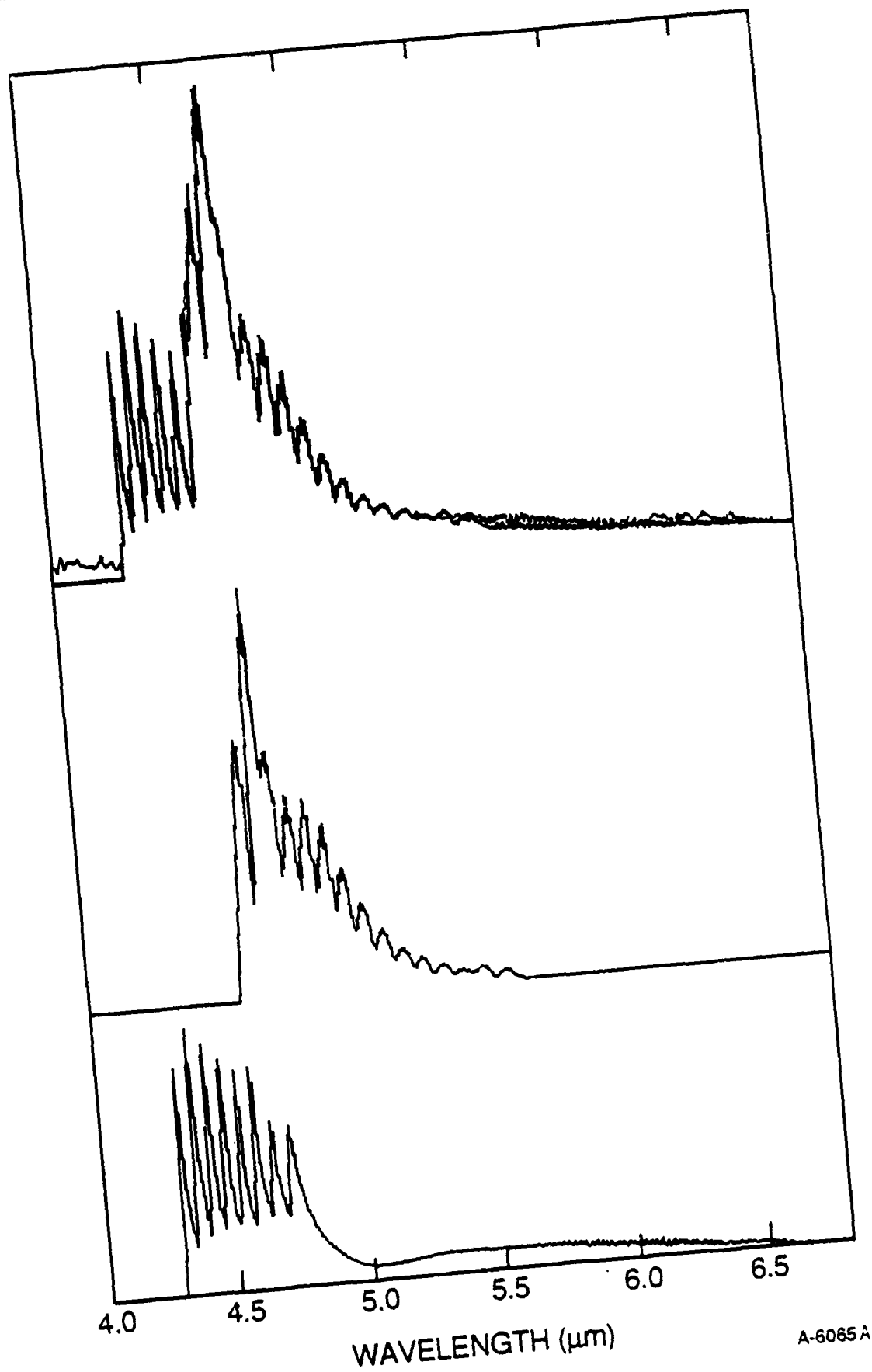
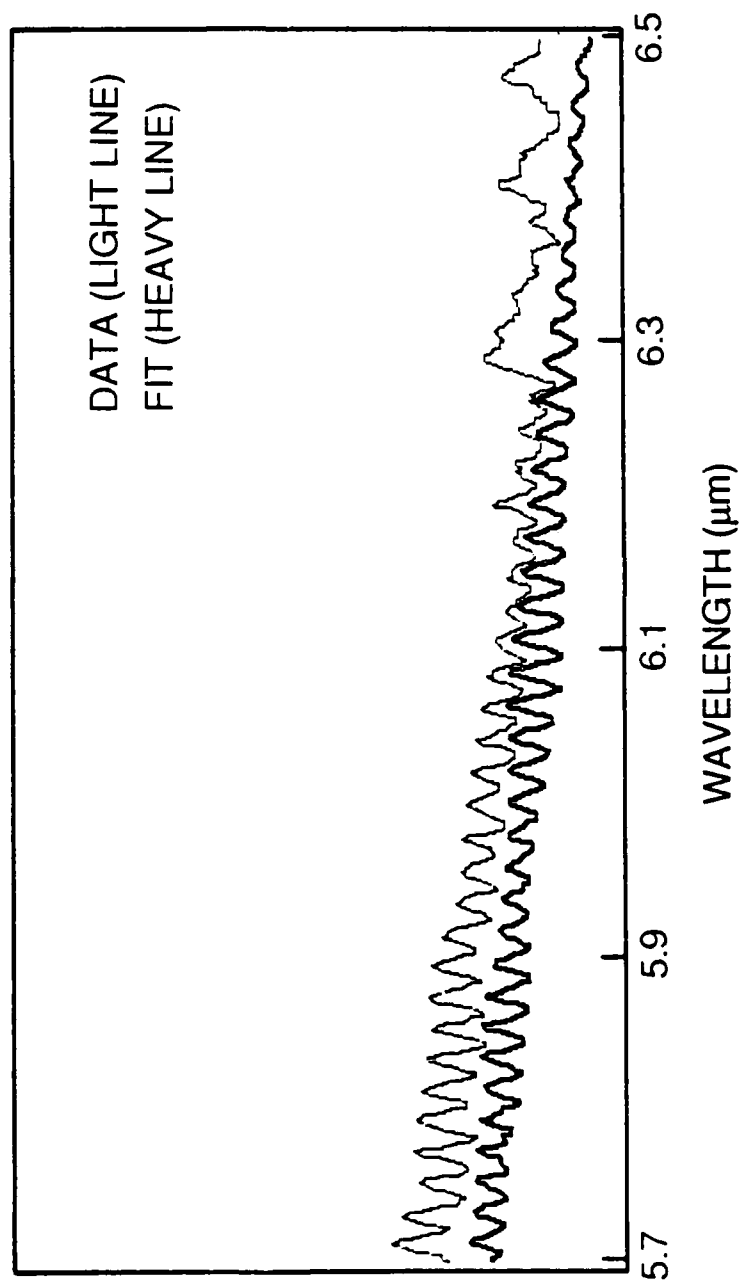


FIGURE 4



A-6124

FIGURE 5

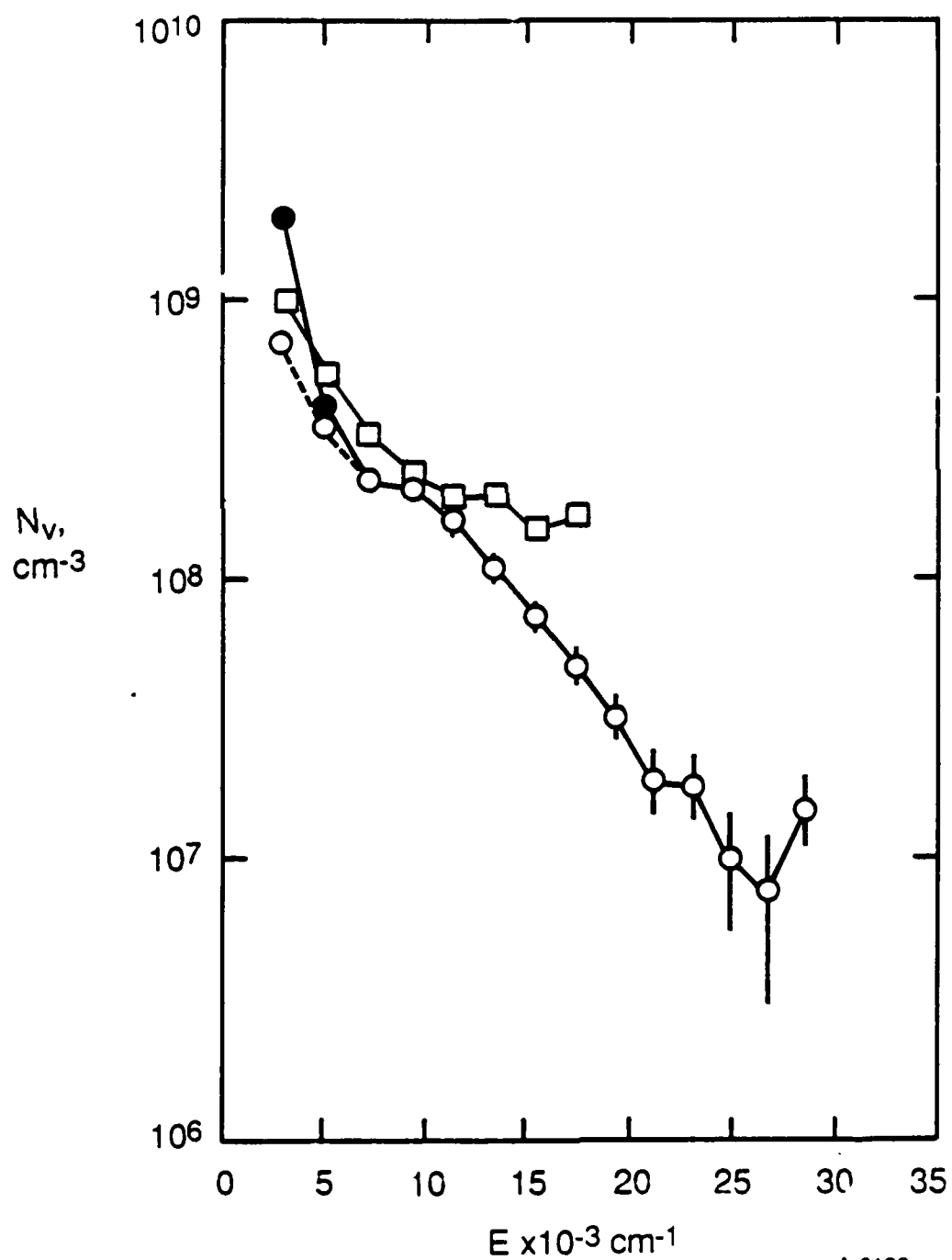


FIGURE 6

A-6132

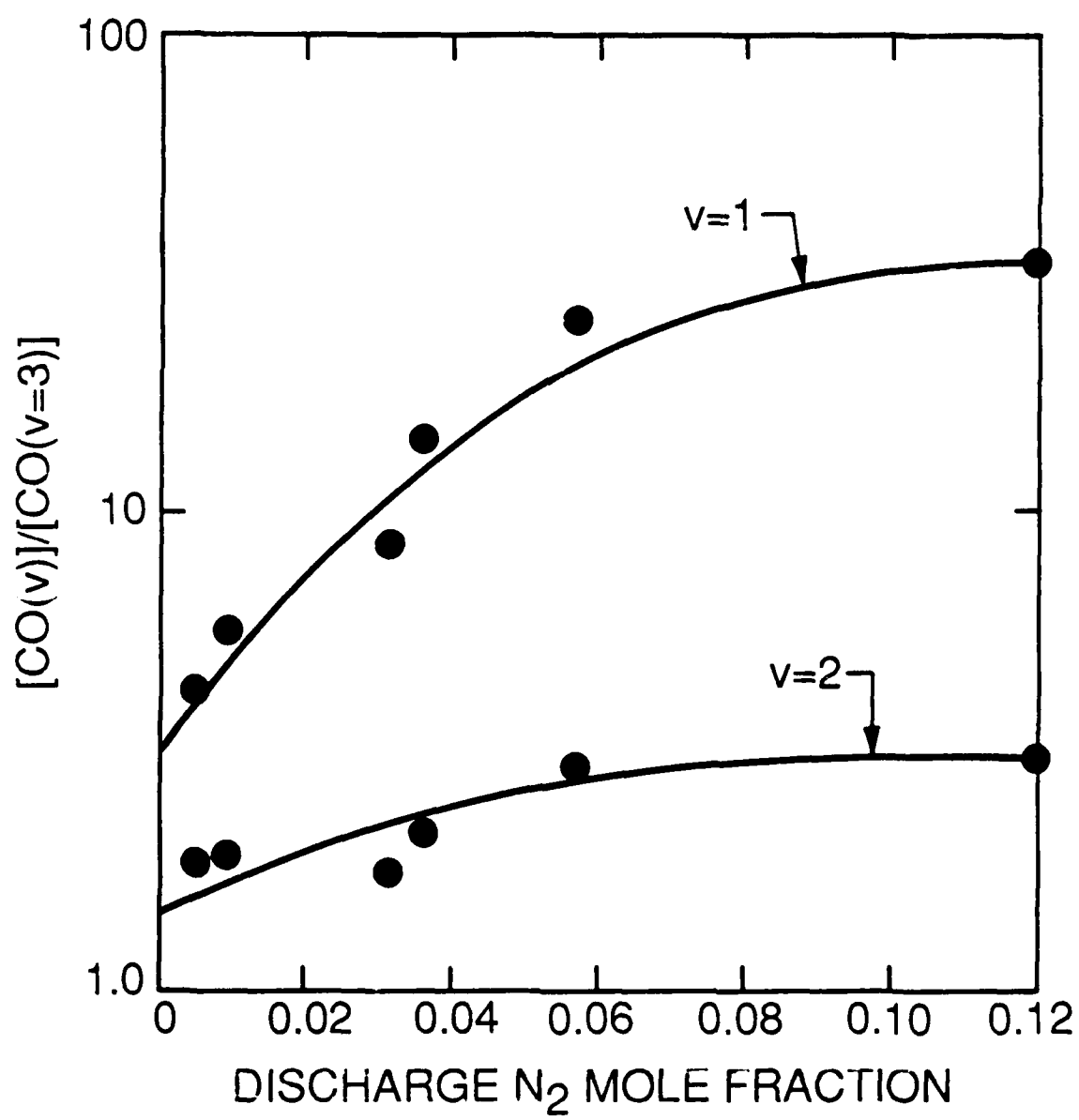
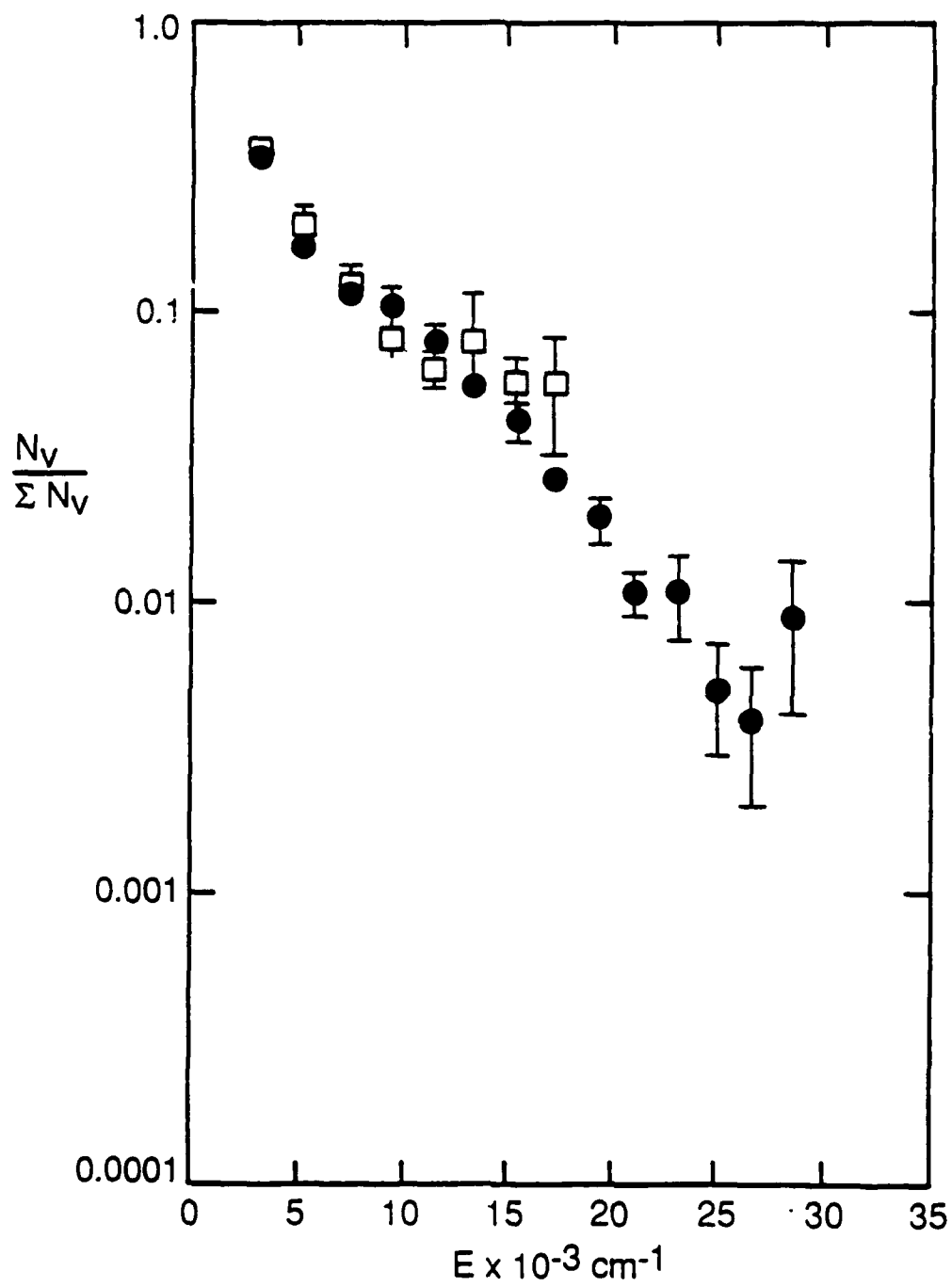


FIGURE 7

A-6130



A-6131A

FIGURE 8

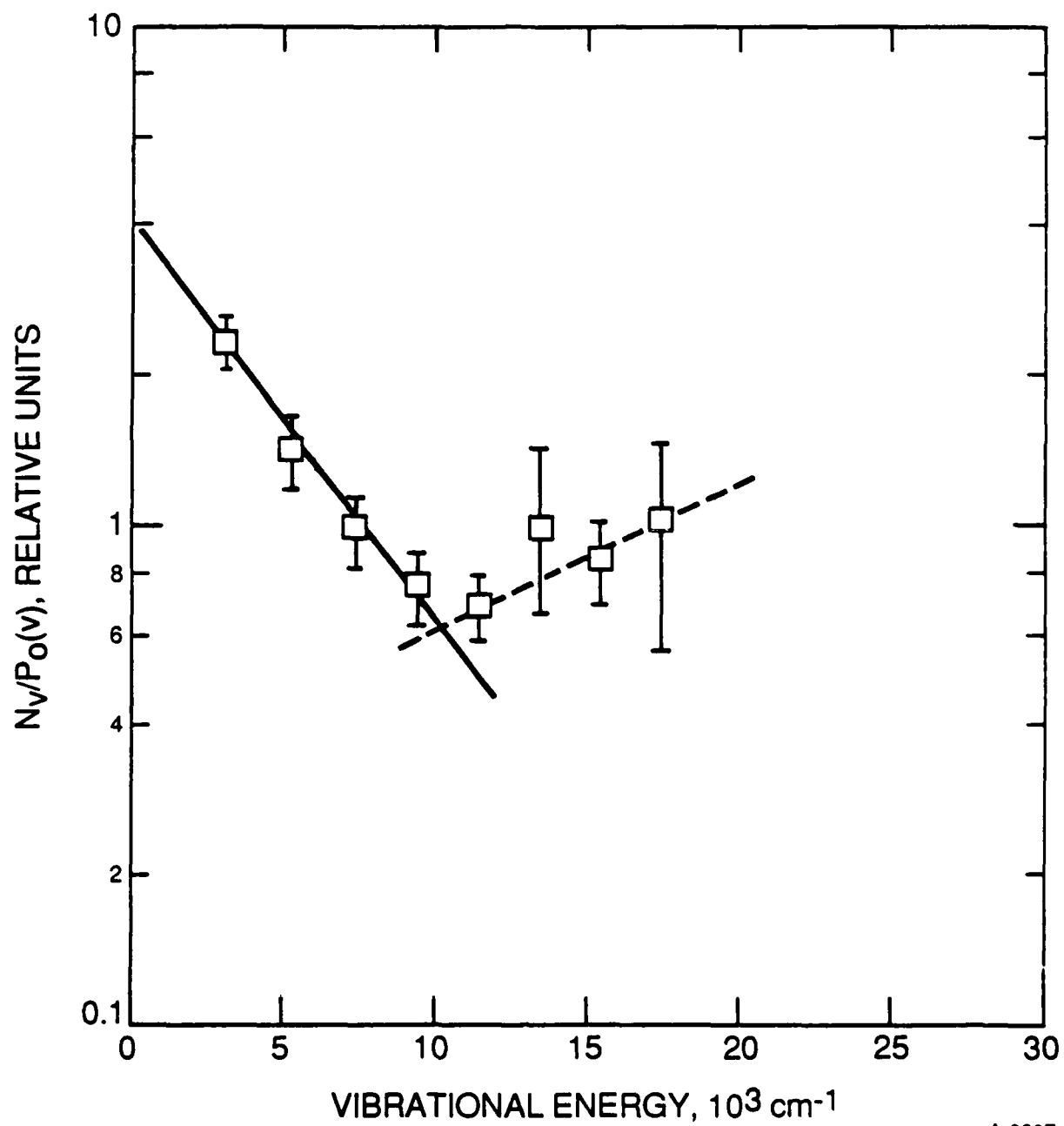


FIGURE 9

A-9607

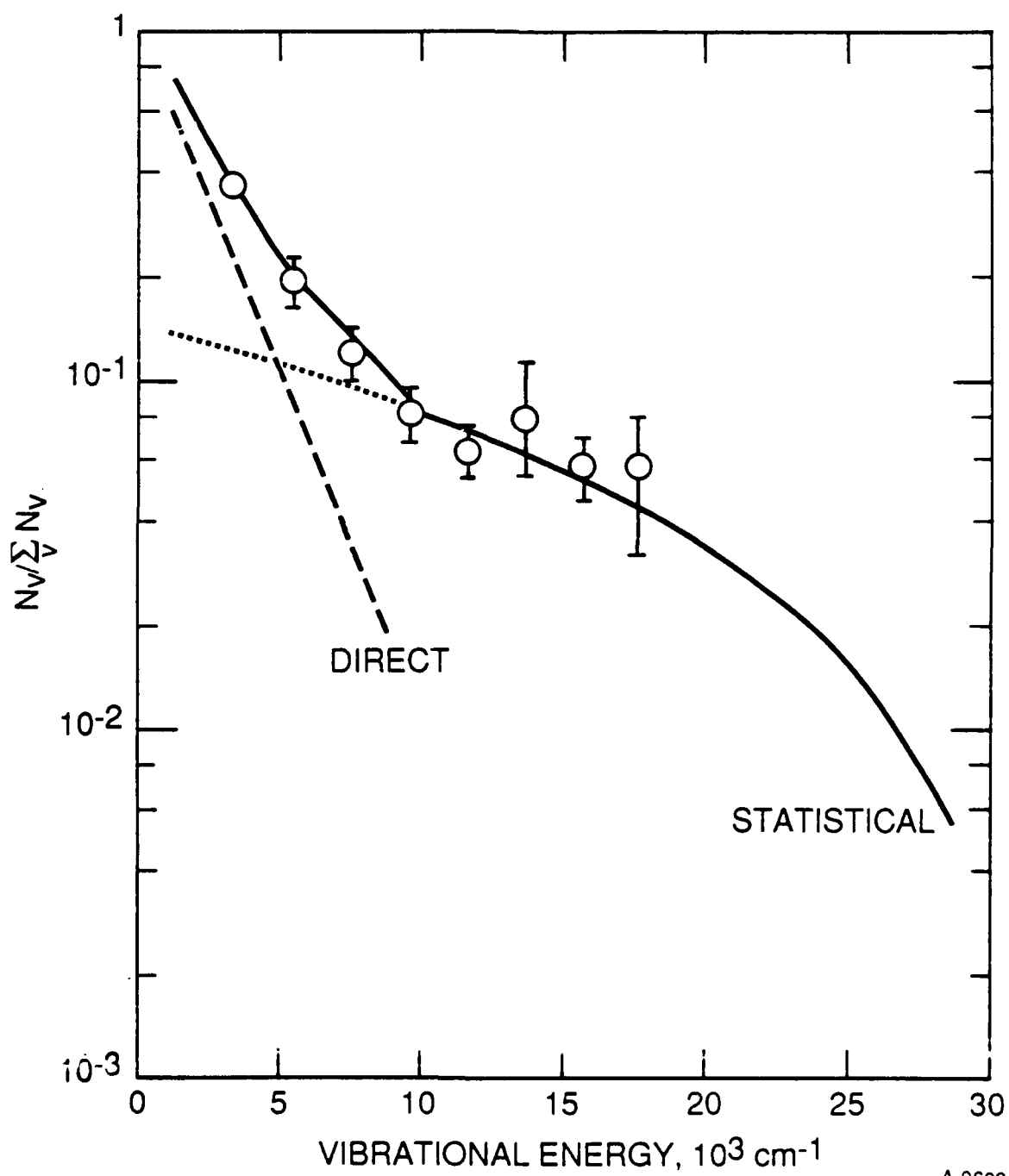
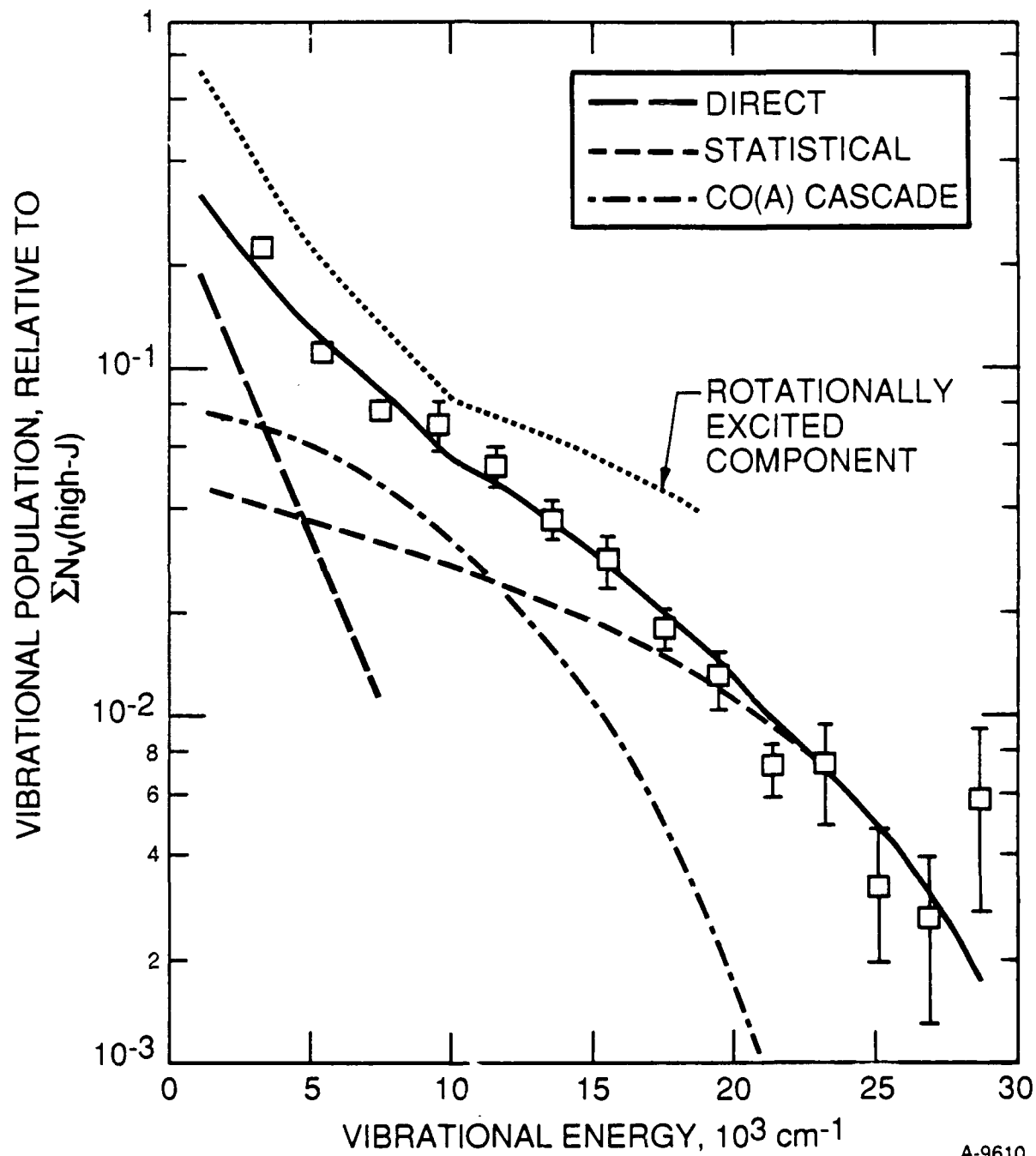


FIGURE 10

A-9609



A-9610

FIGURE 11

APPENDIX R

(PSI-032/TR-567 reproduced in its entirety)

CLASSICAL TRAJECTORY STUDY OF
OZONE RECOMBINATION DYNAMICS:
THE CHAPERON MECHANISM

Quarterly Status Report No. 4

For the Period

1 January 1986 to 31 March 1986

Under Air Force Contract No. F19628-85-C-0032

Prepared by:

Alan Gelb and W.T. Rawlins

Sponsored by:

Air Force Geophysics Laboratory
Air Force Systems Command
U.S. Air Force
Hanscom Air Force Base, Massachusetts 01731

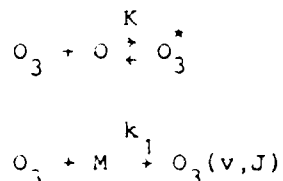
April 1986

TABLE OF CONTENTS

<u>Section</u>		<u>Page</u>
1	INTRODUCTION	1
2	ArO EQUILIBRIUM CONSTANT	3
3	TRAJECTORY CALCULATIONS	8
4	RESULTS AND DISCUSSION	10
	REFERENCES	19
	COST DATA	20

1. INTRODUCTION

The usual mechanism for the recombination of ozone from oxygen atoms and molecules involves a two-step process in which a) an unbound complex of ozone, O_3^* , is formed and b) O_3^* is stabilized collisionally to form bound ozone. The reaction scheme is written as the following:



where M denotes a third body collision partner and $O_3(v,J)$ are the vibrationally-rotationally excited ozone molecules. It is generally assumed that the O_3^* formation is an equilibrium or steady state process so that

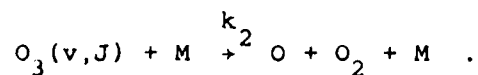
$$K = \frac{[O_3^*]}{[O_2][O]}$$

This is the energy transfer recombination mechanism.

Then the so-called one way flux of ozone molecule production is given by

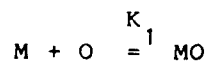
$$\frac{d[O_3]}{dt} = k_1 [O_3^*][M] = K k_1 [O][O_2][M]$$

To compute the observed reaction rate of ozone formation the redissociation of the highly excited nascent ozone must be included according to the following.

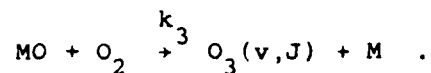


This reaction reduces the rate of formation from the one-way flux value.

An alternative mechanism for ozone formation involves the formation of an oxygen atom-third body bound complex



which collides with oxygen molecules to form stabilized (but probably highly internally excited) ozone molecules



The ozone formation one-way flux is given by

$$\frac{d[\text{O}_3]}{dt} = k_3[\text{MO}][\text{O}_2] = k_3 K_1 [\text{O}][\text{O}_2][\text{M}] .$$

This is the so-called chaperon mechanism. As before, it is necessary to include the collisional redissociation of highly excited ozone molecules into the computation of the observable reaction rate.

In the upper atmosphere, at altitudes of interest for ozone formation, the primary constituents are O_2 , N_2 and O and it is usually assumed that the radical energy transfer mechanism is dominant. However under circumstances in which the third body collision partner is in high concentration (and is not oxygen) the chaperon mechanism may be important. The COCHISE experiments are run under conditions in which there is a large excess of argon. In order to assess the potential contributions of the chaperon mechanism, trajectory calculations were carried out for the reaction of ArO with O_2 to form ozone.

We discuss two aspects of these calculations: 1) calculation of the ArO equilibrium constant and 2) classical trajectory calculations of $\text{ArO}-\text{O}_2$ collisions and redissociation of newly formed ozone molecules by collision with argon atoms.

2. ArO EQUILIBRIUM CONSTANT

We assume that the ArO interaction potential is a Lennard-Jones six-twelve potential given by

$$V(r) = 4\epsilon \left[\left(\frac{\sigma}{r} \right)^{12} - \left(\frac{\sigma}{r} \right)^6 \right]$$

where ϵ is the well depth and σ a molecular parameter. This form for the ArO interaction has been used in our earlier calculations on energy transfer in Ar-O₃ collisions and radical mechanism ozone recombination. Values for ϵ and σ were determined by Aquilanti et al.¹ using a molecular beam scattering technique. The adopted values are:

$$\epsilon = 0.0047 \text{ e.v.}$$

and

$$\sigma = 2.78 \text{ \AA}.$$

The expression for the equilibrium constant of the ArO bound complex is given by²

$$K = \frac{4\pi}{\Gamma(\frac{3}{2})} \int_{\sigma}^{\infty} dr r^2 \exp\left[\frac{-V(r)}{kT}\right] \gamma\left(\frac{3}{2}, \frac{-V(r)}{kT}\right)$$

where $\Gamma(3/2)$ and $\gamma(3/2, -V(r)/kT)$ are complete and incomplete gamma functions respectively. This expression was derived by Hill.² Stogryn and Hirschfelder³ showed this result may be simplified when $V(r)$ is given by a Lennard-Jones 6-12 potential. Using the notation of Kim,⁴ the equilibrium constant may be rewritten as

$$K = \frac{128}{45} \sigma^2 (\pi z^3)^{1/2} F(z) \quad (1)$$

where

$$F(z) = \sum_{n=0}^{\infty} \frac{n!}{\left(\frac{7}{4}\right)_n \left(\frac{9}{4}\right)_n} z^n = {}_2F_2\left(1, 1; \frac{7}{4}, \frac{9}{4}; z\right)$$

$$(a)_n = a(a+1) \dots (a+n-1)$$

and

$$z = \epsilon/kT$$

An asymptotic form in the limit $z = \epsilon/kT \rightarrow \infty$ is given by⁴

$$F(z) \sim \frac{15\pi}{32\sqrt{2}} z^{-2} e^z \left[\sum_{n=0}^{N-1} \frac{\left(\frac{5}{4}\right)_n \left(\frac{3}{4}\right)_n}{n!} z^{-n} + O(z^{-N}) \right]$$

In this limit the equilibrium constant may be written as

$$K \sim \frac{2}{3} \pi \sigma^2 (2\pi kT/\epsilon)^{1/2} e^{\epsilon/kT} \quad (2)$$

This form is appropriate for low temperatures. The lowest temperature we shall consider is 80 K for which

$$kT = 0.16 \text{ kcal/mol} = 0.0069 \text{ e.v.}$$

so that we shall always work in the $z < 1$ case.

The above equilibrium constant includes contributions from ArO molecules below the dissociation limit. Classically, molecules above the dissociation energy (i.e., well depth) but trapped within a centrifugal barrier may also be included. Kim and Ross⁵ computed equilibrium constants including contributions from bound, metastable and orbiting molecules. Their form for the equilibrium constant is given by:

$$K = \frac{8}{15} \pi \sigma^3 \left(\frac{\epsilon}{\pi kT}\right)^{1/2} Q_{\text{rel}} \quad (3)$$

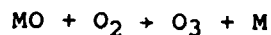
where

$$Q_{\text{rel}} = 10 \sum_{n=0}^{\infty} (-1)^n q_n \left(\frac{\varepsilon}{kT} \right)^n \quad (4)$$

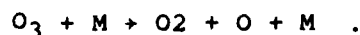
and $\{q_n\}$ are numerical coefficients. Values for the first ten coefficients are listed in the Kim and Ross paper.⁵

In the calculations presented here we consider only the contributions from bound ArO complexes. Our temperature range of interest is between 80 and 400 K so that Eq. (1) will be used to compute the ArO equilibrium constant.

Calculated values for the ArO formation equilibrium constant are given as a function of temperature in Table 1. The values of the equilibrium constant for formation of bound ArO molecules is denoted as K_b . For comparison we also include values of the equilibrium constant including metastables and orbiting pairs (Eq. (3) and (4)), K_m . Two points are noteworthy: (1) as expected the value of the equilibrium constants K_b and K_m increase monotonically with decreasing temperature and (2) K_m is approximately a factor of two larger than K_b at all temperatures considered. Note also that the temperature variation of both K_b and K_m is quite slow, the values varying only an order of magnitude between 400 and 80 K. It is clear that the observed much steeper temperature dependence in the ozone recombination rate cannot be explained by the temperature dependence of the equilibrium constant alone. In order to find agreement with experiment there must be strong temperature dependencies for the association reaction



and redissociation reaction



Results will be discussed later.

Table 1. Computed Values of ArO Equilibrium Constant

Temperature	K_b (cm ³ /molecule) Equation (1)	K_m (cm ³ /molecule) Equations (3) and (4)
80	7.33×10^{-23}	1.40×10^{-22}
100	5.05×10^{-23}	1.03×10^{-22}
120	3.74×10^{-23}	7.94×10^{-23}
150	2.61×10^{-23}	5.78×10^{-23}
200	1.66×10^{-23}	3.8×10^{-23}
300	8.79×10^{-24}	2.12×10^{-23}
400	5.64×10^{-24}	1.39×10^{-23}

Estimates of bound ArO concentrations are given in Table 2. Conditions were chosen to approximately simulate those of the COCHISE experiment with

$$n_{Ar} = 10^{17} \text{ atoms/cm}^3$$

and $n_O = 10^{15} \text{ atoms/cm}^3$.

To compute production rates of ozone molecules according to this mechanism, trajectory calculations were begun. They were used to compute the association reaction and redissociation reactions. We now mention some details of the computation.

Table 2. Computed Values of ArO Concentrations; $n_{Ar} = 10^{17}$ atoms/cm³ and $n_O = 10^{15}$ atoms/cm³, $n_{ArO} = K_m n_{Ar} n_O$

T	n_{ArO} (molecules/cm ³)
80	7.3×10^9
100	5.0×10^9
120	3.7×10^9
150	2.6×10^9
200	1.7×10^9
300	8.8×10^8
400	5.6×10^8

3. TRAJECTORY CALCULATIONS

All calculations were performed using the Murrell-Varandas ozone ground state potential surface with pairwise additive Lennard-Jones potentials between oxygen and argon atoms. This potential surface has been discussed in detail elsewhere.⁶

Trajectories were computed by integrating the classical equations of motion. The trajectory analysis involves a three step procedure: (1) selection of initial conditions, (2) integration of Hamilton's equations of motion, and (3) determination of asymptotic conditions, i.e., products. Each of these steps is discussed in detail in Refs. 7 and 8. We mention here only details specific to the present calculations.

Initial conditions for the ArO molecule were chosen as if the molecule were bound classically, i.e., in terms of its total energy below the Ar-O well depth. The vibrational energy of ArO was chosen from an appropriate classical Boltzmann distribution with a cut-off at the well depth. For simplicity the ArO rotational energy was set equal to zero. This assumption was checked by performing trajectories with rotating molecules and comparing with the results for non-rotating cases. It was found that initial rotational ArO energy made negligible difference in the outcome of trajectories. This was so because the allowed rotational energy is very small because of the shallowness of the ArO potential well. Initial conditions for the initial O₂ molecules were chosen from classical rotational and vibrational energy Boltzmann distributions. Relative translational energies were chosen from the appropriate classical flux distribution.

Hamilton's equations were integrated using a fixed step Runge-Kutta-Gill integrator for the first five time steps and a fixed stepsize Adams-Moulton integrator for the rest of the trajectory. Trajectories were checked for accuracy by observing conservation of energy and angular momentum.

The initial ArO-O₂ separation was chosen so that the interaction between the molecules was negligible. Due to the relatively low temperatures considered this necessitated a fairly large initial separation. This large initial separation and also large exit channel distance cutoff caused the trajectories to be fairly time consuming, with many trajectories requiring some tens of thousands of integration steps. This was particularly true at the lowest temperature considered.

Simulations of the association reaction were carried out at temperatures of 80, 100, 120, 150, 200, 300 and 400 K. Batches of between 6000 and 12000 trajectories were computed at each temperature.

At the end of each trajectory it was determined if a bound ozone molecule was formed. If so, the ozone coordinates were recorded and stored. These coordinates were used as initial conditions in the redissociation reaction computations.

The multiple collision method discussed in Ref. 9 was used to compute the redissociation probability of newly formed ozone molecules in an argon thermal bath. Available computer time only allowed these calculations to be carried out at temperatures of 400, 300 and 200 K. At these temperatures the number of computed initial ozone bound state initial conditions was fairly small. Therefore each set of initial ozone coordinates was used several times in order to generate a reasonably large ensemble of nascent ozone molecules. The initial ensemble sizes varied between 600 and 750 initial ozone molecules. At 300 and 400 K the ensembles were propagated through a sequence of sixty collisions. In the 200 K case computer restrictions forced stopping at 20 collisions. This value seemed sufficient to determine the redissociation probability at 200 K.

4. RESULTS AND DISCUSSION

Computed values of the cross section for the association reaction of ArO and O₂ to form ozone are shown in Figure 1. The cross section is seen to rapidly increase with temperature. At the highest temperatures, 300 and 400 K, the fraction of trajectories leading to stable ozone formation is approximately 0.002. The fraction, P, is readily computed from the values in Figure 1 by the following

$$P = \sigma_{\text{react}} / \pi b_{\text{max}}^2$$

where b_{max} is the maximum impact parameter used in the trajectory calculations (equal to 4Å). The fraction of reactive trajectories increases with decreasing temperature to approximately 0.05 at 80 K. Even at the lowest temperature considered the probability of forming stable ozone is quite small. The nascent ozone molecules were found to be very vibrationally-rotationally excited with total molecular energies very near the dissociation limit. Average ozone molecular energies for the nascent ozone molecules at 200, 300 and 400 K are listed in Table 3. At these temperatures the mean newly formed ozone molecule lies approximately one-half kcal/mol below the dissociation limit. It is clearly anticipated from earlier work on Ar-O₃ dissociation dynamics that there will be a large degree of redissociation as the nascent ozone molecules undergo collisions with the thermal argon bath.

Table 3. Average Energy Below Dissociation Energy for Nascent Ozone

Temperature	Energy Below Dissociation (kcal/mol)
200	0.58
300	0.63
400	0.49

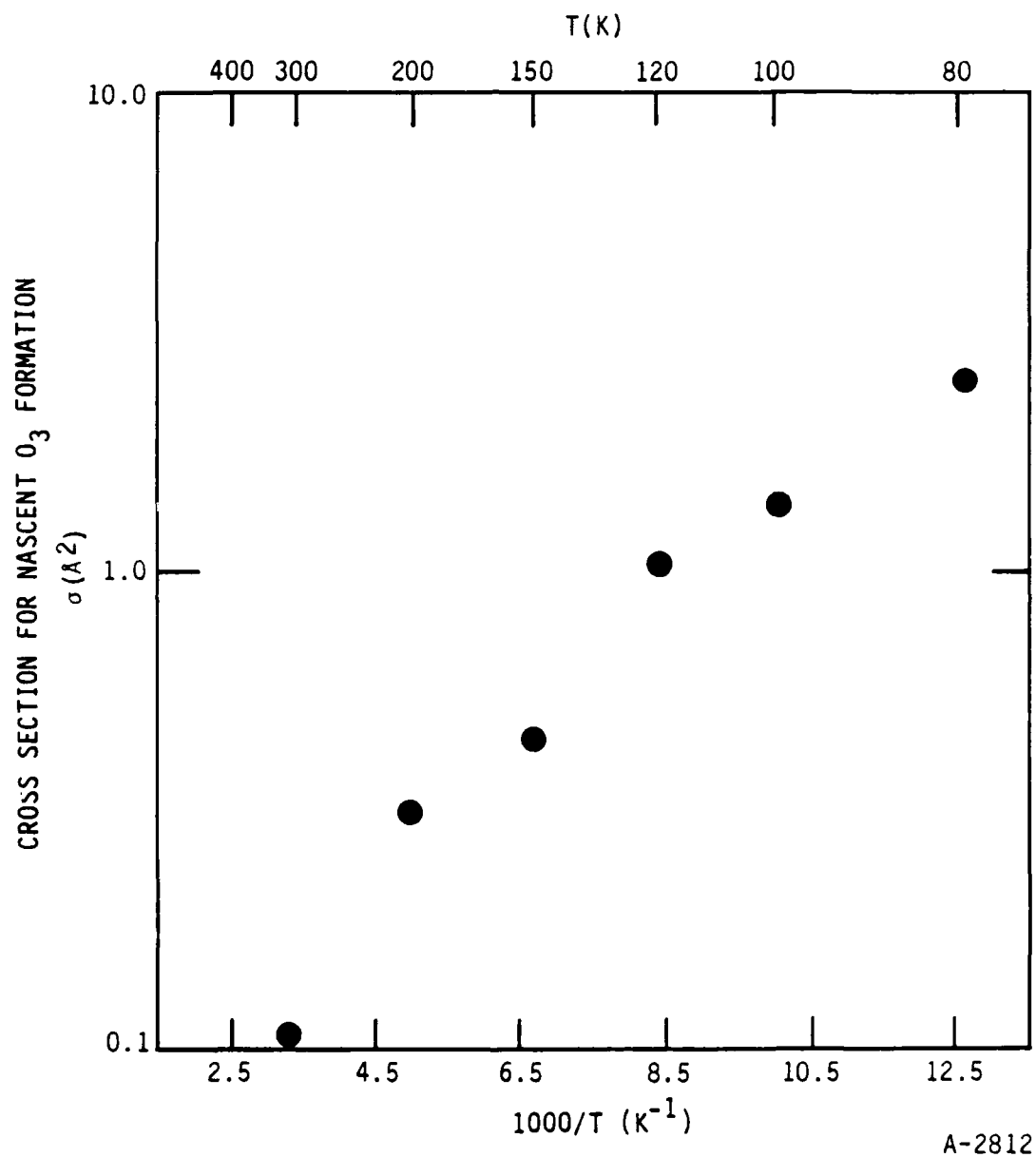


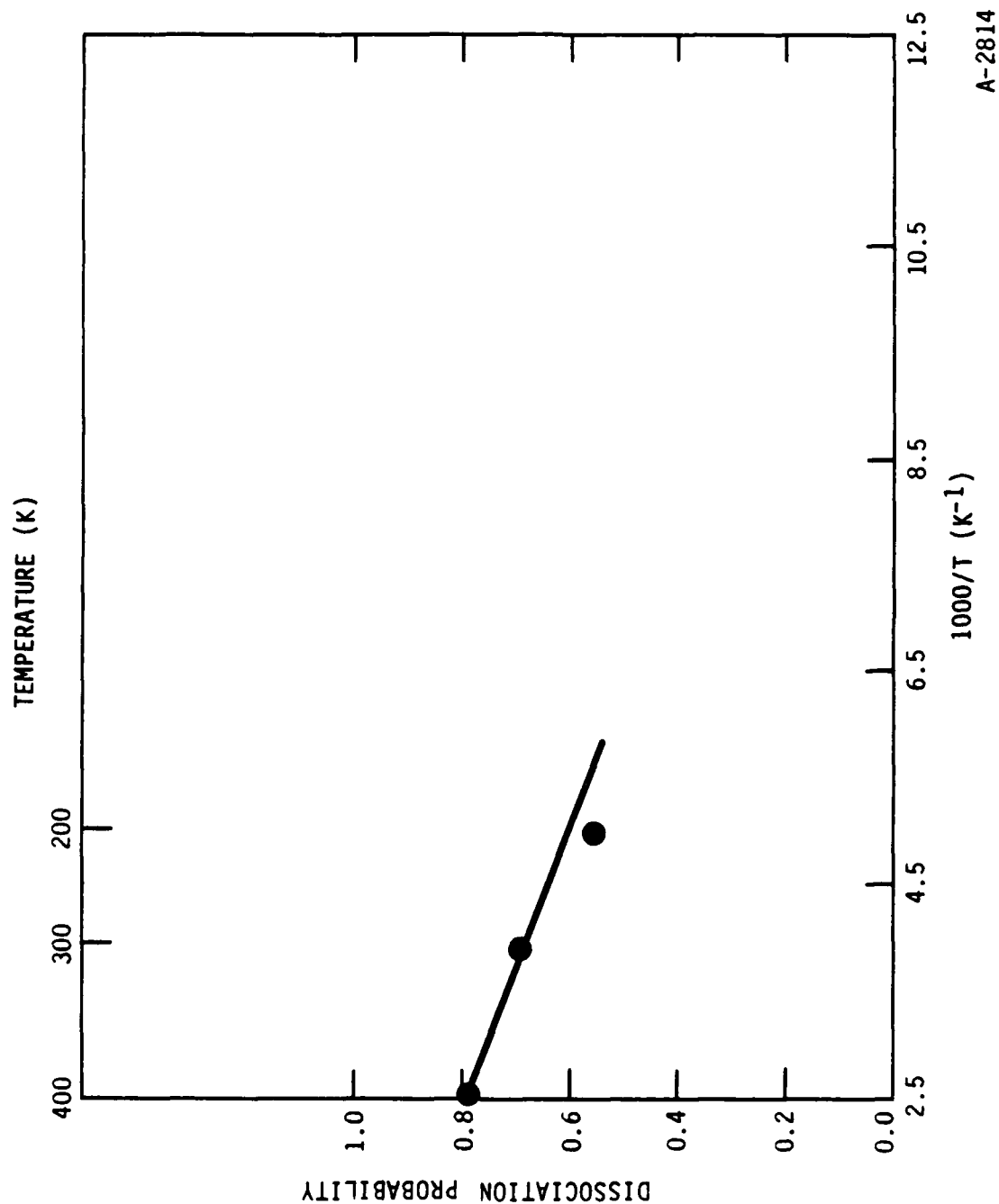
Figure 1. Cross Section for Nascent Ozone Formation Versus Temperature for Chaperon Mechanism

The fraction of nascent ozone molecules undergoing dissociation as a function of bath temperature is shown in Figure 2. At 400 K almost 80 percent of the nascent ozone molecules dissociate. The dissociation probability decreases at the lower temperatures to 0.70 and 0.57 at 300 and 200 K respectively. Since this quantity is necessary for the computation of the overall rate we will use a linear extrapolation of the available data to predict dissociation fractions at lower temperatures. This leads to the following values.

P_{diss}	Bath Temperature (K)
0.5	150
0.35	120
0.25	100
0.10	80

These values are reasonable from our systematic study of ozone dissociation in argon baths.¹⁰ In that work ozone molecules were initialized 25 kcal/mol above the molecular well minimum (or about 1.5 kcal below the dissociation limit). The average translational energy in a Ar-O₃ collision is 2 kT. In the case under consideration here, at 400 K, the average relative translational energy is 1.6 kcal/mol so that the ratio of available energy for dissociation to energy required for dissociation (Table 2) is about 3. The values of this ratio for the 300 and 200 K cases are about 2 and 1.6. We shall assume that the dissociation probability is only dependent on the value of the above ratio so that we may use our previous results to infer dissociation probabilities at lower temperatures.

To check this assertion we note that in the previous work for a 1000 K bath 1.5 kcal/mole below the dissociation limit, the ratio of available to needed energy for dissociation is 1.33 and the computed dissociation probability was found to be 0.61. This compares favorably with the value of 0.57 for a ratio of 1.6 at 200 K. Clearly this procedure requires more elaborate and



A-2814

Figure 2. Dissociation Probability of Newly Formed Ozone Molecules as a Function of Bath Temperature

extensive examination. However we shall use it here without further ado. We also assume the nascent ensemble average energy to be constant with temperature and equal to 0.6 kcal/mol below the well depth. The following values for the dissociation probabilities are found.

P_{diss}	Bath Temperature (K)
0.45	150
0.25	120
0.15	100
0.02	80

This procedure yields values sufficiently close to the simple linear extrapolation values to be in agreement. Note both procedures are used because of necessity and not desirability. The latter values will be adopted.

We now compute effective ozone recombination rates via the chaperon mechanisms. According to earlier discussion the net production rate of ozone, $d[\text{O}_3]/dt$, is given by

$$\frac{d[\text{O}_3]}{dt} = k_3 K_b [\text{O}][\text{O}_2][\text{M}](1 - P_{\text{diss}})$$

where k_3 is the rate constant for the association reaction given by

$$k_3 = \langle v\sigma \rangle$$

where σ is the cross section for association, v the relative velocity and the brackets denote a thermal average. The value of k_3 is adequately approximated as

$$k_3 \approx \bar{v}\sigma$$

where \bar{v} is the average relative thermal velocity. Therefore the overall chaperon mechanism ozone formation rate constant, k , is given

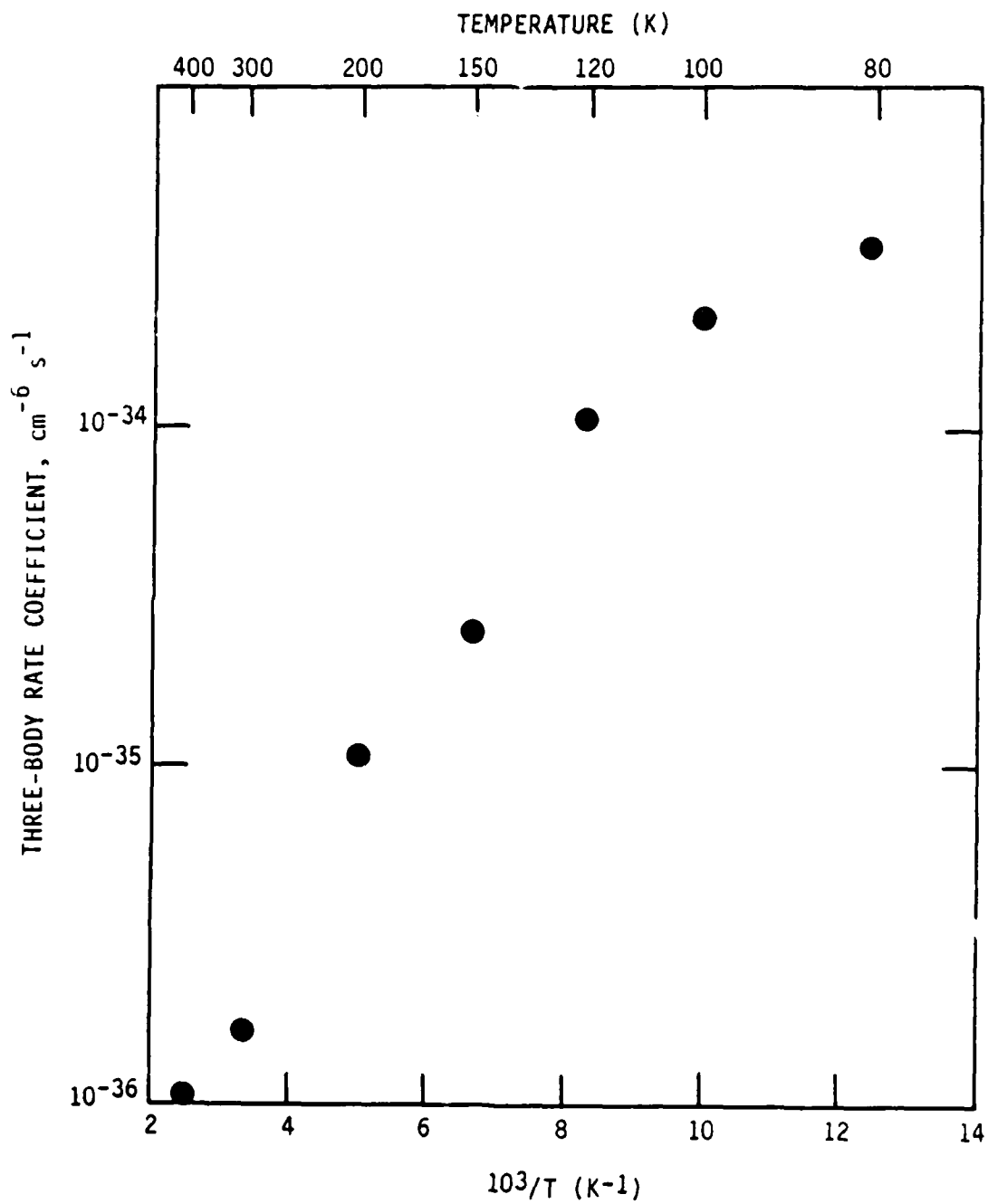
$$k = \bar{v} K_D (1-P) \quad .$$

Computed values of k are shown in Figure 3 as a function of temperature. Recent experimental results are shown in Figure 4.

The trajectory calculation values for the ozone recombination rate constant are clearly much smaller than measured experimentally. This discrepancy may have several sources: 1) the chaperon mechanism may be ineffective in ozone recombination and the recombination is dominated by the energy transfer mechanism, and 2) uncertainties in the Ar-O₃ potential surface.

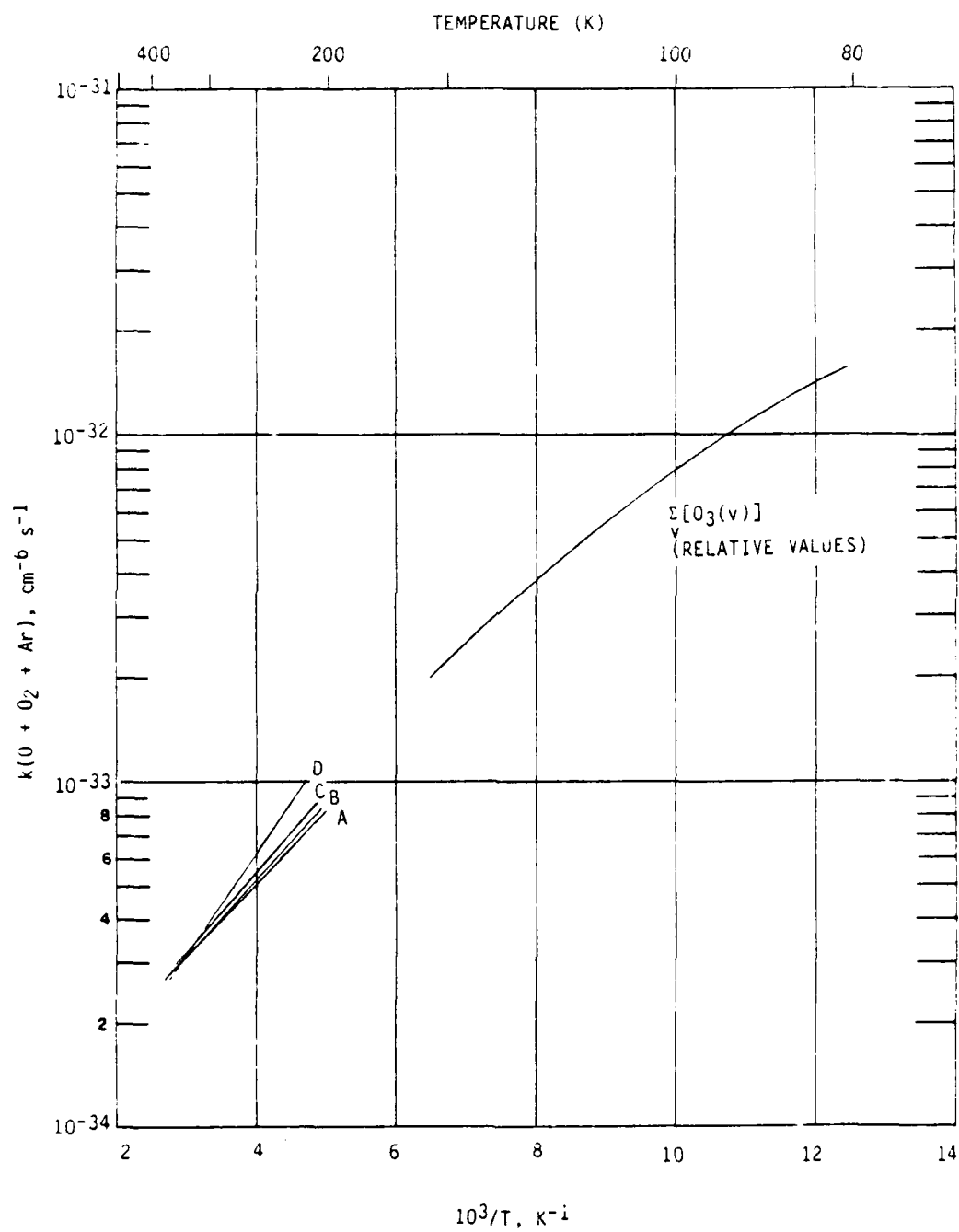
The primary goal of this effort is to assess the importance of the chaperon mechanism. Therefore the first potential source is a result we seek and may not be invoked to explain any discrepancy between theory and experiment. The potential surface used in these calculations is a state-of-the-art potential surface empirically determined ozone surface and the best one currently available. The ArO potentials are from molecular beam scattering data and are expected to be reasonably accurate. In any case the anticipated uncertainties are not expected to produce orders of magnitude variations in the dynamical results. However this conclusion must be viewed as only an assertion.

The low values of the ozone recombination rate constant are due to the magnitude of the equilibrium constant for ArO complexes and the small exchange reaction cross section for the reaction of ArO + O₂. The small exchange cross section may be seen as due to the difficulty with which the relatively stiff oxygen molecule bond is stretched to reach the ozone equilibrium configuration and the difficulty of transferring the released bond energy to relative argon translational energy. The small value of the ArO equilibrium constant is a result of the small ArO well depth. A factor of two increase in the well depth only leads to increases of 4-5 over the current value.



A-2813

Figure 3. Computed Ozone Recombination Rate Constant as a Function of Temperature.



A-1936

Figure 4. Experimental Ozone Recombination Rate Constant as a Function of Temperature.

Within the framework of these calculations we may conclude that the chaperon mechanism does not play a major role in ozone recombination in the COCHISE environment.

As a final point we note that the temperature dependence of the computed rate constant is in fairly good agreement with the experimental values at low temperatures. This agreement would seem to make the chaperon mechanism a disturbingly interesting candidate mechanism. However as noted above its magnitude is substantially below experimental values. A more complete comparison of the chaperon mechanism with the energy transfer mechanism requires computation of the rate constant via the energy transfer mechanism. Such calculations have not yet been performed.

REFERENCES

1. Aquilanti, V., Liuti, G., Vecchio-Cattivi, F., and Volpi, G.G., General Discussion, Disc. Fara. Soc. 55, 187 (1983).
2. Hill, T.L., "Molecular Clusters in Imperfect Gases," J. Chem. Phys. 23, 617 (1955).
3. Stogryn, D.E. and Hirschfelder, J.O., "Contribution of Bound, Metastable and Free Molecules to the Second Virial Coefficient and Some Properties of Double Molecules," J. Chem. Phys. 31, 1531 (1959).
4. Kim, S.K., "Temperature Dependence of the Rate of Termolecular Atomic Recombination," J. Chem. Phys. 46, 123 (1967).
5. Kim, S.K. and Ross, J., "Viscosity of Moderately Dense Gases," J. Chem. Phys. 42, 263 (1965).
6. Varandas, A.J.C. and Murrell, J.N., "Dynamics of the $18\text{O} + 16\text{O}_2(v=0)$ Exchange Reaction on a New Potential Energy Surface for Ground State Ozone," Chem. Phys. Lett. 88, 1 (1982).
7. Bunker, D., "Classical Trajectory Methods," Meth. Comp. Phys. 10, 287 (1972).
8. Porter, R.N. and Raff, C.M., "Classical Trajectory Methods in Molecular Collisions," in Dynamics of Molecular Collisions, Part B, Miller, W.H., Ed., Plenum, New York (1976).
9. Gelb, A., Kapral, R., Burns, G., "Non-Equilibrium Effects in Atomic Recombination Reactions," J. Chem. Phys. 56, 4531 (1972).
10. Gelb, A., "Classical Trajectory Study of Energy Transfer Between Argon Atoms and Vibrationally-Rotationally Excited Ozone Molecules," J. Phys. Chem. 89, 4189 (1985) and unpublished work.

APPENDIX S

(PSI-032/TR-602 reproduced in its entirety)

FORMATION AND STABILIZATION DYNAMICS
OF OZONE COMPLEXES

Quarterly Status Report No. 6

For the Period

1 July 1986 to 30 September 1986

Under Air Force Contract No. F19628-85-C-0032

Prepared by:

A. Gelb and W.T. Rawlins
Physical Sciences Inc.
Research Park, P.O. Box 3100
Andover, Massachusetts 01810

Sponsored by:

Air Force Geophysics Laboratory
Air Force Systems Command
U.S. Air Force
Hanscom Air Force Base, Massachusetts 01731

September 1986

TABLE OF CONTENTS

<u>Section</u>	<u>Page</u>
1. INTRODUCTION	1
2. CLASSICAL TRAJECTORY METHODOLOGY	3
3. CALCULATIONS	9
4. RESULTS AND DISCUSSION	11
4.1 Long-Lived Complex Calculations	11
4.2 Stabilization Calculations	15
4.3 Multicollisional Calculations	17
REFERENCES	31

LIST OF FIGURES

<u>Figure</u>		<u>Page</u>
1	Probability of Long-Lived Complex Formation as a Function of Relative Translational Energy	11
2	Angular Momentum of Ozone Complexes as a Function of Complex Energy	14
3	Collisional Stabilization Probability of Ozone Complexes by Argon Atoms as a Function of Complex Energy	16
4	Average Energy of Ozone Molecules as a Function of Number of Sequential Collisions with Argon Atom Thermal Bath	19
5	Average Energy of Ozone Molecules as a Function of Number of Sequential Collisions with Argon Atom Bath for (0.02,0.0) case	19
6	Average Energy of Ozone Molecules as a Function of Number of Sequential Collisions with Argon Atom Bath for (0.03,0.0) case	20
7	Average Energy of Ozone Molecules as a Function of Number of Sequential Collisions with Argon Atom Bath for (0.04,0.0) case	20
8	Average Energy of Ozone Molecules as a Function of Number of Sequential Collisions with Argon Atom Bath for (0.02,0.01) case	21
9	Average Energy of Ozone Molecules as a Function of Number of Sequential Collisions with Argon Atom Bath for (0.02,0.02) case	21
10	Average Energy of Ozone Molecules as a Function of Number of Sequential Collisions with Argon Atom Bath for (0.03,0.01) case	22
11	Average Energy of Ozone Molecules as a Function of Number of Sequential Collisions with Argon Atom Bath for (0.04,0.01) case	22
12	Average Energy of Ozone Molecules as a Function of Number of Sequential Collisions with Argon Atom Bath for (0.04,0.02) case	23

LIST OF FIGURES (Cont.)

<u>Figure</u>		<u>Page</u>
13	Distribution of Recombined Ozone Total Internal Energies: a) Nascent Distribution and b) After Fifty Sequential Collisions with Argon Atom Bath	24
14	Distribution of Recombined Ozone Total Internal Energies: a) Nascent Distribution and b) After Fifty Sequential Collisions with Argon Atom Bath	25
15	Distribution of Recombined Ozone Total Internal Energies: a) Nascent Distribution and b) After Fifty Sequential Collisions with Argon Atom Bath	25
16	Distribution of Recombined Ozone Total Internal Energies: a) Nascent Distribution and b) After Fifty Sequential Collisions with Argon Atom Bath	26
17	Distribution of Recombined Ozone Total Internal Energies: a) Nascent Distribution and b) After Fifty Sequential Collisions with Argon Atom Bath	26
18	Distribution of Recombined Ozone Total Internal Energies: a) Nascent Distribution and b) After Fifty Sequential Collisions with Argon Atom Bath	27
19	Distribution of Recombined Ozone Total Internal Energies: a) Nascent Distribution and b) After Fifty Sequential Collisions with Argon Atom Bath	27
20	Distribution of Recombined Ozone Total Internal Energies: a) Nascent Distribution and b) After Fifty Sequential Collisions with Argon Atom Bath	28
21	Distribution of Recombined Ozone Total Internal Energies: a) Nascent Distribution and b) After Fifty Sequential Collisions with Argon Atom Bath	28

LIST OF TABLES

<u>Table</u>		<u>Page</u>
1	Computed Probabilities for the Formation of Long-Lived Complexes	12
2	Dissociation Probabilities of Nascent Ozone Ensembles in a 200 K Argon Atom Bath	18
3	Average Nascent Ozone Ensemble Energy Below Dissociation Formed by Stabilization of Complexes of Varying Energy	18

1. INTRODUCTION

According to the radical molecule mechanisms the recombination of ozone occurs by the following steps:



Reaction (1) involves the collision of an oxygen atom with an oxygen molecule to form an unbound ozone complex, O_3^* . Since O_3^* is formed above the dissociation limit of ozone it has a finite lifetime and will dissociate unless stabilized by a collision with another molecule or atom (denoted as M in Reaction (2)). The newly recombined ozone molecules, $O_3(v,J)$, will in general be very vibrationally-rotationally excited and undergo collisions with bath molecules that will lead to either relaxation or redissociation:



or



The net rate of production (in the bath) of stable ozone molecules is given by the rate of production of nascent ozone corrected by the fraction of nascent molecules that subsequently dissociate, P_d , i.e.,

$$\frac{d[O_3]}{dt} = k_2[O_3^*][M](1 - P_d) \quad (1)$$

The computation of the dissociated fraction requires a multiple collision treatment.

In this report we discuss the results of a classical trajectory study of the formation of long-lived complexes of ozone, their stabilization by

collisions with argon atoms and subsequent relaxation of newly formed ozone molecules in a 200 K argon atom thermal bath. The calculations were designed to gain an understanding of the molecular quantities that control each of the processes involved in the overall recombination reaction in order to aid in the interpretation of available experimental data from the COCHISE experiments at AFGL.

The organization of this report is as follows. We begin with a discussion of the classical trajectory formulation for calculation of the ozone recombination dynamics. A brief discussion of the computational details and calculations performed follows. Results and discussion are then presented and finally the implications of this work to the COCHISE experiments are given.

2. CLASSICAL TRAJECTORY METHODOLOGY

The rate of change of unbound ozone complexes is given by:

$$\frac{d[O_3^*]}{dt} = k_1[O][O_2] - k_2[O_3^*] - k_3[M][O_3^*] \quad (2)$$

A steady state approximation for the O_3^* concentration yields

$$[O_3^*] = \frac{k_1[O][O_2]}{k_2 + k_3[M]} \quad (3)$$

The value of k_2^{-1} is the average lifetime of an O_3^* complex and the term $k_3[M]$ is the rate of collisional removal of O_3^* . We will assume that the total gas pressure is sufficiently low and the complex lifetime sufficiently short so that

$$k_2 \gg k_3[M] \quad (4)$$

This is surely valid at pressures up to several atmospheres. The ozone complex concentration becomes

$$[O_3^*] = \frac{k_1[O][O_2]}{k_2} \equiv K(T)[O][O_2]$$

where $K(T)$ is the equilibrium constant for the formation of an unbound ozone complex. The rate of production of stable ozone molecules is now written from Eq. (1) as

$$\frac{d[O_3]}{dt} = k_3 K(T)[O][O_2][M](1-P_d) \quad (5)$$

The dynamical simulation of the ozone recombination process requires three separate computations. First, a complex equilibrium constant $K(T)$ must be computed. Second, the single collision rate constant for complex stabilization, k_{39} , must be determined, and finally the multicollisional redissociation probability of newly formed ozone molecules is computed (R4).

We follow the work of Bunker¹ and Blint² for the calculation of the ozone complex formation equilibrium constant. The complex equilibrium constant may be related to the cross section for the formation of an O_3^* complex by collision of O_2 with O , $\sigma(E_v, E_R, E_t)$ at fixed O_2 vibrational energy, E_v , rotational energy, E_R and relative translational energy, E_t , by the following relation

$$K(T) = \left[\left(\frac{2}{\pi} \right)^{1/2} \left(\frac{\mu}{kT} \right)^{3/2} \frac{1}{Q_R Q_v} \sum_{E_R} \sum_{E_v} e^{-(E_R + E_v)/kT} \left[\int_0^v \sigma(E_v, E_R, E_t) e^{-E_t/kT} v^3 dv \right] \right] \quad (6)$$

where Q_R is the diatom partition function, Q_v the vibrational partition function, V the atom-diatom relative velocity and μ the reduced mass. In a purely classical treatment the sums are replaced by integrals.

A relationship is needed between the complex formation cross section and classically computed quantities. This relationship is

$$\sigma(E_v, E_R, E_t) = 2\pi \int_0^\infty \tau(E_v, E_R, E_t) P(E_v, E_R, E_t) b db \quad (7)$$

where $\tau(E_v, E_R, E_t)$ is the lifetime of the complex and $P(E_v, E_R, E_t)$ is the complex formation probability.

To compute the values of $\tau(E_v, E_R, E_t)$ and $P(E_v, E_R, E_t)$, the phase space volume of an ozone collision complex must be defined. A convenient although not unique procedure is that a complex is formed whenever the distance between either of the diatom oxygen atoms and the incoming oxygen atom is less than a given cutoff value. An intuitively appealing cutoff value is a multiple of the equilibrium O-O distance in stable ozone. The value should be chosen large enough so that no multiple crossings of this region occur. If there are no multiple crossings the lifetime of the complex is simply the time between when the incoming oxygen atom first crosses the cutoff value and when it recrosses. Since no further recrossing is assumed to occur, the colliding pair separate asymptotically after recrossing.

The classical procedure for the computation is therefore the following: a) collision pairs of oxygen atoms and oxygen molecules are chosen from the appropriate Boltzmann and flux distributions, b) for collisions in which the oxygen atom separation decreased below the cutoff value, the value $P(E_V, E_R, E_t)$ is set equal to unity and the time between the initial crossing and recrossing is recorded; otherwise $P(E_V, E_R, E_t)$ equals zero and c) the procedure is summed over all impact parameters.

The choice of complex formation cutoff parameter does not seem critical. This is because for two values of the cutoff parameter, the time spent traversing the distance between should be small compared to the lifetime of the complex. Some computer experimentation is necessary. As mentioned earlier it is necessary to choose a cutoff parameter such that multiple crossings do not occur. If they occur the computation can be substantially complicated. A reasonable remedy to that problem would be an asymmetric set of cutoff parameters. For example, a smaller value in the entrance channel for the critical oxygen atom distance and a larger value in the exit channel would likely eliminate multiple crossings.

Computer programs for the calculation of $K(T)$ have been completed and tested for accuracy. However calculations have not yet been undertaken.

The next step in the calculation of the ozone recombination rate is the determination of the collisional stabilization probability of ozone complexes by argon atoms. This calculation may be carried out by fairly standard Monte-Carlo classical trajectory techniques except for the initial ozone complex conditions.

The ozone complex initial conditions may be chosen using either of two procedures: 1) random sampling from appropriate distributions or 2) using coordinates of complexes determined from the calculation of $K(T)$. The first method has the advantage of being self-contained, i.e., it does not depend on the previous calculations. However it has the very serious difficulty of not readily relating to the phase space of collisionally formed complexes. One

may readily choose initial conditions from the appropriate distribution functions to match the total average energies and angular momentum of collisionally formed complexes (assuming them to be known; such averages require fairly extensive complex lifetime calculations). However it seems impossible to show (without extensive additional calculation) that the lifetime and phase space distributions are the same for collisionally formed complexes as those chosen by a Monte-Carlo phase space sampling procedure. Therefore it is much more efficient to use the coordinates of complexes computed directly from O-O₂ collisions as initial conditions for complex stabilization computations.

The procedure to be followed is as follows: a) random initial conditions for O-O₂ collisions are chosen, b) the trajectory is integrated and the formation of a complex is determined using the aforementioned criteria, and c) if a complex is formed the coordinates are recorded and stored as initial conditions for the stabilization calculation. In order not to waste too much computational time with very short lived complexes that cannot contribute effectively to the ozone production rate, a cutoff value for the complex's lifetime must be chosen. An appropriate criterion is to use the time for an argon atom to move from the asymptotic regime to its distance of closest approach in the stabilization calculation, i.e., a lifetime long enough so that the complex does not fall apart before the argon atom arrives. Some computational experimentation is clearly warranted.

A practical advantage of this procedure is that the initial complex coordinates can be generated without significant additional calculation during the calculation of $K(T)$. This may be quite substantial since these calculations will be quite computer intensive.

The final step in the simulation of the recombination process is to compute the redissociation probability and relaxation of newly formed (nascent) ozone molecules. For purposes of computing new reaction rates only the redissociation probability is necessary. However it is of interest to examine relaxation of the recombined ozone molecules in order to predict the radiative characteristics of such a recombining gas. The COCHISE facility is designed

to measure radiation from recombining ozone. However, this is not possible in a collision free environment and therefore measured radiative levels have been affected by some degree of relaxation. It is therefore important to gain insight into the relaxation processes. This information will also be useful in understanding processes involving ozone recombination in the upper atmosphere where the rate of relaxation of the nascent distribution may differ substantially from that in the COCHISE experiments.

The appropriate simulation of the relaxation/redissociation processes employs the multicollision simulation of the Boltzmann equation. This simulation technique has been discussed earlier³ so only a brief outline will be given.

The Boltzmann equation for the recombining ozone in argon mixture may be written as:

$$\frac{\partial [n_{O_3}(t) f_{O_3}(E, T, t)]}{\partial t} = - L n_{O_3}(t) f_{O_3}(E, T, t) + R \quad (8)$$

where $n_{O_3}(t)$ is the concentration of ozone molecules, $f_{O_3}(E, T, t)$ is the phase space distribution function of ozone molecules, L is the Boltzmann collision operator, R is a reactive sources term and E and T refer to the ozone internal coordinates and bath temperature respectively. The reactive source term is computed from the preceding calculation and is the so-called one way flux production term.⁴

Using the notation of Ref. 3 the time dependent rate coefficient may be written as

$$k_r(n\tau) = k_r^0 - \sum_{j=1}^{n-1} \int X_j L_d d\vec{v} dE / [n_O n_{O_2}] \quad (9)$$

where

$$X_j = (1 - L\tau)^j X_0, \quad (10)$$

$$X_0 = \tau R(T, E) n_O n_{O_2}$$

and L_d is the part of the Boltzmann collision operator leading to dissociation. The one-way flux distribution of recombined ozone molecules is given by X_0 and is computed from the prior stabilization calculation. The ozone distribution that results from j bath collisions with X_0 is X_j and is the primary quantity computed in the multicollisional calculation.

After a sufficient number of collisions enough relaxation occurs so that the redissociation probability of a recombined molecule becomes zero. The rate constant then achieves a steady state value. Previous calculations on diatomic systems³ indicate between 20 and 50 collisions are sufficient for achieving a steady state recombination rate. At that point recombined molecules are still highly excited but far enough down the potential so that collisional dissociation does not occur. It is anticipated that similar numbers of collisions will be required to describe ozone redissociation. Further relaxation of the recombining system is followed by simply computing more sequential collisions.

The methodology described above provides a systematic computational scheme for the calculation of the ozone recombination rate constant. Computational limitations have prevented such a program from being completed. A limited set of calculations were completed on the formation of long-lived complexes and their subsequent dissociation and relaxation. These calculations were quite extensive and systematically studied the dynamics of complex formation. They are reported in the following sections of this report.

3. CALCULATIONS

Classical trajectory calculations were performed for the formation of long-lived complexes of ozone by collision of O-atoms with O₂ molecules and stabilization of formed complexes by argon atoms. The calculations were purely classical with the initial diatom vibrational energy chosen from the classical distribution function. All calculations involving O-O₂ collisions were performed using the Murrell-Sorbie-Varandas ozone potential energy surface.⁵ Calculations of Ar-O₃ collisions were performed using the Murrell-Sorbie-Varandas potential energy surface for the ozone portion and additive Lennard-Jones 6-12 potentials between the argon atom and each oxygen atom.^{6,7}

The dependence of long-lived complex ($>1.2 \times 10^{-10}$ s) formation on relative translational and diatom energies was computed. Calculations were performed at relative translational energies of 0.239, 0.478, 0.717, 0.956, 1.194, 1.433, 1.672, 1.911, 2.150, 2.389, and 2.628 kcal/mol and diatom rotational energies of 0.0, 0.239, 0.478, 0.717, and 0.956 kcal/mol (for each translational energy). Higher values of relative translational energy calculations (2.867, 3.106, 3.344, 3.583, and 4.061 kcal/mol) were performed at initial diatom rotational energy equal to zero. At translational energies below or equal to 2.150 kcal/mol batches of at least 750 trajectories were computed for each value of initial relative translational-diatom rotational energy. At higher translational energies batches of 500 trajectories were computed. A total of approximately 42,000 trajectories were computed. At low translational and rotational energies the computing times became very large due to the relatively long lifetimes of the O₃^{*} collision complexes.

Calculations were performed in order to determine stabilization probabilities of complexes by collision with argon atoms. A 200 K argon atom thermal bath was employed in all stabilization calculation. The calculations were designed to investigate variations in stabilization probability with complex energy and initial formation conditions. It is convenient to characterize the complexes by the initial relative translational energy and the initial diatom rotational energy, (E_t, E_R). Thirteen cases were used for stabilization

calculations. These included: (0.239,0.0), (0.478,0.0), (0.717,0.0), (0.956,0.0), (1.672,0.0), (2.389,0.0), (0.239,0.239), (0.478,0.239), (0.717,0.239), (0.956,0.239), (1.433,0.239), (0.478,0.478), and (0.956,0.478). Six hundred or more trajectories were computed for each stabilization calculation. Since the number of long-lived trajectories determined from the O-O₂ trajectories was always less than 600, each of the initial conditions was used several times in the stabilization calculations. For the higher total energy cases very few long-lived complexes were found and the statistics of stabilization may be suspect. A total of approximately 80,000 trajectories were computed for these calculations.

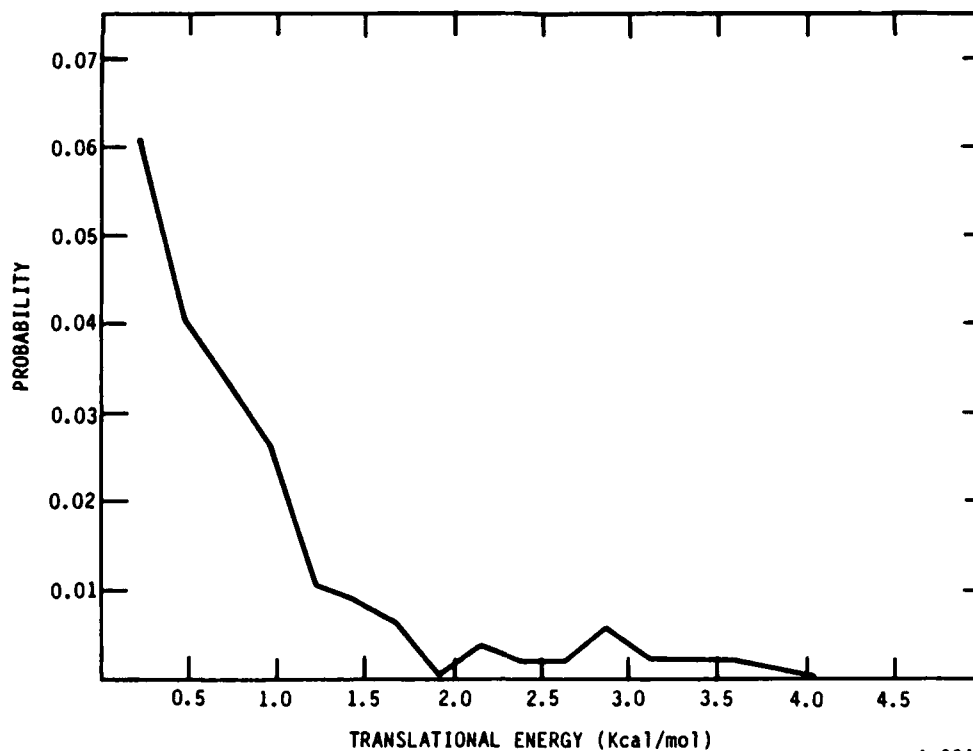
Multicollisional calculations were carried out to compute redissociation probabilities and energy relaxation of nascent recombined ozone. The cases considered were: (0.239,0.0), (0.478,0.0), (0.478,0.239), (0.717,0.0), (0.478,0.478), (0.717,0.239), (0.956,0.0), (0.956,0.239) and (0.956,0.478). In each case the initial batch of stabilized ozone molecules were subjected to a sequence of 50 collisions with a 200 K ozone thermal bath. Initial batches varied from 120 to 150 ozone molecules. These calculations required the computation of more than 50,000 trajectories.

4. RESULTS AND DISCUSSION

In this section we discuss the results of the calculations for the formation, stabilization and subsequent relaxation of long-lived complexes. Our goal is to interpret the results of the formation/stabilization calculations in terms of the energy transfer characteristics found in Ref. 7. The results of the relaxation calculations will be used as an aid to the interpretation of the COCHISE experimental results and atmospheric processes.

4.1 Long-Lived Complex Calculations

Probabilities of long-lived complex formation as a function of initial relative oxygen atom-oxygen molecule translational energy is shown in Figure 1 for the case of an initially non-rotating diatom. As is readily seen, complex formation probabilities decrease rapidly with increasing translational energy.



A-3818

Figure 1. Probability of Long-Lived Complex Formation as a Function of Relative Translational Energy

Even at the lowest translational energy the probability of forming complexes of lifetime greater than 1.2×10^{-10} s is quite small. At relative translational energies than about 2 kcal/mol there was generally one (or no) trajectory that produced a long-lived complex. A complete list of computed probabilities is listed in Table 1.

Table 1. Computed Probabilities for the Formation of Long-Lived Complexes

E_R/E_t	0.0	0.239	0.478	0.717	0.956
	(kcal/mol)	(kcal/mol)	(kcal/mol)	(kcal/mol)	(kcal/mol)
0.239	0.062	0.002	0.001	0.00	0.00
0.478	0.044	0.010	0.008	0.003	0.001
0.717	0.033	0.009	0.007	0.00	0.001
0.956	0.026	0.011	0.008	0.005	0.005
1.194	0.011	0.005	0.005	0.005	0.003
1.433	0.009	0.007	0.005	0.004	0.004
1.672	0.007	0.011	0.001	0.001	0.001
1.911	0.00	0.003	0.004	0.002	0.001
2.150	0.004	0.001	0.003	0.001	0.003
2.389	0.002	0.006	0.002	0.002	0.00
2.628	0.002	0.00	0.002	0.006	0.00
2.867	0.006	0.00			0.002
3.106	0.002				
3.344	0.002				
3.583	0.002				
4.061	0.00				
4.778	0.00				

The values listed in Table 1 clearly show that increasing initial diatom rotational energy decreases the probability of long-lived complex formation. This is most clear at low translational energies. At the lowest translational energies and highest rotational energies the diatoms are relatively hot and readily transfer some of their rotational energy to relative translational energy thereby reducing the complex formation probability. A complex can only be formed when some of the relative atom-diatom translational energy is transferred into internal motion of the complex. The incoming atom becomes trapped when enough energy is lost so that it cannot overcome the attractive forces in the complex. Excess rotational energy is easily transferred from the diatom

so that a rotationally excited diatom will have little chance of forming a long-lived complex. Also at higher translational energies the amount of energy that must be transferred into internal complex modes is greater and that reduces the probability.

At intermediate translational energies (above about 1 kcal/mol) the effect of rotational energy is present but not so powerful. This reduced effect may simply be seen as due to the fact that at higher translational energies the same amount of rotational energies produces less hot diatoms. Above approximately 1.5 kcal/mol relative translational energy very few long-lived trajectories were computed and the statistical uncertainties of the results listed in Table 1 are large.

An implication of the rapid decrease of the formation of long-lived complexes is that the equilibrium constant, $K(T)$ will show a strong decrease with increasing temperature. This is simply because the anticipated lifetime of complexes formed at higher energies will be shorter. A systematic discussion of the temperature variation awaits computation of $K(T)$.

Some characterization of the long-lived complexes is useful for understanding their subsequent collisional behavior. The energy of the complex is of course the sum of the initial relative translational and diatom internal energies. Therefore complexes formed at higher relative translational and diatom rotational energies (assuming constant diatom vibrational energy) will have to lose more energy by collision with third bodies to form a stable ozone molecule than those formed at lower initial energies. A naive assessment would predict a decreasing stabilization probability with increasing long-lived complex energy. However another factor must be taken into consideration, the total angular momentum of the complex. In earlier work⁷ on Ar-O₃ collisional energy transfer, the triatomic angular momentum was found to be the controlling factor in both the magnitude and the sign of energy transferred between highly excited ozone and argon. In particular, molecules with low angular momentum are found to gain energy by collision despite very high internal energy. The significance of this observation for stabilization of

complexes is that energy relaxation to form stable molecules will be favored by higher complex angular momentum. However, higher complex angular momentum implies in general complexes formed at high total energy requiring larger energy transfers for stabilization.

The variation in the average long-lived complex angular momentum as a function of total energy of the complex is shown in Figure 2 . Three cases are shown: complexes formed by collisions with non-rotating diatoms, formed by collisions with diatoms having 0.239 kcal/mol initial rotational energy and for initial diatom rotational energies of 0.478 kcal/mol. Since at higher collision energies the number of computed complexes was very small, the behavior shown in Figure 2 is not reliable from a quantitative point of view due to statistical uncertainties. The increase of complex angular momentum

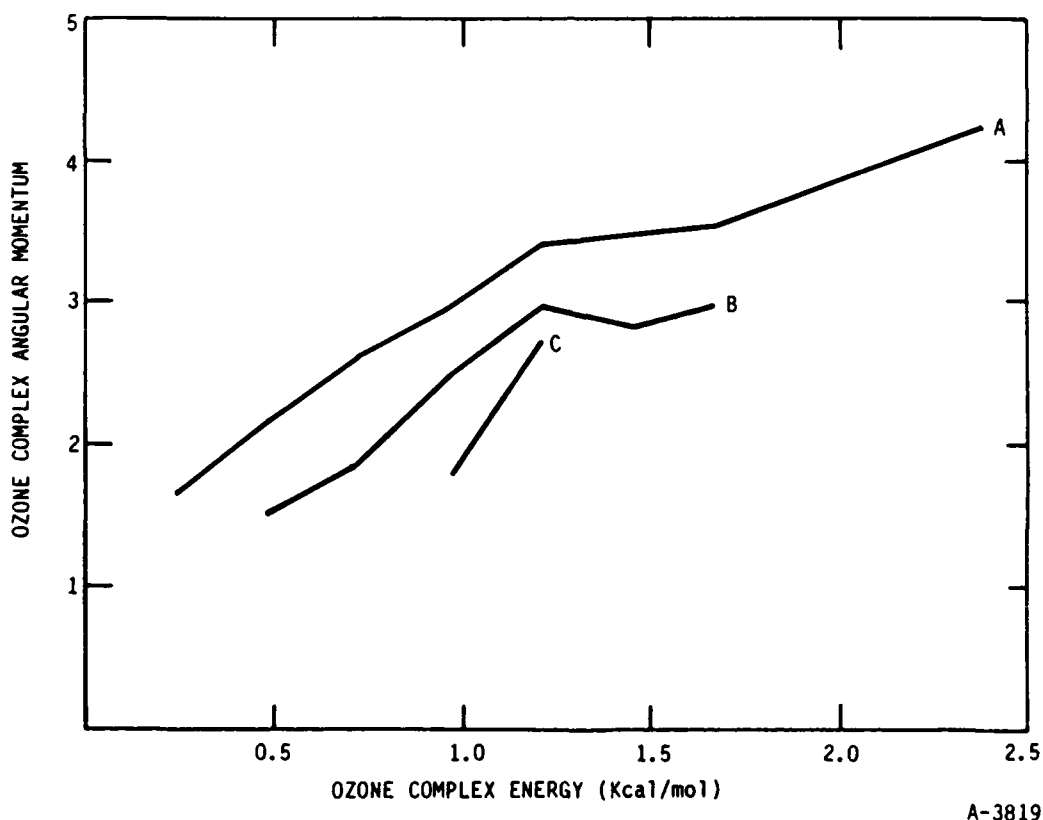


Figure 2. Angular Momentum of Ozone Complexes as a Function of Complex Energy. Curves denote initial diatom rotational energy as follows: A, 0.0 kcal/mol; B, 0.239 kcal/mol; C, 0.478 kcal/mol.

with complex energy is readily seen for the non-rotating case. The Murrell-Sorbie-Varandas ozone potential surface is quite directional so that a complex is formed only when the three atoms are in a narrow range of configurations. This fixes the allowed range of impact parameters for complex formation. As the relative translational energy increases the orbital angular momentum for this range of impact parameters increases. The orbital angular momentum is converted into complex angular momentum.

For the rotating cases the situation is more difficult since the vector coupling of orbital and diatom angular momentum determine the total complex angular momentum. However the computed values show a clear increase in the complex angular momentum with increasing complex energy. In the next section the results of stabilization calculations will be presented.

4.2 Stabilization Calculations

Calculations were performed to determine the stabilization probability of long-lived complexes by collision with argon atoms. An argon atom bath of 200 K is used for all the calculations. Calculations were done using coordinates from a previously determined long-lived complex as the initial triatom coordinates. Relative atom-triatom coordinates were chosen randomly from appropriate Boltzmann distributions.

Computed probabilities of stabilization verses complex energy are shown in Figure 3. Each set of connected points are for complexes formed from diatom collisions with a given value of initial rotational energy (A:0.0; B:0.239 kcal/mol and C:0.478 kcal/mol, initial diatom rotational energy). The most obvious feature of the computed stabilization probabilities is that there is no discernable dependence on complex energy. From the earlier discussion this may be attributed to the near balancing of two opposite effects. Higher energy complexes require larger energy transfers for stabilization and should have lower stabilization probabilities. On the other hand higher energy complexes have higher angular momentum which facilitates energy transfer from the triatom. These two effects seem to cancel one another leading to no obvious

dependence for stabilization probability on complex energy (for the range of energies and angular momenta studied). Again these conclusions should be tempered by the fact that the sample sizes were exceedingly limited due to the low probability of forming long-lived complexes at higher energies.

The implication for the general computation of recombination rates for ozone is that the temperature dependence arises primarily from the dependence of $K(T)$ on temperature. Higher energy complexes would be more prevalent at higher temperatures. On the basis of the present calculation stabilization does not seem to depend strongly on complex energy. We have not, however, examined stabilization probability as a function of argon atom bath temperature. Earlier, systematic studies of energy transfer between highly vibrationally-rotationally excited ozone and argon indicates that the energy transfer is most controlled by the triatom angular momentum. Stabilization calculations at different bath temperatures are clearly warranted. On the

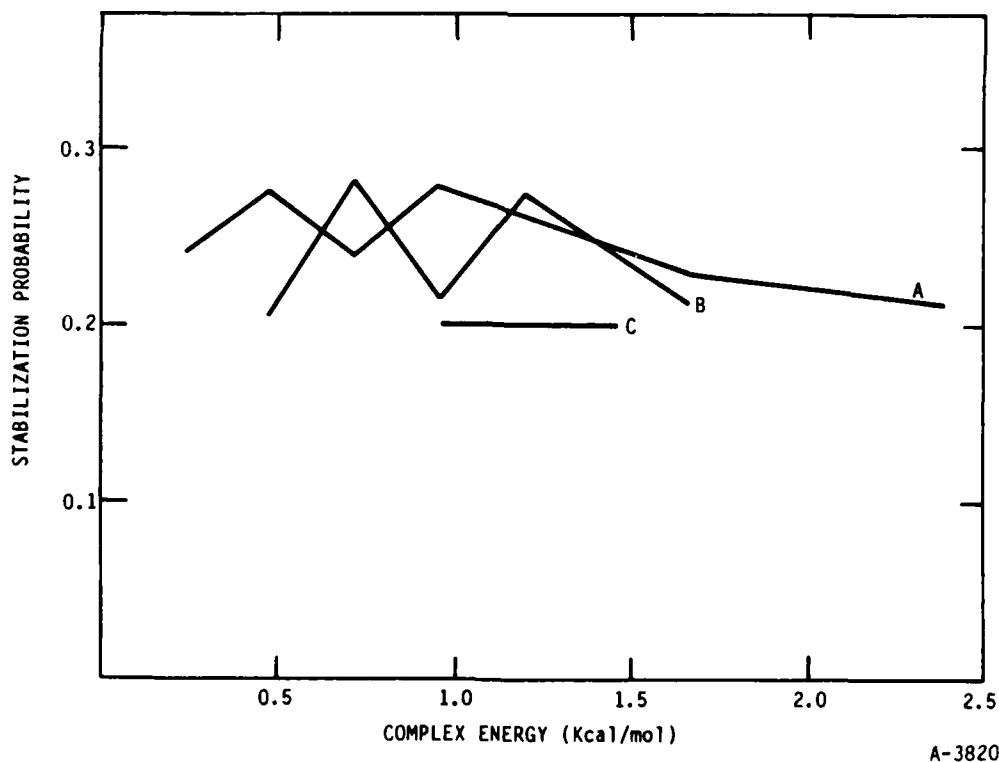


Figure 3. Collisional Stabilization Probability of Ozone Complexes by Argon Atoms as a Function of Complex Energy. Curves are labeled as in Figure 2.

basis of the limited data from the present calculations, stabilization probabilities will be weakly dependent on temperature. Complex formation is (as shown earlier) strongly dependent on the colliders' energy.

We now consider the behavior of newly recombined ozone molecules in an argon thermal bath.

4.3 Multicollisional Calculations

Calculations were performed to simulate the relaxation of newly recombined ozone molecules in a 200 K argon bath. The calculations were done using the methodology described in Ref. 3. The evolution of each batch of nascent ozone molecules was followed for 50 collisions.

The primary quantities of interest from these calculations are the dissociation probability of recombined ozone molecules and the rate of energy relaxation. First we discuss dissociation probabilities.

Computed redissociation probabilities are listed in Table 2. The nascent ozone ensembles are labeled by the energies of the unbound complexes from which they are collisionally stabilized. Generally the computed redissociation probabilities are quite large, varying from 59 to 15 percent. In a complete calculation of a thermal recombination rate these values (when properly averaged) would be used in Eq. (1) and would constitute a significant correction to the so-called one-way flux recombination rate constant.

An obvious but curious trend in the values listed in Table 2 is that the molecules formed from higher energy complexes have lower redissociation probabilities. To understand this behavior we consider the energies of the nascent ozone molecules formed by stabilization of the ozone complex. These values are listed in Table 3. It is quite clear from the listed values that the higher energy complex produce lower energy molecules. This is readily seen as due to the larger angular momentum of the higher energy complexes. The effect of molecular angular momentum on energy transfer was discussed earlier.

Table 2. Dissociation Probabilities of Nascent Ozone Ensembles in a 200 K Argon Atom Bath. Ensembles are labeled by the energies of the long-lived complexes from which they are derived.

E_t/E_j	0.00 (kcal/mol)	0.239 (kcal/mol)	0.478 (kcal/mol)
0.239	0.59		
0.478	0.37	0.44	0.28
0.717	0.26	0.30	
0.956	0.22	0.15	0.20

Table 3. Average Nascent Ozone Ensemble Energy Below Dissociation Formed by Stabilization of Complexes of Varying Energy. All energies in units of kcal/mol.

E_t/E_j	0.00 (kcal/mol)	0.239 (kcal/mol)	0.478 (kcal/mol)
0.239	-0.599		
0.478	-0.861	-0.812	-0.975
0.717	-0.896	-0.964	
0.956	-1.145	-1.474	-1.397

It is reasonable that lower energy molecules will suffer fewer dissociation collisions. Therefore the trend observed in Table 2 for redissociation probabilities is simply that higher energy complexes produce lower energy molecules that have lower redissociation probabilities.

The multicollisional energy relaxation of recombined ozone molecules is now considered. The average total internal energy of a relaxing ensemble of recombined ozone molecules is shown as a function of collision with the 200 K argon bath in Figures 4 through 12. The behavior of each case is fairly similar, relaxing to about 6 kcal/mol below the dissociation limit of the ozone

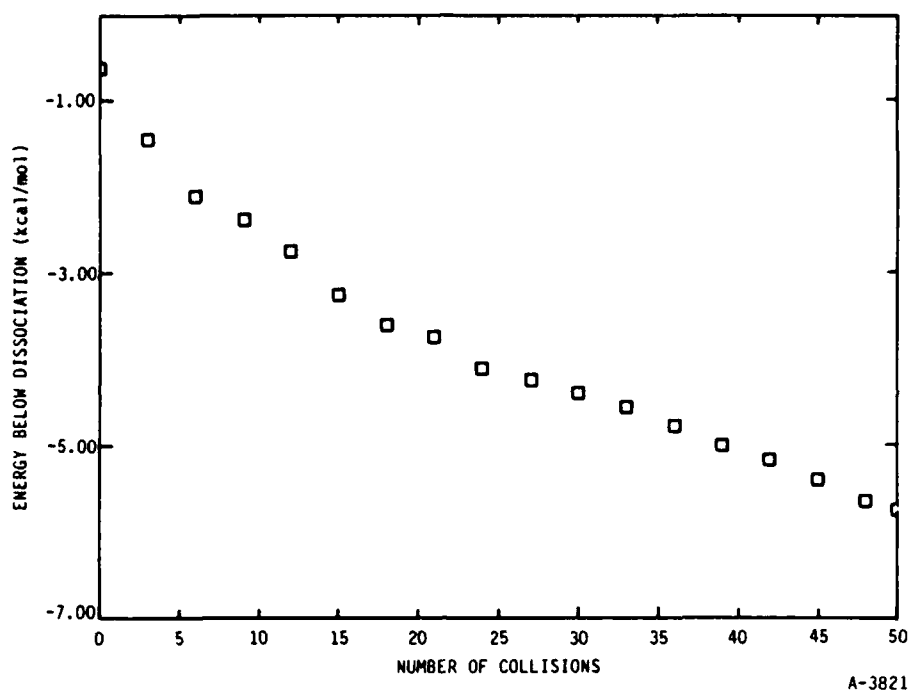


Figure 4. Average Energy of Ozone Molecules as a Function of Number of Sequential Collisions with Argon Atom Thermal Bath. Ozone ensemble is labeled by the energies of the long-lived complexes from which they are derived. Calculation is for (0.01,0.0) case.

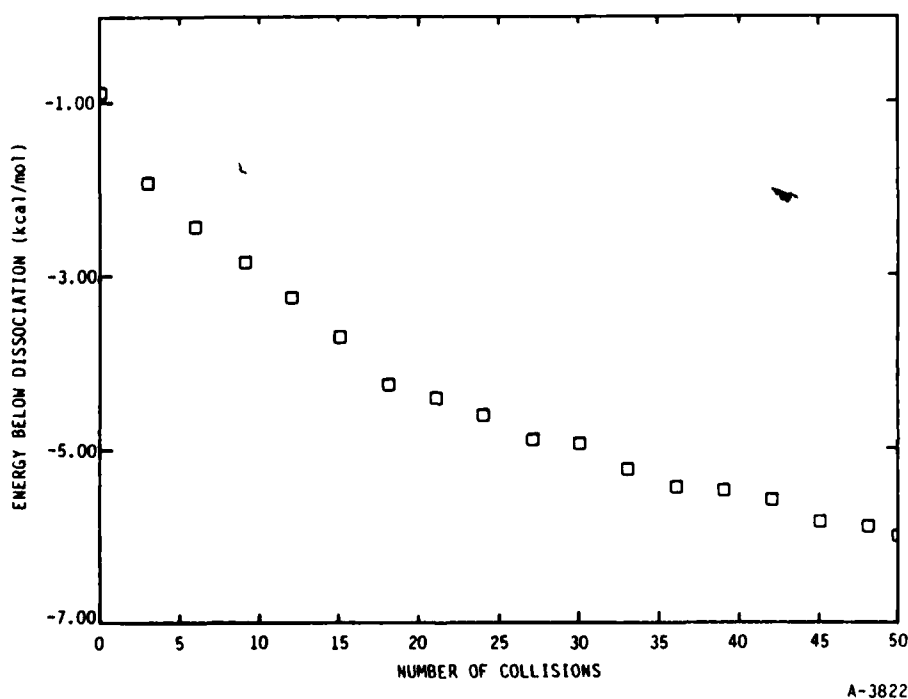
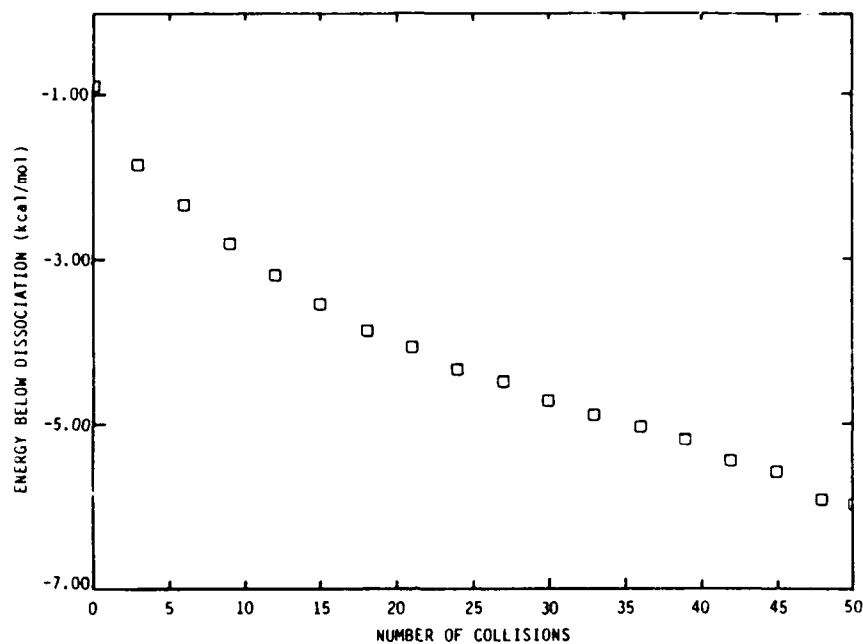
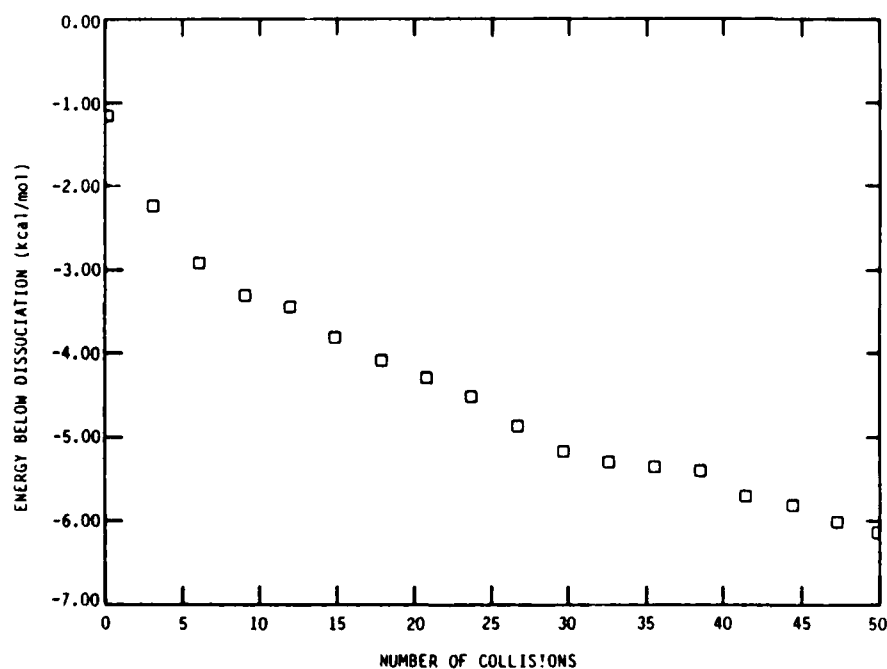


Figure 5. Average Energy of Ozone Molecules as a Function of Number of Sequential Collisions with Argon Atom Bath for (0.02,0.0) case. See Figure 4 for notation.



A-3823

Figure 6. Average Energy of Ozone Molecules as a Function of Number of Sequential Collisions with Argon Atom Bath for (0.03,0.0) case. See Figure 4 for notation.



A-3824

Figure 7. Average Energy of Ozone Molecules as a Function of Number of Sequential Collisions with Argon Atom Bath for (0.04,0.0) case. See Figure 4 for notation.

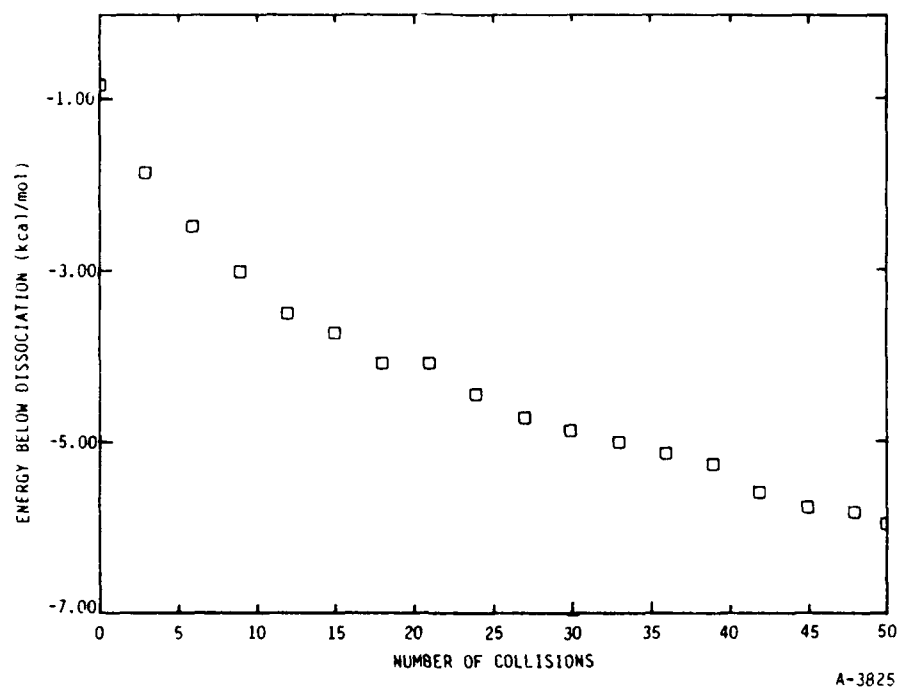


Figure 8. Average Energy of Ozone Molecules as a Function of Number of Sequential Collisions with Argon Atom Bath for (0.02,0.01) case. See Figure 4 for notation.

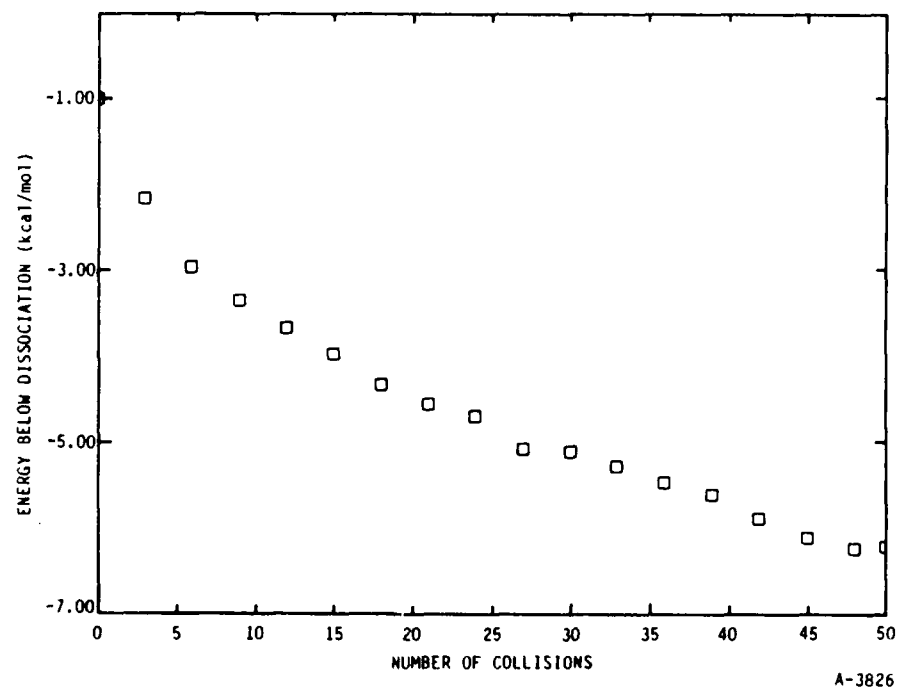


Figure 9. Average Energy of Ozone Molecules as a Function of Number of Sequential Collisions with Argon Atom Bath for (0.02,0.02) case. See Figure 4 for notation.

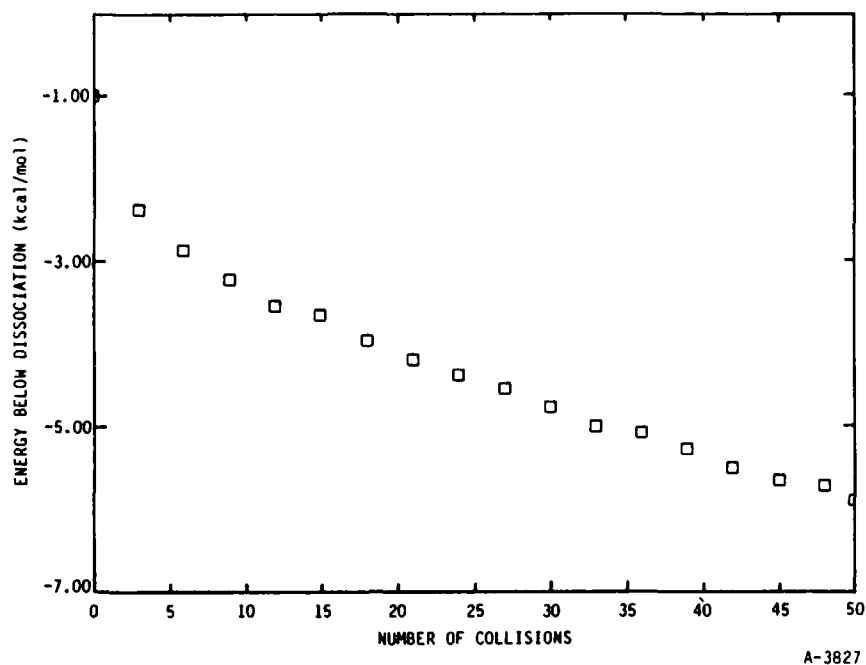


Figure 10. Average Energy of Ozone Molecules as a Function of Number of Sequential Collisions with Argon Atom Bath for (0.03,0.01) case. See Figure 4 for notation.

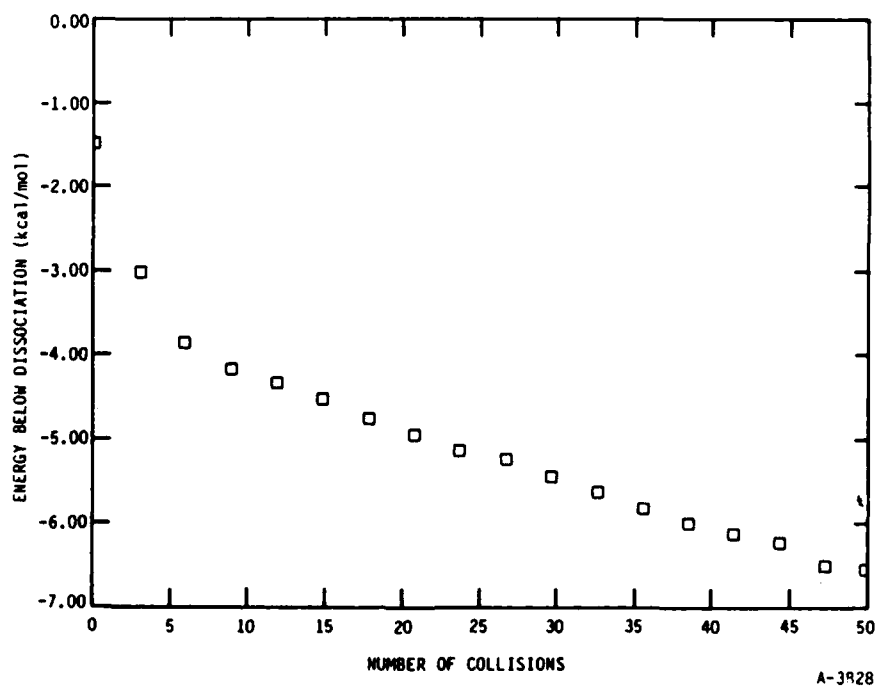
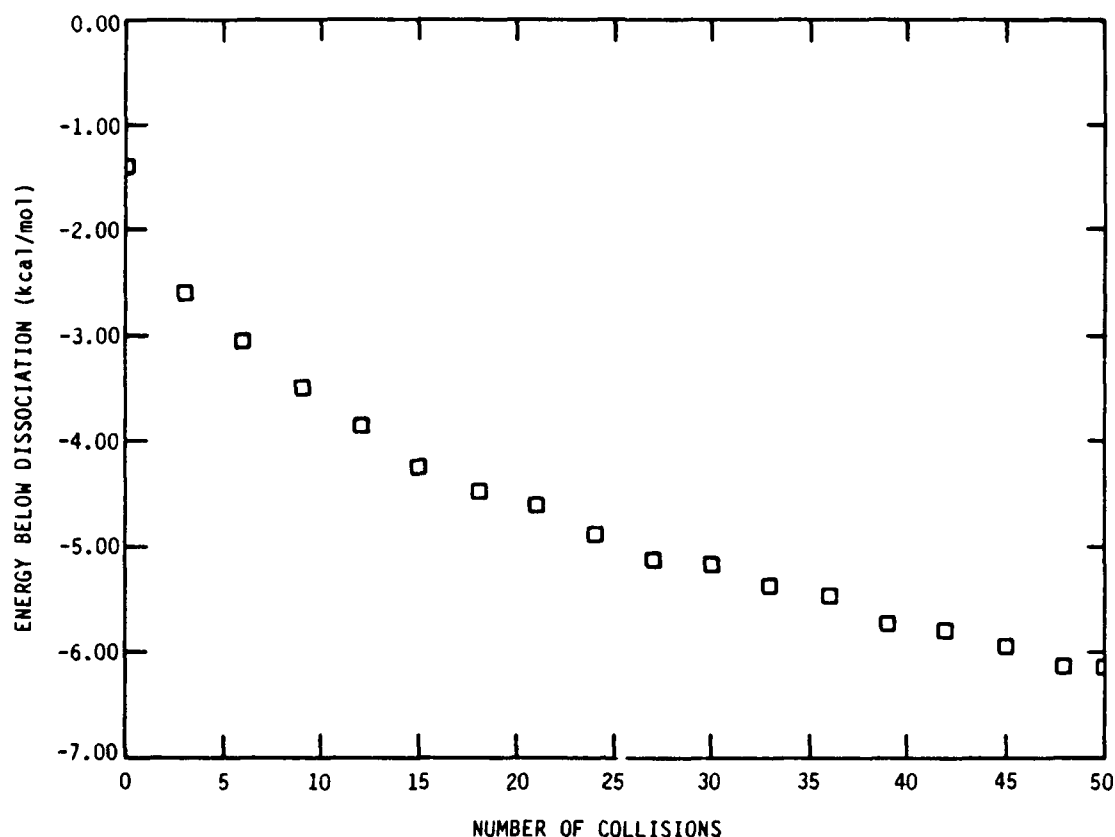


Figure 11. Average Energy of Ozone Molecules as a Function of Number of Sequential Collisions with Argon Atom Bath for (0.04,0.01) case. See Figure 4 for notation.



A-3829

Figure 12. Average Energy of Ozone Molecules as a Function of Number of Sequential Collisions with Argon Atom Bath for (0.04,0.02) case. See Figure 4 for notation.

molecule after fifty collisions. Redissociation of newly formed molecules occurs only at early times. Very little redissociation occurs beyond the twentieth sequential collision. The duration of redissociation processes is a function of the argon thermal bath energy. Hence it is not possible to extend this conclusion to different temperature baths.

The energy relaxation appears to show two regimes: 1) an early time regime during which redissociation occurs and the energy relaxation is faster and 2) a long time regime with slower energy relaxation. The slightly faster energy relaxation of the early time regime may be attributed to redissociation. Redissociation selectively removes higher energy molecules from the ensemble and thereby increases the apparent rate of relaxation. This sort of behavior has been observed earlier for the relaxation of recombined bromine molecules in an argon thermal bath.³

The overall ozone internal energy relaxation is fairly slow. The average initial ensemble internal energies are in each case between 0.5 and 1.5 kcal/mol below the dissociation limit, i.e., they have vibrational-rotational energies of about 24.5 to 25.5 kcal/mol. After 50 collisions the molecules are still very vibrationally-rotationally excited with energies of about 19-20 kcal/mol. This slow energy relaxation is consistent with earlier single collision and ensemble relaxation calculations.

Histograms of internal energy distributions are shown for each case in Figures 13 through 21. Each figure shows the initial internal distribution after collisional stabilization of the ozone complex and the internal energy distribution after fifty sequential collisions with the 200 K argon bath. The behavior in each case is similar so that we may discuss Figure 14 as characteristic of all the cases.

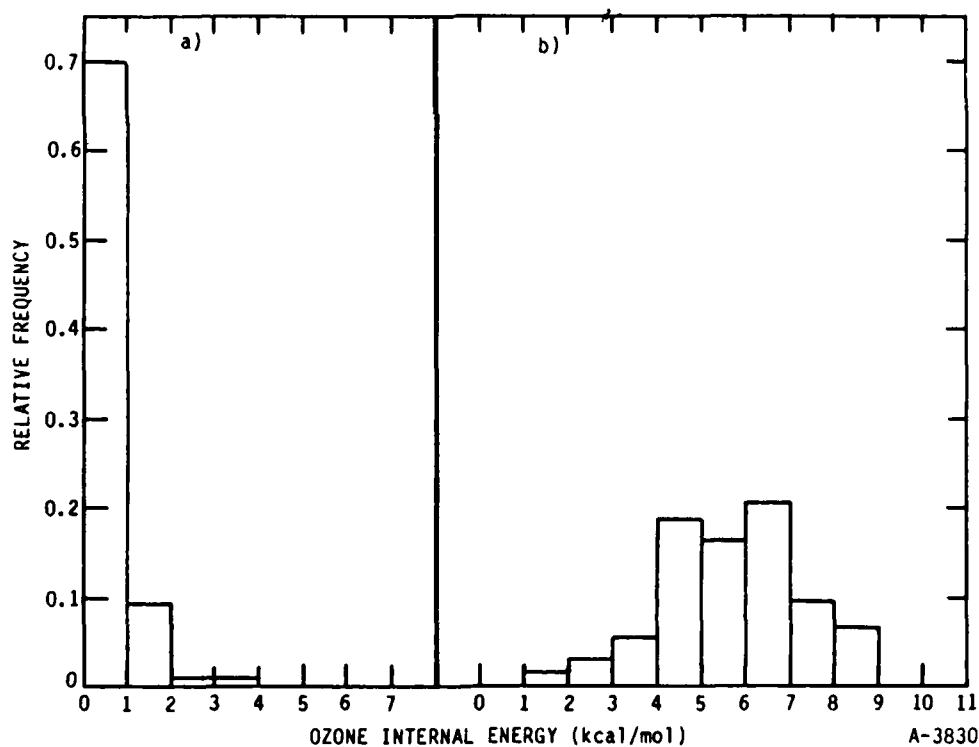


Figure 13. Distribution of Recombined Ozone Total Internal Energies: a) Nascent Distribution and b) After Fifty Sequential Collisions with Argon Atom Bath. Case shown is (0.01,0.0). See Figure 4 for notation.

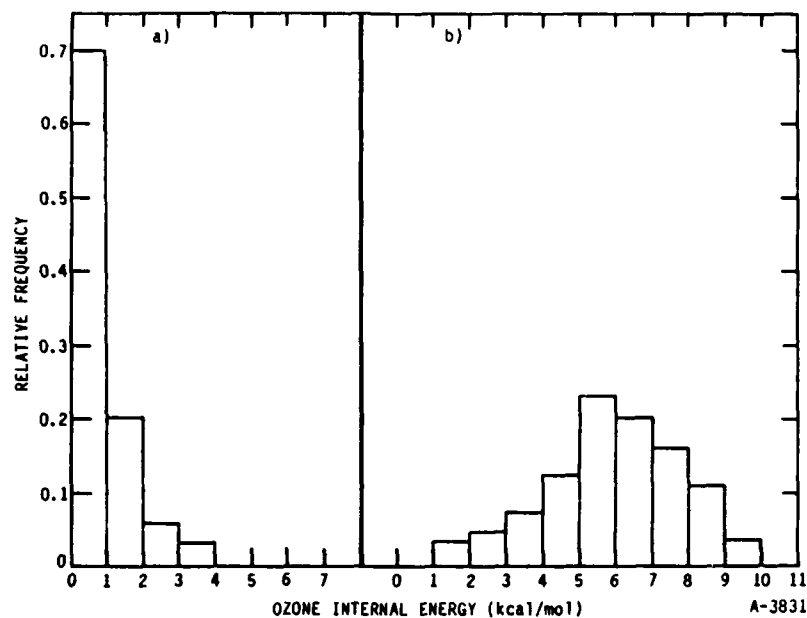


Figure 14. Distribution of Recombined Ozone Total Internal Energies: a) Nascent Distribution and b) After Fifty Sequential Collisions with Argon Atom Bath. Case shown is (0.02,0.0). See Figure 4 for notation.

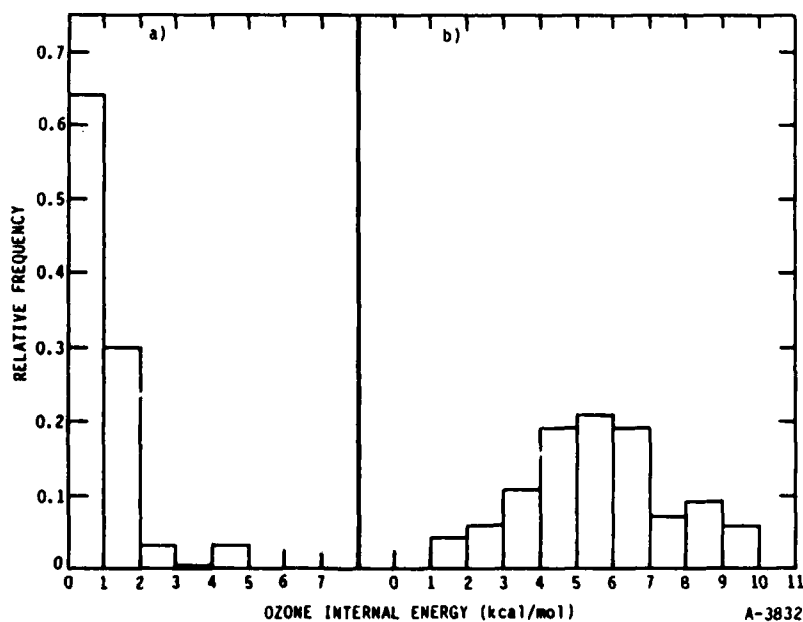


Figure 15. Distribution of Recombined Ozone Total Internal Energies: a) Nascent Distribution and b) After Fifty Sequential Collisions with Argon Atom Bath. Case shown is (0.03,0.0). See Figure 4 for notation.

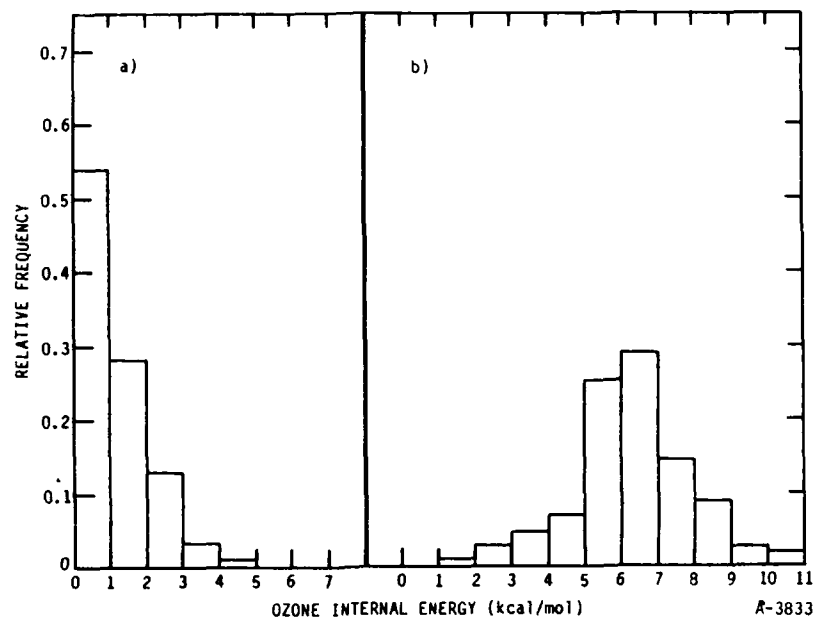


Figure 16. Distribution of Recombined Ozone Total Internal Energies: a) Nascent Distribution and b) After Fifty Sequential Collisions with Argon Atom Bath. Case shown is (0.04,0.0). See Figure 4 for notation.

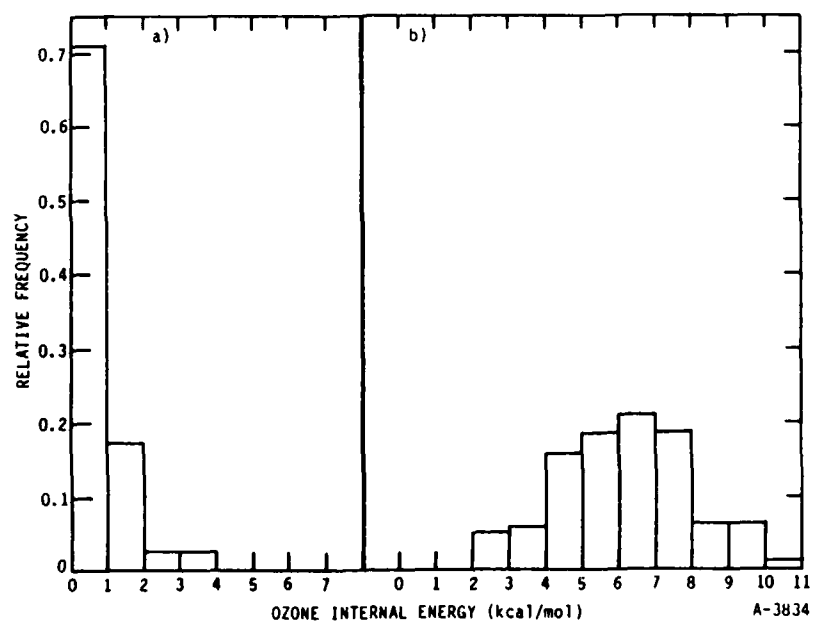


Figure 17. Distribution of Recombined Ozone Total Internal Energies: a) Nascent Distribution and b) After Fifty Sequential Collisions with Argon Atom Bath. Case shown is (0.02,0.01). See Figure 4 for notation.

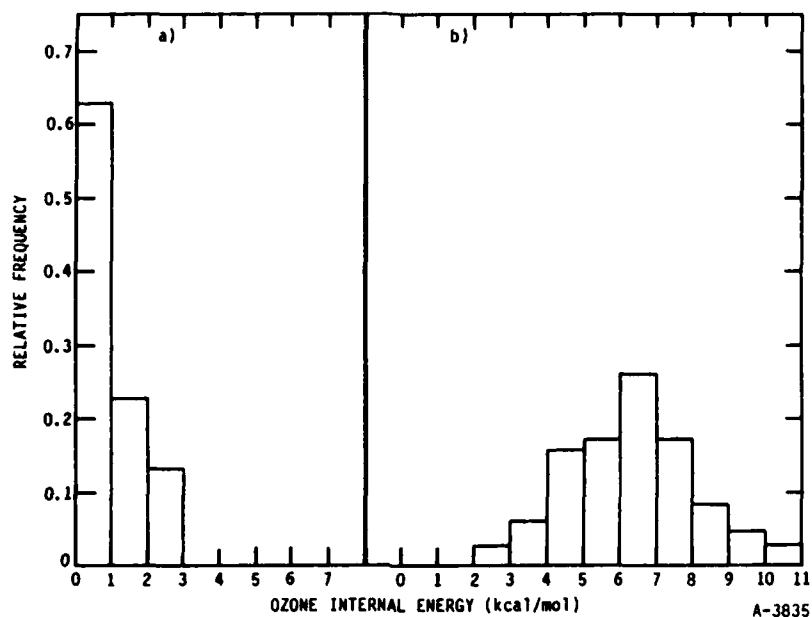


Figure 18. Distribution of Recombined Ozone Total Internal Energies: a) Nascent Distribution and b) After Fifty Sequential Collisions with Argon Atom Bath. Case shown is (0.02,0.02). See Figure 4 for notation.

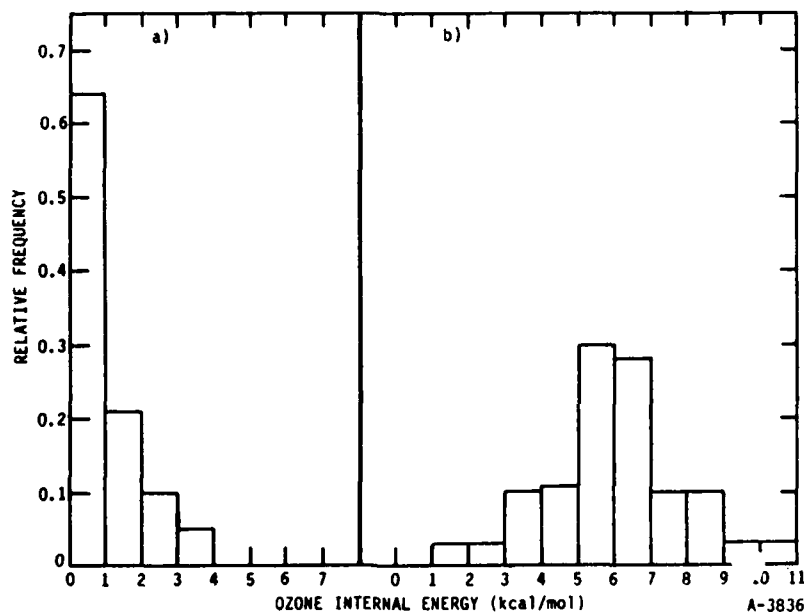


Figure 19. Distribution of Recombined Ozone Total Internal Energies: a) Nascent Distribution and b) After Fifty Sequential Collisions with Argon Atom Bath. Case shown is (0.03,0.01). See Figure 4 for notation.

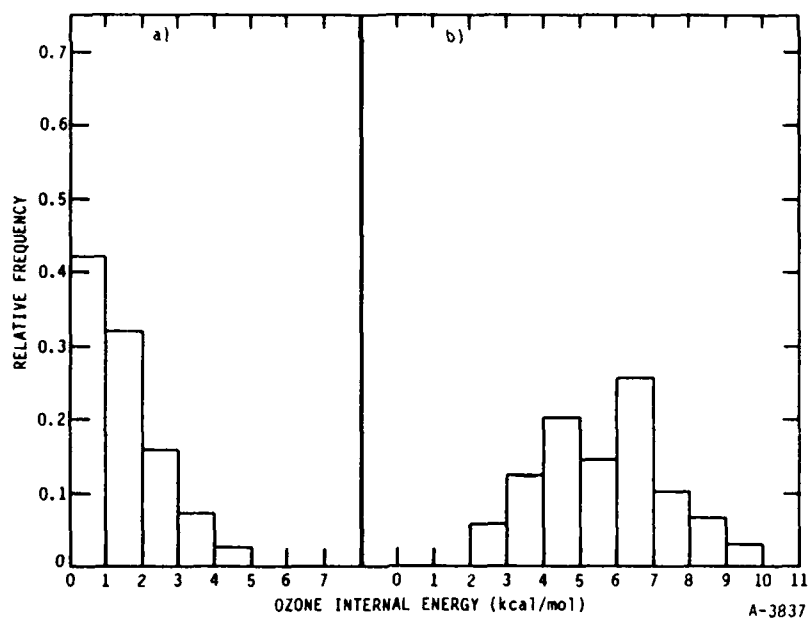


Figure 20. Distribution of Recombined Ozone Total Internal Energies: a) Nascent Distribution and b) After Fifty Sequential Collisions with Argon Atom Bath. Case shown is (0.04,0.01). See Figure 4 for notation.

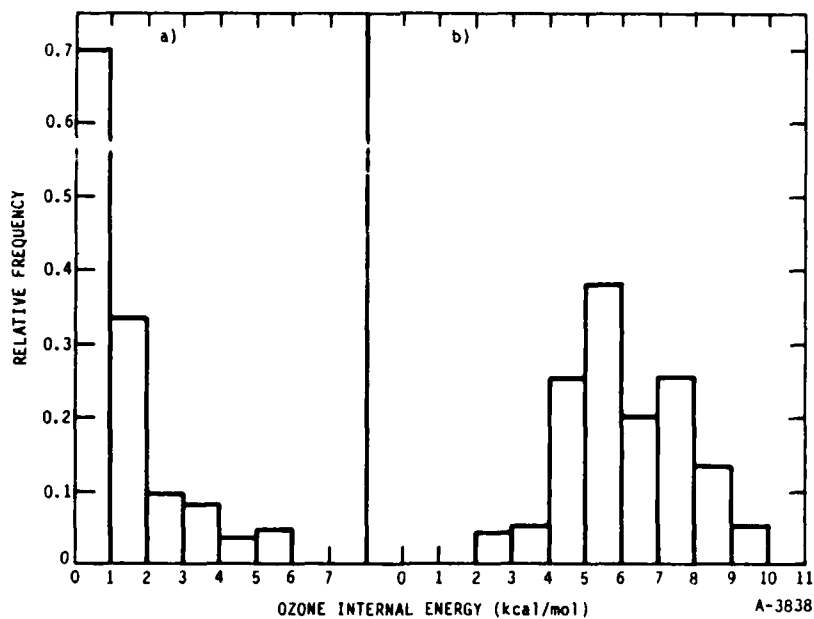


Figure 21. Distribution of Recombined Ozone Total Internal Energies: a) Nascent Distribution and b) After Fifty Sequential Collisions with Argon Atom Bath. Case shown is (0.04,0.02). See Figure 4 for notation.

Most of the newly recombined ozone molecules are within 1 kcal/mol of the dissociation limit. The lowest energy molecules are less than 4 kcal/mol below the dissociation limit. Over 90 percent of the nascent distribution lies within 2 kcal/mol of the dissociation. The narrowness of the nascent distribution is most likely a function of the bath temperature since the magnitude of collisional energy transfer depends on the relative translational energy. It is anticipated that at higher temperatures than 200 K a broader nascent distribution would be found.

After fifty sequential collisions the ensemble internal distribution has shifted to lower energies and broadened compared to the nascent distribution. The shift is readily seen by noting that very few molecules remain in the range of 0 to 4 kcal/mol below the dissociation limit (Figure 14b). This is of course due to energy transfer from the molecules to the thermal bath and redissociation of molecules close to the dissociation limit. The distribution is reasonably symmetric about the peak range of 5 to 7 kcal/mol below dissociation and has a width of about 9 kcal/mol. The lowest energy molecules are 9 to 10 kcal/mol below dissociation.

The above behavior is characteristic of all the cases studied. The initial distribution is fairly narrow, 3 to 4 kcal/mol, with most molecules within 1 kcal/mol of dissociation. After fifty collisions the high energy portion of the distribution is depleted with very few molecules in the 0 to 3 or 4 kcal/mol energy range. The distributions are broadened with widths approximately 8 to 10 kcal/mol of the dissociation limit. It should be noted that within approximately fifteen to twenty sequential collisions relaxation of each ensemble is very similar due to loss of initial state memory.

In either the upper atmosphere or the COCHISE experiments newly recombined ozone molecules will undergo collisions. Estimates based on the characteristics of the nozzle expansion in the COCHISE apparatus indicate perhaps as many as several thousand collisions before the recombined ozone molecules enter the collision free zone. The present calculations may be extrapolated to this longer time regime. The procedure indicates that the recombined

molecules will have relaxed to about half way down the molecular well after several hundred collisions. Since these collisions occur in a time interval short compared with the vibrational radiative lifetime, it is anticipated that radiation from the upper levels near the dissociation limit will be collisionally quenched and therefore not observed. This prediction is consistent with the experimental observation that radiation is seen from vibrational levels only up to $v = 5$.

REFERENCES

1. Bunker, D.L., J. Chem. Phys. 32, 1001 (1960).
2. Blint, R.J., J. Chem. Phys. 73, 765 (1980).
3. Gelb, A., Kapral, R. and Burns, G., J. Chem. Phys. 56, 4631 (1972).
4. Widom, J. Chem. Phys. 55, 44 (1971).
5. Varandas, A.J.C. and Murrell, J.N., Chem. Phys. Lett. 88, 1 (1982).
6. Stace, A.J. and Murrell, J.N., J. Chem. Phys. 68, 3078 (1978).
7. Gelb, A., J. Phys. Chem. 89, 4189 (1985).

APPENDIX T

(PSI-032/TR-607 reproduced in its entirety)

MULTICOLLISIONAL TRAJECTORY STUDIES
OF VIBRATIONALLY/ROTATIONALLY EXCITED
OZONE MOLECULES BY ARGON ATOMS

Quarterly Status Report No. 8

For the Period

1 January 1987 to 31 March 1987

Under Air Force Contract No. F19628-85-C-0032

Prepared by:

A. Gelb and W.T. Rawlins
Physical Sciences Inc.
Research Park, P.O. Box 3100
Andover, MA 01810

Sponsored by:

Air Force Geophysics Laboratory
Air Force Systems Command
U.S. Air Force
Hanscom Air Force Base, Massachusetts 01731

August 1987

TABLE OF CONTENTS

	<u>Page</u>
INTRODUCTION	1
Calculations	1
Potential Energy Surface	3
Results and Discussion	3
REFERENCES	13
COST DATA	14

INTRODUCTION

In this report we describe the results of a multicollisional study of the relaxation of vibrationally-rotationally excited ozone molecules in a bath of argon atoms. The primary objective of the study is to systematically study the effects of the ozone initial state and the thermal bath on the relaxation of highly excited ozone molecules.

The relaxation of highly excited ozone molecules is of considerable significance in the study of the upper atmosphere. Ozone molecules are thought to be formed by the following three-body recombination reaction:



where the initially recombined ozone molecule, $\text{O}_3(\nu, J)$, is formed in vibrational-rotational states near the dissociation limit. The newly formed ozone molecule can undergo a number of processes including: 1) collisional dissociation by energy transfer into the molecule, 2) collisional relaxation to a lower internal energy state, and 3) radiative emission of an infrared photon. Additional processes might include reactions with various atmospheric species. These processes are not included in this study.

The relative rates of relaxation/dissociation versus the emission rate will determine the mode of relaxation of highly excited ozone. Considerable interest exists in understanding the ozone radiative contribution and collisional rate of relaxation. A theoretical understanding of these processes is also necessary for proper interpretation of the ozone recombination and emission experiments conducted at AFGL.

Calculations

All calculations reported here were performed using the multicollisional classical trajectory technique.¹ The computation of classical trajectories has become standard and is well reviewed by Bunker² and Porter and Raff.³ The

multicollisional classical trajectory procedure is discussed in Ref. 1. We mention only calculational procedures specific to the present calculations.

Calculations were performed to systematically investigate the effect of thermal bath temperature on the relaxation/dissociation of highly excited ozone. Calculations were performed for initial ensembles of ozone molecules excited 25 kcal/mol above the well minimum (above 1.5 kcal/mol below dissociation) with zero molecular angular momentum at argon atom bath temperatures of 200, 300, 400, 500, 750, and 1000 K. Initial ensemble sizes varied between 150 (at 200, 300, and 400 K bath temperatures) and 200 (at 500, 750, and 1000 K bath temperatures). In the 200 K bath temperature case, the evolution of the ensemble was followed for a sequence of 50 collisions. In all other cases, the ensemble was subjected to a sequence of 100 bath collisions.

Several calculations were performed at an argon atom bath temperature of 300 K to investigate the effect of initial triatom rotational energy on relaxation/dissociation and the effect of total triatom internal energy.

Several other cases were also considered: 1) ozone initially excited 26 kcal/mol above the well minimum and zero rotational energy, 2) 26 kcal/mol above the well minimum with an initial triatom rotational energy of 2 kcal/mol, 3) 27 kcal/mol internal energy with zero rotational energy, and 4) 27 kcal/mol internal energy with 1 kcal/mol rotational energy. Note that the total initial internal energy of 27 kcal/mol is above the dissociation limit. On the employed potential surface, the dissociation limit of ozone to an oxygen molecule and atom is 26.3 kcal/mol. Sequences of 50 successive collisions were computed for cases 2-4 and 100 for case 1.

Calculations were performed for collisional dissociation of ozone molecules dissociated by energy transfer from the argon atom thermal bath. The criterion for dissociation was based on the distance between any pair of oxygen atoms exceeding a cutoff distance. This cutoff distance was taken as 3.0Å. Hence in several cases molecules with greater than the dissociation energy were retained for further collisions. In fact, for the higher initial energy

ensembles, the average ensemble energy exceeded the dissociation limit. The retention of these unbound or quasibound molecules amounts to assuming that their lifetimes are very long and that they will not dissociate before undergoing further collisions. In other computations on ozone complexes very long-lived unbound complexes have been observed and some test calculations indicated this behavior often occurs for the complexes considered here. This assumption however implies that the dissociation probabilities are lower bounds. More than 150,000 Ar-O₃ trajectories were computed in this effort.

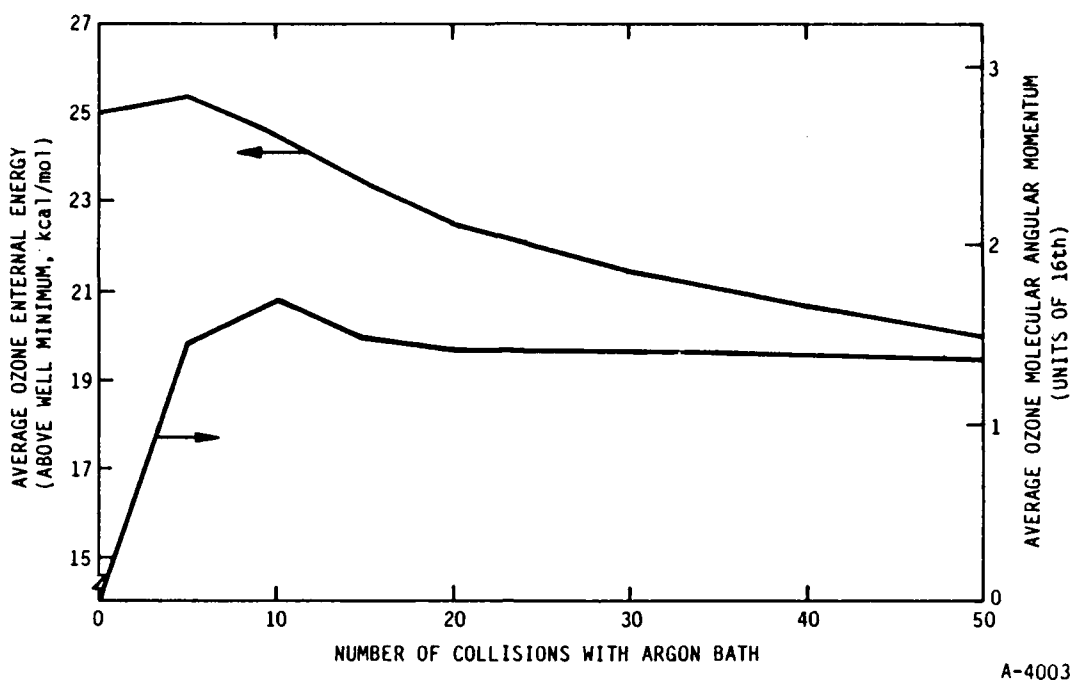
Potential Energy Surface

All calculations were performed using the Murrell-Sorbie-Varandas⁴ potential energy surface for ozone and pairwise additive Lennard-Jones 6-12 potentials between the argon atom and each oxygen atom. The details of the potential energy surface are given elsewhere.⁵

Results and Discussion

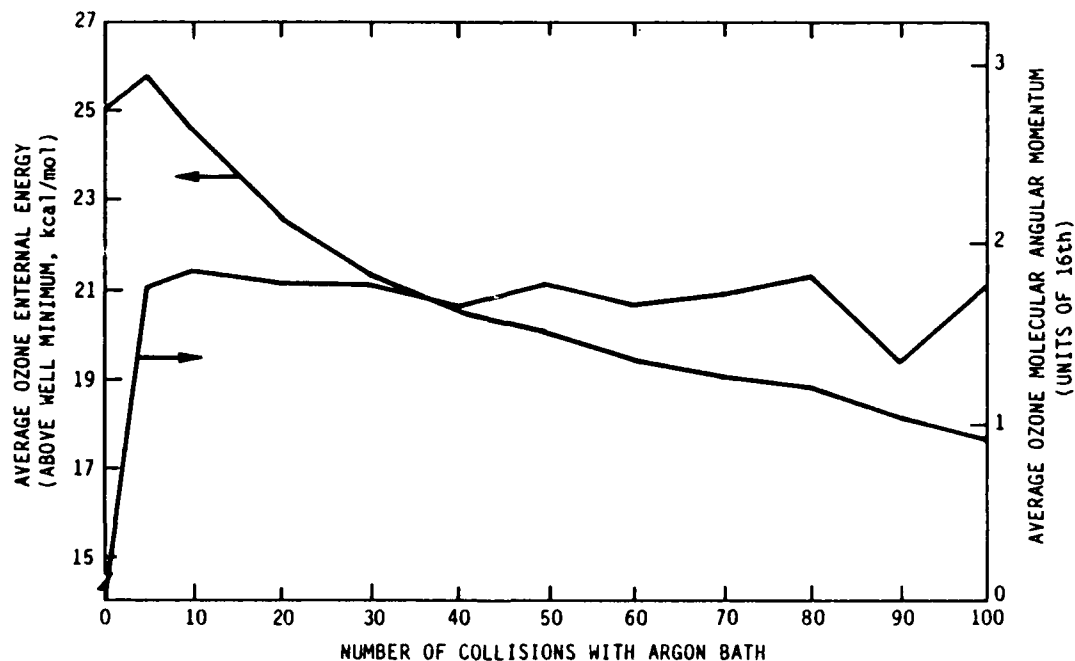
The behavior of total ozone internal molecular energy and angular momentum as a function of number of collisions with the argon atom thermal bath is shown in Figures 1 to 10 for all the cases considered. We first consider the results shown in Figures 1 through 6. These results are for ensembles of ozone molecules vibrationally excited 25 kcal/mol above the ozone well minimum with zero initial molecular angular momentum. Each figure corresponds to a different argon atom bath temperature. The behavior for argon atom bath temperatures of 200, 300, 400, 500, 750, and 1000 K are shown in Figures 1 through 6, respectively. The behavior shown in Figure 2 for a 300 K argon atom bath is qualitatively similar to the others. Therefore, we discuss it in more detail as representative of all the cases shown.

Initially the ozone molecular angular momentum in the ensemble is set equal to zero. This corresponds to non-rotating molecules. Collisions with the bath rapidly transfer angular momentum into the molecule. This process occurs within approximately 5 to 10 molecule-bath collisions. After the



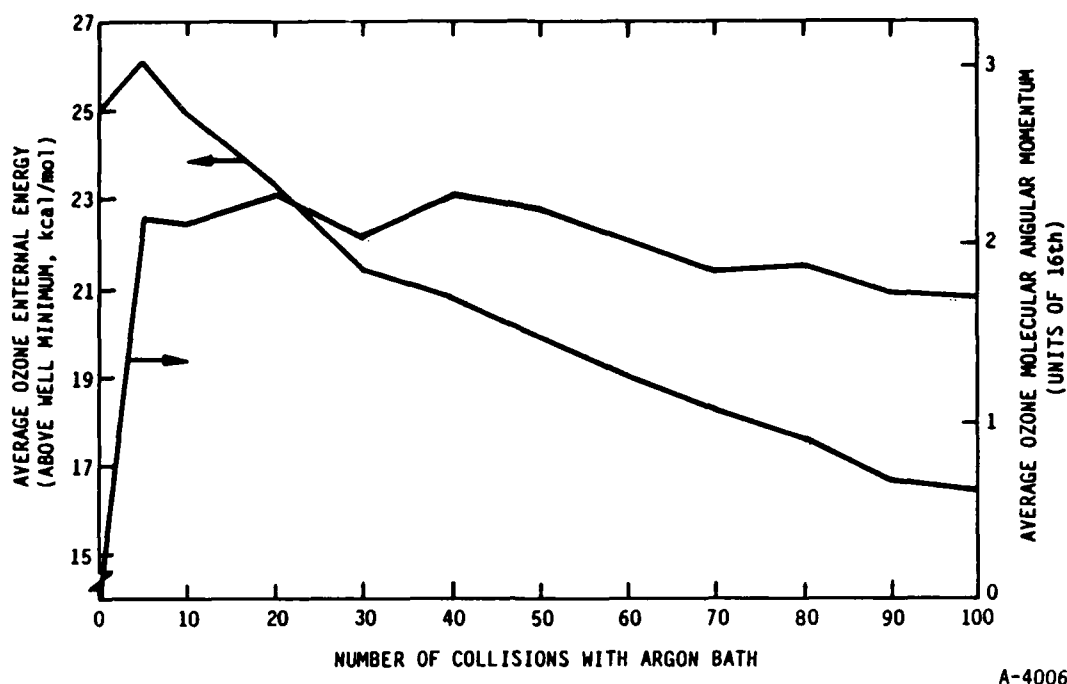
A-4003

Figure 1. Variation of Average Ozone Internal Energy and Molecular Angular Momentum with Number of Sequential Collisions with Argon Atom Bath. Initial total ozone internal energy equals 25 kcal/mol; initial ozone angular momentum equals zero; bath temperature equals 200 K.



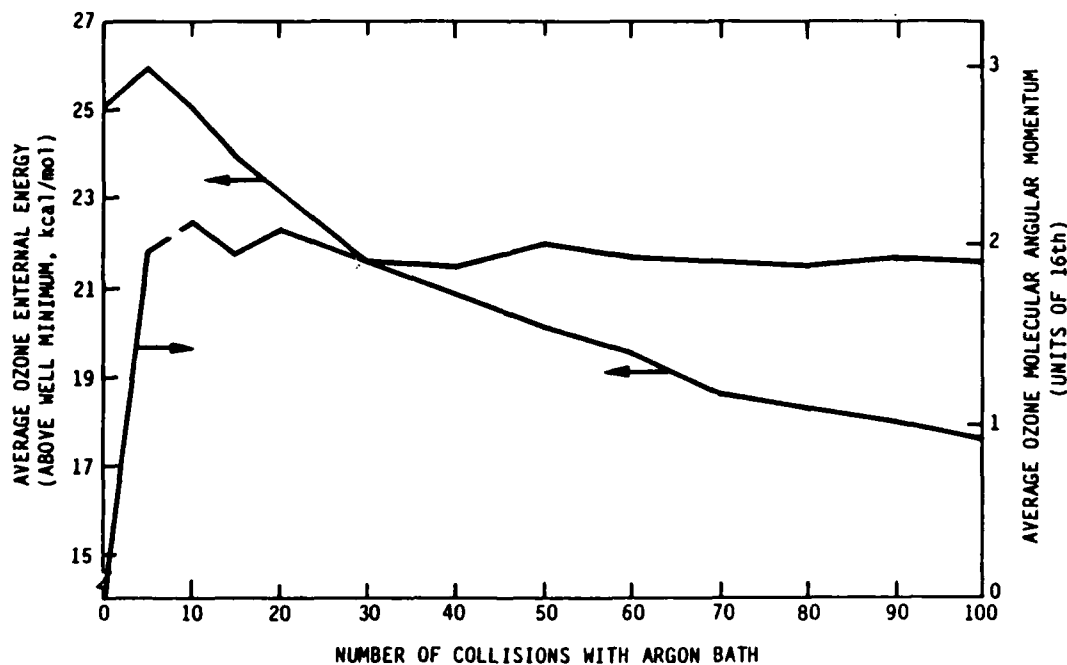
A-4004

Figure 2. Variation of Average Ozone Internal Energy and Molecular Angular Momentum with Number of Sequential Collisions with Argon Atom Bath. Initial total ozone internal energy equals 25 kcal/mol; initial ozone angular momentum equals zero; bath temperature equals 300 K.



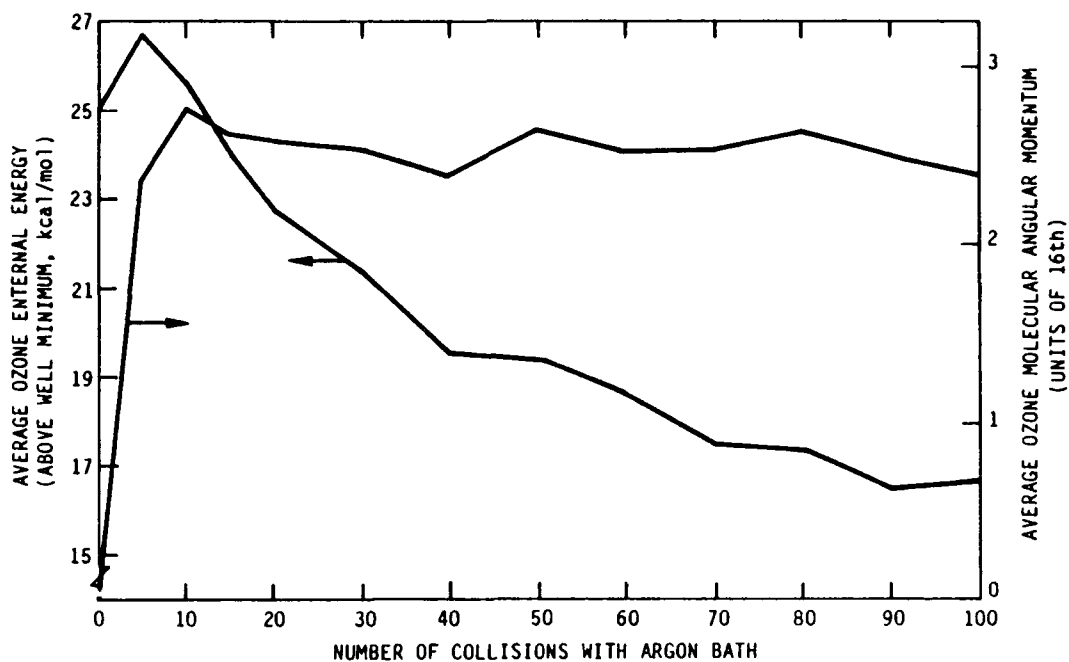
A-4006

Figure 3. Variation of Average Ozone Internal Energy and Molecular Angular Momentum with Number of Sequential Collisions with Argon Atom Bath. Initial total ozone internal energy equals 25 kcal/mol; initial ozone angular momentum equals zero; bath temperature equals 400 K.



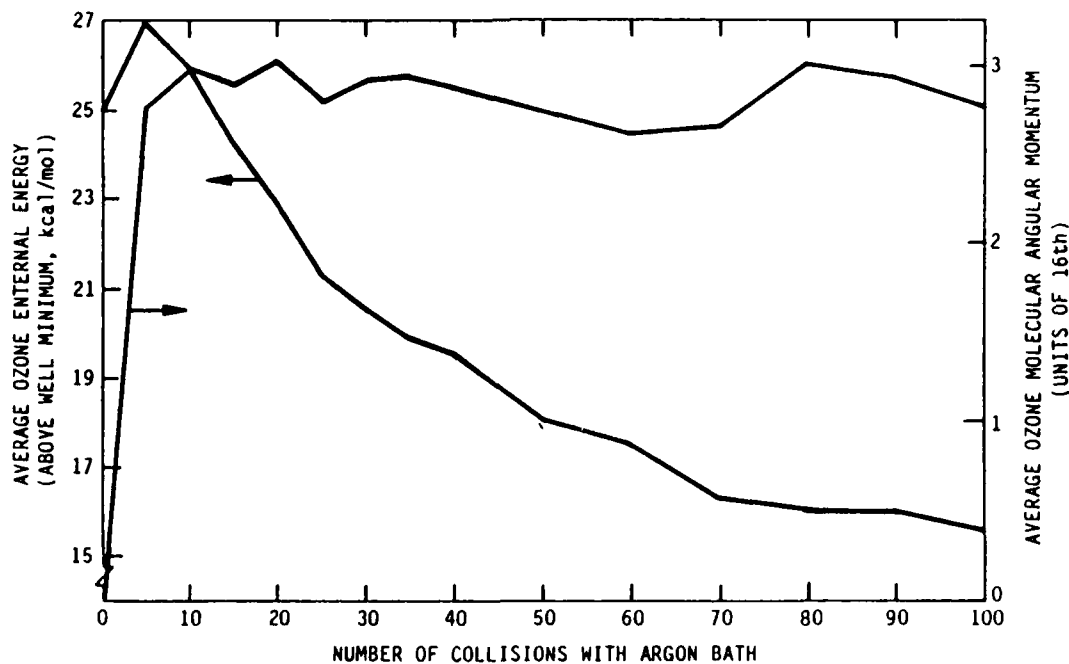
A-4005

Figure 4. Variation of Average Ozone Internal Energy and Molecular Angular Momentum with Number of Sequential Collisions with Argon Atom Bath. Initial total ozone internal energy equals 25 kcal/mol; initial ozone angular momentum equals zero; bath temperature equals 500 K.



A-4007

Figure 5. Variation of Average Ozone Internal Energy and Molecular Angular Momentum with Number of Sequential Collisions with Argon Atom Bath. Initial total ozone internal energy equals 25 kcal/mol; initial ozone angular momentum equals zero; bath temperature equals 750 K.



A-4008

Figure 6. Variation of Average Ozone Internal Energy and Molecular Angular Momentum with Number of Sequential Collisions with Argon Atom Bath. Initial total ozone internal energy equals 25 kcal/mol; initial ozone angular momentum equals zero; bath temperature equals 1000 K.

initial transient period, the molecular angular momentum varies only slowly. (Fluctuations in angular momentum or energy are most probably the result of using finite size ensembles rather than physical processes.) As noted in earlier work on single collision Ar-O₃ dynamics, rotational energy is transferred readily to relative translational energy.⁵ Thus the value of the molecular angular momentum reflects the argon atom bath temperature. The rapidness of rotational-translational exchange is verified by the few, 5 to 10, collisions required to bring the ozone ensemble angular momentum to its near steady state value.

The behavior of the ozone total internal energy is slightly more complicated. Two regimes are evident. During the first few collisions, i.e., 1 to 10, energy is pumped into the molecule as the molecular angular momentum increases. This occurs despite the fact that the molecules are very highly excited. Similar behavior has been seen earlier.⁵ After the initial transient, the molecular energy relaxes monotonically.

As noted earlier the ozone energy relaxation is qualitatively similar over the temperature range considered. The two most significant variations with temperature are the increase in energy of the ozone during the initial transient, and the steady state value of the ozone molecular angular momentum.

The amount of energy pumped into the molecule as the molecular angular momentum is built up to its steady state value increases monotonically with the argon thermal bath temperature. At a bath temperature of 200 K, the increase in ensemble average energy is about 0.7 kcal/mol. At a bath temperature of 1000 K, this value increases to 1.9 kcal/mol. This variation will become significant when we consider dissociation. In the 1000 K bath case, the average ozone molecular energy reaches 26.9 kcal/mol. This value is above the dissociation limit of ozone on the employed potential surface (26.3 kcal/mol).

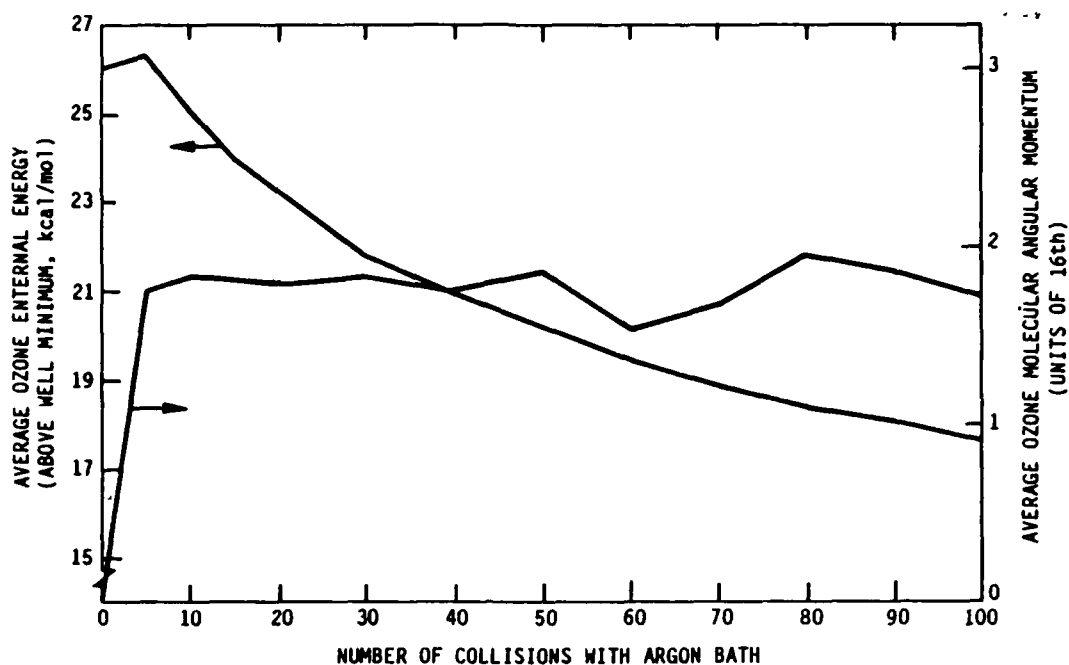
Closely related to transient energy increase is the value of the steady state molecular angular momentum. Since molecular rotational energy and

relative translational energy are exchanged relatively rapidly, the molecular angular momentum tends to reflect the thermal bath temperature. The steady state value at 200 K is about 20 while at 1000 K its value is about 45 . Since rotational energy scales as the square of angular momentum, these values scale as the increase in relative translational energy of the argon atom thermal bath as the temperature is increased from 200 to 1000 K.

The rate of molecular internal energy relaxation is seen from Figures 1 through 6 to increase slightly as the bath temperature is increased. The interpretation of this variation is complicated by the fact that the ensemble is simultaneously undergoing relaxation and dissociation. Dissociation is biased towards higher energy molecules. Therefore, without further study, we may not infer a faster energy-transfer relaxation rate at higher temperatures. In fact the rate probably slows down. The variation shown in Figures 1 through 6 show the rate of energy relaxation of molecules undergoing energy transfer and dissociation.

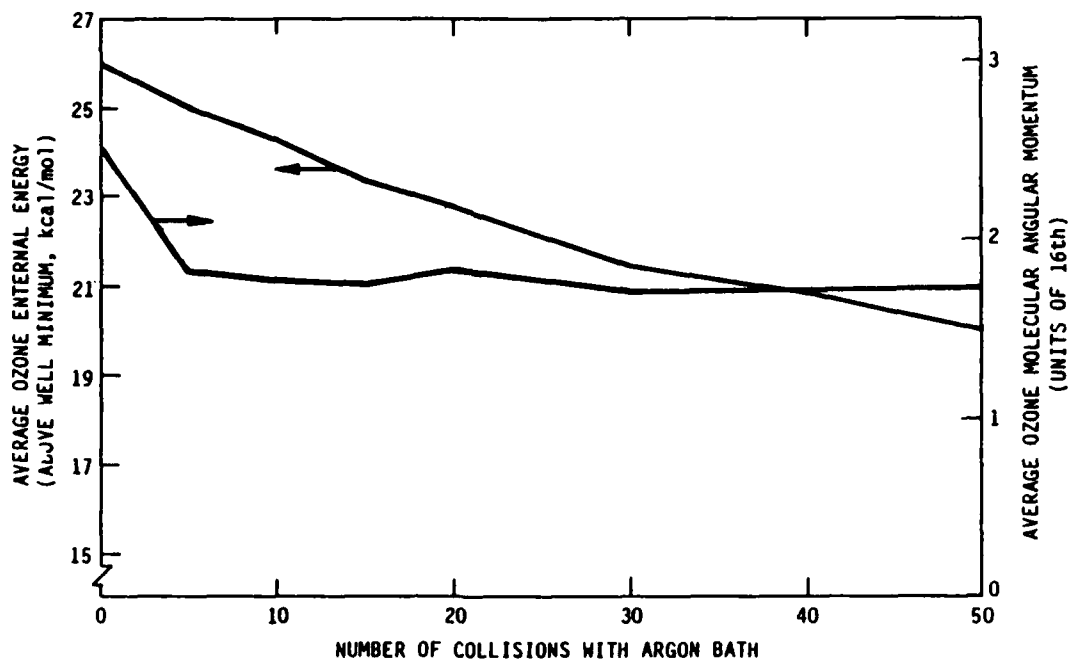
We now discuss the results shown in Figures 7 through 10. In each of these cases the argon atom bath is 300 K. The long-term (past ten collisions with the bath) variation of the ozone molecular angular momentum is controlled by the atom bath temperature. This is due to relatively facile transfer of rotational and relative translational energy. This was mentioned earlier for cases in Figures 1 through 6. Comparisons of Figures 7 through 10 with Figure 2 show the same long-term behavior of the molecular angular momentum at 300 K bath temperature.

Figures 7 and 9 show the internal relaxation of initially non-rotating ozone molecules. For molecules excited 26 kcal/mol above the well minimum (Figure 7) the behavior is virtually identical to the earlier case of molecules excited 25 kcal/mol in a 300 K atom bath (Figure 2). For molecules excited 27 kcal/mol above the well minimum there is some variation in relaxation behavior. As mentioned earlier, these molecules are above the ozone dissociation limit. Therefore, unless stabilized by collisions with the argon bath,



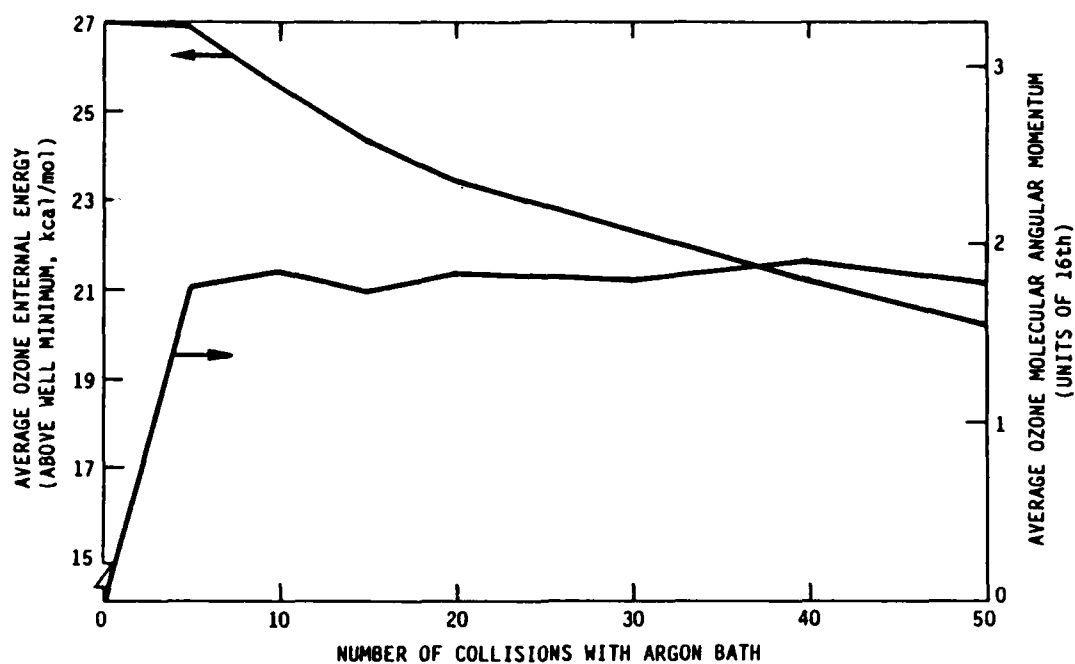
A-4009

Figure 7. Variation of Average Ozone Internal Energy and Molecular Angular Momentum with Number of Sequential Collisions with Argon Atom Bath. Bath temperature equals 300 K; initial ozone rotational energy equals zero; initial ozone internal energy equals 26 kcal/mol.



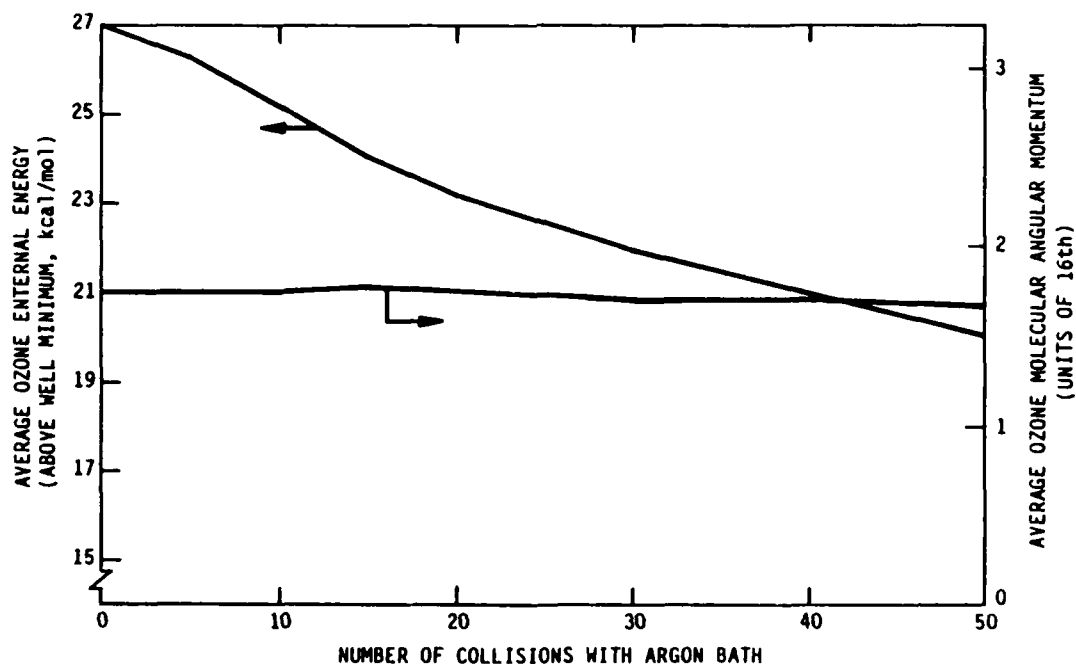
A-4010

Figure 8. Variation of Average Ozone Internal Energy and Molecular Angular Momentum with Number of Sequential Collisions with Argon Atom Bath. Bath temperature equals 300 K; initial ozone rotational energy equals 2 kcal/mol; initial ozone internal energy equals 26 kcal/mol.



A-4011

Figure 9. Variation of Average Ozone Internal Energy and Molecular Angular Momentum with Number of Sequential Collisions with Argon Atom Bath. Bath temperature equals 300 K; initial ozone rotational energy equals zero; initial ozone internal energy equals 27 kcal/mol.



A-4012

Figure 10. Variation of Average Ozone Internal Energy and Molecular Angular Momentum with Number of Sequential Collisions with Argon Atom Bath. Bath temperature equals 300 K; initial ozone rotational energy equals 1 kcal/mol; initial ozone internal energy equals 27 kcal/mol

they will dissociate. The short-time increase in internal energy due to buildup of rotational energy is absent in this case (Figure 9). This may simply be attributed to the fact that molecules that do not lose energy leave the ensemble by dissociation. In the earlier cases, Figures 1 through 6, molecules can acquire total internal energies above the dissociation limit by rotational energy transfer from the bath. In most of those cases, however, the molecular vibrational energy is insufficient for dissociation. Dissociation occurs most effectively through vibrational motion. Thus molecules with energies above the dissociation limit but without sufficient vibrational energy alone for dissociation may survive for long periods. This occurs at the higher bath temperatures 25 kcal/mol initial excitation and for 26 kcal/mol initial excitation where the ensemble average interval energy goes above the dissociation limit. On the other hand when the initial vibrational energy exceeds the dissociation limit (Figure 9) the lifetime of the unbound molecules is too short and many molecules that gain energy are removed. Thus the average energy of the ensemble does not show the characteristic increase in energy at short times.

The effect of initial molecular rotation on the relaxation is shown by comparison of Figure 7 with Figure 8 and Figure 9 with Figure 10. The presence of initial rotational energy reduces or eliminates the initial short time increase in the ensemble internal energy. This is clearly shown in Figure 8 and 10. The memory of initial rotational energy disappears after about ten collisions. Energy relaxation after that point is the same for all cases. We now discuss dissociation in these relaxing ensembles.

The computed probability of dissociation for each ensemble is presented in Table 1. The listed values are the asymptotic dissociation probabilities (i.e., the fraction of the initial ensemble that is removed by dissociation after a large number of sequential collisions. Several trends are immediately evident.

Dissociation probabilities increase monotonically as the thermal bath temperature is increased. For initially non-rotating molecules, the dissociation probability increases as the ozone internal energy is increased. The

Table 1. Computed Dissociation Probabilities

Ensemble Energy (kcal/mol)	200	Bath Temperature (K)			750	1000
		300	400	500		
$E_T = 25$ $E_R = 0.0$	0.05	0.23	0.29	0.34	0.55	0.61
$E_T = 26$ $E_R = 0.0$		0.37				
$E_T = 26$ $E_R = 2.0$		0.13				
$E_T = 27$ $E_R = 0.0$		0.76				
$E_T = 27$ $E_R = 1.0$		0.43				

effect of rotation is to decrease the dissociation probability, i.e., for molecules of the same total internal energy, vibration is substantially more efficient in inducing dissociation than rotation.

The primary result of this effort is to demonstrate the relative effects of rotational and vibrational energy in collisional dissociation of excited ozone. Vibrational energy is clearly more effective in enhancing dissociation than rotational energy.

For molecules excited within 1-2 kcal/mol of the dissociation limit, dissociation probabilities can be quite large. This can have a substantial effect on computational models for ozone formation in the upper atmosphere.

REFERENCES

1. Gelb, A., Kapral, R., Burns, G., "Non-Equilibrium Effects in Atomic Recombination Reactions," J. Chem. Phys. 56, 4531 (1972).
2. Bunker, D., "Classical Trajectory Methods," Meth. Comp. Phys. 10, 287 (1972).
3. Porter, R.N. and Raff, C.M., "Classical Trajectory Methods in Molecular Collisions," in Dynamics of Molecular Collisions, Part B, Miller, W.H., Ed., Plenum, New York (1976).
4. Varandas, A.J.C. and Murrell, J.N., "Dynamics of the $^{18}\text{O} + ^{16}\text{O}_2(v=0)$ Exchange Reaction on a New Potential Energy Surface for Ground State Ozone," Chem. Phys. Lett. 88, 1 (1982).
5. Gelb, A., "Classical Trajectory Study of Energy Transfer Between Argon Atoms and Vibrationally-Rotationally Excited Ozone Molecules," J. Phys. Chem. 89, 4189 (1985) and unpublished work.

APPENDIX U

(PSI-032/TR-582 reproduced in its entirety)

RELAXATION OF VIBRATIONALLY
EXCITED OXYGEN MOLECULES BY
COLLISION WITH OXYGEN ATOMS

Quarterly Status Report No. 7

For the Period

1 October 1986 to 31 December 1986

Under Air Force Contract No. F19628-85-C-0032

Prepared by:

A. Gelb and W.T. Rawlins
Physical Sciences Inc.
Research Park, P.O. Box 3100
Andover, MA 01810

Sponsored by:

Air Force Geophysics Laboratory
Air Force Systems Command
U.S. Air Force
Hanscom Air Force Base, Massachusetts 01731

December 1986

TABLE OF CONTENTS

<u>Section</u>	<u>Page</u>
1. INTRODUCTION	1
2. POTENTIAL ENERGY SURFACE	2
3. CALCULATIONS	3
4. SINGLE COLLISION CALCULATIONS: RESULTS AND DISCUSSION	5
5. CALCULATIONS OF STATE-TO-STATE CROSS SECTIONS	16
6. MULTIPLE COLLISION CALCULATIONS	20
REFERENCES	39

LIST OF FIGURES

<u>Figure No.</u>		<u>Page</u>
1	Energy Transferred from O ₂ in an O ₂ -O Collision as a Function of Initial O ₂ Vibrational Energy	5
2	Energy Transferred from O ₂ in an O ₂ -O Collision as a Function of Initial O ₂ Rotational Energy	6
3	Energy Transferred from O ₂ in an O ₂ -O Collision as a Function of Initial O ₂ Rotational Energy for Several Values of Initial Diatom Relative Translational Energy, E _t , and Vibrational Energy, E _v	7
4	Energy Transferred from O ₂ in an O ₂ -O Collision as a Function of Initial O ₂ Rotational Energy with Total O ₂ Initial Interval Energy Equal to 21.50 kcal/mol	8
5	Distribution of O ₂ Internal Energy Transfers in a Collision with O	9
6	Distribution of O ₂ Internal Energy Transfers in a Collision with O	10
7	Relative Frequency of Energy Transfers in Reactive O ₂ -O Encounters	12
8	Relative Frequency of Energy Transfers in Non-reactive O ₂ -O Encounters	12
9	Oxygen Atom Exchange Probability as a Function of O ₂ Initial Vibrational Energy for Several Values of Relative Translational Energy, E _t	13
10	Oxygen Atom Exchange Probability as a Function of O ₂ Initial Rotational Energy for Several Values of Oxygen Vibrational, E _v , and Relative Translational Energy, E _t	13
11	Oxygen Atom Exchange Probability as a Function of O ₂ Initial Rotational Energy for a Fixed Initial O ₂ Internal Energy Equal to 21.50 kcal/mol	14
12	Computed Oxygen Vibrational Deexcitation Cross Sections, σ(1→j), for an O ₂ -O Collision as a Function of Relative Translational Energy	18
13	Computed v=2 to v=0 Oxygen Vibrational Deexcitation Cross Section, σ(2→0), for an O ₂ -O Collision as a Function of Relative Translational Energy	18

LIST OF FIGURES (Continued)

<u>Figure No.</u>		<u>Page</u>
14	Variation of Oxygen Diatom Total Internal Energy, Y_1 , Vibrational Energy, Y_2 , and Rotational Energy, Y_3 , with Number of Collisions of Oxygen Molecules with Oxygen Atom Thermal Bath	21
15	Variation of Oxygen Diatom Total Internal Energy, Vibrational Energy and Rotational Energy with Number of Collisions with Oxygen Atom Thermal Bath. Initial conditions are: oxygen internal energy, E_I , equals 26.3 kcal/mol, oxygen rotational energy, E_R , equals 0.0, and oxygen atom bath temperature, T_B , equals 400 K.	22
16	Variation of Oxygen Diatom Total Internal Energy, Vibrational Energy and Rotational Energy with Number of Collisions with Oxygen Atom Thermal Bath. Initial conditions are: oxygen internal energy, E_I , equals 26.3 kcal/mol, oxygen rotational energy, E_R , equals 0.0, and oxygen atom bath temperature, T_B , equals 500 K.	22
17	Variation of Oxygen Diatom Total Internal Energy, Vibrational Energy and Rotational Energy with Number of Collisions with Oxygen Atom Thermal Bath. Initial conditions are: oxygen internal energy, E_I , equals 26.3 kcal/mol, oxygen rotational energy, E_R , equals 0.0, and oxygen atom bath temperature, T_B , equals 750 K.	23
18	Variation of Oxygen Diatom Total Internal Energy, Vibrational Energy and Rotational Energy with Number of Collisions with Oxygen Atom Thermal Bath. Initial conditions are: oxygen internal energy, E_I , equals 26.3 kcal/mol, oxygen rotational energy, E_R , equals 0.0, and oxygen atom bath temperature, T_B , equals 1000 K.	23
19	Variation of Oxygen Diatom Total Internal Energy, Vibrational Energy and Rotational Energy with Number of Collisions with Oxygen Atom Thermal Bath. Initial conditions are: oxygen internal energy, E_I , equals 26.3 kcal/mol, oxygen rotational energy, E_R , equals 2.39 kcal/mol, and oxygen atom bath temperature, T_B , equals 300 K.	24

LIST OF FIGURES (Continued)

<u>Figure No.</u>		<u>Page</u>
20	Variation of Oxygen Diatom Total Internal Energy, Vibrational Energy and Rotational Energy with Number of Collisions with Oxygen Atom Thermal Bath. Initial conditions are: oxygen internal energy, E_I , equals 26.3 kcal/mol, oxygen rotational energy, E_R , equals 2.39 kcal/mol, and oxygen atom bath temperature equals T_B , equals 400 K.	24
21	Oxygen Internal Energy Above the Equilibrium Value, $E_I - E_{eq}$, as Function of Number of Collisions with Oxygen Atom Thermal Bath. Initial bath and oxygen molecule ensemble initial conditions are: diatom internal energy, E_I , equals 26.3 kcal/mol, rotational energy, E_R , equals zero, and bath temperature, T_B , equals 300 K.	28
22	Oxygen Internal Energy Above the Equilibrium Value, $E_I - E_{eq}$, as Function of Number of Collisions with Oxygen Atom Thermal Bath. Initial bath and oxygen molecule ensemble initial conditions are: diatom internal energy, E_I , equals 26.3 kcal/mol, rotational energy, E_R , equals 0.0, and bath temperature, T_B , equals 400 K.	28
23	Oxygen Internal Energy Above the Equilibrium Value, $E_I - E_{eq}$, as Function of Number of Collisions with Oxygen Atom Thermal Bath. Initial bath and oxygen molecule ensemble initial conditions are: diatom internal energy, E_I , equals 26.3 kcal/mol, rotational energy, E_R , equals 0.0, and bath temperature, T_B , equals 500 K.	29
24	Oxygen Internal Energy Above the Equilibrium Value, $E_I - E_{eq}$, as Function of Number of Collisions with Oxygen Atom Thermal Bath. Initial bath and oxygen molecule ensemble initial conditions are: diatom internal energy, E_I , equals 26.3 kcal/mol, rotational energy, E_R , equals 0.0, and bath temperature, T_B , equals 750 K.	29
25	Oxygen Internal Energy Above the Equilibrium Value, $E_I - E_{eq}$, as Function of Number of Collisions with Oxygen Atom Thermal Bath. Initial bath and oxygen molecule ensemble initial conditions are: diatom internal energy, E_I , equals 26.3 kcal/mol, rotational energy, E_R , equals 0.0, and bath temperature, T_B , equals 1000 K.	30

LIST OF FIGURES (Continued)

<u>Figure No.</u>		<u>Page</u>
26	Oxygen Internal Energy Above the Equilibrium Value, $E_I - E_{eq}$, as Function of Number of Collisions with Oxygen Atom Thermal Bath. Initial bath and oxygen molecule ensemble initial conditions are: diatom internal energy, E_I , equals 26.3 kcal/mol, rotational energy, E_R , equals 2.89 kcal/mol, and bath temperature, T_B , equals 300 K.	31
27	Oxygen Internal Energy Above the Equilibrium Value, $E_I - E_{eq}$, as Function of Number of Collisions with Oxygen Atom Thermal Bath. Initial bath and oxygen molecule ensemble initial conditions are: diatom internal energy, E_I , equals 26.3 kcal/mol, rotational energy, E_R , equals 2.89 kcal/mol, and bath temperature, T_B , equals 400 K.	32
28	Distribution of O_2 Molecular Energies for O_2 Initially Excited 26.3 kcal/mol After One Collision with O-Atom Bath at 500 K	34
29	Distribution of O_2 Molecular Energies for O_2 Initially Excited 26.3 kcal/mol After Five Collisions with O-Atom Bath at 500 K	35
30	Distribution of O_2 Molecular Energies for O_2 Initially Excited 26.3 kcal/mol After Ten Collisions with O-Atom Bath at 500 K	36
31	Distribution of O_2 Molecular Energies for O_2 Initially Excited 26.3 kcal/mol After Twenty Collisions with O-Atom Bath at 500 K	37
32	Distribution of O_2 Molecular Energies for O_2 Initially Excited 26.3 kcal/mol after Twenty-Five Collisions with O-Atom Bath at 500 K	38

LIST OF TABLES

<u>Table No.</u>		<u>Page</u>
1	Vibrational Energy Levels of O ₂ (kcal/mol)	16
2	Computed Vibrational Deexcitation Rate Constants	19

1. INTRODUCTION

In the following report we present a classical trajectory study of the energy transfer processes occurring in collisions between highly vibrationally-rotationally excited oxygen molecules and oxygen atoms. This system has several features that make its study interesting.

Most theoretical studies of inelastic processes in atom-diatom collisions have focussed on rare gas atom-diatom collisions. This is probably so because reasonably adequate potential energy surfaces may be constructed. The general features of the interactions for such systems are characterized by a weak long-range attraction and a strong short-range repulsion. In such systems facile energy transfer only occurs between rotation and translation. Classical trajectory studies indicate vibration is lost very inefficiently and often only through intermediate transfer to rotation. The energy transfer is dominated by small energy transfers.

A different sort of behavior is anticipated for systems with attractive short range forces. In systems such as $O-O_2$, in which a stable three-body configuration exists, qualitatively different behavior is anticipated. In these systems relaxation can be dominated by large transfers resulting from the strong attractive forces. Additionally, energy transfer may be facilitated by complex formation and exchange collisions. Of particular interest here is the rapid relaxation of excited recombined oxygen molecules by oxygen atoms in the upper atmosphere.

In the upper atmosphere oxygen atoms are produced by a number of chemical and photochemical processes. These atoms can then recombine by a three-body mechanism to form oxygen molecules. Theoretical and experimental studies on diatom recombination indicate that such recombined diatoms will be very highly internally excited. The post-recombination relaxation of oxygen molecules is of considerable interest to the energy and chemical balance in the upper atmosphere. A primary purpose of this work is to elucidate energy transfer processes that might occur during the recombination/relaxation process.

2. POTENTIAL ENERGY SURFACE

The dynamics of the O-O₂ system were computed using the Varandas-Murrell ground state potential surface for ozone. This surface was derived by Murrell et al.¹ using available spectroscopic and ab initio data. It has been used earlier by Varandas and Murrell^{1,2} to study the dynamics of the O+O₂ exchange reaction under thermally equilibrated conditions. Additionally this potential surface has been used as the ozone portion of potential surface for computing Ar-O₃ trajectories.³ The detailed form of the Varandas-Murrell ozone potential surface is given in Refs. 2 and 3.

3. CALCULATIONS

The technology of classical trajectory calculations has become standard. Only details relevant to the calculations presented here will be discussed. For detailed descriptions of the classical trajectory technique the reader is referred to the review articles of Bunker⁴ and Porter and Raff.⁵ Trajectories were computed using a fixed step Adams-Moulton integrator with a Runge-Kutta integrator for the first five steps. The accuracy of the trajectories was checked by observing conservation of energy and angular momentum. Generally both energy and angular momentum were conserved to better than one part in 10^6 . Selected trajectories were back integrated to initial conditions.

Two types of calculations were performed in this study: 1) single collision studies to systematically investigate energy transfer in O-O₂ collisions as a function of relative translational, vibrational and rotational energy and 2) multiple collisional calculations in which the evolution of an ensemble of O₂ molecules is followed by computing the effects of sequences of O-atom collisions on the ensemble properties.

Single collision calculations were performed at relative translational energies of 0.24, 0.48, 0.96 and 1.91 kcal/mol, at initial diatom vibrational energies of 2.39, 4.78, 7.17, 9.56, 14.33 and 21.50 kcal/mol and at initial diatom rotational energies of 0, 0.24, 0.48, 0.96 kcal/mol. At least 500 trajectories were computed for each initial value of relative translational, rotational and vibrational energy. Additionally, several calculations were performed at fixed initial diatom internal energy with varying partitioning between initial rotational and vibrational energies. Total initial diatom internal energy was fixed at 21.50 kcal/mol with initial vibrational energies of 16.72, 11.94, 11.67, 2.39 and 0.0 kcal/mol. These calculations were performed at relative translational energies of 0.48 and 0.96 kcal/mol. Batches of five hundred or more trajectories were computed for each set of initial conditions.

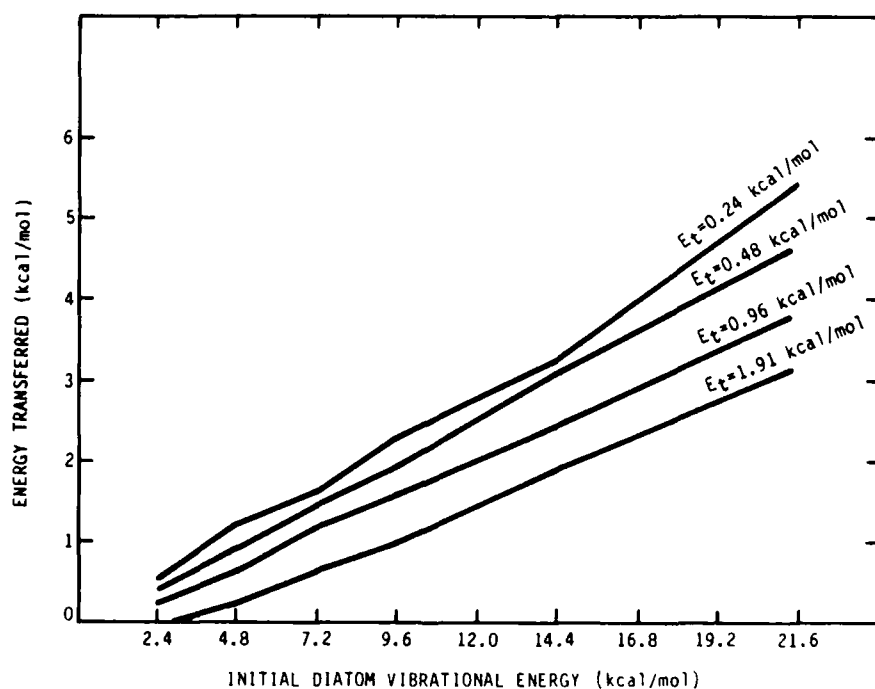
Multiple collision calculations were performed to study the relaxation of an ensemble of internally excited oxygen molecules in a bath of oxygen atoms. Given the model nature of this study we assumed that only collisions occurring on the ground state potential surface need be considered. Additionally, only collisions between the excited oxygen molecules and oxygen atoms are considered. In effect we assume a dilute oxygen molecule concentration in an oxygen atom thermal bath. This situation may well be relevant to the initial stages of relaxation of a recombining O-atom gas. The atom gas was assumed at a fixed temperature. The methodology of these multiple collision calculations has been discussed in detail elsewhere.⁶ Some brief comments are given later.

Calculations were performed for initial diatom internal energies equal to 26.28 kcal/mol. Several atomic bath temperatures were considered: 300, 400, 500, 750 and 1000 K. In most calculations the initial diatom rotational energy was set equal to zero so that all the initial diatom energy was present as vibrational energy. Some calculations were performed with initial diatom rotational energy equal to 2.39 kcal/mol. For this case relaxation was followed at thermal bath temperatures of 300 and 400 K.

Batches of 250 oxygen diatoms were used to simulate ensemble relaxation. The relaxation was followed through at least 25 successive collisions with the atom bath. After each collision the diatom internal energy and angular momentum were saved and used as initial conditions for the next collision. Relative translational energies for each collision were computed assuming a Boltzmann distribution. With this procedure the only memory of previous collisions is contained in the diatom internal coordinates. No memory is retained in the O-atom bath. This is reasonable for a dilute concentration of diatoms.

4. SINGLE COLLISION CALCULATIONS: RESULTS AND DISCUSSION

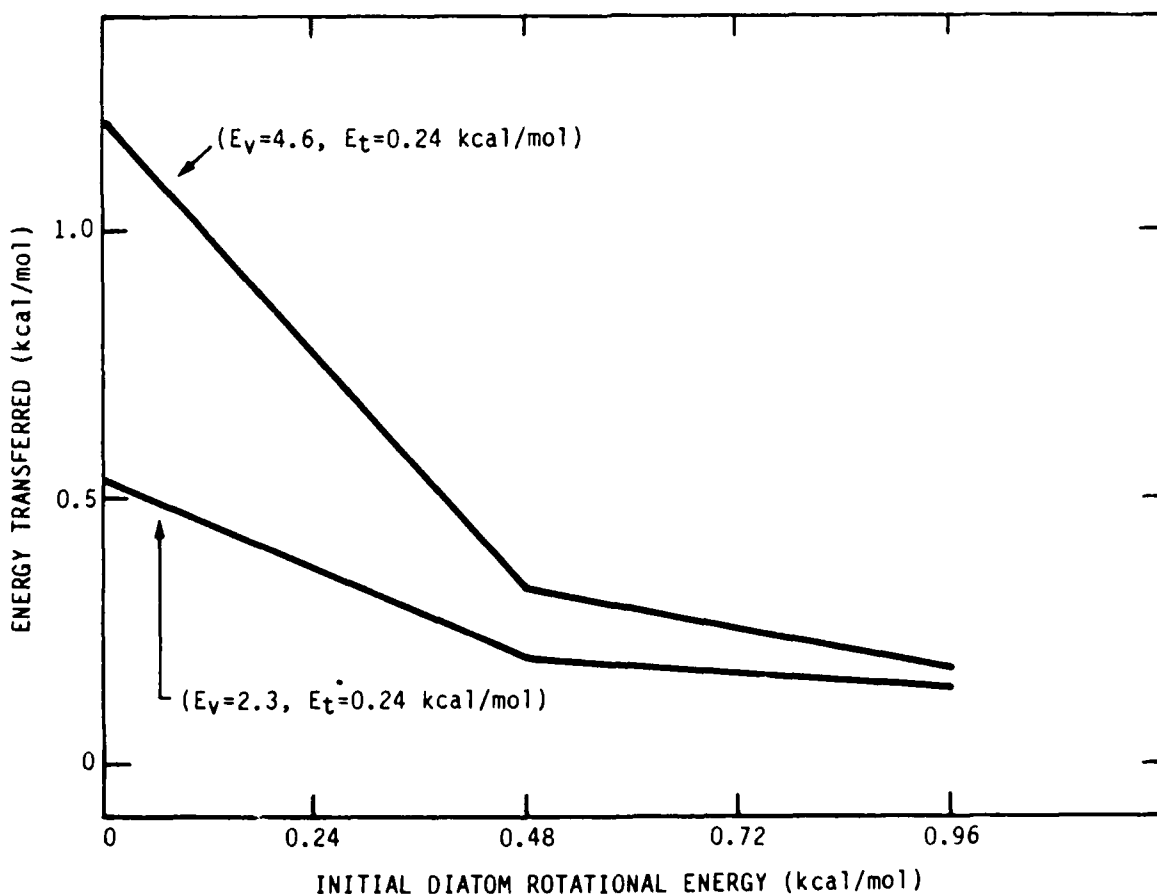
Average energy transferred per collision as a function of initial diatom vibrational energy at several relative translational energies is shown in Figure 1. These calculations were performed with the diatom initial rotational energy equal to zero. In these and all other calculations presented in this paper the maximum impact parameter was set equal to 4\AA . Two points are noteworthy. The magnitude of the diatom energy loss per collision (i.e., energy transferred from the diatom internal to relative translational energy) increases as the initial diatom vibrational energy is increased. This behavior is clearly shown in Figure 1. For a given value of initial diatom vibrational energy the diatom energy loss decreases monotonically with increasing relative translational energy. Both these variations are readily understood in terms of the relative excess of diatom initial internal energy compared to the initial translational energy. Molecules having more initial vibrational energy may transfer more energy into translation. Higher translational energy reduces the relative excess of diatom internal energy.



A-3261

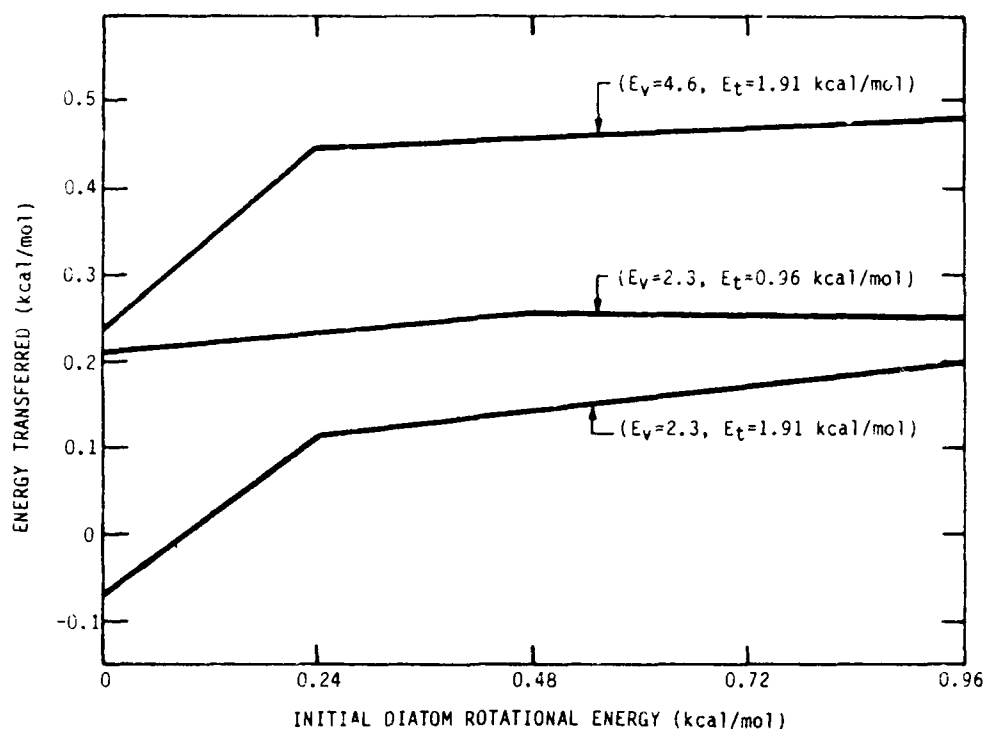
Figure 1. Energy Transferred from O_2 in an O_2 -O Collision as a Function of Initial O_2 Vibrational Energy. Results are shown for several values of relative translational energy, E_t .

The effect of initial diatom rotational energy on average energy transferred per collision is more complicated and depends on the relative translational energy. At the lowest translational energy considered (0.24 kcal/mol) initial diatom rotational energy substantially reduces the average energy transferred per collision. This is shown in Figure 2. However, at the highest considered value of relative translational energy, 1.91 kcal/mol, the initial diatom of rotational energy increases the average energy transferred (see Figure 3). At a relative translational energy of 0.96 kcal/mol and initial diatom vibrational energy of 2.3 kcal/mol an increase in diatom rotational energy has little effect on the magnitude of the energy transferred (Figure 3).



A-3262

Figure 2. Energy Transferred from O_2 in an O_2-O Collision as a Function of initial O_2 Rotational Energy. Results are shown for two values of initial relative translational energy, E_t , and initial vibrational energy, E_v .

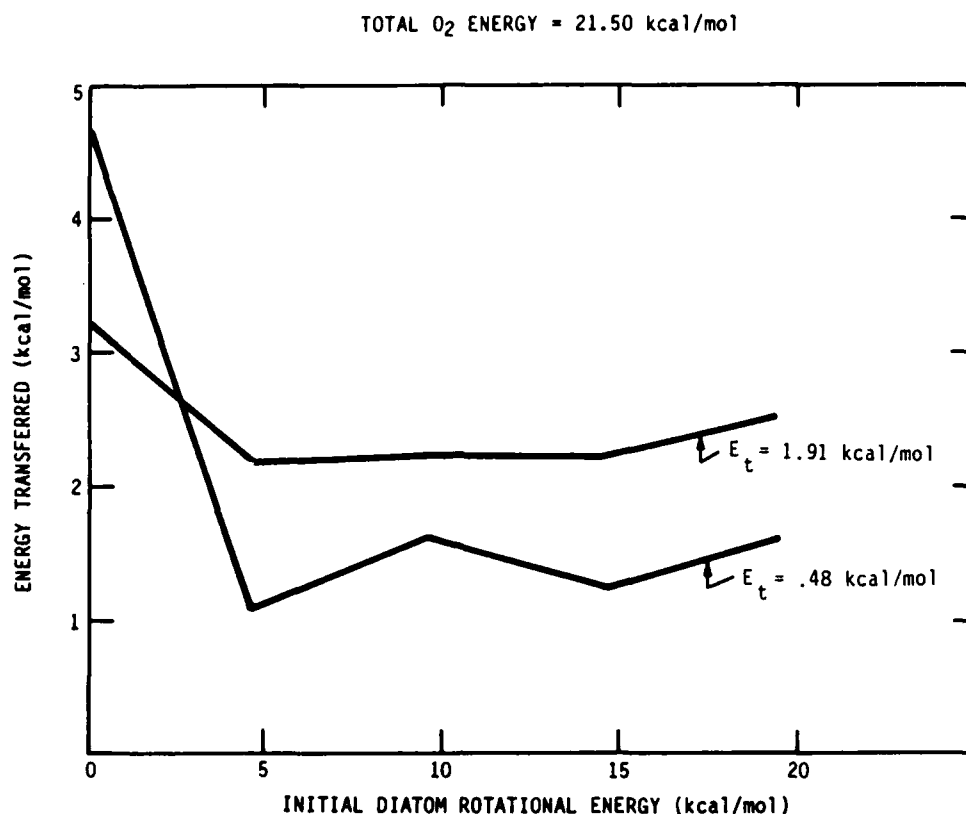


A-3263

Figure 3. Energy Transferred from O_2 in an O_2 -O Collision as a Function of Initial O_2 Rotational Energy for Several Values of Initial Diatom Relative Translational Energy, E_t , and Vibrational Energy, E_v

These calculations indicate that in this strongly interacting system rotational energy decreases the efficiency of energy transfer when the molecules are relatively vibrationally hot compared to translation. However, at lower relative vibrational excitations (i.e., higher translational energies) the behavior is reversed and increasing rotational energy increases energy transfer from the diatom.

Calculations of energy transfer from highly vibrationally-rotationally excited O_2 molecules were performed with fixed total internal energy equal to 21.5 kcal/mol for several initial partitionings between rotational and vibrational energies. Since vibrational-rotational modes are not strictly separable (especially at higher internal energies) it is more correct to state that we are examining the variation of energy transfer with diatom angular momentum. The initial diatom rotational energies were computed assuming the diatom at its equilibrium internuclear distance. The results of these calculations are presented in Figure 4.



A-32b4

Figure 4. Energy Transferred from O₂ in an O₂-O Collision as a Function of Initial O₂ Rotational Energy with Total O₂ Initial Interval Energy Equal to 21.50 kcal/mol. Results are shown for two values of relative translational energy, E_t .

At the lower relative translational energy of 0.48 kcal/mol the average energy transferred decreases rapidly as rotational energy is added to the diatom. Above 0.5 kcal/mol initial rotational energy the average energy transferred becomes essentially constant and independent of the initial partitioning between vibration and rotation. At 1.91 kcal/mol relative translational there is similar behavior although the decrease within initial rotational energy is substantially less. The difference in rotational energy dependences at these two translational energies has the following consequences.

At zero or very low initial rotational energies, energy transferred decreases with increasing translational energy. However, at high initial rotational energies, energy transfer increases with increasing translational energy.

Histograms of post collision diatom internal energy transfers are presented in Figures 5 and 6. Note that the total classical cross section, Πb_{\max}^2 , equals 50.3 \AA^2 . In the cases shown in Figures 5 and 6 the initial diatom internal energy is equal to 21.5 kcal/mol and initial translational energy 1.91 kcal/mol. For the calculations in Figure 5 the initial rotational energy is equal to zero and for those in Figure 6 initial rotational energy equals 4.78 kcal/mol. In both cases there is a very large proportion of extremely large energy transfers. Energy transfers of more than 10 kcal/mol are quite frequent. The cross section for energy transfers greater than 10 kcal/mol is 7 \AA^2 for the case in Figure 5 and 4 \AA^2 for that in Figure 6. This behavior is very different than seen in rare gas atom-diatom collisions. In rare gas atom-diatom collisions large energy transfers are extremely rare

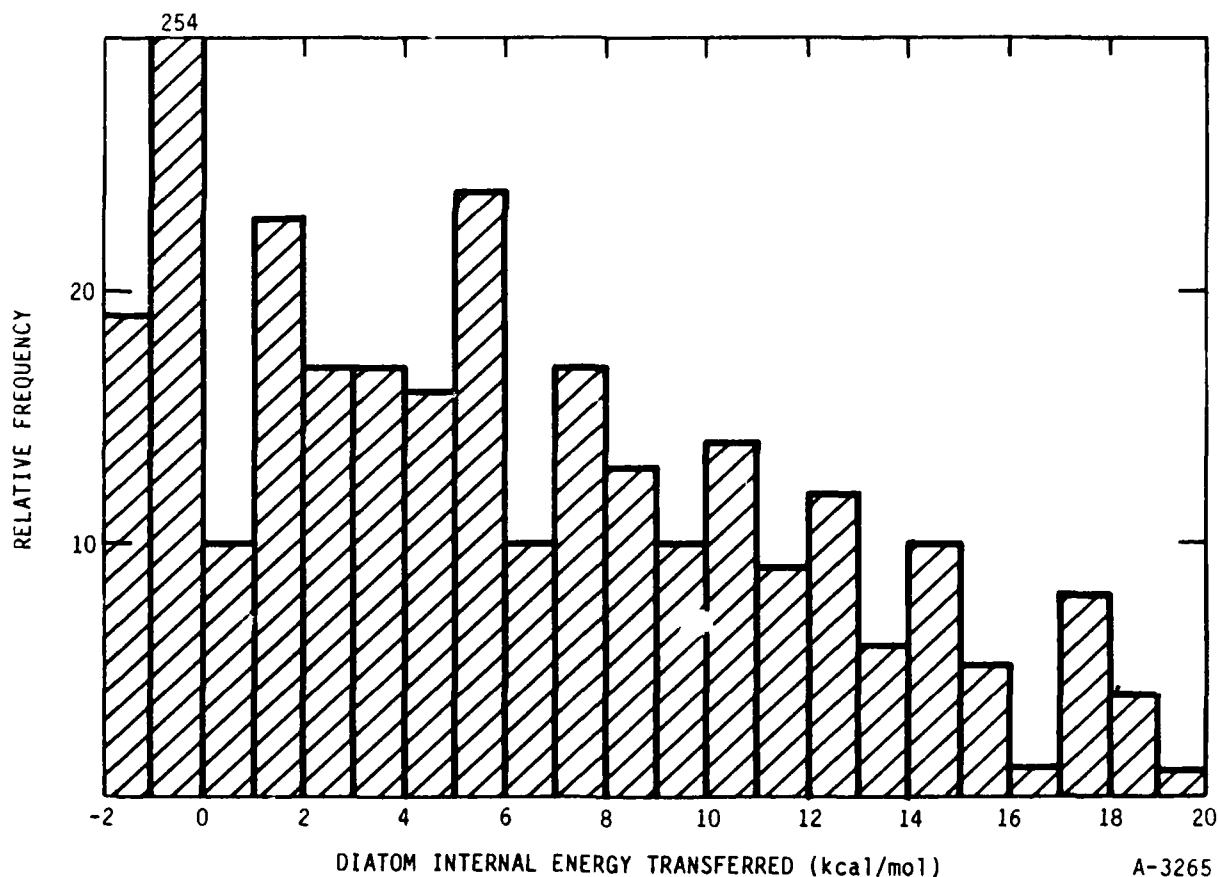


Figure 5. Distribution of O_2 Internal Energy Transfers in a Collision with O. Collision initial conditions are: O_2 internal energy equals 21.50 kcal/mol, O_2 rotational energy equals zero, and relative translational energy equals 1.91 kcal/mol.

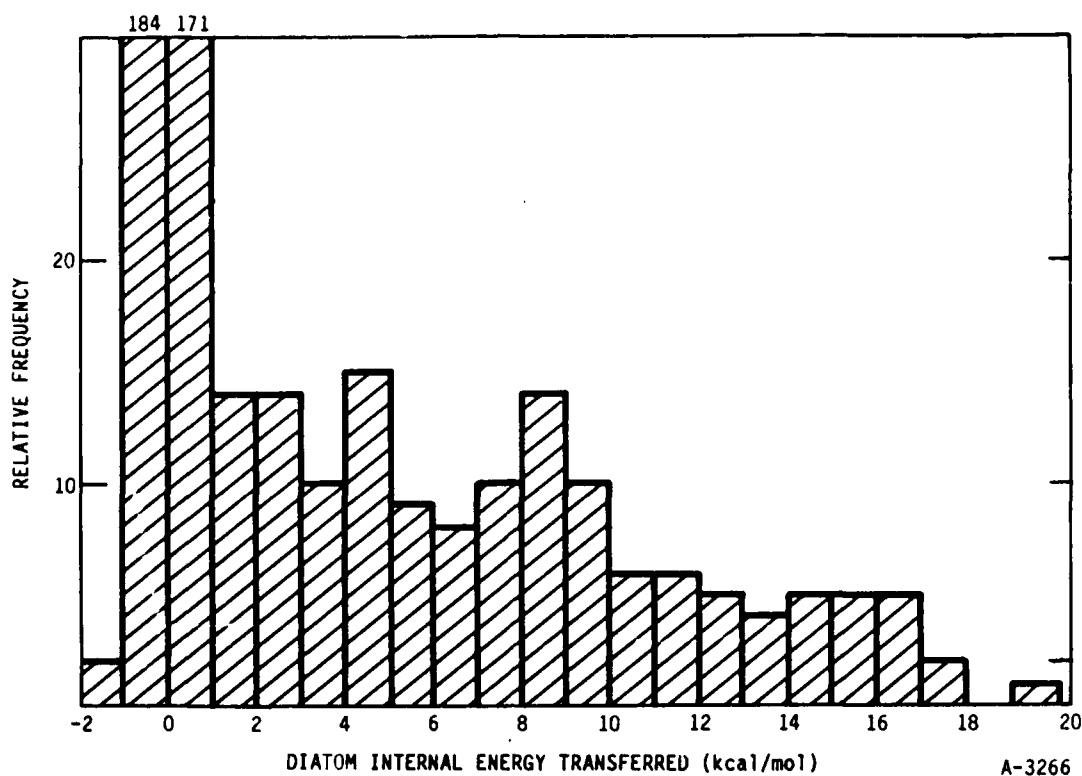


Figure 6. Distribution of O_2 Internal Energy Transfers in a Collision with O. Collision initial conditions are: O_2 internal energy equals 21.50 kcal/mol, O_2 rotational energy equals 4.78 kcal/mole, and relative translational energy equals 1.91 kcal/mol.

(in the translational energy range under consideration). Small energy transfers dominate. That behavior of course accounts for the relatively slow relaxation of vibrationally excited diatoms in a rare gas atomic bath. In this case we anticipate very rapid relaxation of excited diatoms due to the large average energy transferred per collision and the high frequency of very large energy transfers.

The differences between the O- O_2 relaxation and a system such as Ar- O_2 are clearly attributable to the much stronger interactions in the O- O_2 system. Experience with rare-gas atom-molecule collisions indicates that the transfer of vibration to translation is not facile. In fact energy transfer often seems to occur by a vibration-to-rotation-to-translation pathway in highly excited diatom and polyatomic relaxation by rare gas atoms. Similar behavior has been noticed in the relaxation of other atom-diatom systems in which strong interactions are present. Osborn and Smith⁷ recently investigated

vibrational energy transfer in a model $A+BC(v)$ system. They concluded that even fairly moderate intermolecular attraction can appreciably enhance the degree of vibrational energy transfer and lead to large energy transfers. This type of interaction is clearly found on the Murrell-Sorbie-Varandas ozone potential surface.

We also found that the role of long-lived collisions is minor in initially excited O_2-O collisions. At the highest internal excitation energies virtually no collisions longer than 1 ps were observed. At the lowest energies the collision lifetime increased substantially. However, the observed energy transfer for longer-lived collisions appeared similar to those for more direct collisions. This again is in substantial agreement with the implications of the Osborn and Smith model study. We have also compared energy transfer in reactive and non-reactive collisions. Histograms of collisional energy transfers for reactive and non-reactive encounters are shown in Figures 7 and 8, respectively. These histograms are for the case shown in Figure 5. For larger energy transfers, i.e., greater than 3 kcal/mol transferred from diatom internal energy to relative translational energy, the distributions for reactive and non-reactive encounters are qualitatively similar. The non-reactive case is of course dominated by collisions that produce little or no energy transfer. A possible interpretation of the similarity between the histograms to larger energy transfers is that the magnitude of the energy transfer is controlled by the strength of the interactions in the three-body complex and not by a peculiarity of the atom exchange process. A few points on the dependence of the exchange probability on internal excitation and relative translational energy are appropriate.

At zero initial diatom rotational energy the exchange probability increases monotonically with increasing initial vibrational excitation. Also, the exchange probability decreases with increasing translational energy. This is shown clearly in Figure 9. An increase in initial rotational energy causes a rapid decrease in the exchange cross section. This behavior is shown in Figure 10 for initial diatom vibration excitations of 2.4 and 4.8 kcal/mol. The effect of rotation is greatest at the lowest translational energies. The

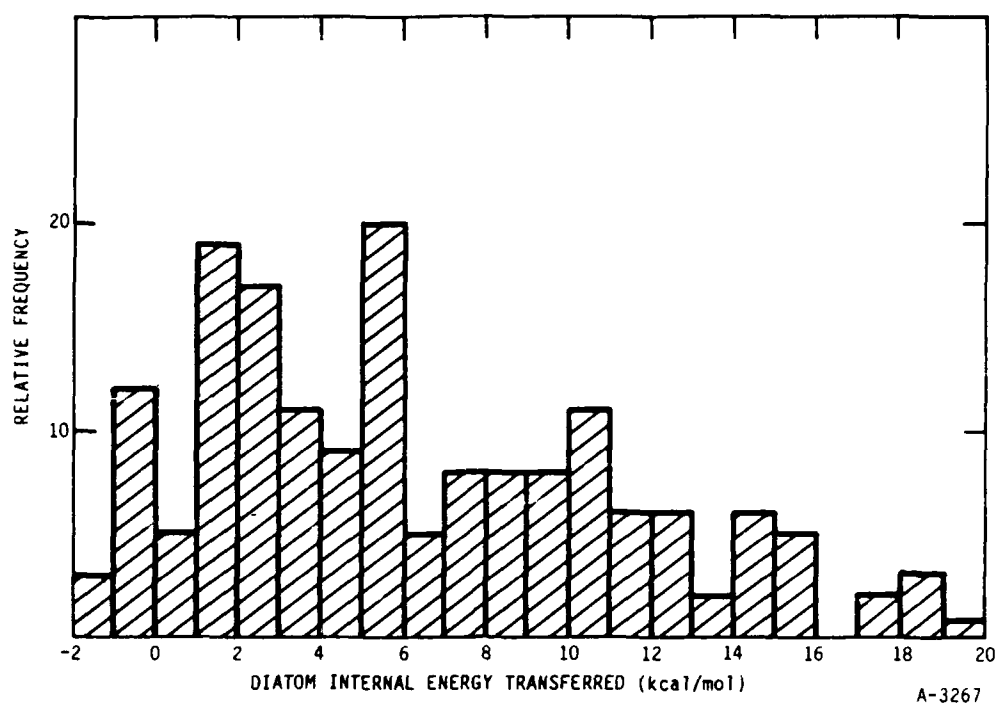


Figure 7. Relative Frequency of Energy Transfers in Reactive O₂-O Encounters Initial collision conditions same as in Figure 5

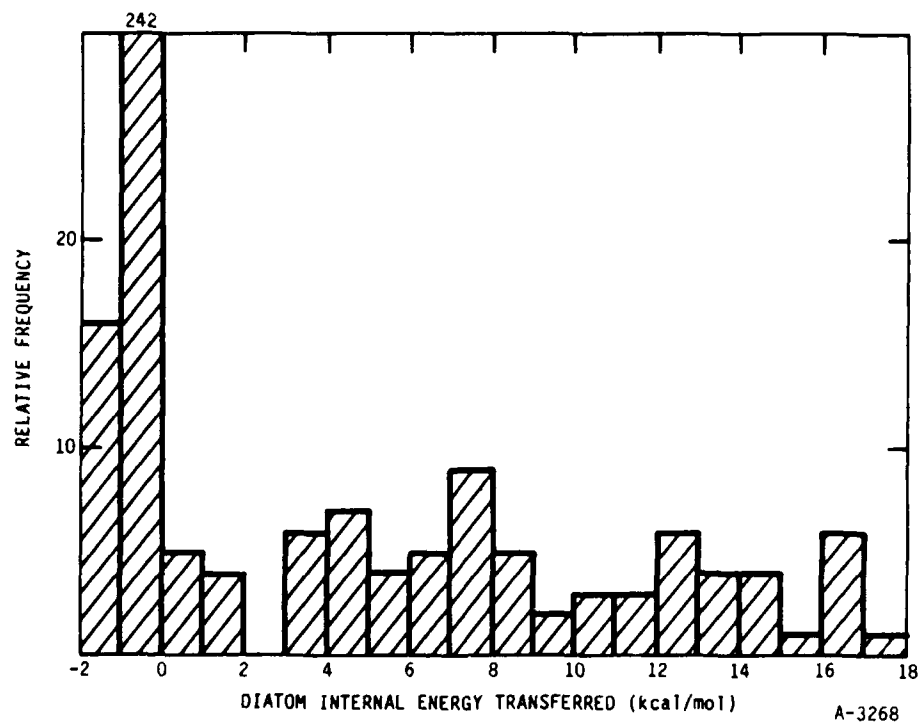
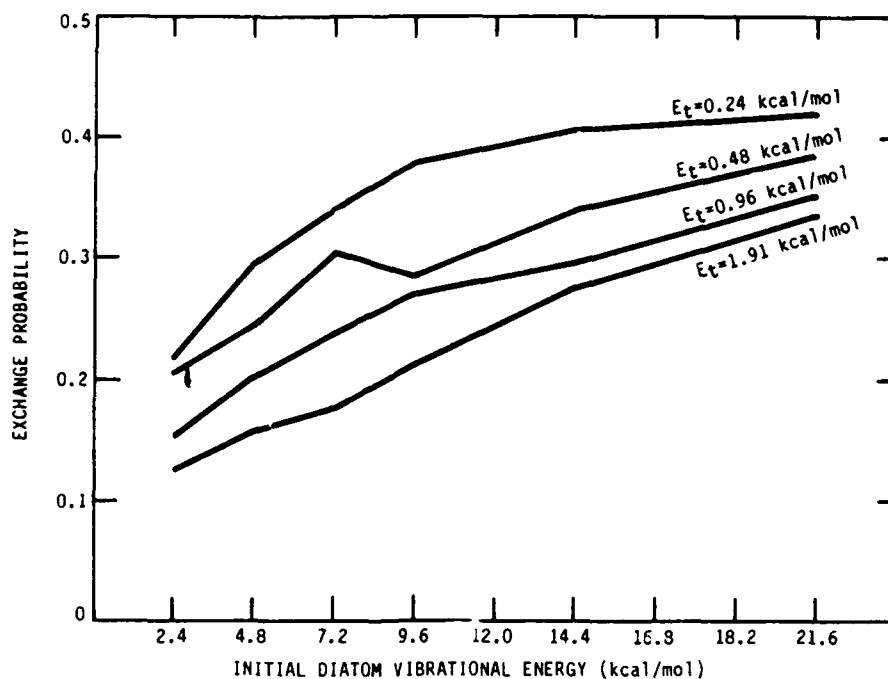
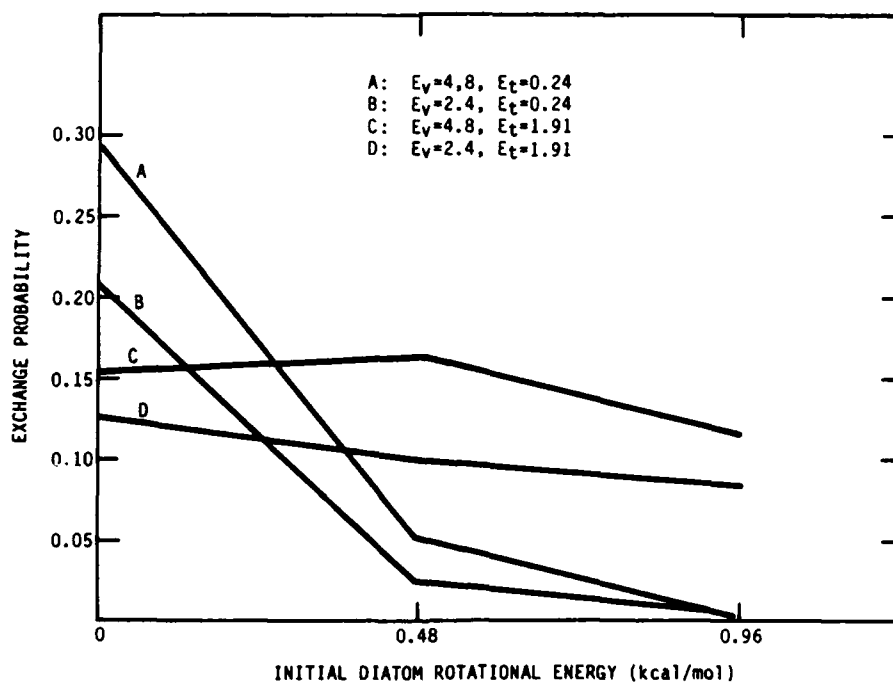


Figure 8. Relative Frequency of Energy Transfers in Non-reactive O₂-O Encounters. Initial collision conditions same as in Figure 5.



A-3269

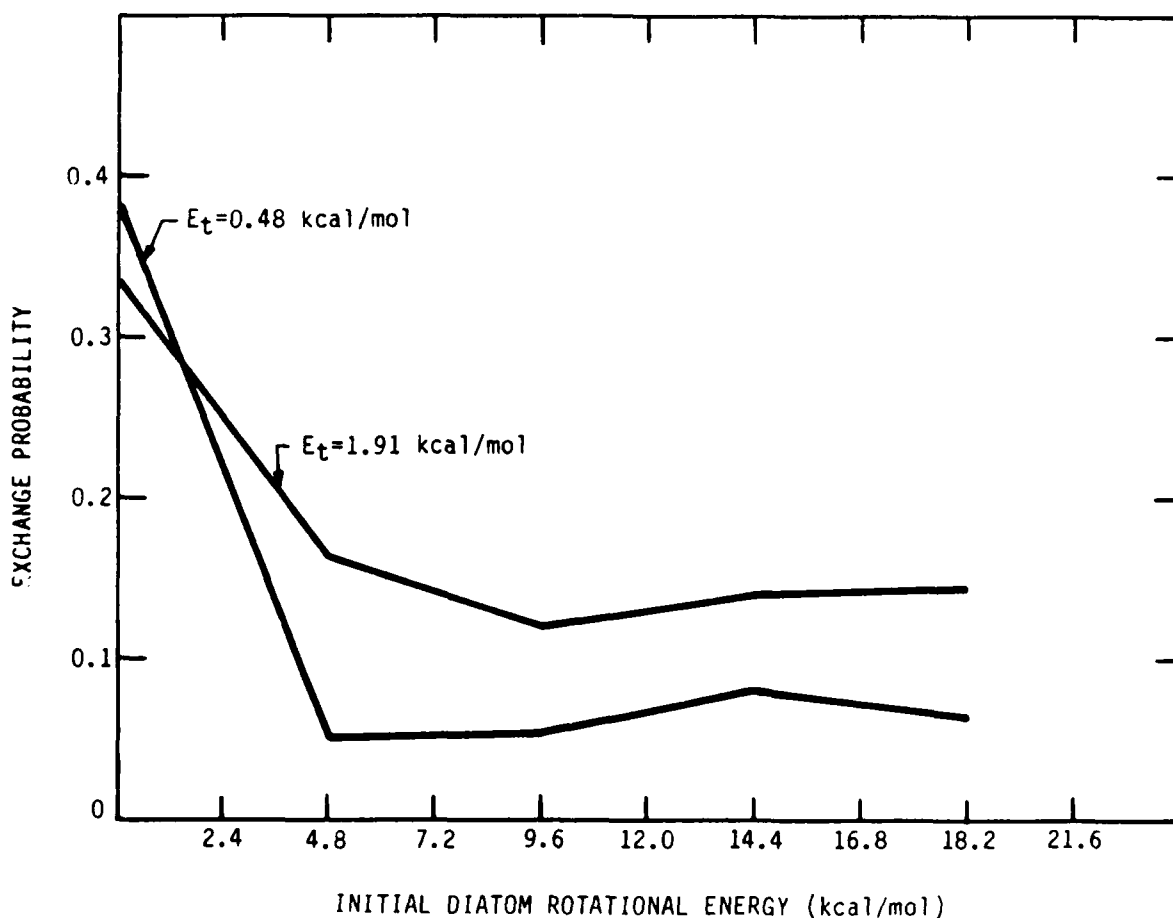
Figure 9. Oxygen Atom Exchange Probability as a Function of O_2 Initial Vibrational Energy for Several Values of Relative Translational Energy, E_t



A-3270

Figure 10. Oxygen Atom Exchange Probability as a Function of O_2 Initial Rotational Energy for Several Values of Oxygen Vibrational, E_v , and Relative Translational Energy, E_t

calculations involving diatoms initially excited at 21.5 kcal/mol show similar decreases in exchange probability with increasing rotational energy. Variation in exchange probability for initial total diatom excitation of 21.50 kcal/mol with varying partitioning between rotation and vibration is shown in Figure 11 for two values of initial relative translational energy, 0.48 and 1.91 kcal/mol. The variation in exchange probability with initial rotational energy is again much greater at the lower relative translational energy. A possible physical explanation for this behavior is as follows. At zero or very low initial diatom rotational energies, the motion of the colliding pair is dominated by the long range molecular attraction on the ozone potential surface that orients the triatom system into a lowest potential



A-3271

Figure 11. Oxygen Atom Exchange Probability as a Function of O_2 Initial Rotational Energy for a Fixed Initial O_2 Internal Energy Equal to 21.50 kcal/mol. Results are shown for two values of relative translational energy, E_t .

energy configuration approximating an ozone molecule. In such a configuration, exchange can occur without overcoming an energy barrier. The Murrell-Sorbie-Varandas potential surface is highly directional, i.e., configurations deviating substantially from the lowest energy path to form the triatomic are quite repulsive. As the initial diatom rotational energy is increased the long range attraction cannot orient the diatom as effectively. Therefore more collisions occur in configurations where exchange is energetically difficult. Thus the reaction probability decreases.

This effect should be greatest for lower relative translational energies since the ability of the diatom to orient will decrease as the collision time decreases at higher collision velocities. Therefore, this picture is also consistent with the general decrease in exchange probability with translational energy. For higher translational energies interferences due to diatom rotation should be relatively less important since the diatom has less time to orient itself into a favorable configuration for exchange. A less dramatic decrease with rotational energy is therefore expected at higher translational energies.

This picture may also be used to rationalize the general behavior of the average energy transfer per collision with relative translational and diatom rotational energy. Large energy transfer occurs for collisions that feel the strong attractive forces of the triatom system near its equilibrium configuration. Collisions that occur at configurations where the forces are repulsive should be qualitatively similar to rare-gas atom diatom collisions and result in smaller energy transfers. According to this picture collisions at low translational energies and rotational energies will allow a larger fraction to probe the strong attractive forces. Therefore, energy transfer should decrease with increasing translational energy and diatom rotational energy.

5. CALCULATIONS OF STATE-TO-STATE CROSS SECTIONS

The present calculations were done for purely classical atoms. However, we may use a boxing procedure to estimate quantal cross sections. First we consider the case in which molecules are excited 21.5 kcal/mol above the well minimum. The vibrational levels of the oxygen molecule are listed in Table 1. These values are derived from the spectroscopic constants given by Herzberg⁸ assuming oxygen can be described adequately as a harmonic oscillator.

Table 1. Vibrational Energy Levels of O₂ (kcal/mol)

v=0	2.258
v=1	6.773
v=2	11.29
v=3	15.80
v=4	20.32
v=5	24.84

The initial diatom vibrational energy of 21.50 corresponds to an energy slightly above the value for v=4. We assume that it adequately represents v=4. Calculations having initial vibrational energy of 7.17 kcal/mol will be used to describe v=1. To compute state to state cross sections we assume a quasiclassical boxing procedure as described by Porter and Raff.⁵ The purpose of the effort was not primarily to compute cross sections but to follow the evolution of ensemble of relaxing molecules. This procedure although somewhat approximate will yield reasonable estimates.

The cross section of interest is the total cross section for a transition between two vibrational states, $\sigma(v, v')$, without regard to final rotational state. It is given by

$$\sigma(v; v') = \sum_{J'} \sigma(v, J; v', J') .$$

To compute the final state vibrational energy we write the diatom rotational energy as

$$E_R = BJ^2$$

where J is the diatom rotational angular momentum and B is the equilibrium rotational constant. The vibrational energy transfer, ΔE_v , is then given by

$$\begin{aligned}\Delta E_v &= E_v^i - E_v^f \\ &= E_d^i - E_d^f - E_R^i + E_R^f\end{aligned}$$

where E_v^i and E_v^f are diatom initial and final vibrational energies, E_d^i and E_d^f are the diatom initial and final rotational energies.

The computed cross sections for transitions from the v=4 oxygen vibrational state as a function of relative translational energy are shown in Figure 12. Values for transition from v=2 are shown in Figure 13. The values for these cross sections are quite large. A general trend for decreasing cross section with increasing translational energy can be seen in Figures 12 and 13.

We can also calculate the rate constant for each transition using the equation

$$k = v\sigma$$

This quantity is probably of more interest to modelers trying to simulate upper atmospheric behavior. The computed values are listed in Table 2. The rate constants are listed as a function of approximate temperature corresponding to the relative translational energy.

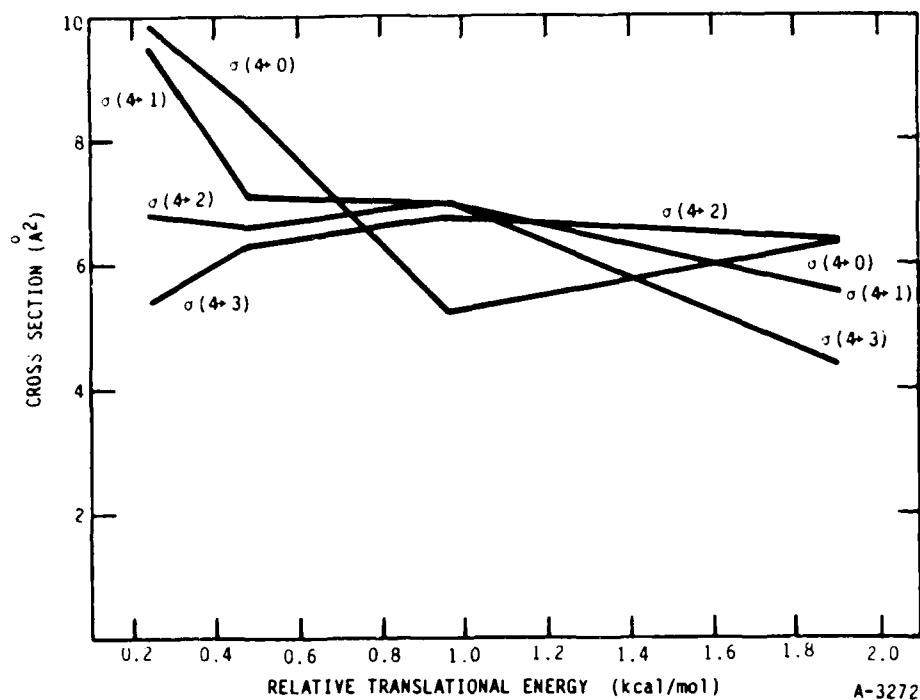


Figure 12. Computed Oxygen Vibrational Deexcitation Cross Sections, $\sigma(4+j)$, for an O_2-O Collision as a Function of Relative Translational Energy

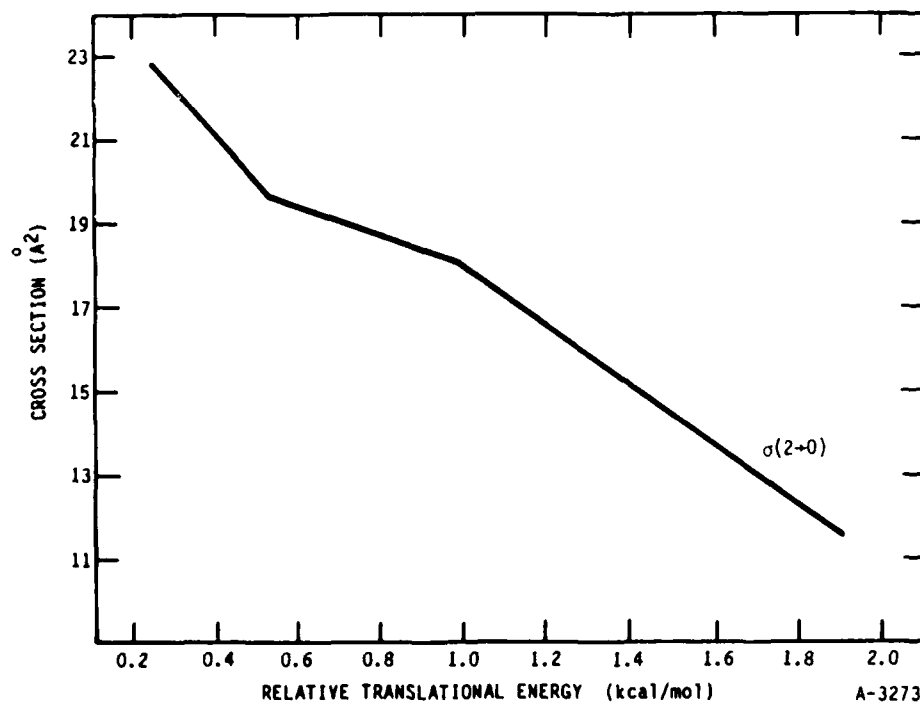


Figure 13. Computed $v=2$ to $v=0$ Oxygen Vibrational Deexcitation Cross Section, $\sigma(2+0)$, for an O_2-O Collision as a Function of Relative Translational Energy

Table 2. Computed Vibrational Deexcitation Rate Constants

	60 K	120 K	240 K	480 K
$k(4 \rightarrow 0)$	4.3×10^{-11}	5.2×10^{-11}	4.5×10^{-11}	7.7×10^{-11}
$k(4 \rightarrow 1)$	4.1×10^{-11}	4.3×10^{-11}	6.1×10^{-11}	6.7×10^{-11}
$k(4 \rightarrow 2)$	2.9×10^{-11}	4.0×10^{-11}	6.1×10^{-11}	7.7×10^{-11}
$k(4 \rightarrow 3)$	2.4×10^{-11}	3.9×10^{-11}	5.8×10^{-11}	5.4×10^{-11}
$k(1 \rightarrow 0)$	9.9×10^{-11}	1.2×10^{-10}	1.6×10^{-10}	1.4×10^{-10}

6. MULTIPLE COLLISION CALCULATIONS

The multiple trajectory technique is based on an approximate solution to the Boltzmann equation given as follows

$$\frac{df}{dt} = Lf \quad (1)$$

where L is the Boltzmann collision operator and f is the ensemble distribution function. The essence of the multiple collision technique is 1) to approximate a solution to Eq. (1) as

$$f(t+\tau) = (1+L\tau)f(t) \quad (2)$$

where τ is chosen to correspond to a mean collision time; 2) to identify the term $(1+L\tau)f(t)$ as the ensemble after one collision of each member of the ensemble; and 3) to use Monte Carlo trajectory calculations to compute the collision dynamics of each member of the ensemble. The simulation is accomplished by picking a finite ensemble of molecules (in this case 250) in a given initial state. Each molecule undergoes a sequence of collisions. The initial conditions for the collision are chosen according to the ensemble thermal characteristics. The evolution is constructed by using the molecule post collision variables, i.e., energy and angular momentum, as initial conditions for the next collision. After n collisions the ensemble describes the evolution after $n\tau$. The primary quantities of interest to this study are the average total diatom energy, vibrational energy and rotational energy.

We first discuss the evolution of mean oxygen diatom quantities. The oxygen diatom relaxation is assumed to occur in a bath of thermally equilibrated oxygen atoms with a small concentration of diatoms. Therefore diatom-diatom collisions are neglected. It is furthermore assumed that no translational motion memory is retained between collisions so that the relative translational energy of distribution of colliding pairs is given by a Boltzmann distribution.

The evolution of the average total internal diatom energy, diatom vibrational and diatom rotational energies are shown in Figures 14 through 20. For the cases shown in Figures 14 through 18 the initial rotational energy was equal to zero. For the cases in Figures 19 and 20 the initial rotational energy was set equal to 2.39 kcal/mol. In all cases the initial internal energy was equal to 26.3 kcal/mol. We first discuss the cases with initially non-rotating diatoms.

Calculations were performed for oxygen atom baths varying between 300 and 1000 K. Qualitatively and quantitatively there is no dramatic variation in relaxation observed with bath temperature. We therefore focus first on the 300 K bath temperature case (Figure 14). Note that we are considering purely classical relaxation and that the equilibrium values of the diatom rotational and vibrational energies are each kT .

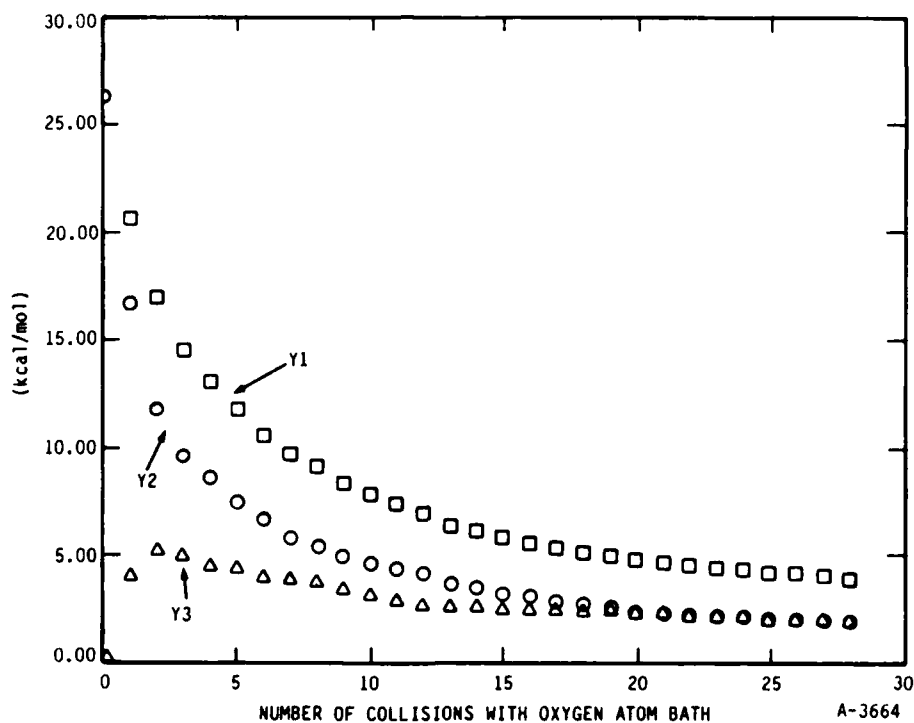


Figure 14. Variation of Oxygen Diatom Total Internal Energy, Y1, Vibrational Energy, Y2, and Rotational Energy, Y3, with Number of Collisions of Oxygen Molecules with Oxygen Atom Thermal Bath. Initial conditions are: oxygen internal energy, E_I , equals 26.3 kcal/mol, oxygen rotational energy, E_R , equals zero, and oxygen atom bath temperature, T_B , equals 300 K.

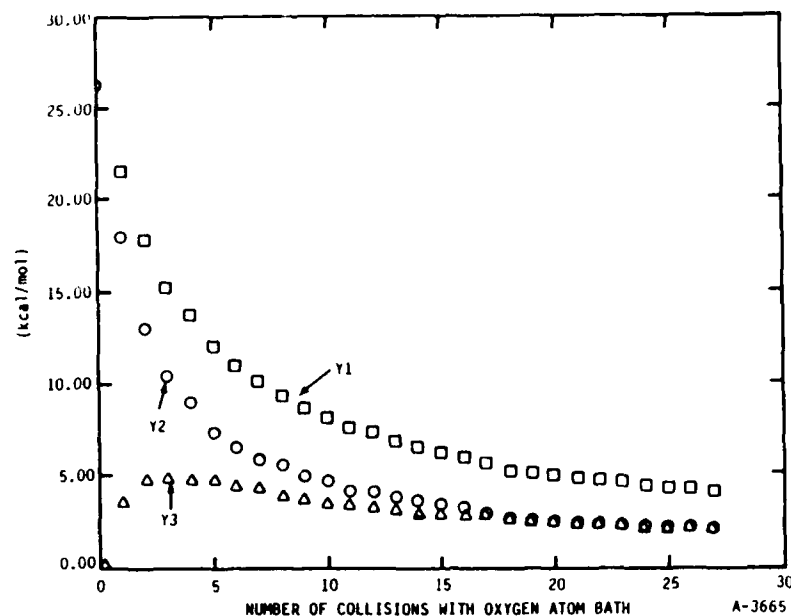


Figure 15. Variation of Oxygen Diatom Total Internal Energy, Vibrational Energy and Rotational Energy with Number of Collisions with Oxygen Atom Thermal Bath. Initial conditions are: oxygen internal energy, E_I , equals 26.3 kcal/mol, oxygen rotational energy, E_R , equals 0.0, and oxygen atom bath temperature, T_B , equals 400 K.

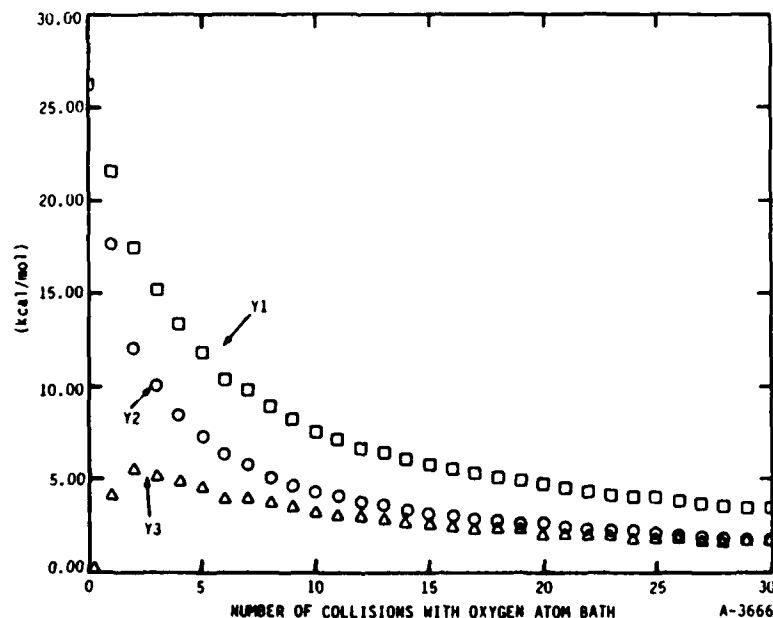


Figure 16. Variation of Oxygen Diatom Total Internal Energy, Vibrational Energy and Rotational Energy with Number of Collisions with Oxygen Atom Thermal Bath. Initial conditions are: oxygen internal energy, E_I , equals 26.3 kcal/mol, oxygen rotational energy, E_R , equals 0.0, and oxygen atom bath temperature, T_B , equals 500 K.

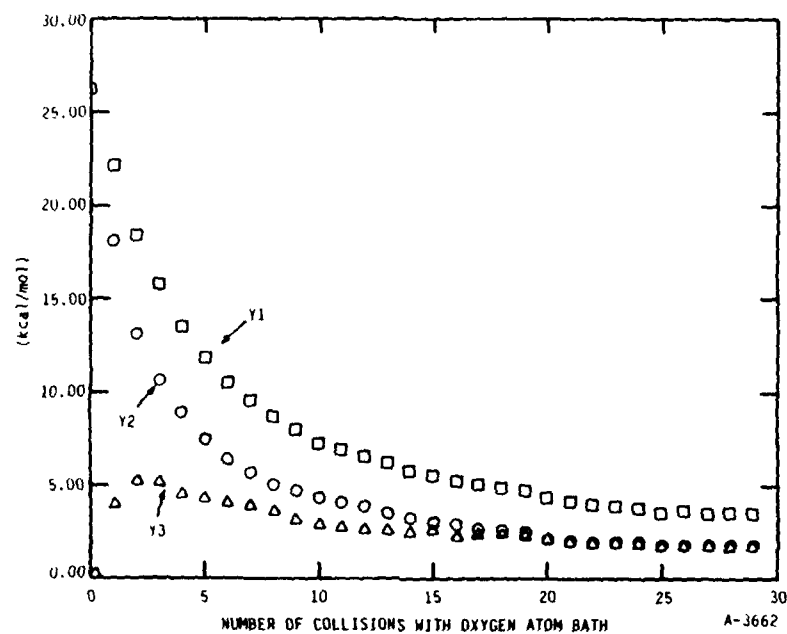


Figure 17. Variation of Oxygen Diatom Total Internal Energy, Vibrational Energy and Rotational Energy with Number of Collisions with Oxygen Atom Thermal Bath. Initial conditions are: oxygen internal energy, E_I , equals 26.3 kcal/mol, oxygen rotational energy, E_R , equals 0.0, and oxygen atom bath temperature, T_B , equals 750 K.

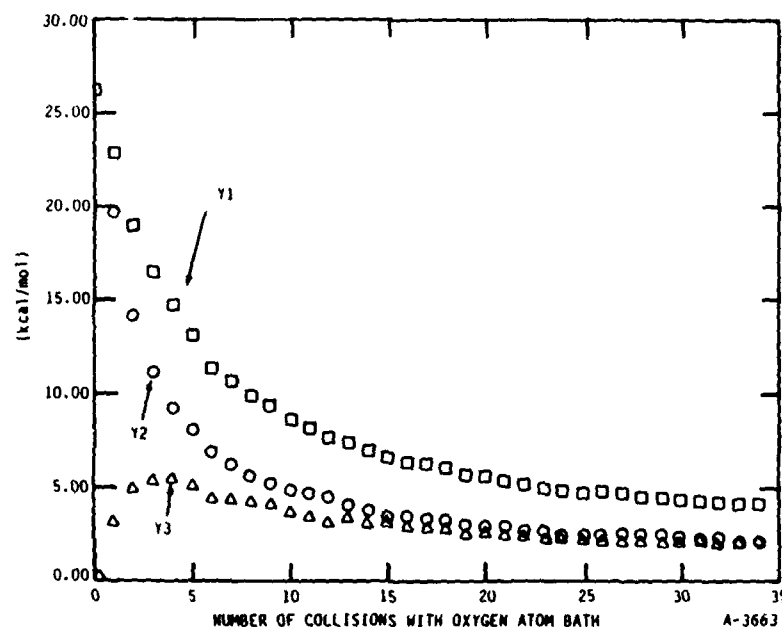


Figure 18. Variation of Oxygen Diatom Total Internal Energy, Vibrational Energy and Rotational Energy with Number of Collisions with Oxygen Atom Thermal Bath. Initial conditions are: oxygen internal energy, E_I , equals 26.3 kcal/mol, oxygen rotational energy, E_R , equals 0.0, and oxygen atom bath temperature, T_B , equals 1000 K.

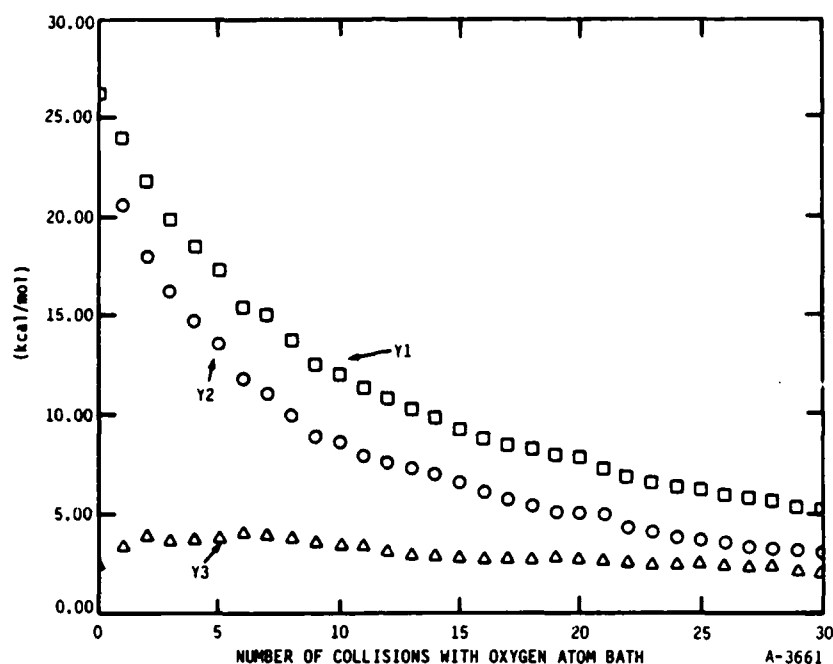


Figure 19. Variation of Oxygen Diatom Total Internal Energy, Vibrational Energy and Rotational Energy with Number of Collisions with Oxygen Atom Thermal Bath. Initial conditions are: oxygen internal energy, E_I , equals 26.3 kcal/mol, oxygen rotational energy, E_R , equals 2.39 kcal/mol, and oxygen atom bath temperature, T_B , equals 300 K.

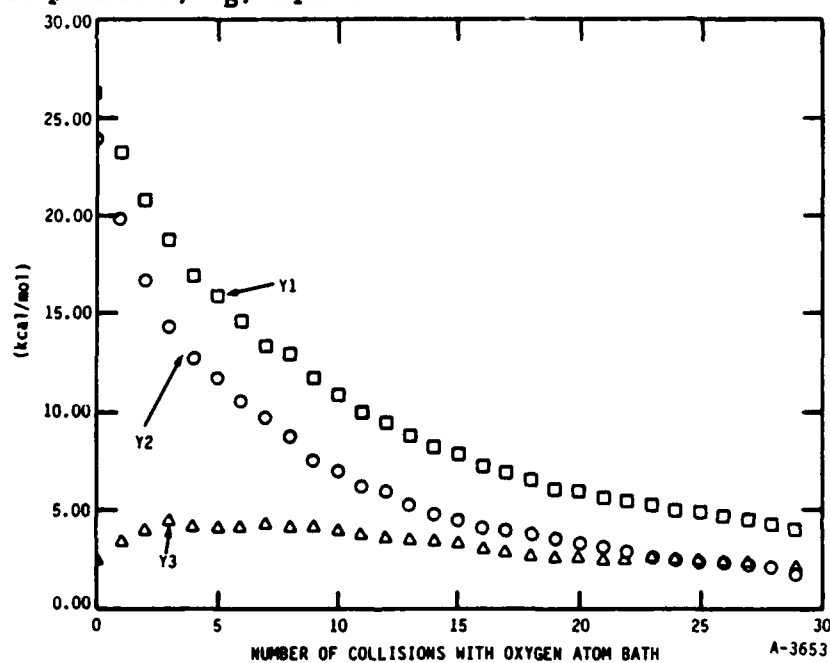


Figure 20. Variation of Oxygen Diatom Total Internal Energy, Vibrational Energy and Rotational Energy with Number of Collisions with Oxygen Atom Thermal Bath. Initial conditions are: oxygen internal energy, E_I , equals 26.3 kcal/mol, oxygen rotational energy, E_R , equals 2.39 kcal/mol, and oxygen atom bath temperature, T_B , equals 400 K.

The ensemble internal energy drops very rapidly for the first several collisions. Approximately 5 kcal/mol internal energy is lost in the first collision. Very large average energy transfers persist up to approximately the fifth collision. After the fifth collision the ensemble internal energy is approximately 12 kcal/mol, implying that over 14 kcal/mol has been transferred out of the molecule. Beyond approximately the fifth collision the relaxation slows quite dramatically. Between collisions five and twenty-eight an additional 8 kcal/mol are transferred from the diatom. At the end of the calculation, after the twenty-eighth collision, the average diatom internal energy is 3.9 kcal/mol. The equilibrium value for the internal energy of a classical diatom in a 300 K bath is 1.2 kcal/mol. Thus, after twenty-eight collisions approximately 90 percent of the excess internal diatom energy has been lost to the bath. This is indeed rapid relaxation for a vibrating molecule.

The average diatom vibrational energy is initially equal to the total internal energy in this case. It drops rapidly with collision number. Again very large energy transfers occur in the first few collisions. By the fifth collision the vibrational energy has decreased from 26.3 to 7.4 kcal/mol. The average vibrational energy drops by approximately 10 kcal/mol in the first collision. Between collisions five and twenty-eight the vibrational energy decreases much more slowly from 7.4 to 2.0 kcal/mol. The initial very rapid transfer of vibrational energy is associated with two processes: intermolecular transfer of vibrational energy and intramolecular transfer between vibrational and rotational energy.

In the case under consideration (Figure 14) the initial rotational energy is equal to zero. After one collision the average diatom rotational energy is 4.0 kcal/mol. The value of the average rotational energy peaks at the second collision at a value of 5.2 kcal/mol. After the second collision, the average rotational energy decreases. Note that the rotational relaxation does not decouple from the vibrational energy relaxation over the time scales considered. For this classical, strongly interacting system rotational and vibrational energies relax at the same rates. By the twentieth collision the

average rotational and vibrational energies are approximately equal. From that collision on, both modes relax at the same rate. This behavior is observed in all the cases considered over the computed relaxation times. A plausible explanation for this behavior is the large coupling between rotational and vibrational motion on the Murrell-Sorbie-Varandas ozone potential surface. This strong coupling does not allow separation of time scales for rotational and vibrational relaxation.

In the more frequently studied cases of rare gas atom-diatom relaxation, the interaction potentials may be separated into terms separately leading to vibrational and rotational energy transfers. The coupling between diatom vibration and translational motion tends to be very inefficient in the energy range considered here and the diatom vibrational energy relaxes very slowly. Rotational coupling to translational motion is generally quite efficient resulting in rapid rotational relaxation. Thus, at least for low values of vibrational excitation rotational relaxation occurs on a faster time scale. This behavior is generally not found for high values of vibrational excitation even in rare gas atom-diatom systems.⁶ Therefore for low collision numbers strong coupling is expected. However, the strong coupling that exists even for vibrational energies only a few kilocalories above the well minimum would seem due to the strong interactions in the O-O₂ system.

An additional feature of interest is the number of collisions required for the rotational energy to build up in the molecule by collisions with the bath. This is the number of collisions for the rotational energy to reach a peak value before beginning to relax. As is readily seen in Figures 14 through 18 this occurs in three to five collisions with the bath. This number of collisions corresponds to an intramolecular energy transfer collisional relaxation time and is very fast. The rapidity of this transfer is indicative again of the strong coupling between vibration and rotation on the Murrell-Sorbie-Varandas ozone potential surface.

It is of interest to see whether or not a single relaxation time is sufficient to characterize the molecular relaxation. This would seem unlikely

for the non-rotating initial oxygen molecule ensemble due to the strong dependence of total energy transfer on rotational energy. As discussed earlier in single collision calculations for highly excited molecules, increasing rotational energy causes a sharp decrease in the average collisional energy transfer (Figure 4) at low values of relative translational energy. Therefore for the initially non-rotating cases the early time relaxation will be characterized by large energy transfers characteristic of non-rotating molecules. Within three to five collisions with the bath, rotational energy is built up in the diatoms and relaxation will occur at the slower rate of rotating molecules. This can be significant since as mentioned earlier for the 300 K non-rotating case since most of the excess diatom energy is lost within five collisions with the bath.

The total molecular energy in excess of its classical equilibrium value as a function of collision number is shown for each case in Figures 21 through 27. The plots are presented on semi-log paper so that in a regime in which the relaxation is described by a single exponential decay a linear curve should result. First we consider the cases in which the molecules are non-rotating (Figures 21 through 25).

Two regimes regions are readily identified: a short time (zero to five collisions) rapid relaxation regime and longer time (>five to ten collisions) slower relaxation. As mentioned earlier the short time regime corresponds to the time in which rotational energy (or angular momentum) is being transferred into the molecule. As noted earlier, (Figure 1) collisional energy transfer decreases strongly with diatom rotational energy. Therefore the molecules relax more rapidly during the first few collisions before rotational energy is built up. This effect is most pronounced at the lower atom bath temperatures because as seen earlier for non-rotating diatoms the collisional energy transfer from the diatom decreases with increasing atom-diatom translational energy. Therefore the initial molecular relaxation rate (zero to five collisions) increases with decreasing bath temperature. This is seen in Figures 21 through 25. At longer times the situation is reversed. For vibrationally-rotationally excited molecules with substantial rotational energy, collisional

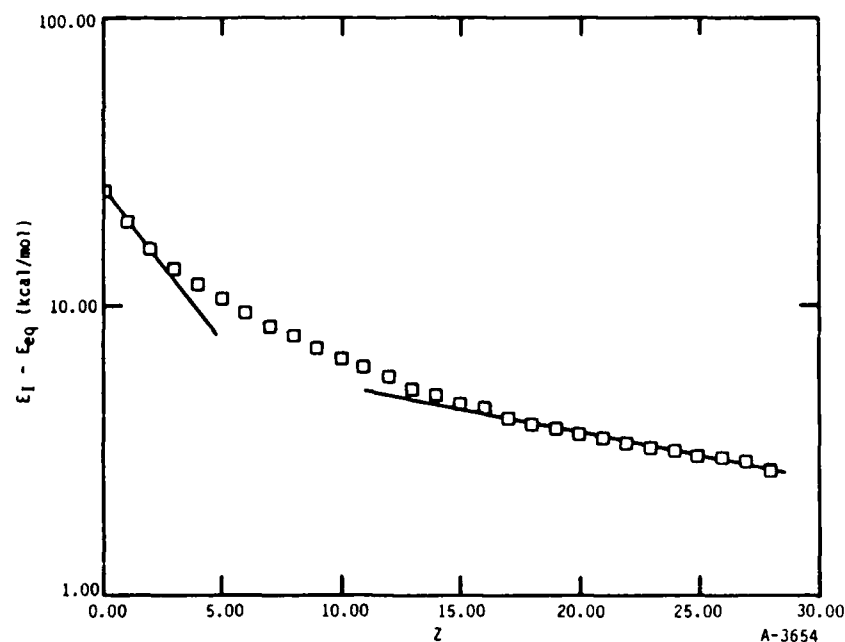


Figure 21. Oxygen Internal Energy Above the Equilibrium Value, $E_I - E_{eq}$, as Function of Number of Collisions with Oxygen Atom Thermal Bath. Initial bath and oxygen molecule ensemble initial conditions are: diatom internal energy, E_I , equals 26.3 kcal/mol, rotational energy, E_R , equals zero, and bath temperature, T_B , equals 300 K.

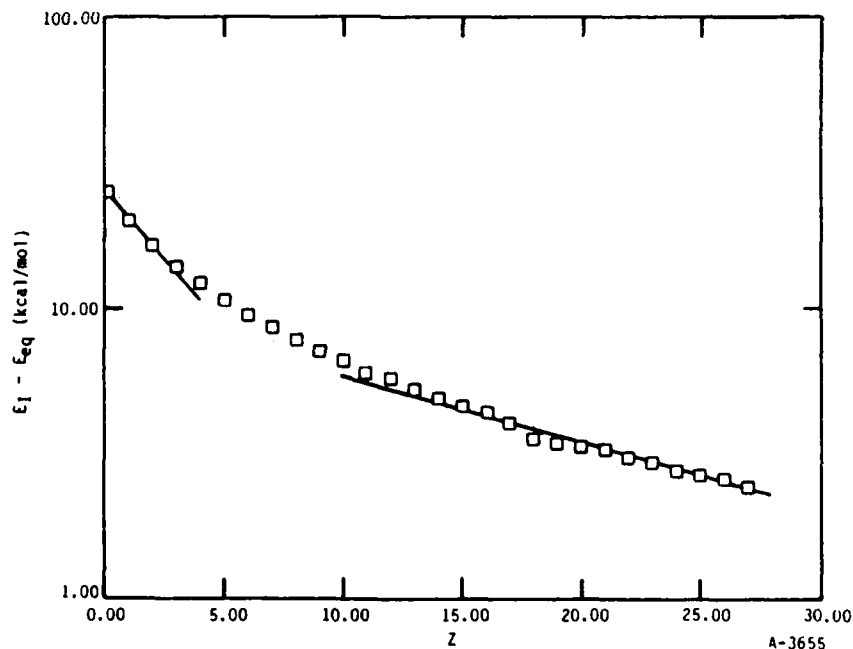


Figure 22. Oxygen Internal Energy Above the Equilibrium Value, $E_I - E_{eq}$, as Function of Number of Collisions with Oxygen Atom Thermal Bath. Initial bath and oxygen molecule ensemble initial conditions are: diatom internal energy, E_I , equals 26.3 kcal/mol, rotational energy, E_R , equals 0.0, and bath temperature, T_B , equals 400 K.

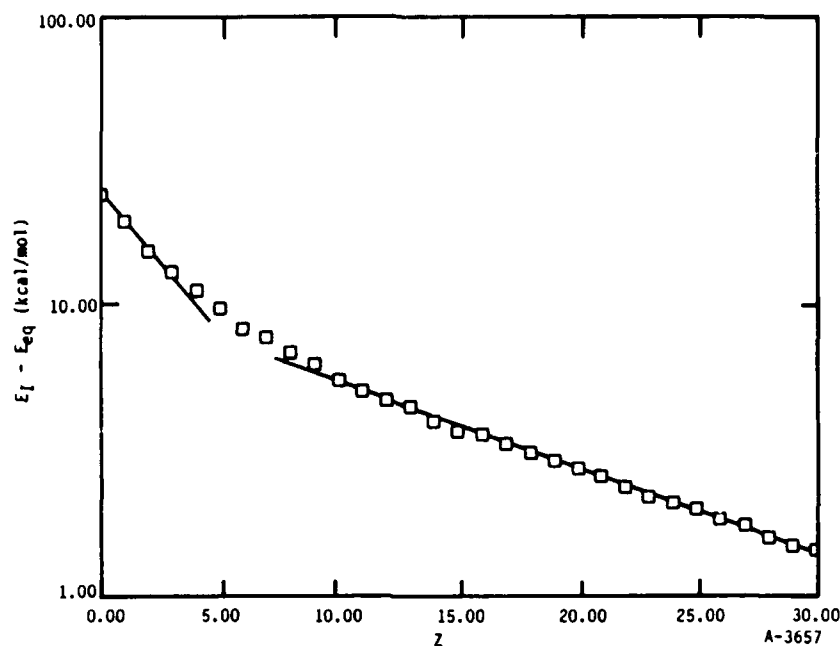


Figure 23. Oxygen Internal Energy Above the Equilibrium Value, $E_I - E_{eq}$, as Function of Number of Collisions with Oxygen Atom Thermal Bath. Initial bath and oxygen molecule ensemble initial conditions are: diatom internal energy, E_I , equals 26.3 kcal/mol, rotational energy, E_R , equals 0.0, and bath temperature, T_B , equals 500 K.

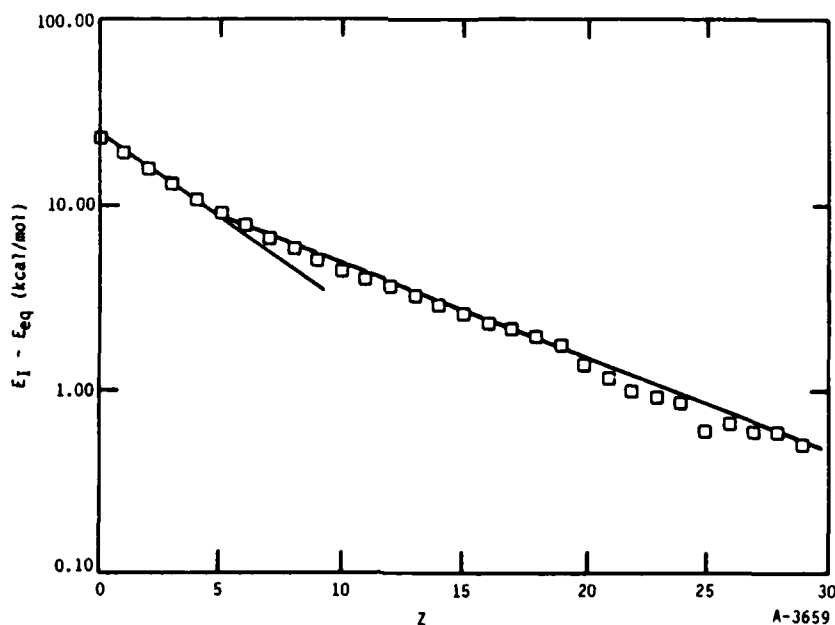


Figure 24. Oxygen Internal Energy Above the Equilibrium Value, $E_I - E_{eq}$, as Function of Number of Collisions with Oxygen Atom Thermal Bath. Initial bath and oxygen molecule ensemble initial conditions are: diatom internal energy, E_I , equals 26.3 kcal/mol, rotational energy, E_R , equals 0.0, and bath temperature, T_B , equals 750 K.

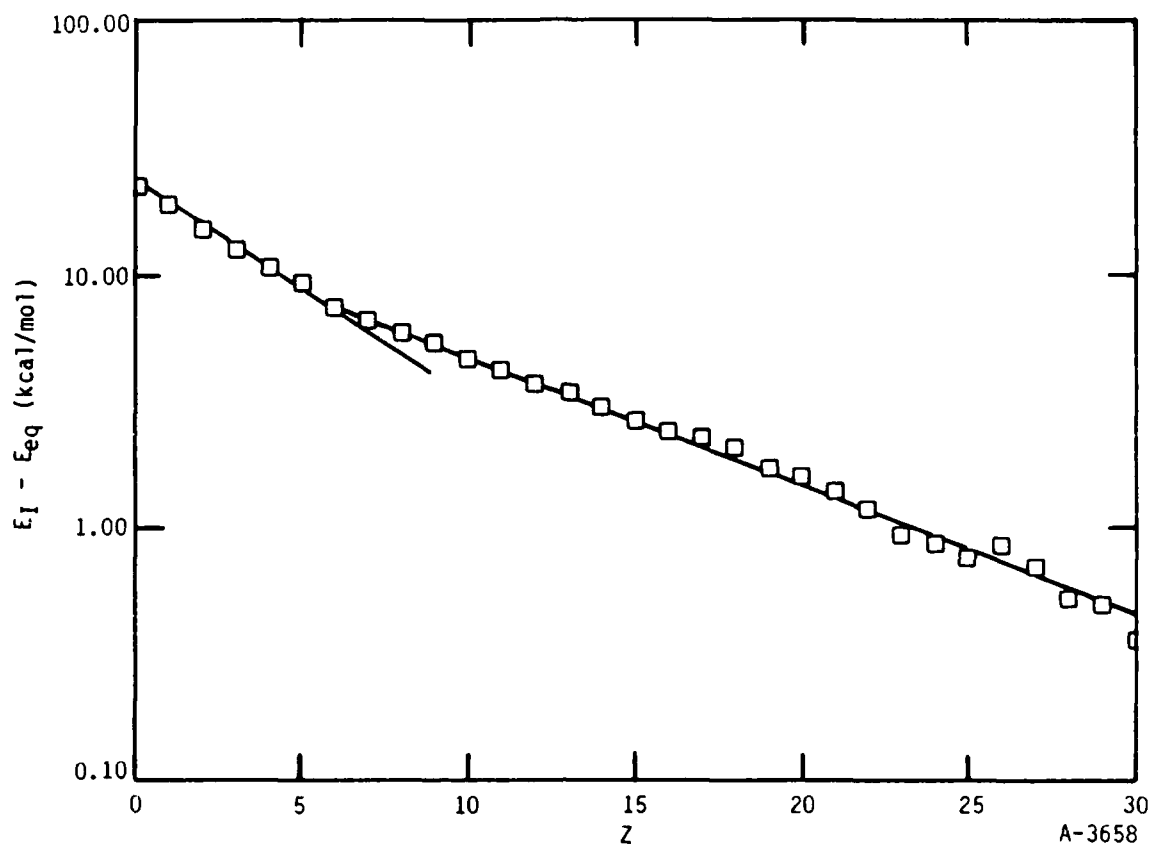


Figure 25. Oxygen Internal Energy Above the Equilibrium Value, $E_I - E_{eq}$, as Function of Number of Collisions with Oxygen Atom Thermal Bath. Initial bath and oxygen molecule ensemble initial conditions are: diatom internal energy, E_I , equals 26.3 kcal/mol, rotational energy, E_R , equals 0.0, and bath temperature, T_B , equals 1000 K.

energy transfer increases with increasing relative translational energy. Therefore after the initial transient in which rotational energy is pumped into the molecule the relaxation rate increases with bath temperature. This again is seen in Figures 21 through 25.

In summary two relaxation regimes are seen for the relaxation of highly excited oxygen diatoms in an atomic bath. The first regime is a short time regime persisting until rotational energy is transferred into diatom. During this period relaxation is very rapid and the rate increases with decreasing bath temperature. A second relaxation regime occurs after a rotational steady state is built up in the diatom. Relaxation proceeds at a slower rate and the rate of relaxation increases with bath temperature.

The behavior of the two cases in which some of the initial molecular energy was put into rotational energy is shown in Figures 26 and 27. Note that the initial value of the rotational energy was below the value of the steady state value and an increase in average diatom rotational energy was computed during the first few collisions. The average rotational energy increases from its initial value of 2.3 kcal/mol to about 4.5 kcal/mol after three collisions for both the 300 and 400 K atom baths. Nevertheless the effect of initial rotational energy is readily seen by comparing Figure 21 with Figure 26 for the 300 K bath case and correspondingly Figure 22 with Figure 27 for the 400 K bath case.

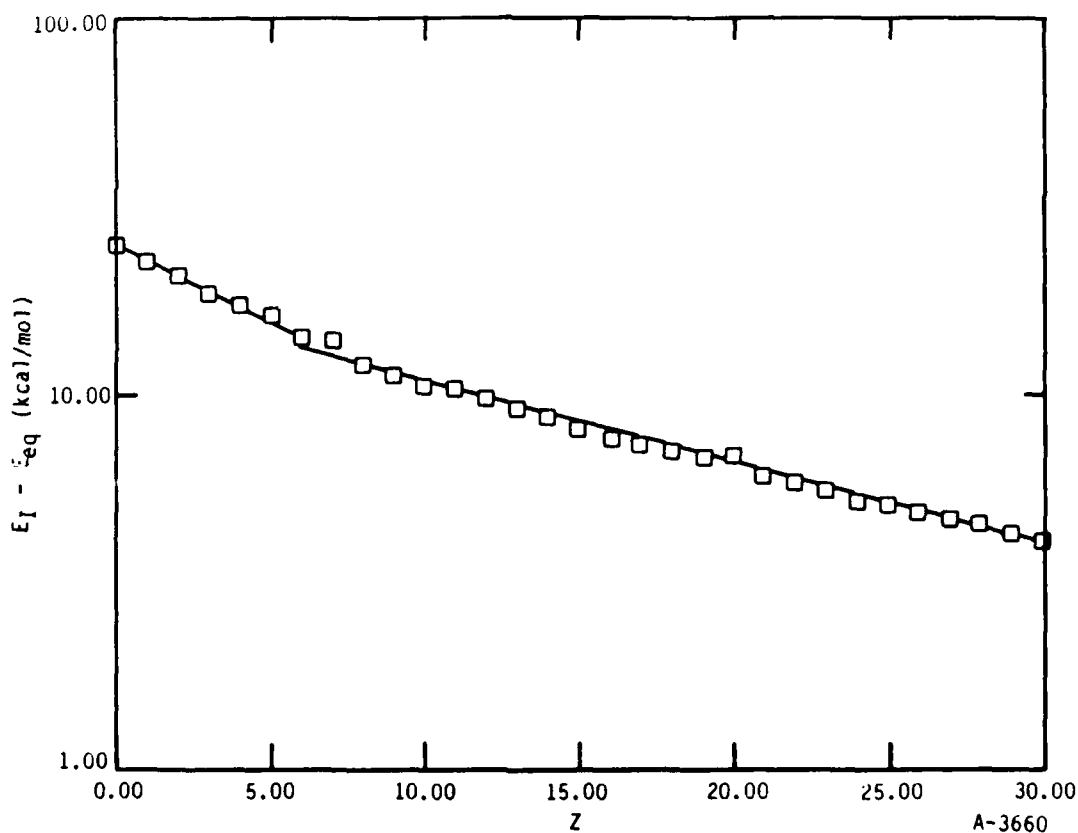


Figure 26. Oxygen Internal Energy Above the Equilibrium Value, $E_I - E_{eq}$, as Function of Number of Collisions with Oxygen Atom Thermal Bath. Initial bath and oxygen molecule ensemble initial conditions are: diatom internal energy, E_I , equals 26.3 kcal/mol, rotational energy, E_R , equals 2.89 kcal/mol, and bath temperature, T_B , equals 300 K.

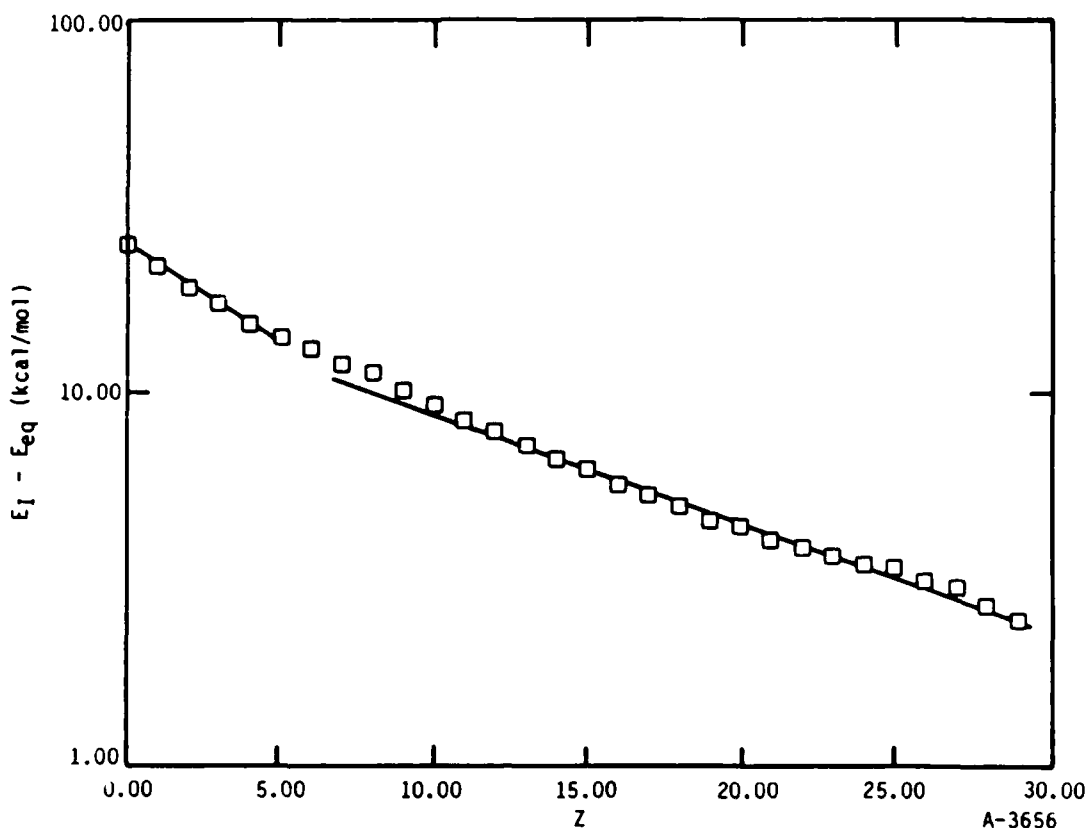


Figure 27. Oxygen Internal Energy Above the Equilibrium Value, $E_I - E_{eq}$, as Function of Number of Collisions with Oxygen Atom Thermal Bath. Initial bath and oxygen molecule ensemble initial conditions are: diatom internal energy, E_I , equals 26.3 kcal/mol, rotational energy, E_R , equals 2.89 kcal/mol, and bath temperature, T_B , equals 400 K.

Initial diatom rotational energy reduces the initial rapid relaxation rate in the early time regime. The differences in relaxation vanish after about ten collisions by which time a rotational energy steady state is achieved. The long time relaxation rates of initially rotating and non-rotating ensembles are identical. However, since much of the ensemble relaxation occurs during the first few collisions, the non-rotating cases show an overall faster relaxation rate. It is anticipated that an ensemble containing rotational energy equal to the steady state value would relax according to a single exponential decay law.

The evolution of the average molecular energy distribution as a function of number of collisions with the atomic bath is a quantity of interest. The

initial distribution function is a delta function at 26.3 kcal/mol. At equilibrium, when fully relaxed by the thermal bath, it becomes a Boltzmann function. The molecular energy distributions after one, five, ten, twenty and twenty-five collisions are shown in Figures 28 through 32 respectively for an initially non-rotating diatom in a 500 K atomic bath.

After one bath collision (Figure 28) the distribution of energies has broadened substantially from the initial delta function at 26.3 kcal/mol. Memory of the initial distribution is seen from the large peak for energies between 26 and 28 kcal/mol. The occurrence of large single energy transfers is readily seen by the large number of molecules below 16 kcal/mol. That part of the distribution is due to single collision energy transfers in excess of 10 kcal/mol. After five collisions (Figure 29) the molecular energy distribution is quite flat between 2 and 20 kcal/mol. Memory of the initial energy distribution is not apparent. After ten collisions (Figure 30) the distribution begins to take on a Boltzmann-like form. The bulk of the ensemble molecules have relatively low internal energies with the highest histogram peak for molecular energies between 0 and 2 kcal/mol. Note, however, that there are still substantial numbers of molecules with high values of total energy. At twenty collisions (Figure 31) the high energy part of the distribution is substantially reduced. This behavior becomes more apparent at twenty-five collisions (Figure 32) by which point 80 percent of the molecules have energies below 6 kcal/mol. It is clear that the rate of relaxation for this O_2/O model system is remarkably fast.

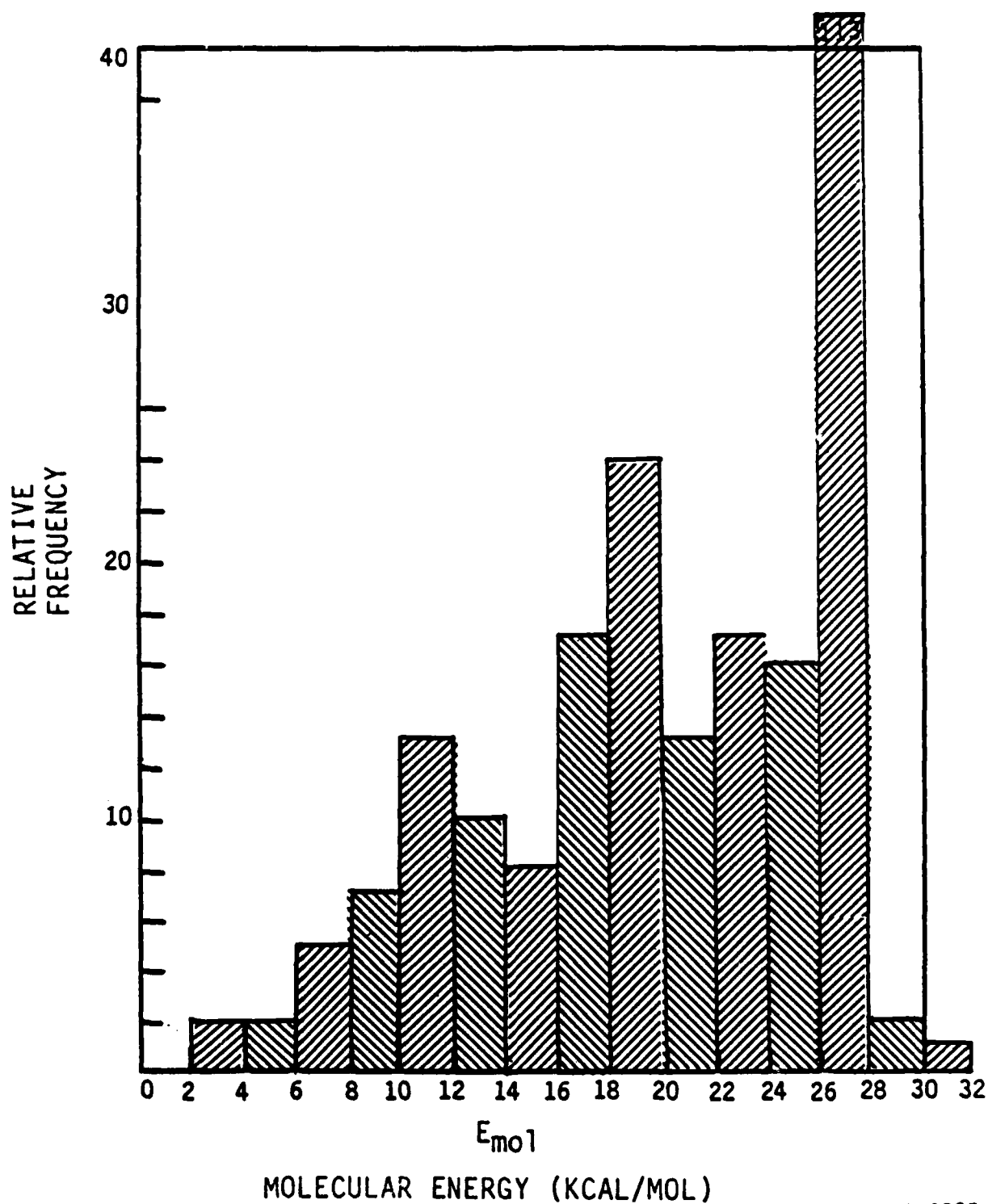
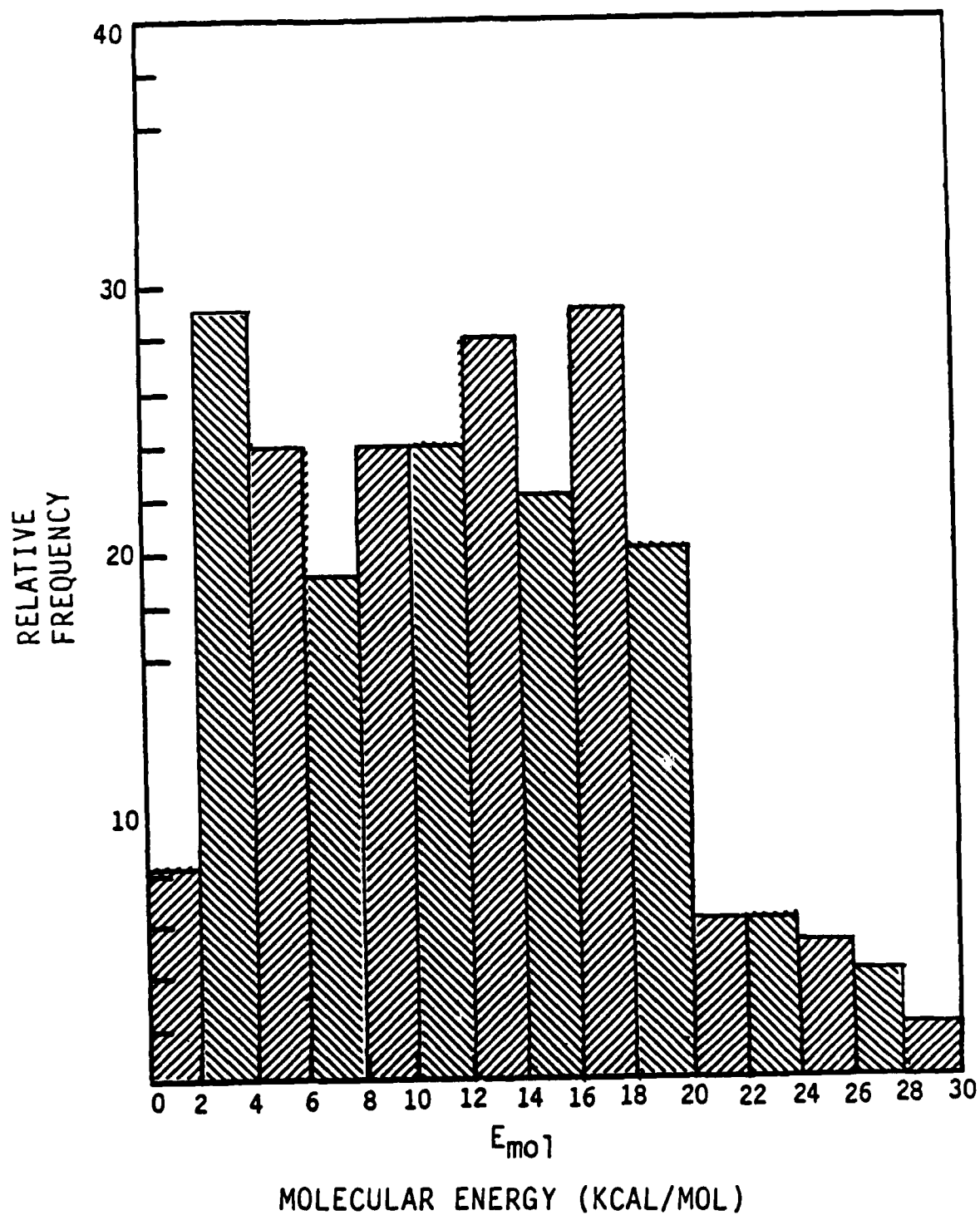


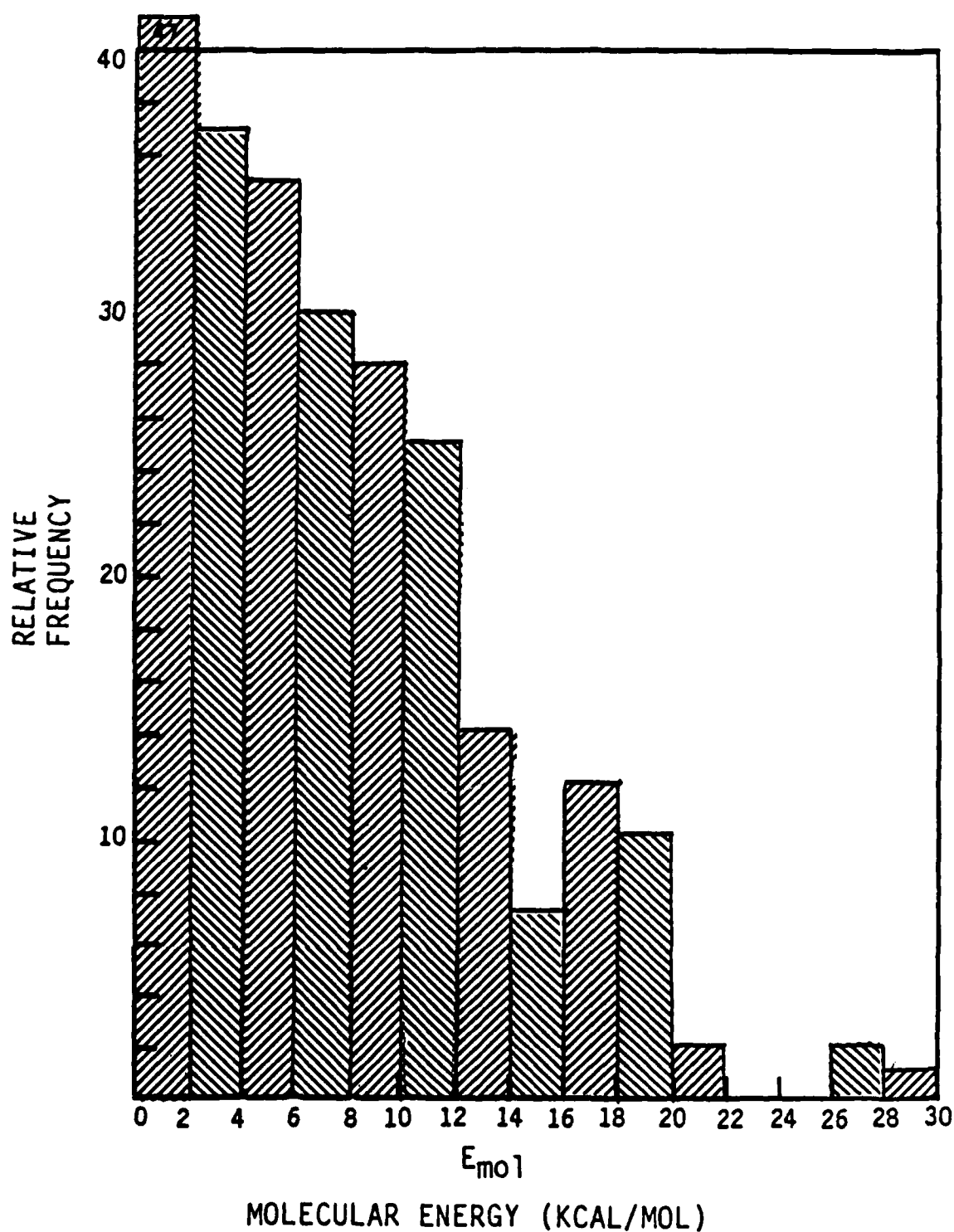
Figure 28. Distribution of O_2 Molecular Energies for O_2 Initially Excited 26.3 kcal/mol After One Collision with O-Atom Bath at 500 K

A-2035



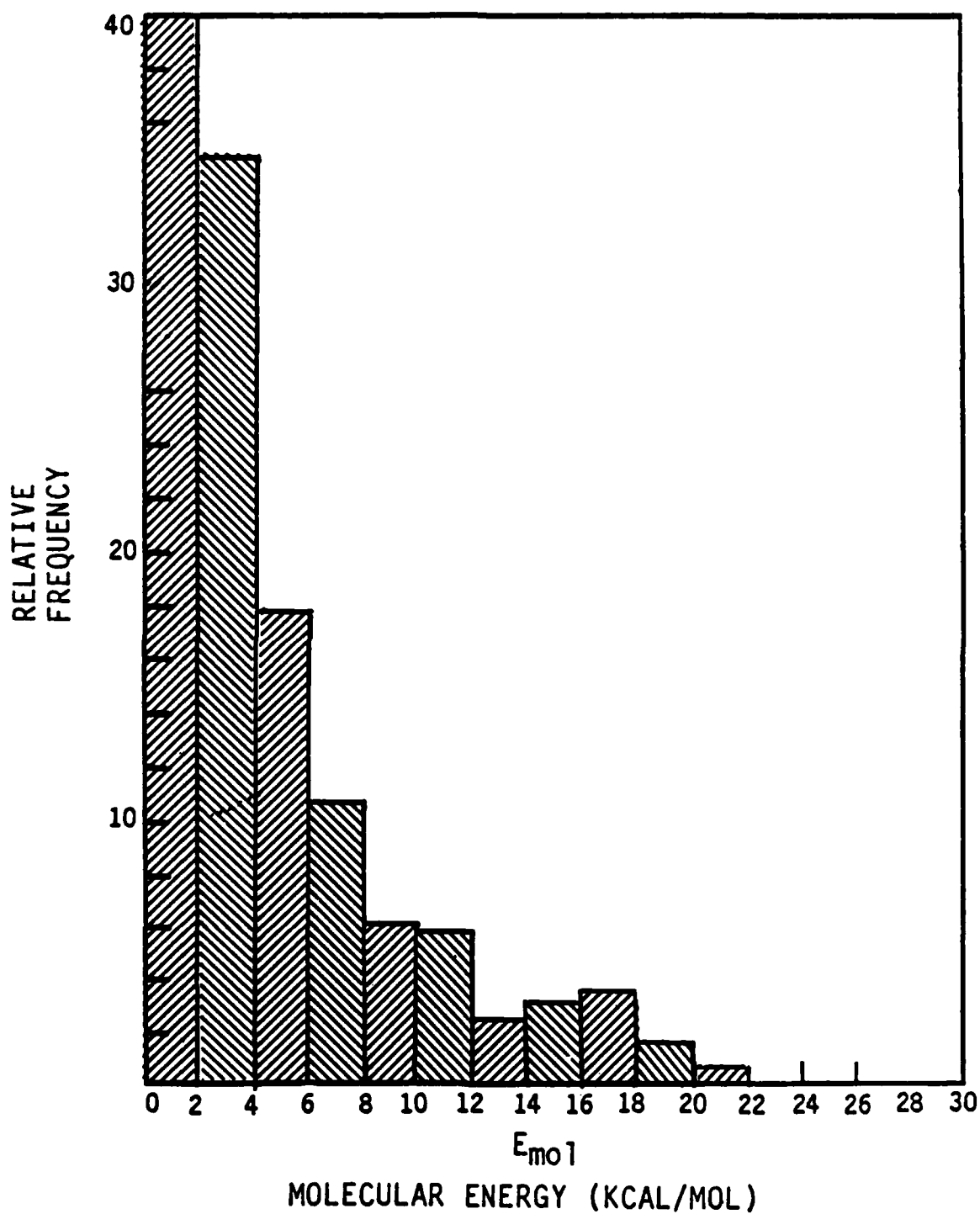
A-2034

Figure 29. Distribution of O₂ Molecular Energies for O₂ Initially Excited 26.3 kcal/mol After Five Collisions with O-Atom Bath at 500 K



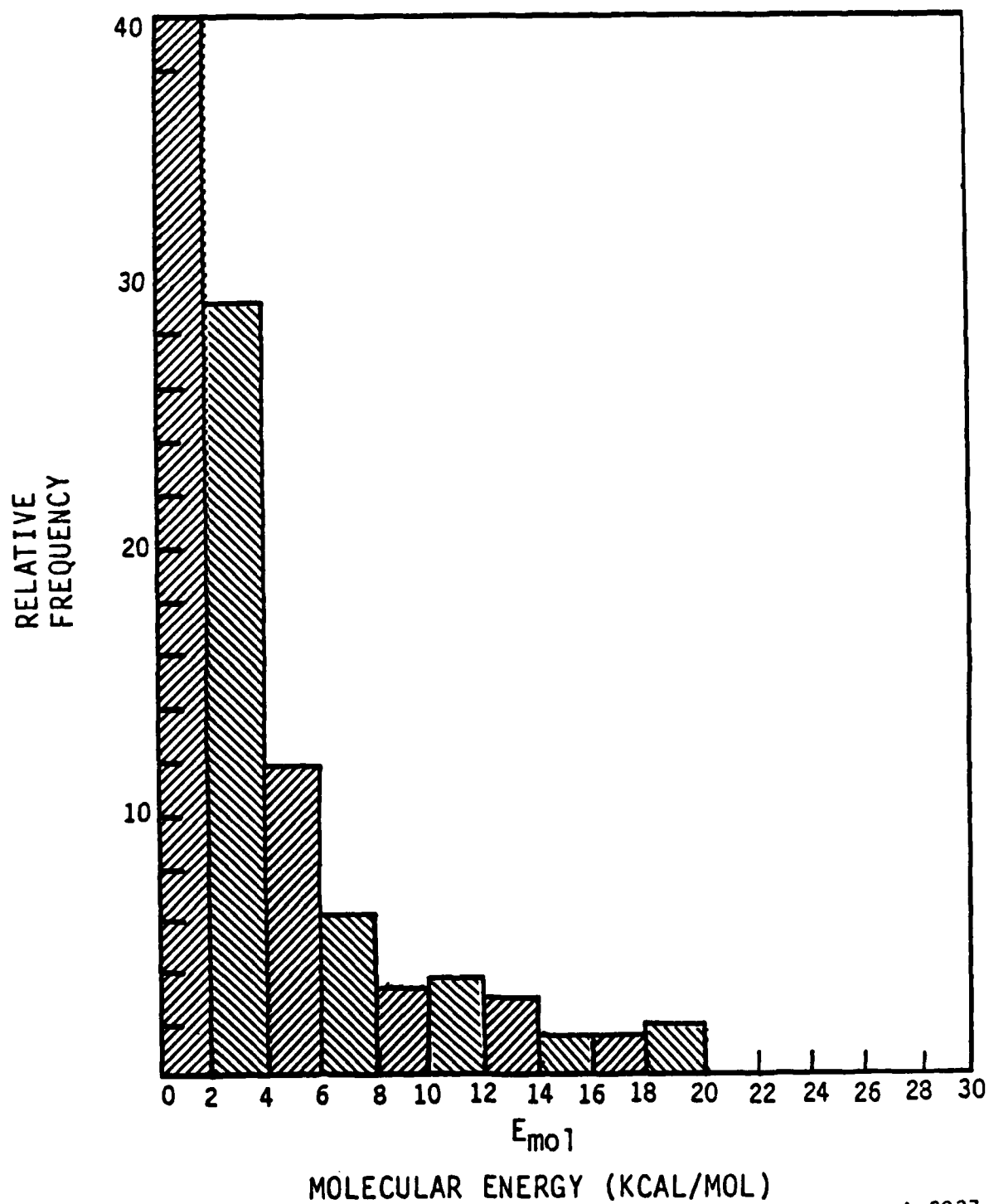
A-2036

Figure 30. Distribution of O₂ Molecular Energies for O₂ Initially Excited 26.3 kcal/mol After Ten Collisions with O-Atom Bath at 500 K



A-2038

Figure 31. Distribution of O₂ Molecular Energies for O₂ Initially Excited 26.3 kcal/mol After Twenty Collisions with O-Atom Bath at 500 K



A-2037

Figure 32. Distribution of O_2 Molecular Energies for O_2 Initially Excited 26.3 kcal/mol after Twenty-Five Collisions with O-Atom Bath at 500 K

REFERENCES

1. Stace, A.J. and Murrell, J.N., J. Chem. Phys. 68, 3078 (1978).
2. Varandes, A.J.C. and Murrell, J.N., Chem. Phys. Lett. 88, 1 (1982).
3. Gelb, A., J. Phys. Chem. 89, 4189 (1985).
4. Bunker, D.C., Meth. Comp. Phys. 10, 287 (1972).
5. Porter, R.N. and Raff, L.M. in Dynamics of Molecular Collisions, Part B, edited by W.H. Miller, Plenum, New York (1976).
6. Gelb, A., Kapral, R., and Burns, G., J. Chem. Phys. 56, 4531 (1972).
7. Osborn, M.K. and Smith, I.W.M., Chem. Phys. 91, 13 (1984).
8. Herzberg, G., Molecular Spectra and Molecular Structure. I. Spectra of Diatomic Molecules, Van Nostrand Reinhold Co., New York (1950).

DISTRIBUTION LIST

Ms. Mary Crawford, ACO
DCASMA
495 Summer Street
Boston, MA 02210

Ms. D. Cusick
Electronic Systems Division, PKR
Air Force Systems Command, USAF
Hanscom AFB, MA 01731-5000

W. Blumberg
Infrared Effects Div./LSI
Air Force Geophysics Laboratory
Hanscom AFB, MA 01731